Spring 1-1-2016

Ballistic Capture into Lunar and Martian Distant Retrograde Orbits

Collin J. Bezrouk
University of Colorado at Boulder, collin.bezrouk@colorado.edu

Ballistic Capture into Lunar and Martian Distant Retrograde Orbits

by

Collin J. Bezrouk

B.S., Engineering Mechanics and Astronautics, University of Wisconsin - Madison, 2012

M.S., Aerospace Engineering Sciences, University of Colorado - Boulder, 2013

A thesis submitted to the

Faculty of the Graduate School of the

University of Colorado in partial fulfillment

of the requirements for the degree of

Doctor of Philosophy

Department of Aerospace Engineering Sciences

2016

This thesis entitled:
Ballistic Capture into Lunar and Martian Distant Retrograde Orbits
written by Collin J. Bezrouk
has been approved for the Department of Aerospace Engineering Sciences

Jeffrey S. Parker

Dr. Daniel Kubitschek

Prof. Daniel Scheeres

Prof. Elizabeth Bradley

Prof. Daven Henze

Date

The final copy of this thesis has been examined by the signatories, and we find that both the content and the form meet acceptable presentation standards of scholarly work in the above mentioned discipline.

Bezrouk, Collin J. (Ph.D., Aerospace Engineering Sciences)

Ballistic Capture into Lunar and Martian Distant Retrograde Orbits

Thesis directed by Prof. Jeffrey S. Parker

Distant retrograde orbits (DROs) are a neutrally stable class of three-body orbits. Because of their stability, DROs cannot be targeted with a low-energy transfer along a stable manifold like unstable three-body orbits in the circular restricted three-body problem (CR3BP). However, in more complicated dynamical models, the effects of small perturbing forces can be exploited to build ballistic capture trajectories (BCTs) into DROs. We develop a method for building sets of BCTs for a particular reference DRO with recommendations for minimizing computational effort. Sets of BCTs are generated in the Earth-Moon system and the Mars-Phobos system due to their applicability to near-term missions and large difference in mass parameters. These BCT sets are stochastically analyzed to determine the range of conditions necessary for using a BCT, such as energy, solar system geometry, and origin. The nature of the DRO after the spacecraft is captured is studied, including minor body flyby altitudes and variations in the size and shape over time.

After a spacecraft has used a BCT, it can decrease its sensitivity to perturbations and extend its mission duration with a series of stabilizing maneuvers. Quasi-periodic orbits are constructed in the Earth-Moon CR3BP that lie on the boundary of stability, and closely resemble the DROs that result from using a BCT. Minimum cost transfers are then constructed between these quasi-periodic orbits and a target periodic DRO using a variety of methods for searching and optimizing. It is discovered that BCTs that target planar quasi-periodic DROs can be stabilized for about 15% of the cost of stabilizing a BCT with large out-of-plane motion.

Once a spacecraft is in a stable DRO, the long duration evolution of that orbit is of interest. Using a high fidelity dynamical model and numerical precision techniques, the evolution of several DROs in the Earth-Moon system is studied over a period of 30,000 years. The perturbing forces that cause a DRO to transition into an unstable orbit are identified and analyzed. DROs larger

than 60,000 km grow in amplitude due to solar gravity until they depart the Moon after several centuries. DROs smaller than 45,000 km remain stable for 25,000 years or more, but decay in size due to the Moon's solid tide bulge, which eventually causes the DRO to depart the Moon. The DROs evolve chaotically and occasionally experience periods of relatively fast amplitude growth when the period of the DRO is in resonance with the frequency of particular perturbing forces.

Dedication

To Maddy Jensen, my darling wife

Without you, this would have taken me several extra years to finish. Your drive, tenacity, and diligence are always an inspiration to me.

To Mom and Joe

Your constant love and overwhelming support made this possible. You are always there when we need you most, especially when we tried to plan our wedding for a week after my defense.

To Dad

When I was tempted by big salaries to leave school early, you reminded me that money will come, but this accomplishment will last forever.

In memory of Dr. George H. Born

Acknowledgements

It has been a privilege to work with so many people who made this dissertation possible. I wish to express my sincerest gratitude to Dr. Jeffrey Parker, my advisor and committee chair. His commitment to my success, support, patience, and advice for academia and for life, all while working two jobs, have made the challenges of doctoral work a pleasure. I would also like to express my deepest thanks to the rest of my committee. I am greatly appreciative to Dr. Dan Kubitschek for filling in for Dr. Born on such short notice and for encouraging me to finish like there was a fire under my heels. It has been a pleasure working with and learning from Dr. Dan Scheeres; his lessons in celestial mechanics and optimal trajectories became an integral part in several areas of my research, and I will remember his patience while I grasped to learn how to build invariant tori. I would also like to thank Dr. Daven Henze, whose course in numeric methods taught me how to solve so many problems in my research, and prepared me for more interview questions than I ever expected. I am also grateful to Dr. Liz Bradley for her assistance when parts of my research turned to chaos.

I have had the pleasure of working with many friends and colleagues at the Colorado Center for Astrodynamics Research. I would like to start by thanking Kate Davis, who taught my favorite course (with Jeff) and later let me help teach it. Her assistance with low-energy research was invaluable. To my roommate Jordan, I am glad you were willing to share an apartment with me; sorry I ate so much food. Thanks are also owed to Jake and Ann who helped me struggle through our coursework and reminded me to take our online quizzes. I enjoyed going through this experience with my friends Matt, Sibylle, Tyler, Jason, Kevin, Ryan, Nathan, Jon, Stijn, Carlos, and Jenny.

Generous support was provided for this research by the National Defense Science and Engineering Graduate (NDSEG) Fellowship program via the Air Force Office of Scientific Research and by the Lockheed Martin Space Systems Company. I am grateful for the generosity of these programs and I could not have pursued this research without it.

I'd also like to thank those outside the University that helped with this research, including Joshua Hopkins, William Pratt, and their team at the Lockheed Martin Space Systems Company for their valuable insights and probing questions. I also extend my gratitude to Nathan Strange and Gregory Lantoine from NASA's Jet Propulsion Laboratory for their guiding suggestions.

Finally, I'd like to express my appreciation for my family who supported and encouraged me through my graduate school career. This accomplishment belongs to you as much as it belongs to me.

Contents

Chapter

1 Introduction 1

1.1 Motivation 4

1.2 Literature Review 5

1.2.1 Classical Studies of the Three-Body Problem 5

1.2.2 Stability in the CR3BP 6

1.2.3 Transfers to Distant Retrograde Orbits 7

1.2.4 Optimal Trajectories 8

1.2.5 Orbital Capture 9

1.3 Dissertation Organization 9

2 Dynamical Models 12

2.1 The General Three-Body Problem 12

2.2 Circular Restricted Three-Body Problem 13

2.2.1 Equations of Motion 14

2.2.2 Jacobi Constant 15

2.2.3 Transformation Between Inertial and Rotating Frames 18

2.3 Elliptic Restricted Three-Body Problem 21

2.4 Jet Propulsion Laboratory's Development Ephemeris Model 21

2.5 Distributed Mass Models 22

2.5.1 Spherical Harmonic Gravity Field . . . 23
2.5.2 Polyhedral Model . . . 26
2.5.3 Mass Concentration Model . . . 29

3 Constructing Distant Retrograde Orbits 30
3.1 Distant Retrograde Orbits . . . 30
3.2 Generating DROs in the Circular Restricted Three-Body Problem . . . 34
3.2.1 Single Shooting and Continuation Method . . . 34
3.2.2 Curve-Fitting Initial Conditions . . . 39
3.3 Transforming DROs into the Full Ephemeris . . . 48
3.3.1 Orthogonal Crossing . . . 49
3.3.2 Multiple Shooting Differential Corrector . . . 51
3.3.3 Method Comparison . . . 54

4 Stability of Distant Retrograde Orbits 57
4.1 Stability Definitions . . . 57
4.2 Local Stability in the CR3BP . . . 59
4.3 Stability of DROs in the CR3BP . . . 62
4.3.1 Periodic DRO Stability . . . 62
4.3.2 Quasi-Periodic DROs . . . 64
4.4 Stability of DROs in High Fidelity Models . . . 69
4.4.1 Perturbation Analysis Setup . . . 69
4.4.2 Results of the Perturbation Survey . . . 71
4.4.3 Inclined DRO Stability . . . 76
4.4.4 Two-Dimensional Stability Maps . . . 77
4.4.5 Higher Dimensional Stability Maps . . . 80

5 Ballistic Capture into Earth-Moon Distant Retrograde Orbits 83

5.1 Ballistic Capture into DROs . . . 83

5.1.1 Stability Maps . . . 83

5.1.2 Characterizing Ballistic Capture Trajectories . . . 88

5.1.3 Lunar Flyby Geometry . . . 92

5.1.4 Trajectories Prior to Capture in the Earth-Moon System . . . 97

5.1.5 Geometry at Arrival of the Earth-Moon System . . . 101

5.1.6 Conclusions Regarding Ballistic Capture . . . 104

5.2 Changing the Epoch of a Ballistic Capture Trajectory . . . 104

5.2.1 Identifying Ideal Epochs . . . 105

5.2.2 Adjusting Capture State . . . 109

6 Ballistic Capture into Mars-Phobos Distant Retrograde Orbits 112

6.1 Motivation . . . 112

6.2 Constructing Distant Retrograde Orbits at Phobos . . . 114

6.3 Dynamical Modeling and Orbit Propagation . . . 115

6.3.1 Mass-Concentration Model . . . 115

6.4 Mars-Phobos Stability Maps . . . 117

6.4.1 Adaptive Meshing for Stability Maps . . . 118

6.4.2 Alternate Analyses Enabled by Adaptive Meshing . . . 121

6.4.3 Building Mars-Phobos Stability Maps . . . 123

6.4.4 Refining Stability Maps . . . 125

6.5 One-Way Stable Trajectories . . . 129

6.5.1 During and After Capture . . . 129

6.5.2 Before Capture . . . 133

6.5.3 On Approach to Phobos . . . 136

6.6 Conclusion . . . 136

7 Stabilizing a Distant Retrograde Orbit 140

7.1 Optimal Trajectory Theory . . . 140

7.1.1 Necessary Conditions . . . 141

7.1.2 Optimally Controlled Arcs . . . 142

7.1.3 Impulsive Transfers . . . 145

7.1.4 Constructing the Primer Vector . . . 148

7.1.5 Indirect Optimization with Primer Vector Theory . . . 150

7.2 Selecting Quasi-Periodic DROs . . . 152

7.3 Targeting the Reference DRO . . . 154

7.4 Transfers to an Arbitrary DRO . . . 158

7.5 Stabilizing Maneuvers . . . 160

8 Long Duration Stability of Distant Retrograde Orbits 165

8.1 Conventions and Nomenclature . . . 165

8.2 DRO Selection . . . 166

8.3 Orbit Propagation . . . 167

8.3.1 Mitigating Numerical Errors . . . 167

8.3.2 The Integrator . . . 170

8.3.3 High-Fidelity Dynamical Model . . . 172

8.4 Long Duration Evolution . . . 175

8.4.1 The 36,000 km DRO . . . 177

8.4.2 The 45,000 km DRO . . . 179

8.4.3 The 62,500 km DRO . . . 181

8.4.4 The 67,000 km DRO . . . 183

8.5 Root Cause of Unstable Evolution . . . 184

8.6 Conclusions on DRO Evolution . . . 186

9 Summary and Conclusions 189

9.1 Contributions to the Field 189

9.1.1 Summary of Ballistic Capture Techniques 190

9.1.2 Summary of Stabilizing Maneuvers 192

9.1.3 Summary of Long Duration Stability of DROs 192

9.2 Conclusions 193

9.3 Future Work 193

Bibliography 196

Appendix

A Fitted Functions for DRO Initial Conditions 204

A.1 Initial Velocity 204

A.2 Period 205

List of Tables

Table

4.1 A list of the average magnitude of each perturbation. DRO dependent values assume a 65,000 km (∼12.5 day) orbit. 71

5.1 Number of trajectories in each category for the 50,000 km and 70,000 km DROs. . . 88

5.2 Maximum altitude range of each flyby geometry after the lunar flyby. 95

6.1 Classifications for trajectories in a stability map 119

6.2 Initial cells of the quadtree meshing algorithm 120

8.1 A list of the size bands where DROs remain stable for more than 100 years. The orbit selected from each band is listed in the third column. 166

8.2 A comparison between double, double-double arithmetic (DDA), and quadruple precision. 170

8.3 The energy drift comparison between a DDA and a double precision integrator. . . . 171

A.1 The coefficients for use in Equations A.6. 205

A.2 The coefficients for use in Equations A.10. 206

List of Figures

Figure

1.1 Stability maps in three dynamical models. 3

1.2 An example of a ballistic capture trajectory arriving from interplanetary space and being captured around the Moon. 3

2.1 The mass parameter and distance units for many three-body systems in the solar system. The legend indicates the major body. 15

2.2 The coordinate frame for the CR3BP. The primaries sit on the x-axis. r_1 and r_2 are the distances from the primaries to the massless body. 16

2.3 The zero-velocity curves for eight Jacobi constants. 17

2.4 A polyhedron with a surface defined by a set of triangular faces 27

3.1 DROs in the rotating and inertial frames 32

3.2 A DRO with incremental τ values, which define a position along the path of the orbit. 33

3.3 Initial velocity for a DRO compared to a circular orbit 38

3.4 The Jacobi constant for DROs in the Earth-Moon CR3BP. 39

3.5 The periodic DRO's x-intercept after half of a period surrounded by the trajectories that are 50% closer and further away from the minor body. 41

3.6 The log of the initial velocity forms a hyperbola with respect to the log of the mass parameter. 41

3.7 The hyperbola's six coefficient values as a function of the initial radius. Polynomials are fit to these curves. 44
3.8 The period can be modeled as a sigmoid function with respect to the log of the mass parameter. 46
3.9 The derivative of the S-curves forms a skewed normal distribution. 46
3.10 The coefficients for the Equation 3.35 as a function of the log of initial radius from the minor body. 47
3.11 DRO initial conditions in full ephemeris inertial states 49
3.12 Velocity after correcting for full ephemeris. 50
3.13 The direct transformation of the DRO patchpoints from the CR3BP to an inertial frame does not create a continuous trajectory. 52
3.14 The propagated patchpoints after Level 1 correction; the trajectory is continuous in position and time, but not velocity. 53
3.15 The 70,000 km DRO has been successfully transformed into an inertial, full ephemeris frame after four iterations of level 1 and level 2 correction. 55
3.16 A comparison between the two methods for generating initial conditions. 56

4.1 Examples of systems with different stability classifications 58
4.2 Stability of DROs in the CR3BP 64
4.3 A two-dimensional torus can uniquely define a position on its surface with two angle coordinates. 65
4.4 The discretization scheme shown on a standard torus. Subscript n corresponds to θ_1 and subscript m corresponds to θ_2. 67
4.6 The initial guess for the 1D torus (blue). After propagating for one period, the final torus (red) does not match the initial torus and must be corrected. 68
4.7 Stability of a set of DROs under different perturbations. Colored lines represent stable orbits. 72

4.8 Two mode shapes in high fidelity DROs 73
4.9 The Poincaré section of a quasi-periodic, planar 65,000 km DRO in the CR3BP and the bounding unstable periodic orbit that surrounds its stable region 74
4.10 Poincaré sections for all of the xz-plane crossings for orbits between 30,000 and 110,000 km. The bottom row includes the effects of solar gravity, while the top row does not have perturbations applied. 76
4.11 The stability duration of inclined DROs between 20,000 and 70,000 km. The red line shows the boundary of the stable region in the CR3BP for comparison. 78
4.12 The mean of 28 inclined DRO pseudo-inclination stability maps spanning the lunar period. 79
4.13 The 2D stability map for the 45,000 km DRO. 80

5.1 Stability maps in three dynamical models. 85
5.2 The stability map for a DRO with initial conditions outside of the case 2 stable regions found in Section 4.4.2 86
5.3 A high resolution stability envelope with solar gravity. Blue points represent ballistic capture trajectories that are stable for at least 100 years. 87
5.4 The stability maps for a 50,000 km DRO (a) and a 70,000 km DRO (b). 88
5.5 Examples of indirect (top) and direct (bottom) capture trajectories shown in the inertial (left) and rotating frames (right). Indirect captures orbit the Earth before a close flyby of the Moon brings the body into a DRO. Direct captures are immediately captured into DROs. 89
5.6 A logarithmic histogram of the time between capture in the Earth-Moon system and capture into the 70,000 km DRO. 91
5.7 The vector field plots showing the states of the capture trajectories in the synodic frame at the lunar periapse prior to capture into the DRO. 93

5.8 The four DRO capture geometries. These plots show the states along the four bands propagated forward in time for 100 days. 94

5.9 Histogram of the Jacobi constant for each BCT evaluated at the capture lunar flyby. 95

5.10 The forward stable trajectory's points on the stability maps for a 50,000 km DRO (a) and a 70,000 km DRO (b), colored by their family designations. Alongside each axis are four the kernel density functions, which approximate the density of points of each family along that axis (like a histogram). Family 1 - blue, family 2 - red, family 3 - green, and family 4 - black. 96

5.11 This map shows stable manifolds that are divided by their closest approach to Earth. Red points pass within 192,000 km, and blue points do not. Many of the blue points are direct capture trajectories. 97

5.12 A histogram of the Sun-Earth-Moon angle at the time where each trajectory makes its capture flyby of the Moon. Angles greater than zero mean the Moon is in a waning phase, and angles less than zero mean the Moon is in a waxing phase. . . . 98

5.13 A scatter plot of the heliocentric semi-major axis and eccentricity of a BCT prior to capture by the Earth-Moon system. 98

5.14 ΔV requirement at Earth periapse for entering a BCT based on V_∞ at arrival in the Earth-Moon system. 99

5.15 A scatter plot of the heliocentric semi-major axis and inclination relative to the ecliptic of a BCT prior to capture by the Earth-Moon system. 100

5.16 The V_∞ histogram for the BCTs arriving at Earth from interplanetary space. 101

5.17 A scatter plot of the right ascension and declination of the BCTs as they arrive at the Earth-Moon system. 102

5.18 A vector field plot showing the incoming BCTs at the point where they enter the Earth-Moon SOI (event one). 103

5.19 Histograms of longitude and elevation angles when the 70,000 km DRO's BCTs arrive at the Earth-Moon SOI. They are separated by family designation to show family trends. 103

5.20 The magnitude of the acceleration difference between a BCT state at the original epoch and at times surrounding a target epoch. 108

5.21 The BCT in the rotating frame translated to three different epochs: the epoch with the smallest acceleration difference (blue), the local minima that is closest to the target epoch (red), and the target epoch itself (gold). 108

5.22 The BCT in the rotating frame before and after a PSO adjusts the final patchpoint for minimum variations in amplitude. 111

6.1 The log of the acceleration error-vector's magnitude for the 1,000 mascon model when compared to a truth solution for the Phobos shape model. These errors are computed around Phobos' equator. 117

6.2 The rotating frame and the VNC coordinate frame are aligned at the starting epoch. Not drawn to scale. 118

6.3 The four cells used to initialize the quadtree algorithm. Red points mark the position of the cell. Blue points show what $\Delta\vec{v}$ is used to evaluate the class of the cell. 120

6.4 Stability map boundaries for different DRO sizes in the Earth-Moon CR3BP. 122

6.5 The size of the stable region in a stability map versus the propagation time. 123

6.6 The stability map for a 26 km DRO where Phobos is treated as a point mass. 124

6.7 The stability map for a 26 km DRO in the Mars-Phobos system using the high fidelity dynamical model. 125

6.8 The 26 km DRO's stable points (green), the convex hulls (black) for each stable region, and the minimum bounding ellipses (blue) and larger bounding ellipses (orange). 126

6.9 The refined stability map for a 26 km DRO, based on the larger bounding ellipses shown in Figure 6.8. Light blue points are ballistic capture trajectories. The cell borders are not drawn because they obscure high resolution data. 128

6.10 The position and velocity at the first flyby, which leads to capture into a DRO around Phobos. 130

6.11 The time to travel from 200 km to the capture flyby. 131

6.12 The minimum and maximum radii the BCTs have after their capture flyby. The black line shows a 1:1 slope, meaning trajectories on this line had their minimum radius when they were captured. 132

6.13 The distribution of out-of-plane or z-amplitude for the set of ballistic capture trajectories. 132

6.14 The true anomaly of Phobos at the time of each capture flyby. 133

6.15 The average semi-major axis and inclination of each BCT with respect to Mars prior to capture. 134

6.16 The period of the walking orbits leading to a ballistic capture at Phobos. 135

6.17 A stability map seeded from the capture flyby state of the reference trajectory. These states are only propagated forwards in time. Green states stay around Phobos for >10 days, blue states escape, and red states impact within 10 days. 137

6.18 The reference trajectory as it approaches from 200 km, performs the capture flyby, and winds onto the DRO. Black points separate 30 minute increments for the first 12 hours. 138

7.1 An example of a two-impulse transfer's switching function. 145

7.2 An example of an impulsive transfer with a cusp, or a discontinuity in $\dot{S}$. 147

7.3 Examples of transfers that violate the condition that $\dot{p} = 0$ at impulses. 150

7.4 A trajectory that needs a third impulse to drive $p \leq 1$ for the whole transfer. 151

7.5 The stability map for the 70,000 km DRO in the Earth-Moon CR3BP. 153

7.6 The stable points and boundary of stability for the 70,000 km DRO in the Earth-Moon CR3BP. The red points are used as a set of quasi-periodic orbits to build minimum cost transfers into less sensitive periodic DROs. 153

7.7 The cost of a transfer from a position on the quasi-periodic orbit (τ_1) to a position on the periodic DRO (τ_2). 156

7.8 The example transfer (black) between the quasi-periodic orbit (blue) and the periodic DRO (red) after being fully optimized. It has a cost of 12.0 m/s. 157

7.9 The ΔV to transfer to the periodic orbit (blue) compared with the ΔV used to generate the quasi-periodic orbit (red). 158

7.10 The ΔV to transfer to an arbitrary periodic orbit (blue) compared with the ΔV used to generate the quasi-periodic orbit (red). 160

7.11 Stability map boundaries built at various longitudes around the reference DRO. The boundary still represents velocity perturbations, but is drawn on the reference orbit to indicate its origin and longitude. 162

7.12 A quasi-periodic orbit before (blue) and after (red) an optimal stabilizing impulse. . 163

8.1 The mean of 28 inclined DRO stability maps spanning the lunar period. 167

8.2 The selected DROs plotted in the Earth-Moon rotating frame for three periods. . . . 167

8.3 A graphical representation of the division of bits between the mantissa (fraction) and the exponent for IEEE 754 double-precision format.[48] Image retrieved from www.wikipedia.org. 169

8.4 An illustration of the consistent geometry of the Earth and Moon's solid tides in the rotating frame. 174

8.5 The exterior and interior bounding ellipses for 10 years of stored states from the 36,000 km DRO. 176

8.6 The evolution of the x, y, and z-amplitudes of the 36,000 km DRO. 177

8.7 The evolution of the period of the 36,000 km DRO. 178

8.8 The evolution of the x, y, and z amplitudes of the 45,000 km DRO. 179

8.9 The evolution of the period of the 45,000 km DRO. 180

8.10 The evolution of the x, y, and z-amplitudes of the 62,500 km DRO. 182

8.11 The evolution of the period of the 62,500 km DRO. 182

8.12 The evolution of the x, y, and z-amplitudes of the 67,000 km DRO, inclined by 178°. 183

8.13 The evolution of the period of the 67,000 km DRO. 184

8.14 The evolution of the x, y, and z amplitudes of the 45,000 km DRO when the aspherical gravity and solid tide perturbations are not considered. 186

8.15 The evolution of the x, y, and z amplitudes of the 62,500 km DRO when the Sun's gravity is not considered. 187

Chapter 1

Introduction

Distant retrograde orbits (DROs) are becoming an increasingly popular target for several near-term missions. These orbits have been studied since the 1960s, but no spacecraft to date has used this type of orbit. The Jupiter Icy Moons Orbiter (JIMO) mission proposed by NASA planned on using a DRO around the Jovian moons, but was canceled in 2005.[73] NASA's proposed Asteroid Redirect Robotic Mission aims to retrieve an asteroid and may place it into a DRO around the Moon.[18,119]

Previous work by many different researchers show that DROs are stable orbits, even in the presence of some common perturbing forces. Stability for DROs has been demonstrated analytically in the Hill's Problem and numerically in the circular restricted three-body problem (CR3BP) using dynamical system theory.[11–13,19,50–52] This dissertation investigates the stability of DROs in higher fidelity dynamical models using stochastic methods. Mode shapes are discovered that can be activated by different perturbing forces. From this study, we identify DRO size ranges that offer the highest degree of stability. Advanced numerical techniques are applied to enable the propagation of DROs accurately for tens of thousands of years. This is used to study the long term effects of certain perturbing forces and which DROs they affect. It has the benefit of identifying resonances which can cause relatively rapid growth of the orbit in its mode shapes.

Because DROs are stable orbits in simplified dynamical models like the CR3BP, they do not have stable and unstable manifolds that offer low-energy transfer options as is typical with many types of three-body orbits. Past studies on transfers to DROs from some other trajectory can be

characterized in one of three ways. The first is a direct transfer, which involves two or more high-thrust maneuvers and potentially including powered flybys. These transfers often use the most fuel, but have the shortest time of flight.[126] The second type of transfer is a low-energy transfer to an unstable three-body staging orbit that intersects at least one position on the target DRO.[33] Then, at the intersection of the DRO and the staging orbit, an impulsive maneuver is used to enter the DRO. The third type of transfer is similar to the second; it follows a stable manifold of an unstable staging orbit, but transitions to the DRO gradually using low thrust.

An interesting byproduct of the methods used to characterize a DRO's stability in this dissertation is the discovery of trajectories that ballistically approach the DRO. The construction, characterization, and application of these low-energy, also known as weak stability boundary,[9,10] trajectories are the primary focus of this dissertation. We develop the stability map: a graphical depiction of the behavior of a reference DRO with a wide array of velocity perturbations. Ballistic capture trajectories are stable forward in time, but unstable backwards in time, and these types of trajectories exist near the boundary of stability of a DRO. They are made possible largely due to a perturbing force outside the three-body system. In the Earth-Moon system, the Sun's gravity converts part of a DRO's stable boundary into a chaotic dynamical system. Figure 1.1 below illustrates this by showing how introducing solar gravity causes the stable region (green) to be replaced with a chaotic border (red and blue). A fascinating conclusion from this is that these trajectories exist for many different DRO sizes, regardless of how stable they are. This discredits the notion that smaller, more stable DROs cost more fuel to enter than larger DROs, since they may all be targeted ballistically. A caveat to this conclusion is that DROs that are more stable are more difficult to target ballistically than their larger, less-stable neighbors.

Sets of the ballistic trajectories are constructed from a single reference DRO and they are characterized to determine their trends and limitations. This is applied to many parameters that are useful in mission design such as V_∞, Earth-Moon geometry, energy, etc. A portion of this dissertation focuses on interplanetary trajectories that arrive at the Earth-Moon system onto ballistic capture trajectories (BCTs) like the example shown in Figure 1.2, though this method has also

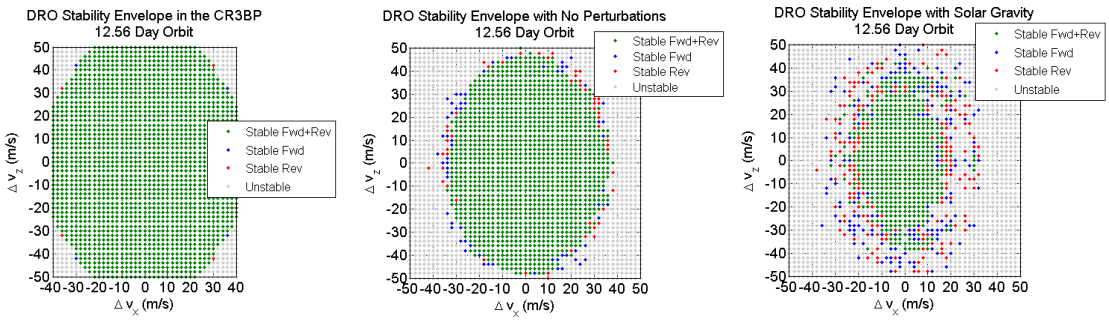

(a) CR3BP (b) Full ephemeris Earth and Moon (c) Solar gravity

Figure 1.1: Stability maps in three dynamical models.

been used to create BCTs that arrive from the Earth as well.[95] We also study BCTs that exist for DROs in the Mars-Phobos system and compare the findings with Earth-Moon BCTs. Some heuristic techniques are discussed for building and manipulating these BCTs in a high fidelity dynamical model. When a spacecraft arrives on a BCT at its host body, it is stable for some duration. However, it exists as a nearly unstable quasi-periodic DRO, and may be susceptible to departure due to mismodeled dynamics or state errors. We construct transfers from these quasi-periodic trajectories to less sensitive and longer lasting DROs. This is not only an exercise in building optimal transfers, but it also provides guidelines for what type of BCT to target for a mission to keep fuel costs low.

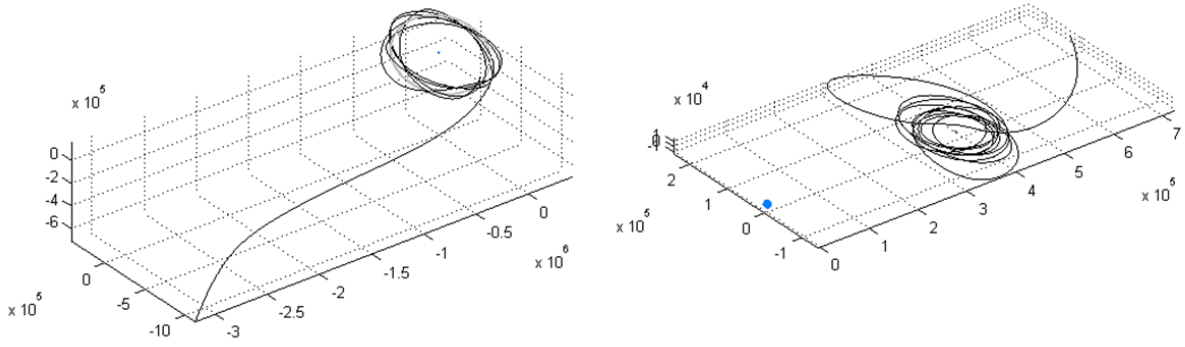

Figure 1.2: An example of a ballistic capture trajectory arriving from interplanetary space and being captured around the Moon.

1.1 Motivation

This research has applications to spacecraft mission design and is relevant to several proposed missions. One proposed and funded mission is the Asteroid Redirect Robotic Mission (ARRM), which will use a low-thrust engine to tow a small asteroid or a boulder from an asteroid, which has a high mass compared to a standard spacecraft. This high inertia means that any minimization in ΔV will translate to massive fuel savings. Using a BCT to enter a DRO around the Moon reduces the amount of time spent performing low-thrust maneuvers in the vicinity of the Earth and Moon. This reduces the risk of the asteroid ending up in an undesirable orbit if a spacecraft system fails, which could ultimately lead to an impact with the Earth or Moon.

A Mars Sample Return (MSR) mission can also take advantage of a DRO and its stability properties. One challenge with designing an MSR mission is the need to follow planetary protection guidelines,[34] which define rules to protect people from harmful substances in the extraterrestrial samples. Rather than return the sample to Earth, it can be placed in a DRO, which bypasses the need to design a safe reentry system. The sample can then be studied remotely, though in proximity to the Earth, or by sending crewed vehicles to the sample. The stability analysis in this dissertation will demonstrate how this sample can remain in a DRO without the need for correcting maneuvers for over tens of thousands of years.

Finally, a DRO may be useful for lunar far-side navigation and communications. Typically missions for this purpose are designed to have long-term coverage of the Moon's far side, such as L_2 halo orbits. While the DRO is at a disadvantage for having access to the far side for less than half of its orbital period, it has two distinct advantages over the unstable libration point orbits. First, the orbit is stable and does not require station-keeping maneuvers, which greatly increases the lifetime of the satellite. Second, the DRO can be much closer to the lunar surface than a halo orbit, which reduces communication lag and may give more accurate navigation results. Though DROs are typically planar, this thesis will show how they can remain stable as quasi-periodic orbits oscillating out of the Earth-Moon plane. Smaller DROs can oscillate more and can therefore avoid

many lunar occultations which would prevent far-side communication.

1.2 Literature Review

This literature review is written to identify the state of knowledge on several topics relevant to this dissertation. It provides a context for the work described in future chapters and how that works fits into and impacts the astrodynamics and low-energy mission design fields.

1.2.1 Classical Studies of the Three-Body Problem

The three-body problem was first examined in detail by Isaac Newton in *Philosophiae Naturalis Principia Mathematica*, also known as his "Principia", which was published in 1687.[87] He examined the general problem of the motion of three massive bodies under mutual gravitational attraction and applied this work to understand the motion of the Moon around the Earth accounting for perturbations from the Sun.

The first simplification to the general three-body problem was introduced by Leonhard Euler when he proposed the restricted three-body problem (R3BP), which studies the motion of a massless body in the presence of two massive bodies. In 1765, he published a paper regarding rectilinear motion in the general three-body problem, and discovered collinear equilibrium points between the two massive bodies.[37] In 1772, Joseph-Louis Lagrange extended this work by introducing the circular restricted three-body problem, which assumes that the two massive bodies are in circular orbits about their barycenter. He discovered the five libration points (L_1 through L_5) as fixed point solutions in the rotating frame of the CR3BP. Euler is generally credited with the three co-linear points (L_1, L_2, and L_3) and Lagrange is credited with the two equiangular (triangular) points (L_4 and L_5). Euler and Lagrange made contributions to the general three-body problem as well.

Newton showed that in the two-body problem, energy and angular momentum are conserved. In 1836, Carl Gustav Jacob Jacobi discovered a different integral of motion that exists in the CR3BP, which is called the Jacobi Integral or the Jacobi Constant.[61] Felix Tisserand applied the CR3BP to the study of comets making close approaches to planets in 1889.[122] He created an approximation of

the Jacobi constant called the Tisserand constant which is purely a function of the semi-major axis, eccentricity, and inclination of the comet. The Keplerian orbital elements before and after a close approach to a massive body lead to approximately the same Tisserand constant. In 1887, Heinrich Bruns proved that no other integrals of motion could exist as a function of position and velocity of the bodies.[20] Several years later, Henri Poincaré showed that there were also no integrals of motion that could be expressed if the mass parameter of the CR3BP was included in the expression as well.

Despite these discoveries, King Oscar II of Sweden offered a monetary prize for a solution to the general N-body problem ($N > 2$). He recognized that a solution might not exist and thus offered the reward to any work which significantly aided in the understanding of the N-body problem. It was eventually awarded to Henri Poincaré for his work describing the chaotic nature of the motion in the three-body problem and development of the Poincaré map.[7] The original problem that was proposed by King Oscar II was solved for $N = 3$ by Karl Sundman in 1912, when he derived an infinite series that gives the solution to the general three-body problem.[120] Unfortunately, this series has slow convergence and requires a prohibitive number of terms, even with modern computers, to be useful. An equally impractical infinite series for the full N-body was published in by Qiudong Wang in 1991.[107] Charles Delaunay created a useful, though still quite large, series to describe the Moon's motion under perturbations in 1846.[32]

1.2.2 Stability in the CR3BP

The study of stability in the CR3BP began with Gascheau in 1843 when he demonstrated the criterion for linear instability at the triangular Lagranian points.[41] Routh extended this study to prove the instability of the collinear libration points.[111] The true pioneer of studying stability in the CR3BP was Henri Poincaré. He discovered the characteristic exponent, as well as invariant (stable and unstable) manifolds emanating from periodic orbits.[7] In 1889 while revising a paper with an erroneous proof of stability in the three-body problem, he concluded that invariant manifolds of periodic orbits could intersect one another, resulting in chaotic motion. This prompted him to

create a highly used tool called a Poincaré return map or section. Poincaré's research and tools have been fundamental to studying periodic orbits in the three body problem and exhaustive research has been conducted using them.[3,43,59,70–72,93,109] The study of quasi-periodic orbit stability became possible with the formulation of Kolmogorov-Arnold-Moser (KAM) theory[5,68,83] in 1961, which enabled the study of a higher dimensional flow through phase-space.[63,64,90,91]

The study of stability of DROs in particular began in the 1960s. Hénon first showed in the late 1960s that DROs are stable in Hill's problem and have no true upper bound on size.[51,52] Broucke studied periodic orbits, including DROs in the Earth-Moon restricted three-body problem around the same time as Hénon.[19] In the mid 1970s, Benest studied the stability of orbits in the planar circular restricted three-body with varying mass ratios.[11–13] Since then, several people have researched the stability of DROs in full ephemeris and higher fidelity dynamical models for different three-body systems.[73,119]

1.2.3 Transfers to Distant Retrograde Orbits

There have been several different methods that have been studied in the literature for transferring to DROs. One method is to use direct impulsive transfers. This method was first studied for DROs in 1993 with Ocampo and Rosborough.[88] They examined two-impulse transfers into Sun-Earth DROs, which originate from Earth, the minor body. Welch and Parker performed a similar analysis on transfers from Earth (the major body) to DROs around the Moon.[126] They also included the cost benefit of performing a powered or unpowered lunar flyby on the way to the DRO, which often reduced the total ΔV cost. Minghu et al. also perform this study, but in a full ephemeris dynamical model.[82]

Another method uses dynamical systems theory and invariant manifolds to reduce the cost of part of the transfer. In 2007, Demeyer and Gurfil examined using stable manifolds to reduce the cost of a two-impulse transfer to a DRO. The first burn sends the spacecraft away from Earth along a stable manifold of an L_1 or L_2 Lyapunov orbit that tangentially intersects the position of the DRO. The second impulse is the velocity correction that transitions the spacecraft from

the Lyapunov orbit to the DRO. Scott also used manifold theory to build transfers using Fast Lyapunov Indicator maps.[116,117] He shows how a period-3 or period-4 DRO is unstable in the CR3BP, meaning it has stable and unstable manifolds which bring the spacecraft in the vicinity of a period-1 DRO. These transfers do not necessarily originate at a particular body. Capdevila et al. also studies low-energy and direct transfers to DROs.[23]

A third class of transfer options involves using weak stability boundary trajectories, such as Ballistic Lunar Transfers (BLTs).[9,10] Parker discusses BLTs to unstable libration point orbits in the Earth-Moon system, which use the Sun's gravity to raise a trajectory's perigee until it intersects the Moon's orbit.[93] This thesis uses weak stability boundary to build free transfers to DROs.

1.2.4 Optimal Trajectories

The theory behind optimal trajectories was founded by Lawden when he computed the necessary conditions for a two-body trajectory with maneuvers performed by a constant specific impulse engine. He went on to develop the necessary conditions for impulsive transfers as well.[75–77] In 1968, Lion and Handelsman created an indirect optimization method that showed how a reference trajectory could be adjusted to meet Lawden's necessary conditions by adjusting the timing of the initial and final impulse, and by adding an interior impulse to the transfer when necessary.[47] That same year, Jezewski and Rozendaal published an efficient method for computing optimal trajectories using an arbitrary number of interior impulses using a nonlinear programming algorithm.[62] Conway has a comprehensive summary of the work from these researchers, though he uses an optimal control theory formulation rather than the calculus of variations formulation used by Lawden.[28] Prussing developed the conditions for building optimal trajectories for spacecraft with variable specific impulse engines, such as those driven by solar electric propulsion.[103] He has applied primer vector theory to a number of problems with varying constraints.[104–106] All of the work described thus far was built specifically for the two-body problem. In 1992, Hiday developed followed the work of the Lawden and Lion and Handelsman to derive the necessary conditions and proofs for the elliptic restricted three-body problem. In 2006, Davis performed a similar derivation

for the necessary conditions in the circular restricted three-body problem. Both authors applied their work to building optimal transfers into libration point orbits.

1.2.5 Orbital Capture

In the three-body problem, it is possible for the bodies to exchange energy in such a way that one body that was previously on a hyperbolic trajectory is transitioned into an elliptic trajectory. This is an instance of orbital capture, and it has been studied extensively since the 1920s. The final motions of the three-body problem were fully characterized into seven classes of solutions in 1922 by Chazy.[26] One of these classes was called HE_k, or hyperbolic-elliptic, in which one body escapes while the other two remain in an elliptic orbit about their barycenter. This means that while the system energy must remain constant, the energy of individual bodies can be exchanged. Fesenkov is credited in 1946 with first conceiving of the mechanism of orbital capture through energy transfer with the close passage of several bodies.[94] One year later, Schmidt had shown that this was achievable with a minimum of three bodies. Sitnikov demonstrated with an example that this was possible numerically in 1953, and ten years later, Alexeyev used analytical methods to do the same.[2] This framework was applied in the 1970s to investigate the notion that some moons of other planets are actually captured bodies, like comets or asteroids.[6,21,53,58,81,86,100,121] For example, both of Mars' moons are believed to be captured asteroid belt objects.

1.3 Dissertation Organization

Chapter 2 defines the dynamical models and nomenclature used throughout the dissertation. These models are related to the three-body problem and its many simplifications, ranging from the general three-body problem to high fidelity models using full ephemeris positions for the planets and complicated perturbing forces. It also discusses methods for modeling the mass distribution of irregular bodies such spherical harmonic expansions, mass concentration models, and the polyhedron potential model.

Chapter 3 begins with a thorough description of distant retrograde orbits. It then discusses

the techniques and algorithms commonly used to generate three-body orbits in the dynamical models discussed in Chapter 2. This covers the single/multiple shooting differential corrector, orthogonal plane crossing detection, and algorithms for converting from simple models to high fidelity ones. This chapter also covers a new function that can be used to generate a DRO's initial conditions in the CR3BP given a desired mass parameter and DRO size.

Chapter 4 describes and applies dynamical systems theory to DROs in the CR3BP to understand the stability of the orbits. Methods for determining the stability of quasi-periodic orbits are discussed as well. Then the chapter turns to investigating stability of DROs in higher fidelity models. It begins by viewing a set of periodic DROs under a variety of perturbations to determine which forces will dominantly affect stability. Then we investigate quasi-periodic DROs which are generated by perturbing the initial velocity in one or two directions. This identifies which DRO sizes are and are not stable in the Earth-Moon system.

Chapter 5 uses the stability analysis from the previous chapter to construct ballistic capture trajectories by analyzing the behavior of a trajectory in forwards and backwards in time. The entire set of BCTs for two particular DROs is characterized and analyzed for its limitations in implementation for a mission. Chapter 6 applies the same strategy to the Mars-Phobos three-body system. Before doing so, however, it improves the algorithm by implementing an adaptive meshing routine that eliminates the unnecessary orbit propagations. The Mars-Phobos BCTs are analyzed in a similar fashion to the Earth-Moon BCTs and comparisons are made between the two.

Chapter 7 develops the tools used to stabilize a spacecraft after it has been captured onto a DRO using a BCT. We build minimum cost transfers between quasi-periodic DROs that are representative of those generated by ballistic captures and periodic DROs. Several techniques are used to attempt to find globally optimal transfers, but this is not guaranteed. Primer vector theory is applied to ensure transfers are locally optimal.

Chapter 8 investigates how long a spacecraft will remain on a DRO in a high fidelity dynamical model. Four DROs are propagated for up to 30,000 years in a model containing gravity from the Moon, Sun, and all planets, solar radiation pressure, aspherical gravity fields from the Earth and

Moon, and solid tide perturbations. A numerical technique called double-double arithmetic is applied in the integrator to increase the precision of states, which improves the accuracy of the integration over this long time span. The destabilizing perturbations are identified and where they strongly influence the DRO.

Finally, Chapter 9 provides concluding remarks, summarizes important findings, especially those that contribute to the field. Potential directions for future research in these topics are also discussed.

Chapter 2

Dynamical Models

This chapter covers the dynamical models that are used throughout this research. Because many of the topics in this dissertation pertain to three-body orbits, this chapter focuses mostly on variations of the three-body problem. It provides the equations of motion, the reference frames, and methods for transforming between models. This chapter also covers methods for modeling gravity due to irregular bodies.

2.1 The General Three-Body Problem

The general three-body problem is a model containing three massive bodies that act under mutual gravitational attraction. Each body is represented as a point mass. The force acting on body i is given by:

$$\mathbf{F}_i = m_i \ddot{\mathbf{r}}_i = -\sum_{\substack{j=1 \\ j \neq i}}^{N} \frac{G m_i m_j}{r_{ij}^3} \mathbf{r}_{ij} \text{ for } N = 3 \tag{2.1}$$

Where the relative position vector is given by $\mathbf{r}_{ij} = \mathbf{r}_i - \mathbf{r}_j$ which has a norm of $r_{ij} = \|\mathbf{r}_{ij}\|$. G is the gravitational constant and m_i is the mass of body i. These equations of motion are written for an inertial coordinate frame centered on the center of mass of the three-body system.

In many cases, it is convenient to define and propagate orbits relative to one of the bodies rather than the system's center of mass. This is useful when one of the bodies has significantly more mass than the the other two bodies ($m_1 > m_2 >> m_3$). This is the case when studying a satellite flying among two massive bodies such as the Earth and the Moon. Equation 2.1 can be

rearranged into a form that is relative to a central body:

$$\ddot{\mathbf{r}}_{\oplus sat} = -\frac{G(m_{\oplus} + m_{sat})}{r^3_{\oplus sat}}\mathbf{r}_{\oplus sat} + Gm_{\leftmoon}\left(\frac{\mathbf{r}_{sat\leftmoon}}{r^3_{sat\leftmoon}} - \frac{\mathbf{r}_{\oplus\leftmoon}}{r^3_{\oplus\leftmoon}}\right) \tag{2.2}$$

The term on the left side is recognizable as the two-body gravitational acceleration with the central body. The right term has two components, which are coined the direct and indirect effect. The direct effect term accounts for the gravity acting on the satellite from the third body directly. The last term is the indirect effect, which accounts for the acceleration on the central body due to the third body. The acceleration on the central body indirectly affects the acceleration on the satellite. This form of the equation is useful because it can be used to account for the gravity of multiple "third bodies". However, it can cause numerical difficulties if the third-body is a large distance from the central body and the satellite.[123]

2.2 Circular Restricted Three-Body Problem

If the satellite is considered massless, then the two massive bodies can be propagated with a two-body orbit about their barycenter. This is known as the Restricted Three-Body Problem (R3BP). To further study the three-body problem, researchers apply simplifications and approximations to the system. The Circular Restricted Three-Body Problem (CR3BP) is perhaps the most popular method of studying the three-body problem. This model assumes that the mass of one body is negligible compared to the other two bodies just as in the R3BP. It further assumes that the two massive bodies, which are sometimes called the *primaries*, are both in circular orbits about their barycenter. In this dissertation, the more massive primary will be referred to as the major body and the smaller primary is called the minor body. There is a further simplification that also assumes that all three bodies orbit in the same plane. This is called the Planar CR3BP, though this is just the CR3BP with reduced dimensionality. These approximations are quite accurate for many three-body systems and can offer substantial insight to the motion of a satellite in the three-body problem.

2.2.1 Equations of Motion

The CR3BP is defined in a rotating coordinate frame, sometimes called the synodic frame. The x-axis always passes through the centers of the two primaries, which rotate about the barycenter at a constant rate ω. Positive x is defined as pointing from the major body to the minor body. The z-axis is parallel to the system's angular momentum vector; that is, it is perpendicular to the orbit plane of the two primaries. Finally, the y-axis completes the orthonormal, right-handed coordinate system by pointing in the direction of the instantaneous velocity of the minor body. The CR3BP's origin lies at the barycenter of the two primaries.

This model also uses normalized coordinates so that results can be applied to many different systems. Distances are normalized such that the distance between the two primaries is equal to unity. Time is normalized such that the angular velocity of the primaries ω is also unity, which makes their orbital period equal to 2π. In this dissertation, normalized distance and time units are abbreviated as DU and TU, respectively. Finally, we normalize mass units such that the sum of the system's mass $(m_1 + m_2)$ is equal to unity. When we apply these normalizations, and the gravitational constant G is also equal to unity. The mass parameter μ is defined as the mass of the minor body m_2 over the sum of the mass of the primaries, shown in Equation 2.3.

$$\mu = \frac{m_2}{m_1 + m_2} \tag{2.3}$$

The mass parameter, by definition, must always be less than or equal to 0.5. To give an idea of the magnitude of these normalization constants, Figure 2.1 shows the mass parameter and distance units for many three-body systems in our solar system. The legend in this figure indicates the major body in each three-body system. The Pluto-Charon system has the highest mass parameter at 0.1085, followed next by the Earth-Moon system at 0.01215. The Sun-Planet three-body systems have similar mass parameters to many Planet-Moon systems, but with significantly larger distance units.

In the barycentric rotating frame the major body's position is fixed at $[-\mu, 0, 0]^T$ and the minor body is located at $[1-\mu, 0, 0]^T$. The distance of a body with position $[x, y, z]^T$ from the two

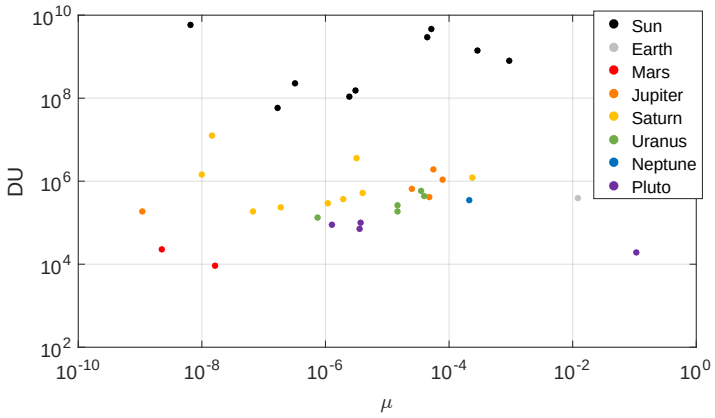

Figure 2.1: The mass parameter and distance units for many three-body systems in the solar system. The legend indicates the major body.

primaries is given by

$$r_1 = \sqrt{(x+\mu)^2 + y^2 + z^2} \tag{2.4}$$

$$r_2 = \sqrt{(x-1+\mu)^2 + y^2 + z^2}. \tag{2.5}$$

The coordinate frame and these relevant distances are shown in Figure 2.2 below. The equations of motion in the CR3BP are given by:[123]

$$\begin{aligned} \ddot{x} &= 2\dot{y} + x - (1-\mu)\frac{x+\mu}{r_1^3} - \mu\frac{x-1+\mu}{r_2^3} \\ \ddot{y} &= -2\dot{x} + y - (1-\mu)\frac{y}{r_1^3} - \mu\frac{y}{r_2^3} \\ \ddot{z} &= -(1-\mu)\frac{z}{r_1^3} - \mu\frac{z}{r_2^3}. \end{aligned} \tag{2.6}$$

2.2.2 Jacobi Constant

The equations of motion in Equation 2.6 can be manipulated to produce a constant of integration known as the Jacobi constant, C. This value is the only integral of motion in the CR3BP, and as such, it cannot be changed unless the body is affected by some perturbing force outside of the CR3BP, such as solar radiation pressure or a thrusting maneuver. C is given by

$$C = x^2 + y^2 + \frac{2(1-\mu)}{r_1} + \frac{2\mu}{r_2} - \dot{x}^2 - \dot{y}^2 - \dot{z}^2 = 2U - V^2. \tag{2.7}$$

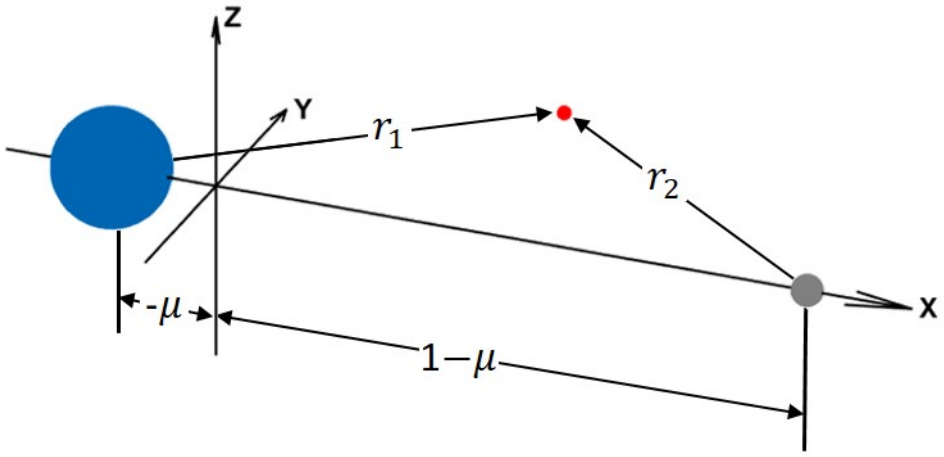

Figure 2.2: The coordinate frame for the CR3BP. The primaries sit on the x-axis. r_1 and r_2 are the distances from the primaries to the massless body.

Where V is the velocity magnitude and U is a force potential-like term with the form

$$U = \frac{1}{2}(x^2 + y^2) + \frac{1-\mu}{r_1} + \frac{\mu}{r_2}. \tag{2.8}$$

An interesting feature of the Jacobi constant is that there is no coupling between velocity and position terms. This means that for some given value of C, there are positions in space that are inaccessible to the spacecraft since the velocity would need to be imaginary ($V^2 < 0$). These regions are bounded by zero-velocity curves, which specifically are the locus of points where a body with a prescribed Jacobi constant could be located with zero velocity. The zero-velocity curves in the Earth-Moon system for eight Jacobi constants are shown in Figure 2.3 where the magenta regions are inaccessible. For Jacobi constants greater than approximately 3.18834, a spacecraft cannot access the Moon from the Earth. Values between 3.17216 and 3.18834 allow a spacecraft to reach the Moon from the Earth, but cannot escape the Earth-Moon system. Any Jacobi constant lower than about 3.17216 can cover any access either body from far beyond the Earth-Moon system, but higher values may need to utilize a lunar flyby to achieve this. Other three-body systems will have the same shape of inaccessible regions, but they will occur at different Jacobi constant values.

A first order Taylor series expansion shows when it is most effective to change the Jacobi constant C with a ΔV maneuver. Let $\mathbf{X}$ be some state vector in the CR3BP with velocity $\mathbf{V}$ and

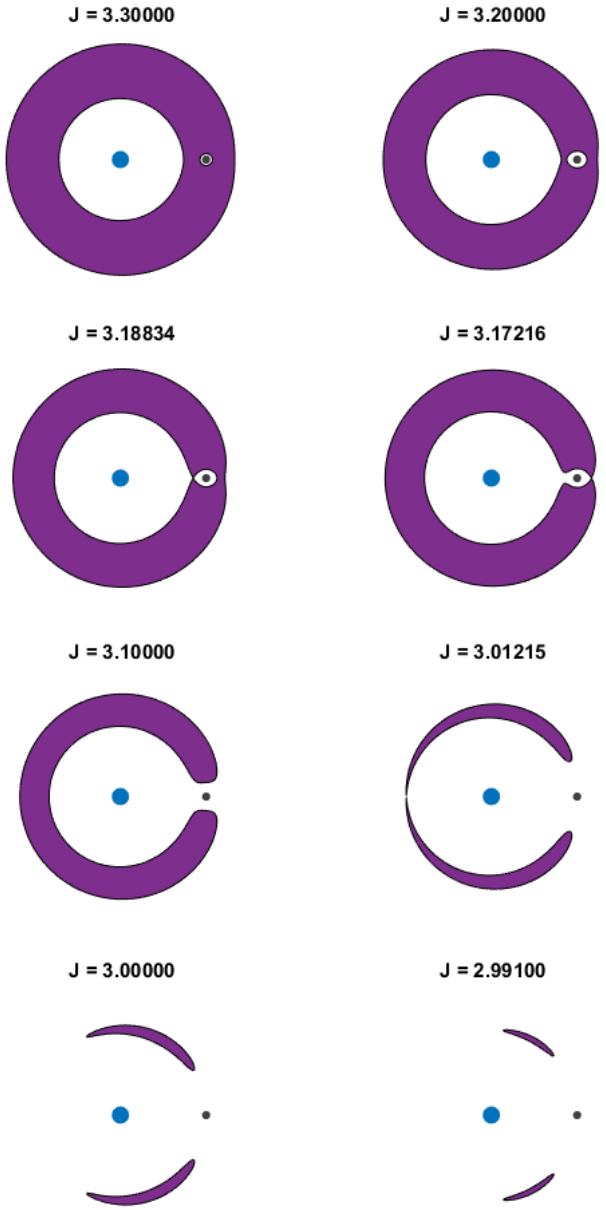

Figure 2.3: The zero-velocity curves for eight Jacobi constants.

let $\mathbf{X}' = \mathbf{X} + \Delta\mathbf{X}$ where $\Delta\mathbf{X} = [0, 0, 0, \Delta V_x, \Delta V_y, \Delta V_z]^T$, representing a velocity perturbation $\Delta\mathbf{V}$.

Equation 2.9 gives the first order Taylor series expansion

$$\begin{aligned} C(\mathbf{X}') &= C(\mathbf{X}) + [\nabla C]^T_{\mathbf{X}} \bullet \Delta\mathbf{X} + \epsilon \\ C(\mathbf{X}') - C(\mathbf{X}) &= [\nabla C]^T_{\mathbf{X}} \bullet \Delta\mathbf{X} + \epsilon \\ \Delta C &= \frac{\partial C}{\partial \dot{x}}\Delta V_x + \frac{\partial C}{\partial \dot{y}}\Delta V_y + \frac{\partial C}{\partial \dot{z}}\Delta V_z + \epsilon. \end{aligned} \tag{2.9}$$

Substituting the partial derivatives from Equation 2.7 gives the following expression for a change in Jacobi constant given a ΔV maneuver:

$$\Delta C = -2\mathbf{V} \bullet \Delta\mathbf{V} + \epsilon. \tag{2.10}$$

From Equation 2.10, it is obvious that in order to maximize a change in the Jacobi constant, the ΔV maneuver should be aligned with the instantaneous velocity vector. A prograde maneuver will decrease the Jacobi constant and a retrograde maneuver will increase it. We can also see that the change in Jacobi constant is proportional to the velocity when the maneuver is performed. These two facts can be used to help design optimal transfers to a trajectory with a different Jacobi constant.

2.2.3 Transformation Between Inertial and Rotating Frames

Mission designers often do preliminary design work in the CR3BP before moving their trajectories into higher fidelity models, which are generally inertial, dimesionalized, and do not follow the circular orbit simplification of the CR3BP. This section will discuss transformations between these models. Following the notation of Anderson,[4] the inertial states are indicated by a subscript i and the rotating frame states are indicated by a subscript r. In addition, let a superscript prime (x_i') denote a coordinate in an intermediate inertial frame that is aligned with the instantaneous rotating frame. The transformation from the rotating frame to an inertial frame begins by changing the origin from the barycenter to one of the primaries, and by accounting for the velocity due to the rotating frame ($\omega \times \mathbf{r}$):

$$[x_i', y_i', z_i', \dot{x}_i', \dot{y}_i', \dot{z}_i']^T = [x_r - d, y_r, z_r, \dot{x}_r - y_r, \dot{y}_r + x_r - d, \dot{z}_r]^T. \tag{2.11}$$

Where $d = \mu$ in dimensionless distance if the central body is the major body and $d = -(1-\mu)$ if the center is the minor body. The value for d can be left at zero to continue using the barycenter as the frame's center. The intermediate state can now be transformed into the desired inertial coordinate frame using a rotation matrix

$$\begin{aligned} \mathbf{r}_i &= T_r^i \mathbf{r}_i' \\ \mathbf{v}_i &= T_r^i \mathbf{v}_i' + \dot{T}_r^i \mathbf{r}_i'. \end{aligned} \tag{2.12}$$

The rotation matrix T_r^i varies depending on the inertial frame that is desired. If we keep the assumption that the primaries are in circular orbits and the desired inertial frame has the same z-axis as the rotating frame, then T_r^i can be written as

$$T_r^i = R_z(\theta) = \begin{bmatrix} \cos\theta & -\sin\theta & 0 \\ \sin\theta & \cos\theta & 0 \\ 0 & 0 & 1 \end{bmatrix} \text{ and } \dot{T}_r^i = \begin{bmatrix} -\sin\theta & -\cos\theta & 0 \\ \cos\theta & -\sin\theta & 0 \\ 0 & 0 & 0 \end{bmatrix}. \tag{2.13}$$

Where θ is the phase between the inertial and rotating frame. If these assumptions are not valid, then T_r^i and its derivative can be constructed from the inertial positions and velocities of the primaries. Let $\mathbf{R}_s$ and $\mathbf{V}_s$ represent the position and velocity of the minor body with respect to the major body in the desired inertial coordinate frame. The rotation matrix can be formed with three unit vectors

$$T_r^i = \begin{bmatrix} \hat{R}_1 & \hat{I}_1 & \hat{C}_1 \\ \hat{R}_2 & \hat{I}_2 & \hat{C}_2 \\ \hat{R}_3 & \hat{I}_3 & \hat{C}_3 \end{bmatrix}, \tag{2.14}$$

where

$$\hat{R} = \frac{\mathbf{R}_s}{\|\mathbf{R}_s\|} \tag{2.15}$$

$$\hat{C} = \frac{\mathbf{R}_s \times \mathbf{V}_s}{\|\mathbf{R}_s \times \mathbf{V}_s\|} \tag{2.16}$$

$$\hat{I} = \hat{C} \times \hat{R}. \tag{2.17}$$

The derivative of T_r^i can be determined with the derivative of the unit vectors

$$\frac{d\hat{R}}{dt} = \frac{\mathbf{V}_s}{\|\mathbf{R}_s\|} - \frac{\mathbf{R}_s}{\|\mathbf{R}_s\|^3}(\mathbf{R}_s \bullet \mathbf{V}_s) \tag{2.18}$$

$$\frac{d\hat{C}}{dt} \approx 0 \tag{2.19}$$

$$\frac{d\hat{I}}{dt} = \frac{d\hat{C}}{dt} \times \hat{R} + \hat{C} \times \frac{d\hat{R}}{dt} \approx \hat{C} \times \frac{d\hat{R}}{dt}. \tag{2.20}$$

The derivative of $\hat{C}$ is approximated as zero because the angular momentum direction vector of the primaries will not undergo any significant change compared to the other two unit vectors. Once the states have been rotated into the desired frame, the last step is to re-dimensionalize them by multiplying positions by DU and velocities by DU/TU.

Sometimes the reverse process is desired. Converting positions from the inertial frame to the rotating frame involves inverting the rotation matrix T_r^i. A property of rotation matrices is that their inverse is also their transpose. Therefore, rearranging from Equation 2.12 gives

$$\mathbf{r}_i = T_r^i \mathbf{r}_i' \tag{2.21}$$

$$\mathbf{r}_i' = [T_r^i]^{-1} \mathbf{r}_i \tag{2.22}$$

$$\mathbf{r}_i' = [T_r^i]^T \mathbf{r}_i. \tag{2.23}$$

Velocity transformations from the inertial to rotating frame can be found by rearranging and substituting into Equation 2.12 as well using

$$\mathbf{v}_i = T_r^i \mathbf{v}_i' + \dot{T}_r^i \mathbf{r}_i' \tag{2.24}$$

$$\mathbf{v}_i = T_r^i \mathbf{v}_i' + \dot{T}_r^i ([T_r^i]^T \mathbf{r}_i) \tag{2.25}$$

$$T_r^i \mathbf{v}_i' = \mathbf{v}_i - \dot{T}_r^i [T_r^i]^T \mathbf{r}_i \tag{2.26}$$

$$\mathbf{v}_i' = [T_r^i]^T (\mathbf{v_i} - \dot{T}_r^i [T_r^i]^T \mathbf{r}_i) \tag{2.27}$$

$$\mathbf{v}_i' = [T_r^i]^T \mathbf{v_i} - [T_r^i]^T \dot{T}_r^i [T_r^i]^T \mathbf{r}_i \tag{2.28}$$

$$\mathbf{v}_i' = [T_r^i]^T \mathbf{v_i} + [\dot{T}_r^i]^T \mathbf{r}_i. \tag{2.29}$$

The two transformations can be summarized with

$$\mathbf{r}'_i = T_i^r \mathbf{r}_i \tag{2.30}$$

$$\mathbf{v}'_i = T_i^r \mathbf{v}_i + \dot{T}_i^r \mathbf{r}_i, \tag{2.31}$$

where $T_i^r = [T_r^i]^{-1} = [T_r^i]^T$ and $\dot{T}_i^r = [\dot{T}_r^i]^T$.

After the position and velocity are converted into the aligned inertial frame, the state should be normalized if it hasn't already. Then, it can be transitioned to the rotating barycentric frame via

$$[x_r, y_r, z_r, \dot{x}_r, \dot{y}_r, \dot{z}_r]^T = [x'_i + d, y'_i, z'_i, \dot{x}'_i + y'_i, \dot{y}'_i - x'_i, \dot{z}'_i]^T. \tag{2.32}$$

2.3 Elliptic Restricted Three-Body Problem

The elliptic restricted three-body problem (ER3BP) is a higher fidelity model than the CR3BP because it assumes the primaries are in elliptical orbits around the barycenter with a known eccentricity. Because the primaries now have radial motion with respect to one another, the ER3BP is set up in a pulsating, rotating frame. The equations of motion for a particle of infinitesimal mass with position $\mathbf{r}$ and velocity $\mathbf{v}$ are:

$$\dot{\mathbf{v}} = (1 + e\cos\nu)^{-1}(U_{\mathbf{r}} - ze\cos\nu\hat{z}) + 2\mathbf{v} \times \hat{z} \tag{2.33}$$

where $U_{\mathbf{r}}$ is the derivative of the force potential term from the Jacobi constant in Equation 2.8, e is the primaries' eccentricity, ν is the true anomaly of the primaries, and $\hat{z}$ is a unit vector in the z-direction.[91]

2.4 Jet Propulsion Laboratory's Development Ephemeris Model

For the highest fidelity dynamical models, we use the Jet Propulsion Laboratory's (JPL) Development Ephemerides (DE), which will be referred to as the full ephemeris model. These files contain Chebyshev polynomial coefficients that can be used to calculate the positions and velocities of the eight planets, the Sun, and many moons, asteroids, and comets. Sometimes orientation data

for some bodies are included as well, such as libration angles for the Moon which is found by propagating a fluid core model. These states are generated by integrating an advanced dynamical model and tuning the parameters of the model so that the trajectory matches known observations of and from a variety of spacecraft. The force model that is used to generate the ephemerides accounts for perturbations from 343 asteroids, aspherical gravity, and solid tide perturbations. It is propagated using quadruple-precision and uses the solar-system barycenter as the center of integration.

This dissertation frequently discusses Earth-Moon DROs, which are propagated using full ephemeris positions from DE430 and DE431 ephemerides,[40] both of which were released in 2013. DE431 provides states for over 30,000 years, spanning 13,200 BC to 17,191 AD. The four inner planets have sub-kilometer accuracy, Jupiter and Saturn are within tens of kilometers, and Uranus and Neptune are estimated to be accurate within several thousand kilometers.[40] DE430's data spans the years 1550 to 2650 and has sub-meter accuracy on lunar position, which is the most accurate to date. JPL's ephemerides use the International Celestial Reference Frame (ICRF). The xy-plane is aligned with the mean equator at the J2000 epoch and the x-axis defined as the intersection of the mean equator of J2000 with the mean ecliptic plane. The origin of the coordinate system is the solar-system barycenter.

In this dissertation, a trajectory that is propagated in a full ephemeris model generally uses Equation 2.2 where the three-body term is summed for all included bodies apart from the central body. The exception is when a solar-system barycenter is used as the center of integration, as in Chapter 8. In this case, the N-body equations of motion in Equation 2.1 are used.

2.5 Distributed Mass Models

The models discussed so far have all assumed that massive bodies behave as a point-mass when computing gravitational potential. The general form for computing gravitational potential

and the point-mass assumption are shown in Equations 2.34 and 2.35, respectively.

$$U(\mathbf{r}) = \int_{\mathbf{V}} \frac{G}{|\mathbf{r} - \rho|} dm \tag{2.34}$$

$$U_{pm}(\mathbf{r}) = -\frac{GM}{\mathbf{r}} \tag{2.35}$$

In this expression, the integral over $\mathbf{V}$ means over the volume of the massive body, $\mathbf{r}$ is a vector pointing from the body's center to the spacecraft, and ρ points from the body's center to some differential volume within the major body. The point-mass formula is also valid if the massive body is a uniform density sphere and the spacecraft is always outside that sphere. This is often a good approximation, especially at great range $\|\mathbf{r}\|$ from the body; however, there are times when the deviations from that perfect sphere are important to account for. This is particularly true in proximity of an irregular body like an asteroid. This section will discuss several ways that a massive body with a nonuniform density or with a shape distorted from a sphere can be modeled.

2.5.1 Spherical Harmonic Gravity Field

The most common method for handling aspherical gravity fields is to modify the potential function in Equation 2.34 so that $\mathbf{r}$ becomes a function of latitude ϕ, longitude λ, and range r. Many researchers have worked to develop an appropriate form for this function[38, 49, 57, 65, 66, 74, 80, 112] and an outline of this effort is given by Vallado.[123] The function was well suited to an infinite series of Legendre polynomials given without derivation in Equation 2.36.

$$U = \frac{\mu}{r}\left[1 - \sum_{l=2}^{\infty} J_l \left(\frac{R_\oplus}{r}\right)^l P_l[\sin(\phi)]\right] + \frac{\mu}{r}\sum_{l=2}^{\infty}\sum_{m=1}^{l}\left(\frac{R_\oplus}{r}\right)^l P_{l,m}[\sin(\phi)]\left\{C_{l,m}\cos(m\lambda) + S_{l,m}\sin(m\lambda)\right\} \tag{2.36}$$

In this expression, $P_l[x]$ is the lth conventional Legendre polynomial which has the properties[74]

$$P_l[x] = \frac{1}{2^l l!}\frac{d^l(x^2-1)^l}{dx^l} \tag{2.37}$$

$$P_l[x] = \frac{1}{2^l}\sum_{j=0}^{l/2}\frac{(-1)^j(2l-2j)!}{j!(l-j)!(l-2j)!}x^{l-2j}. \tag{2.38}$$

The $P_{l,m}$ terms are associated Legendre functions which have the property[74]

$$P_{l,m}[x] = (1-x^2)^{m/2}\frac{d^m}{dx^m}P_l[x]. \tag{2.39}$$

In Equation 2.36, $R_\oplus$ is the radius of the Earth, or the central body in general. The last two undefined terms are the coefficients $C_{l,m}$ and $S_{l,m}$. These are non-dimensional coefficients of degree l and order m that represent the mathematical model for the shape of the central body. The J_l term that appears in Equation 2.36 can be substituted for $-C_{l,0}$. Geodesy is a scientific field concerned with accurately estimating the $C_{l,m}$ and $S_{l,m}$ coefficients. Tracking spacecraft and studying their deviation from two-body motion is one method of determining a body's coefficients. To prevent round-off error on computers, coefficients are sometimes normalized using

$$\bar{S}_{l,m} = \Pi_{l,m}S_{l,m} \tag{2.40}$$

$$\bar{C}_{l,m} = \Pi_{l,m}C_{l,m} \tag{2.41}$$

$$\bar{P}_{l,m} = \frac{P_{l,m}}{\Pi_{l,m}}, \tag{2.42}$$

where

$$\Pi_{l,m} = \sqrt{\frac{(l+m)!}{(l-m)!k(2l+1)}} \tag{2.43}$$

$$k = \begin{cases} 1 & \text{if } m = 0 \\ 2 & \text{if } m \neq 0 \end{cases} \tag{2.44}$$

Since this formulation uses trigonometric arguments in all of the Legendre polynomials, it forms repeating spherical harmonics. Contributions to the aspherical potential can be divided into three classes. Zeroth order harmonics ($m = 0$) are called zonal harmonics. They depend only on latitude, which means they form bands parallel to the central body's equator. The J_2 harmonic is typically attributed to a large body's spin, which causes the equator to bulge out due to centrifugal acceleration. Sectoral harmonics are bands along a line of longitude and occur when the degree and order are equal ($l = m$). All other harmonics are known as tesseral harmonics, and have dependency on both latitude and longitude.

The acceleration is given by taking the gradient of the gravitational potential function

$$\ddot{\mathbf{r}} = \nabla U(\mathbf{r}). \tag{2.45}$$

If we express $\mathbf{r} = [r_i, r_j, r_k]^T$ in the International Terrestrial Reference Frame (ITRF) and take the gradient of Equation 2.36, we get[78]

$$\ddot{\mathbf{r}} = \frac{\partial U}{\partial r}\left(\frac{\partial r}{\partial \mathbf{r}}\right)^T + \frac{\partial U}{\partial \phi}\left(\frac{\partial \phi}{\partial \mathbf{r}}\right)^T + \frac{\partial U}{\partial \lambda}\left(\frac{\partial \lambda}{\partial \mathbf{r}}\right)^T, \tag{2.46}$$

where

$$\begin{aligned}
\frac{\partial U}{\partial r} &= -\frac{\mu}{r^2}\sum_{l=2}^{\infty}\sum_{m=0}^{l}\left(\frac{R_\oplus}{r}\right)^l (l+1)P_{l,m}[\sin(\phi)]\left\{C_{l,m}\cos(m\lambda) + S_{l,m}\sin(m\lambda)\right\} \\
\frac{\partial U}{\partial \phi} &= \frac{\mu}{r}\sum_{l=2}^{\infty}\sum_{m=0}^{l}\left(\frac{R_\oplus}{r}\right)^l \left\{P_{l,m+1}[\sin(\phi)] - m\tan(\phi)P_{l,m}[\sin(\phi)]\right\}\left\{C_{l,m}\cos(m\lambda) + S_{l,m}\sin(m\lambda)\right\} \\
\frac{\partial U}{\partial \lambda} &= \frac{\mu}{r}\sum_{l=2}^{\infty}\sum_{m=0}^{l}\left(\frac{R_\oplus}{r}\right)^l mP_{l,m}[\sin(\phi)]\left\{S_{l,m}\cos(m\lambda) - C_{l,m}\sin(m\lambda)\right\}.
\end{aligned} \tag{2.47}$$

Finally, solving for the partial derivatives of the latitude, longitude, and range with respect to the position vector and substituting Equations 2.47 into Equation 2.46 gives a final expression for acceleration due to a spherical harmonic gravity field:[123]

$$\ddot{r}_i = Ar_i - Br_j \tag{2.48}$$

$$\ddot{r}_j = Ar_j + Br_i \tag{2.49}$$

$$\ddot{r}_k = \frac{1}{r}\frac{\partial U}{\partial r}r_k + \frac{\sqrt{r_i^2 + r_j^2}}{r^2}\frac{\partial U}{\partial \phi}, \tag{2.50}$$

where A and B are given by

$$A = \frac{1}{r}\frac{\partial U}{\partial r} - \frac{r_k}{r^2\sqrt{r_i^2 + r_j^2}}\frac{\partial U}{\partial \phi} \tag{2.51}$$

$$B = \frac{1}{r_i^2 + r_j^2}\frac{\partial U}{\partial \lambda}. \tag{2.52}$$

Note that though the position vector was expressed in a body-fixed frame (ITRF) to compute these accelerations, the position vector must be propagated in an inertial frame such as the Geocentric Celestial Reference Frame (GCRF).

2.5.2 Polyhedral Model

In the previous section, we expanded the $\mathbf{r}^{-1}$ term of Equation 2.34 into a series of Legendre polynomials, which works well for bodies that are mostly spherical with small but significant deviations. More irregular bodies such as asteroids and comets require a high number of coefficients to accurately model the potential field, and these coefficients can be difficult to determine, even while tracking a spacecraft orbiting the body. Werner created an algorithm to derive the potential field based on the shape of the body, which can be determined relatively easily with optical observations like radar, LIDAR, etc.[127]

This method begins by finding a vector function $\mathbf{w}(\xi, \eta, \zeta)$ such that the divergence $\nabla \bullet \mathbf{w} = \mathbf{r}^{-1}$. In this form, the Gauss Divergence Theorem can be applied to turn the volume integral into a surface integral.[46] Werner uses $\mathbf{w} = \hat{r}/2$, where $\hat{r}$ is a unit vector that points from the spacecraft's location to a differential volume element inside the body. Also, $\hat{r}$ is undefined if the spacecraft is on the surface or inside of the body since the Gauss Divergence Theorem only applies to a vector field's flux across the surface. Assuming a uniform density σ, we get

$$U = G\sigma \iiint_{\mathbf{V}} \nabla \bullet \mathbf{w} \; dV = \frac{G\sigma}{2} \iint_{\mathbf{S}} \hat{n} \bullet \hat{r} dS. \tag{2.53}$$

where $\mathbf{S}$ is the exterior surface and $\hat{n}$ is the surface normal vector.

Modeling the body as a polyhedron with triangular, planar faces is common practice and makes convenient simplifications to the integral in Equation 2.53. An example of an arbitrary body with this representation is shown in Figure 2.4. Because the faces are planar, $\hat{n}$ for a particular face is constant. We can also sum the faces' contributions individually. Werner gives the potential contribution due to all planar faces as

$$U = \frac{G\sigma}{2} \sum_{\mathbf{f}} \left(\iint_{f_i} \hat{n}_i \bullet \hat{r} \; dS \right). \tag{2.54}$$

where $\mathbf{f}$ represents the set of all faces. Green's theorem can also be applied, which turns the surface integral over a planar face into a line integral about the boundary.

To find the potential and its gradient due to each face in the shape model, we must rotate

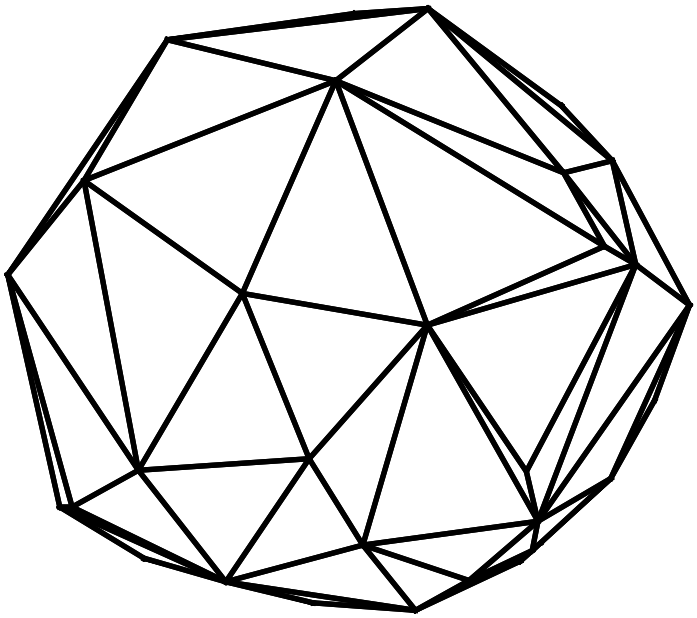

Figure 2.4: A polyhedron with a surface defined by a set of triangular faces

the face's vertices into a face-specific coordinate frame where $\hat{k}$ is aligned with the face's normal direction and $\hat{\imath}$ is along the line from vertex 1 to 2. Let $[\xi_i, \eta_i, \zeta]^T$ be the coordinates of vertex $i \in \{1, 2, 3\}$ in the face-oriented frame and let r_{ij} be the distance between vertex i and j. Let $[x, y, z]^T$ be the coordinates of the spacecraft in the face-oriented frame and compute the coordinate differences $\Delta x_i = \xi_i - x$, $\Delta y_i = \eta_i - y$, and $\Delta z = \zeta - z$. Finally, set the distances r_i equal to the distance of each vertex i from the spacecraft. Werner defines nine expressions that are used to

compute the accelerations:

$$
\begin{aligned}
d_{12} &= \Delta x_1 \Delta y_2 - \Delta x_2 \Delta y_1 \\
d_{23} &= \Delta x_2 \Delta y_3 - \Delta x_3 \Delta y_2 \\
d_{31} &= \Delta x_3 \Delta y_1 - \Delta x_1 \Delta y_3 \\
L_{12} &= \frac{1}{r_{12}} \ln\left(\frac{r_1 + r_2 + r_{12}}{r_1 + r_2 - r_{12}}\right) \\
L_{23} &= \frac{1}{r_{23}} \ln\left(\frac{r_2 + r_3 + r_{23}}{r_2 + r_3 - r_{23}}\right) \\
L_{31} &= \frac{1}{r_{31}} \ln\left(\frac{r_3 + r_1 + r_{31}}{r_3 + r_1 - r_{31}}\right) \\
S_1 &= \arctan\left(\frac{\Delta z A}{[d_{31} d_{12} + \Delta z^2 B]/r_1}\right) \\
S_2 &= \arctan\left(\frac{\Delta z A}{[d_{12} d_{23} + \Delta z^2 C]/r_2}\right) \\
S_3 &= \arctan\left(\frac{\Delta z A}{[d_{23} d_{31} + \Delta z^2 D]/r_3}\right),
\end{aligned}
\tag{2.55}
$$

where the terms A, B, C, and D are independent of the spacecraft position and can be precomputed for each face. They are given by

$$A = \xi_1(\eta_2 - \eta_3) + \xi_2(\eta_3 - \eta_1) + \xi_3(\eta_1 - \eta_2) \tag{2.56}$$

$$B = (\xi_2 - \xi_1)(\xi_1 - \xi_3) + (\eta_2 - \eta_1)(\eta_1 - \eta_3) \tag{2.57}$$

$$C = (\xi_3 - \xi_2)(\xi_2 - \xi_1) + (\eta_3 - \eta_2)(\eta_2 - \eta_1) \tag{2.58}$$

$$D = (\xi_1 - \xi_3)(\xi_3 - \xi_2) + (\eta_1 - \eta_3)(\eta_3 - \eta_2). \tag{2.59}$$

With these terms in Equation 2.55, the potential due to a single triangular face can be found using

$$U_{\text{tri}} = G\sigma \left[\frac{\Delta z}{2}(d_{12}L_{12} + d_{23}L_{23} + d_{31}L_{31}) - \frac{\Delta z^2}{2}(S_1 + S_2 + S_3 - \text{sign}(\Delta z)\pi)\right]. \tag{2.60}$$

Finally, the acceleration components can be computed by taking the gradient of U_{tri} using the

following expressions:

$$\ddot{x} = \frac{\partial U_{\text{tri}}}{\partial x} = -G\sigma\frac{\Delta z}{2}[(\eta_3 - \eta_2)L_{23} + (\eta_1 - \eta_3)L_{31}] \tag{2.61}$$

$$\ddot{y} = \frac{\partial U_{\text{tri}}}{\partial y} = G\sigma\frac{\Delta z}{2}[(\xi_2 - \xi_1)L_{12} + (\xi_3 - \xi_2)L_{23} + (\xi_1 - \xi_3)L_{31}] \tag{2.62}$$

$$\ddot{z} = \frac{\partial U_{\text{tri}}}{\partial z} = G\sigma\left(-\frac{1}{2}[d_{12}L_{12} + d_{23}L_{23} + d_{31}L_{31}] + \Delta z[S_1 + S_2 + S_3 - \text{sign}(\Delta z)\pi]\right). \tag{2.63}$$

Recall that the accelerations are in the face-oriented coordinate frame and must be rotated into a common frame before being summed over all faces. This formulation is an exact solution for the potential field due to the polyhedron model, but the polyhedron is an approximation of the shape of the true body. Therefore, the accuracy of this method depends on the accuracy and resolution of the shape model. Also note that this formulation assumes uniform density throughout the body, which may impact accuracy as well.

2.5.3 Mass Concentration Model

Perhaps the simplest and oldest technique for modeling a non-spherical body is to replace the single point-mass with a set of point masses, called mass concentrations or *mascons*. This technique was commonly used in the late 1960's and early 1970's as a geodesy tool and resulted in improvements on satellite orbit estimation.[44,125,131] Because each mascon can have different mass, they can be used to represent density variations as well as features on the surface of the body such as craters or mountains. The total force due to the body is computed as the sum of the forces due to each mascon. Significant work has been done to optimize the strategies used to select the locations and masses of mascons for specific bodies.[25,27,110,113] These strategies range from using shape models, grids, and stochastic optimization routines to maximize the accuracy of a model with as few mascons as possible. Often, the polyhedral method in Section 2.5.2 is used as a truth solution to compute accuracy of mascon models. A general rule according to Werner and Scheeres[128] is that to decrease the error in a gravitational potential field by an order of magnitude using mascons, the number of mascons must be increased by three orders of magnitude.

Chapter 3

Constructing Distant Retrograde Orbits

This chapter describes what distant retrograde orbits are, how they can be characterized, and explains the features that make them attractive for particular missions. It also covers several methods used to build distant retrograde orbits in the circular restricted three-body problem and higher fidelity dynamical models discussed in Chapter 2.

3.1 Distant Retrograde Orbits

Distant retrograde orbits (DROs) are large three-body orbits that have relevance to current proposed missions and future concepts requiring long duration, hands-off quarantine orbits. DROs make excellent quarantine orbits in the Earth-Moon three-body system for two reasons. First, they are energetically close to escaping the Earth-Moon system, which means they can be entered for little to no ΔV cost when arriving from interplanetary space within a specific energy range.[16] They can also be the target of a low-energy transfer from the major body.[95] Second, DROs have a history of proofs demonstrating they are neutrally stable orbits. Even in a full ephemeris or higher fidelity dynamical model, they can remain stable for long durations, lasting hundreds to thousands of years or more. They are also relevant in other three-body systems with small mass parameters. In cases where the sphere of influence of the minor body is entirely beneath the surface of that body, DROs are generally the only stable orbit available to that body. This is the case in the Mars-Phobos three-body system.

The Asteroid Redirect Robotic Mission (ARRM) is a mission proposed by NASA to tow an

asteroid into an orbit around the Moon.[18,119] Though this asteroid will be too small to cause harm to the Earth, it is desirable that it remains in its final orbit for the foreseeable future to prevent an impact with the Earth or Moon, or an escape from the system. Additionally, because of the asteroid's high mass, the low ΔV cost of entering the DRO from interplanetary space reduces the amount of fuel and time spent thrusting to achieve the orbit. Another mission concept that DROs are useful for as an endgame orbit is the Mars Sample Return (MSR) concept. In this mission, a sample from Mars would be returned to the Earth-Moon system and placed into a DRO rather than returned to Earth. The DRO avoids the complications of Planetary Protection[34] restrictions associated with returning the capsule to the ground. The samples can either be visited by crewed vehicles and studied or returned to Earth at a later time in a potentially more secure vessel. The long duration stability of DROs reduces the probability that the capsule will depart the orbit and possibly impact the Earth. A third mission concept that could utilize a DRO is a Lunar Far-Side Communication/Navigation satellite. This satellite can relay transmissions and provide navigation for crewed or robotic missions on the far side of the Moon. While a DRO orbits the Moon and will not have line-of-sight to the far side for its full orbit, it does have the advantage of not requiring stabilizing maneuvers like halo orbits do. DROs can also withstand substantial z-amplitude motion while still remaining stable, which greatly reduces the time that the satellite is occulted by the Moon. Finally, in the case of some three-body systems, a DRO is potentially the only way to feasibly orbit the minor body for an extended duration. This is the case for the Mars-Phobos system.

DROs are orbits around the minor body in a three-body system and this dissertation will specifically focus on the Earth-Moon system and the Mars-Phobos system. Not only are these two locations relevant to near-term missions, they also represent a wide difference in mass parameters, allowing us to discern how that affects the studies in this research. When viewed in the rotating frame, the DRO orbits around the minor body in the opposite direction that the minor body orbits the barycenter. If the DRO is viewed in barycentric inertial frame however, it orbits in a prograde direction following the minor body. Figure 3.1 shows examples of DROs and their direction of

motion in the rotating (left) and inertial frames (right). Small DROs appear nearly circular, but become elliptical as they get larger. The center of the orbit also begins to drift away from the minor body in the $+x$-direction. Several resonant DROs (2:1, 3:1, and 4:1) are shown in an Earth-centered inertial frame in Figure 3.1b. This shows that DROs are actually a large, prograde, non-Keplerian orbit around the Earth experiencing significant perturbations from the Moon. The 2:1 resonant DRO resembles an ellipse with the Earth near the center instead of at a focus.

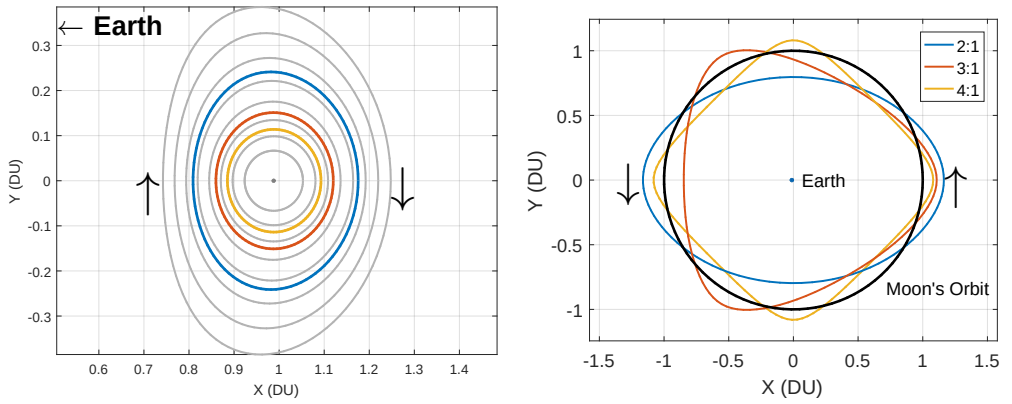

(a) Family of DROs in rotating frame spanning 25,000 to 100,000 km

(b) Resonant DROs in the inertial frame with the Moon's orbit (black)

Figure 3.1: DROs in the rotating and inertial frames

There are several methods used to characterize the size of a DRO. Unlike two-body orbits, there is no general analytical solution to the CR3BP. Planar periodic DROs in the CR3BP can be described uniquely by their orbital period or x- or y-amplitude of oscillation since each of these parameters is unchanged when propagated. The Jacobi constant can be used to uniquely define a planar, periodic DRO. Planar quasi-periodic DROs are more challenging since infinite variants exist for a given Jacobi constant. However, amplitudes over several orbits can be averaged together to describe the DRO's size. The maximum and minimum x- and y-amplitudes, namely the width of amplitude oscillations, can also be used to characterize a quasi-periodic orbit. Non-planar DROs in the CR3BP have been characterized by a pseudo-inclination in literature, which is defined as the angle between the initial velocity vector and the Earth-Moon plane.[73] In high fidelity dynamical models, particularly those using ephemerides for the states of massive bodies, there are no constant

parameters and all DROs are quasi-periodic. The period can be approximated by computing the time to cross the rotating frame's xz-plane. The average of x- and y-amplitudes can be used to describe a quasi-periodic DRO as well.

The position of a body along a DRO's path can be identified by an angle τ, which is analogous to the true anomaly in the two-body problem. The τ angle measures the fraction of the period that the body has completed and can be measured with the elapsed time since passing a reference point or crossing a reference plane. There are typically two choices for the phase constraint of $\tau = 0°$ on a DRO. One is when the orbit path crosses the xz-plane between the two primaries and the other is when this plane is crossed on the far side of the minor body. The latter is shown in Figure 3.2. This dissertation will generally use the latter definition of $\tau = 0°$ and define a DRO's size in any frame by its initial x-amplitude. Figure 3.2 shows how τ maps positions along a DRO.

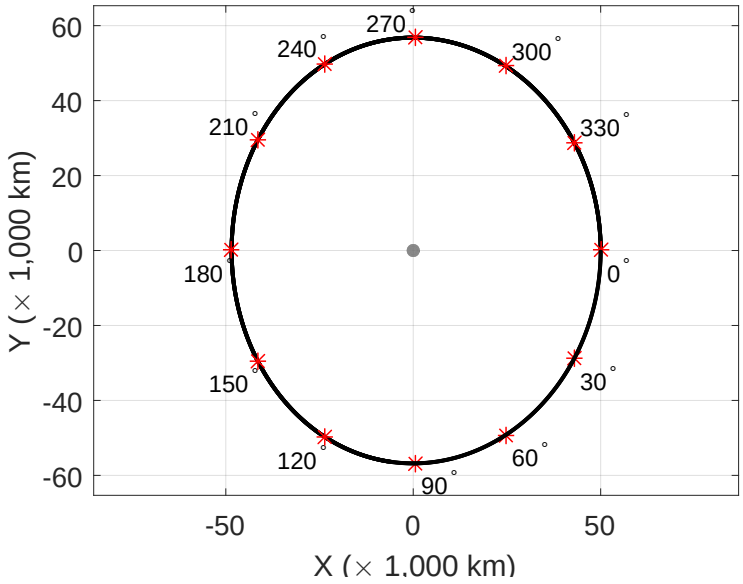

Figure 3.2: A DRO with incremental τ values, which define a position along the path of the orbit.

The limits on the size of a DRO are not well defined in literature. Decreasing the size of a DRO will eventually reduce it to a circular orbit around the minor body. When a DRO is small enough to be effectively characterized as a Keplerian orbit ($r_0 < 25,000$ km in the Earth-Moon system) Adamo refers to them as proximal DROs.[1] Increasing the size of a DRO ($r_0 > 150,000$ km)

will eventually cause it to become a highly eccentric two-body orbit about the major body with relatively small perturbations from the minor body. These large DROs are typically unstable outside of the CR3BP assumptions, especially when external perturbations are considered. In between these ranges, there are sizes where the DRO is influenced by accelerations of similar orders of magnitude from both primaries. Larger DROs begin to experience more gravitational acceleration from the major body and essentially fly in formation with the minor body. This is the case for all DROs in the Mars-Phobos system. The transition between these behaviors is subtle and not always easy to detect.

3.2 Generating DROs in the Circular Restricted Three-Body Problem

It is useful to begin by constructing a family of DROs in the CR3BP. This section will discuss the techniques to do so in the context of the Earth-Moon three-body system, but it is valid for any three-body system. Two methods are derived: a single-shooting algorithm combined with a continuation method, and a curve-fitting procedure.

3.2.1 Single Shooting and Continuation Method

We begin with a retrograde, circular orbit with a semi-major axis (a) the same size as the Moon's radius, though sub-surface starting points are convenient for three-body systems with small mass parameters. Next, we transform this orbit into the CR3BP. We begin along the Earth-Moon line in a Moon-centered inertial frame with no phase between the Earth-Moon rotating frame, which gives it the following coordinates:

$$\mathbf{X}_i' = \left[a,\ 0,\ 0,\ 0,\ -\sqrt{\frac{\mu_{\leftmoon}}{a}},\ 0\right]^T. \tag{3.1}$$

This state is transformed to a non-dimensional, barycentric frame.

$$\mathbf{X}_i' = \left[\frac{a}{DU} + (1-\mu),\ 0,\ 0,\ 0,\ -\sqrt{\frac{\mu_{\leftmoon}}{a}}\frac{TU}{DU},\ 0\right]^T. \tag{3.2}$$

We can convert from an inertial frame to the rotating frame by subtracting the velocity due to the frame rotation.

$$\mathbf{X}_r = \left[\frac{a}{DU} + (1-\mu),\ 0,\ 0,\ 0,\ -\sqrt{\frac{\mu_{\leftmoon}}{a}}\frac{TU}{DU} - \frac{a}{DU},\ 0\right]^T. \tag{3.3}$$

This small circular orbit is used as a starting point because even in the CR3BP, its motion is dominated by the gravity from the Moon and remains nearly periodic.

Next, a single-shooting differential corrector (SSDC) is allowed to correct the initial y-velocity such that the orbit will pass orthogonally through the xz-plane ($\dot{x} = 0,\ \dot{z} = 0$). Howell's SSDC algorithm uses the knowledge that the CR3BP acceleration are symmetric across the xz-plane, and therefore, any periodic orbit must meet the orthogonal symmetry boundary condition at this plane crossing.[60] The SSDC begins with some state $\mathbf{X_0}$ in the CR3BP, which is close to a periodic initial condition beginning on the xz-plane. To be periodic in the CR3BP, this state must have the form

$$\mathbf{X}_0 = [x_0, 0, z_0, 0, \dot{y}_0, 0]^T. \tag{3.4}$$

It is propagated forward in time until its next xz-plane crossing, which occurs half of an orbit later at $t = T/2$, where T is the period of the orbit. If the initial state provided is not perfectly periodic, this second plane crossing will not be orthogonal and may have velocity components in the $x-$ or z-directions, which we will call $\dot{x}_f$ and $\dot{z}_f$. The subscript f indicates the time at which these states are taken, $t = T/2$.

We can learn how to modify the initial conditions such that $\dot{x}_f$ goes to zero by looking at a Taylor series expansion of a function $f(\mathbf{X_0}, \tau_0)$ that maps from the initial state $\mathbf{X}_0$ to some final state $\mathbf{X_f}$ separated by time $\tau = T/2$ (not to be confused with τ that tracks position along the DRO).

$$\mathbf{X}_f = f(\mathbf{X}, t) \tag{3.5}$$

$$f(\mathbf{X}, \tau) = f(\mathbf{X}_0, \tau_0) + \left.\frac{\partial f(\mathbf{X}, t)}{\partial \mathbf{X}}\right|_{\substack{\mathbf{X}=\mathbf{X}_0 \\ t=\tau_0}} (\mathbf{X} - \mathbf{X}_0) + \left.\frac{\partial f(\mathbf{X}, t)}{\partial t}\right|_{\substack{\mathbf{X}=\mathbf{X}_0 \\ t=\tau_0}} (t - \tau_0) + \mathcal{O}(\delta\mathbf{X}_0^2, \delta\tau_0^2). \tag{3.6}$$

This equation can be rearranged and truncated to contain only the first order terms

$$f(\mathbf{X}, \tau) - f(\mathbf{X}_0, \tau_0) = \frac{\partial \mathbf{X}_f}{\partial \mathbf{X}}(\mathbf{X} - \mathbf{X}_0) + \frac{\partial \mathbf{X}_f}{\partial t}(\tau - \tau_0) \tag{3.7}$$

$$\delta \mathbf{X}_f = \frac{\partial \mathbf{X}_f}{\partial \mathbf{X}_0}\delta \mathbf{X}_0 + \frac{\partial \mathbf{X}_f}{\partial t}\delta\tau. \tag{3.8}$$

Equation 3.8 shows a linear approximation of how a deviation in the initial state can be mapped to a deviation in the final state. The first partial derivative matrix in Equation 3.8 is called the *state transition matrix* or STM. The STM is a matrix of the partial derivatives of a state with respect to a state at a different time:

$$\Phi(t, t_0) = \frac{\partial \mathbf{X}(t)}{\partial \mathbf{X}(t_0)}. \tag{3.9}$$

In many cases, including the CR3BP, there is no analytic representation for the STM, but it can be numerically integrated using the following differential equation:

$$\dot{\Phi}(t, t_0) = A\Phi(t, t_0) \tag{3.10}$$

$$\Phi(t_0, t_0) = I, \tag{3.11}$$

where A is the Jacobian of the differential equation $\dot{\mathbf{X}} = f(\mathbf{X})$:

$$A = \frac{\partial f(\mathbf{X})}{\partial \mathbf{X}} = \frac{\partial \dot{\mathbf{X}}}{\partial \mathbf{X}}. \tag{3.12}$$

The other partial derivative matrix in Equation 3.8 is simply the time derivative of the state vector at the xz-plane crossing $\mathbf{X}_f$. This term accounts for how the time to reach the xz-plane crossing changes as the initial state is adjusted.

Substituting the STM into Equation 3.8 gives the relation

$$\delta \mathbf{X}(\tau) = \Phi(\tau, 0)\delta \mathbf{X}(0) + \dot{\mathbf{X}}(\tau)\delta\tau, \tag{3.13}$$

where

$$\delta \mathbf{X} = [\delta x, \delta y, \delta z, \delta \dot{x}, \delta \dot{y}, \delta \dot{z}]^T. \tag{3.14}$$

Let Φ_{ij} represent the element of Φ in the ith row and jth column. Since the function $f(\mathbf{X}, \tau)$ terminates at the xz-plane crossing, δy will always be zero. This information is used to calculate $\delta\tau$ via

$$\delta y = 0 = \Phi_{21}\delta x_0 + \Phi_{25}\delta \dot{y}_0 + \dot{y}\delta\tau \tag{3.15}$$

$$\delta\tau = -\frac{1}{\dot{y}}(\Phi_{21}\delta x_0 + \Phi_{25}\delta\dot{y}_0). \tag{3.16}$$

We can now manipulate the initial state to null the final x- and z-velocities: $\delta\dot{x}$ and $\delta\dot{z}$. Since periodic DROs are planar, z_0 and $\dot{z}_f$ will always be zero. Substituting $\delta\dot{x} = -\dot{x}_f$ into Equation 3.13 yields

$$\delta\dot{x} = \Phi_{45}\delta\dot{y}_0 - \frac{\ddot{x}}{\dot{y}}(\Phi_{21}\delta x_0 + \Phi_{25}\delta\dot{y}_0), \tag{3.17}$$

where $\ddot{x}$ and $\dot{y}$ are evaluated at $t = T/2$. Keeping the initial position ($\delta x_0 = 0$) fixed and maintaining an initial velocity orthogonal to the xz-plane leaves $\delta\dot{y}_0$ as the only control parameter remaining. The final update prediction equation is given in Equation 3.18:

$$\delta\dot{x} = -\dot{x} = \left(\Phi_{45} - \frac{\ddot{x}}{\dot{y}}\Phi_{25}\right)\delta\dot{y}_0. \tag{3.18}$$

Solving for $\delta\dot{y}_0$ and adding it to the initial y-velocity reduces $\dot{x}$ at $T/2$, generally by an order of magnitude or more given a sufficiently good initial guess. This process must be iterated due to the truncation of nonlinear terms in the Taylor series expansion in Equation 3.8. Once the SSDC has converged to a specified tolerance (ϵ), both xz-plane crossings are orthogonal and we are left with the initial conditions for a single periodic DRO.

A continuation method can then be applied to build a family of DROs.[94] To do so, the initial distance from the Moon (x_0) is increased in small increments (δx_0) on the order of 100 to 500 km. The size of the step can vary based on the mass parameter and normalized distance of the three-body system, but too large of a step will cause the algorithm to diverge. Each time it is increased, the SSDC is used to correct the y-velocity to produce another periodic DRO. An initial guess for the y-velocity can be generated from the previous converged periodic DRO's last update. By removing the constraint that the initial position remain fixed, we reformulate the update prediction in Equation 3.18 to include δx_0:

$$\delta\dot{x} \approx 0 = \left[(\Phi_{41} \quad \Phi_{45}) - \frac{\ddot{x}}{\dot{y}}(\Phi_{21} \quad \Phi_{25})\right]\begin{pmatrix}\delta x_0 \\ \\ \delta\dot{y}_0\end{pmatrix} \tag{3.19}$$

$$\left(\Phi_{41} - \frac{\ddot{x}}{\dot{y}}\Phi_{21}\right)\delta x_0 + \left(\Phi_{45} - \frac{\ddot{x}}{\dot{y}}\Phi_{25}\right)\delta\dot{y}_0 \approx 0. \tag{3.20}$$

Note we are able to set Equation 3.20 approximately equal to zero since the values used in the equation are from the previous DRO's last iteration, which converged on $|\dot{x}_f| < \epsilon$. Using this relation, we can generate a prediction on the update $\delta\dot{y}_0$ that corresponds with the position update δx_0:

$$\delta\dot{y}_0 = -\left(\frac{\Phi_{41} - \frac{\ddot{x}}{\dot{y}}\Phi_{21}}{\Phi_{45} - \frac{\ddot{x}}{\dot{y}}\Phi_{25}}\right)\delta x_0. \tag{3.21}$$

Each step in the continuation method is saved and initial conditions for any sized DRO can be interpolated from this set. Figure 3.3 show how the initial velocity and orbital period vary with the size of the DRO as compared to a two-body circular orbit about the Moon. The DRO's orbital

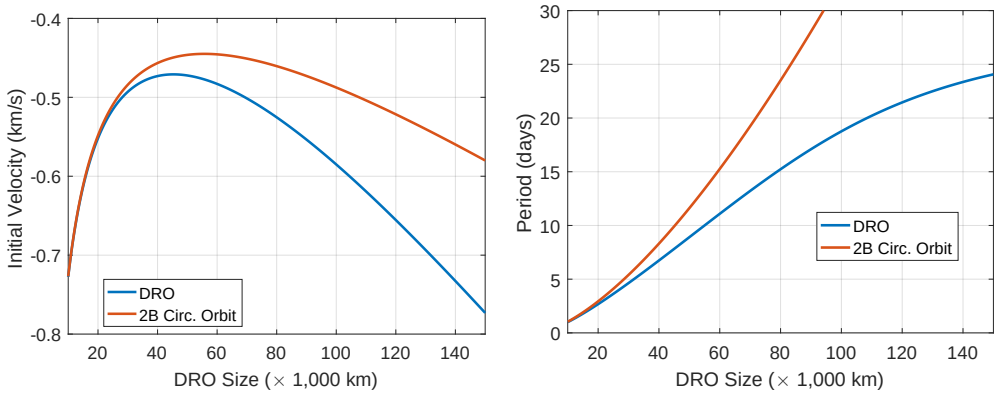

(a) Size vs velocity

(b) Size vs. period

Figure 3.3: Initial velocity for a DRO compared to a circular orbit

period asymptotically approaches the sidereal period of the Moon (27.3 days) while the two-body circular orbit grows as a function of $R^{3/2}$. The initial velocity of the DRO in the rotating frame grows as the orbit gets further from the Moon until about 45,000 km (-470 m/s) where it begins to decline again. At this point, the speed due to the frame rotation has overcome the growth in speed due to the orbit size increasing. The two-body circular orbit is a good approximation for DROs up to about 25,000 km, at which point the DRO becomes more elliptical. The Jacobi constant for these DROs is shown in Figure 3.4.

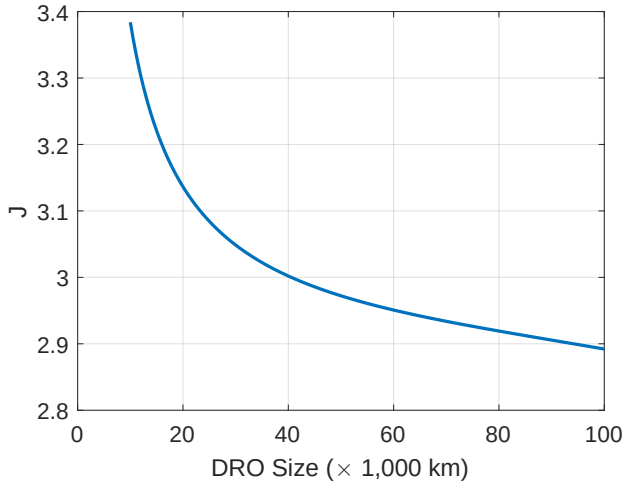

Figure 3.4: The Jacobi constant for DROs in the Earth-Moon CR3BP.

3.2.2 Curve-Fitting Initial Conditions

The SSDC and continuation method provides a set of DRO initial conditions for a particular mass parameter. It can become cumbersome in practice to generate this data set for multiple mass parameters and interpolate to generate the appropriate DRO. To speed up, ease the implementation into code, and expand the method's capabilities to include the mass parameter, a curve-fitting method is used. This section describes the process of building a bivariate function that returns a DRO's initial position, velocity, and its period given a mass parameter and starting distance from the minor body. This function meshes well with the work of Hirani and Russell who developed a method for estimating the states along any planar DRO, but rely on a lookup table for initial conditions.[56]

3.2.2.1 Fitting Initial Velocity Data

To begin, a grid is created that meshes a vector of mass parameters logarithmically spaced between 10^{-10} and 0.5 with a vector of initial distances from the minor body (r_0), which is logarithmically spaced between 10^{-4} and 0.4 in normalized distance units (DU). For each mass parameter, the SSDC and continuation method is used to generate initial conditions that begin on the x-axis between the major and minor bodies as well as the period at each r_0 value. In this data set, the

mass parameter and initial distance vectors contain 250 values each, resulting in initial conditions for 62,500 DROs.

In addition to collecting DRO initial conditions and period, acceptable error limits for the velocity are also derived to help with the curve-fitting process. The x-intercept of the periodic DRO after half of a period is determined and its distance from the minor body (r_0) is computed. We define the upper and lower velocity limits (V_- and V_+) as the velocities that cause an x-intercept at r_- and r_+, which are arbitrarily set at $r_- = 0.5\,r_0$ and $r_+ = 1.5\,r_0$. To find $V_{-/+}$, a modified SSDC algorithm is used, which targets the corresponding x-intercept instead of an orthogonal xz-plane crossing. Equation 3.18 is modified to be

$$\delta x = r_{-/+} - r_0 = \left(\Phi_{15} - \frac{\dot{x}}{\dot{y}}\Phi_{25}\right)\delta\dot{y}_0. \tag{3.22}$$

Additional error handling is required to ensure the iterations of the modified SSDC do not diverge since it is no longer targeting a stable orbit with a large basin of attraction. After $V_{-/+}$ values are determined for a DRO, Howell's SSDC algorithm is used to verify that these velocity limits are still within the basin of attraction for the periodic solution. Figure 3.5 shows an example of the periodic DRO's half period trajectory bounded on both sides by the trajectories that intercept the lower and upper radius targets.

With this data set, we begin to fit a function for the initial velocity. The strategy is to find a function of one parameter that fits the data using coefficients derived from functions of the second parameter. Therefore, the bivariate fitting function with coefficients $c(x_1)$ will have the form $h(c(x_1), x_2)$. Beginning with the velocity function, we plot how the base-10 logarithm (log) of the velocity varies with respect to the log of the mass parameter for several different initial radii from the minor body in Figure 3.6. Each of these curves closely resembles a hyperbola, though the shape, center, and orientation change with respect to the initial radius.

Any conic section can be represented with an implicit second order polynomial

$$Ax^2 + Bxy + Cy^2 + Dx + Ey + F = 0, \tag{3.23}$$

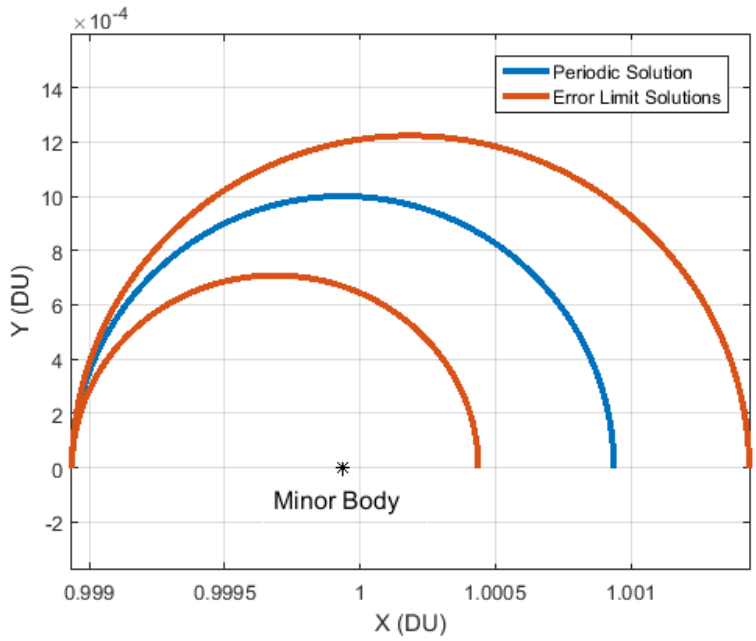

Figure 3.5: The periodic DRO's x-intercept after half of a period surrounded by the trajectories that are 50% closer and further away from the minor body.

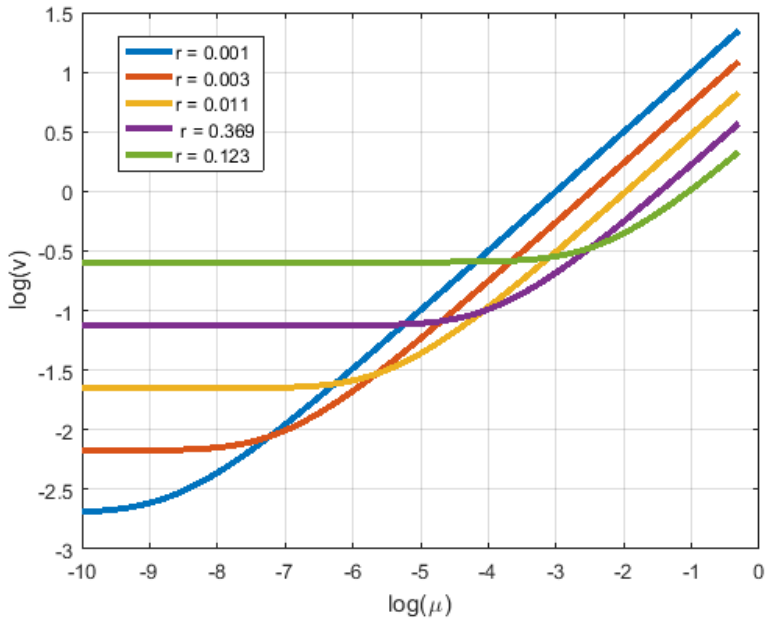

Figure 3.6: The log of the initial velocity forms a hyperbola with respect to the log of the mass parameter.

while a hyperbola can be exclusively found using the discriminant constraint equation:

$$\begin{vmatrix} A & B/2 \\ B/2 & C \end{vmatrix} = AC - \frac{B^2}{4} < 0 \rightarrow B^2 - 4\,AC > 0. \tag{3.24}$$

The coefficients A through F can be arbitrarily scaled, so we impose a constraint to ensure a unique set. This can be done in combination with the hyperbola's discriminant constraint by forcing a specific value for the discriminant.

$$B^2 - 4\,AC = 1 \tag{3.25}$$

Given a set of x data, Equation 3.23 becomes a univariate quadratic equation and y can be determined with the quadratic formula

$$y = \frac{-b \pm \sqrt{b^2 - 4ac}}{2a}. \tag{3.26}$$

where $a = C$, $b = Bx + E$, and $c = Ax^2 + Dx + F$.

For each radius from the minor body, we fit a hyperbola to the log of the corresponding velocities ($y = \log(v)$) and the log of the mass parameters ($x = \log(\mu)$). We substitute these parameters into Equation 3.23, which gives the following linear system:

$$\begin{bmatrix} \log(\mu_1)^2 & \log(\mu_1)\log(v_1) & \log(v_1)^2 & \log(\mu_1) & \log(v_1) & 1 \\ \vdots & \vdots & \vdots & \vdots & \vdots & \vdots \\ \log(\mu_n)^2 & \log(\mu_n)\log(v_n) & \log(v_n)^2 & \log(\mu_n) & \log(v_n) & 1 \end{bmatrix} \begin{bmatrix} A \\ B \\ C \\ D \\ E \\ F \end{bmatrix} = \mathbf{Mc} = \mathbf{0}. \tag{3.27}$$

Because we have more data than coefficients to fit, the problem is overdetermined. While a solution does not exist, the least squares solution will minimize the norm of the residuals ϵ. Following the work of Bookstein,[17] we derive the least squares solution for a conic section. The square of the residuals is given by

$$\mathbf{Mc} = \epsilon \tag{3.28}$$

$$\min \epsilon^T \epsilon = \min(\mathbf{Mc})^T(\mathbf{Mc}) = \min \mathbf{c}^T\mathbf{M}^T\mathbf{Mc}. \tag{3.29}$$

Next, we use Lagrange multipliers λ to minimize the sum of the squares of the residuals under the discriminant constraint in Equation 3.25. The Lagrange expression is written as

$$\mathcal{L}(\mathbf{c}) = \mathbf{c}^T(\mathbf{M}^T\mathbf{M})\mathbf{c} + \lambda \mathbf{c}^T\mathbf{Nc}, \tag{3.30}$$

where the second term is the matrix representation of the discriminant constraint. The **N** matrix has the form

$$N = \begin{bmatrix} 0 & 0 & -2 & \cdots & 0 \\ 0 & 1 & 0 & \cdots & 0 \\ -2 & 0 & 0 & \cdots & 0 \\ \vdots & \vdots & \vdots & \ddots & \vdots \\ 0 & 0 & 0 & \cdots & 0 \end{bmatrix}. \tag{3.31}$$

To minimize our residuals, we set the gradient of Equation 3.30 equal to zero.

$$\nabla \mathcal{L} = (\mathbf{M}^T\mathbf{M})\mathbf{c} + \lambda \mathbf{N}\mathbf{c} = \mathbf{0} \tag{3.32}$$

This convenient form can be solved with an Eigen-Decomposition on the matrix $\mathbf{M}^T\mathbf{M}$. The eigenvector corresponding to the smallest eigenvalue is the least squares solution for the coefficient vector.

The next step in the curve-fitting process is to characterize the least squares coefficients as a function of the initial radius from the minor body. Figure 3.7 shows how the six coefficients in vector $\mathbf{c}_i$ vary with respect to the log of the initial radius. Though A appears constant, it is just two orders of magnitude smaller than the other coefficients. These six curves are each fit with a sixth degree polynomial, shown in Equation 3.33. There are 42 coefficients, which are concatenated into the matrix **k**.

$$\mathbf{c}_i = \sum_{j=0}^{6} k_{i,j} \log(r_0)^j, \quad i \in [1, 6]. \tag{3.33}$$

The final step to fitting a function to the initial velocity data is to optimize all 42 coefficients to produce the most accurate solution across the input space. Take V_0 to be the initial velocities in the SSDC data set and take $V_0' = V_0'(\mathbf{k})$ to be the initial velocity calculated from the the fitted function. A cost function $J(\mathbf{k})$ is given in Equation 3.34, which returns the relative error in the predicted velocity augmented by a penalty for exceeding the V_+ and V_- error limits found with the

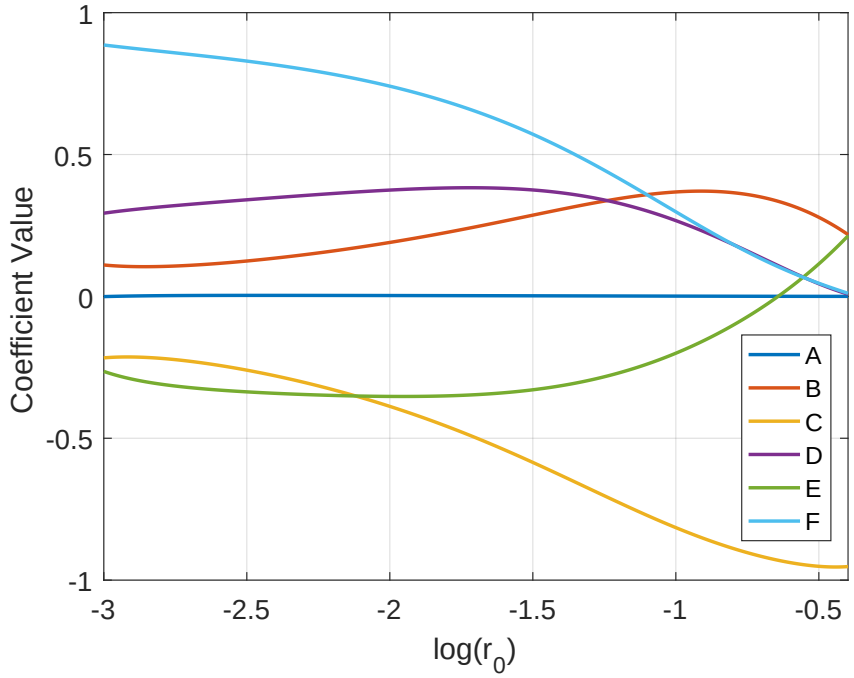

Figure 3.7: The hyperbola's six coefficient values as a function of the initial radius. Polynomials are fit to these curves.

modified SSDC.

$$J(\mathbf{k}) = \frac{V_0' - V_0}{V_0} + w_+ \begin{cases} \dfrac{V_0' - V_+}{V_+}, & \text{if } V_0' > V_+ \\ 0, & \text{if } V_0' \leq V_+ \end{cases} + w_- \begin{cases} \dfrac{V_0' - V_-}{V_-}, & \text{if } V_0' < V_- \\ 0, & \text{if } V_0' \geq V_- \end{cases} \tag{3.34}$$

The $w_{+/-}$ terms are weights for constraint violations. It is important to minimize relative error because the predicted velocity spans several orders of magnitude across the input range, and the size of the basin of attraction for the periodic solution is proportional to the velocity magnitude. MATLAB's *fsolve* optimizer is used with the Levenberg-Marquardt algorithm to obtain the optimal coefficients, which are listed in Table A.1 in Appendix A. Before the optimization of $\mathbf{k}$, the maximum relative error is about 7.9%, the mean error is 0.8%, and 170 of the velocity predictions lie outside the error limits. After optimizing with *fsolve*, the maximum error is 3.9%, the mean error is 0.6% and all solutions are between the velocity limits, and therefore in the basin of convergence for a SSDC algorithm.

This algorithm as it has been developed for this work shows immediate room for improvement.

First, we began by fitting a general conic section to the data, requiring six parameters. Better use of the constraint equation to enforce a hyperbola is used should remove one of the terms in $\mathbf{c}$ that needs to be fit with a polynomial. Additionally, Figure 3.6 shows that each of the hyperbola have asymptotes that point in the same directions. A reparameterization of the hyperbola function will allow us to constrain another term from $\mathbf{c}$. In total, this allows us to eliminate 14 coefficients from the vector $\mathbf{k}$, reducing it from 42 to 28 terms.

3.2.2.2 Fitting Period Data

While estimating the period of a DRO is far less important for generating accurate initial conditions with a SSDC, it is helpful to understand the relationship between DRO size and its period. We fit a function to the DRO's period following the same procedure as the initial velocity fitting. For each DRO that was generated with the SSDC, the log of the period is plotted against the log of the mass parameter. Figure 3.8 shows this comparison for five different values for the initial radius from the minor body. This plot shows that the period is well modeled by a sigmoid function, also known as an S-curve. There are several functional forms that produce sigmoid curves and they are often used to represent cumulative density functions (CDFs). To better identify the appropriate function to fit the period data, we look at its derivative using a first-order forward finite difference method. Figure 3.9 shows that the derivative resembles a skewed normal distribution, so the fitting function will be the CDF for this function type. The CDF of a skewed normal distribution is computed with

$$f(x, \xi, \omega, \alpha) = \Phi\left(\frac{x-\xi}{\omega}\right) - 2T\left(\frac{x-\xi}{\omega}, \alpha\right), \tag{3.35}$$

where $\Phi(x)$ is the CDF of a standard normal distribution:

$$\Phi(x) = \frac{1}{2}\left[1 + \operatorname{erf}\left(\frac{x}{\sqrt{2}}\right)\right], \tag{3.36}$$

and $T(h, a)$ is the Owen's T-function, which has several published algorithms for accurately solving[92,96]

$$T(h, a) = \frac{1}{2\pi}\int_0^a \frac{\exp(-h^2/2(1+x^2))}{1+x^2}\, dx. \tag{3.37}$$

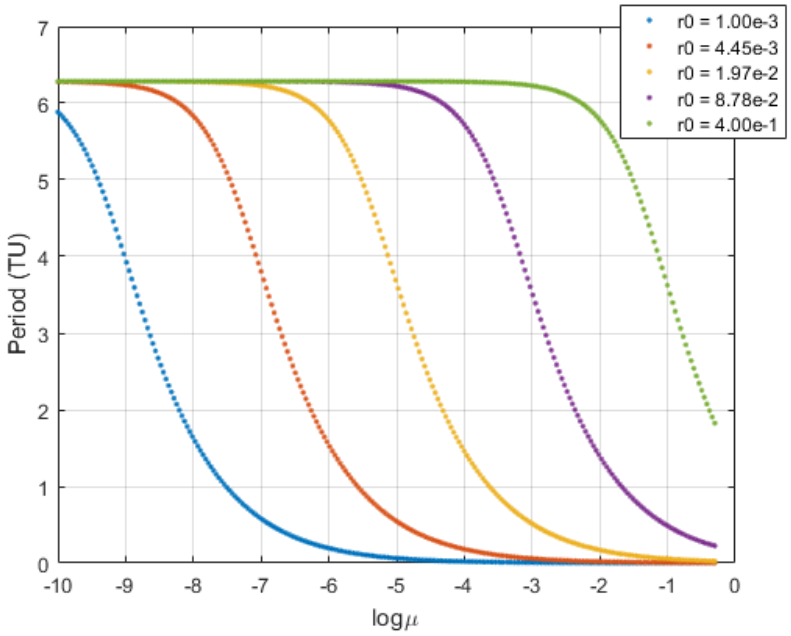

Figure 3.8: The period can be modeled as a sigmoid function with respect to the log of the mass parameter.

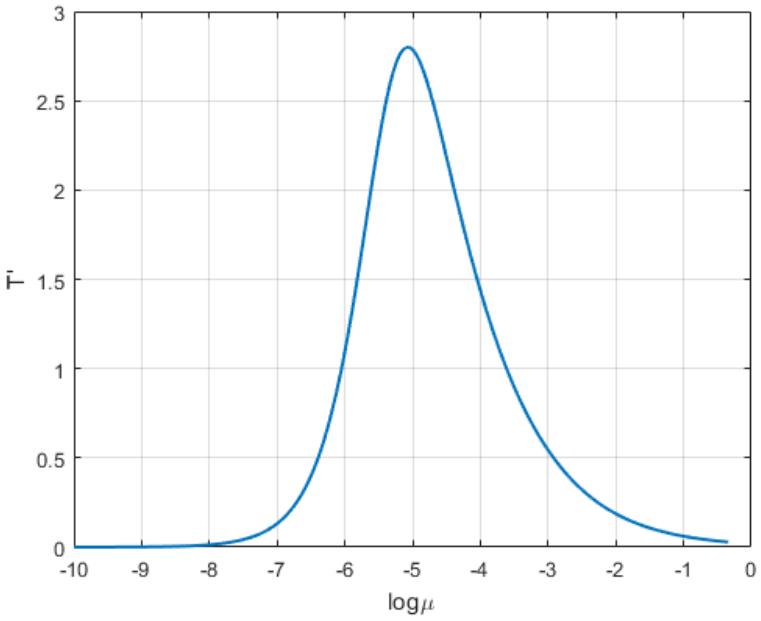

Figure 3.9: The derivative of the S-curves forms a skewed normal distribution.

Setting $x = \log \mu$, we are left with three parameters $\mathbf{c} = [\xi, \omega, \alpha]$ that define the curve as a

function of the initial radius from the minor body. These parameters' values with respect to the log of the initial radius plotted in Figure 3.10. They are each fit with a fifth-degree polynomial,

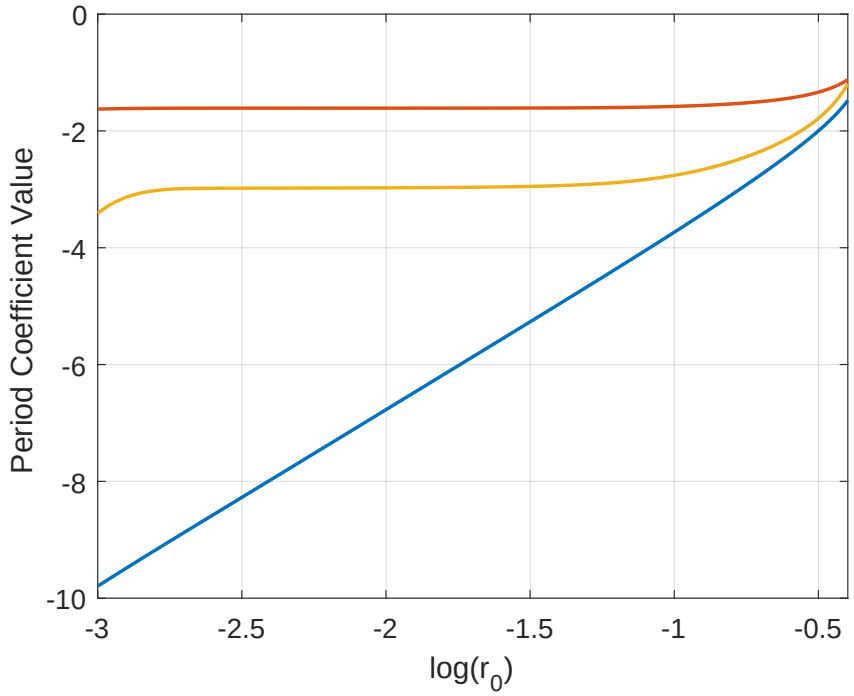

Figure 3.10: The coefficients for the Equation 3.35 as a function of the log of initial radius from the minor body.

shown in Equation 3.38:

$$\mathbf{c}_i = \sum_{j=0}^{5} k_{i,j} \log(r_0)^j, \quad i \in \{1,2,3\}. \tag{3.38}$$

Looking at Figure 3.10, we see that these curves are perhaps better fit by a function form other than a polynomial. Doing so may reduce the total number of coefficients required to reconstruct the period. Regardless, using a polynomial fit gives 18 total coefficients $k_{i,j}$ that define the period of a DRO as a function of mass parameter and initial radius. The CDF given in Equation 3.35 has a range of (0,1) for any value of x, but Figure 3.8 suggests that the period function must have a range of $(0, 2\pi)$. We use Equation 3.39 to fit the period data.

$$P(\mathbf{c}) = 2\pi \left[\Phi\left(\frac{x - \mathbf{c}_1}{\mathbf{c}_2} \right) - 2T\left(\frac{x - \mathbf{c}_1}{\mathbf{c}_2}, \mathbf{c}_3 \right) \right] \tag{3.39}$$

The final step is to optimize the coefficients using MATLAB's *fsolve* function with the

Levenberg-Marquardt algorithm. The goal of the optimization is to minimize the absolute error in the period generated by the fitted function. The coefficients as generated are nearly optimal, and *fsolve* is only able to reduce the error by about 0.1%. After optimizing, the maximum absolute error on the period is 9.4×10^{-2} TU, which translates to 9.6 hours of error on a DRO with a period of 20.8 days in the Earth-Moon system. The optimal coefficients are listed in Appendix A.

3.3 Transforming DROs into the Full Ephemeris

For DRO propagations in models that use the full ephemeris, the initial conditions must be transformed into an inertial frame where the assumptions of the CR3BP no longer apply. Any periodic orbit in the CR3BP will become quasi-periodic in the full ephemeris inertial frame, and the goal of this section is to transform these coordinates such that the variations in the orbit across multiple periods are minimized. There are several methods for doing this, each with its own merits.

One strategy is to directly transform the DRO states from the CR3BP directly into the inertial frame with the algorithm discussed in Section 2.2.3. This method is the fastest to compute, but the assumption that the Moon and Earth are in circular orbits around the barycenter does not apply in realistic dynamical models. The Moon's varying distance from Earth due to its eccentricity, coupled with the sensitivity of the orbit to its initial conditions, make this conversion ineffective, especially for the velocity components of the state. Figure 3.11a shows a 70,000 km DRO, whose initial conditions are transformed into full ephemeris, inertial states and propagated for one period. Each plotted orbit uses the same CR3BP initial conditions, but is translated when the Moon is at perigee, apogee, and in between (lunar true anomalies $\nu = 0°$, $90°$ and $180°$). All three transformations are poor representations of what the true state should be, particularly because the velocity does not translate well. A simple alternative to computing velocity transformations is to only transform positions into the inertial frame. Given sufficiently frequent position data, a finite difference method can be used to estimate the velocity at each state. This is shown in Figure 3.11b where the initial position and a position 60 seconds in the future are differenced to find the velocity. At apogee, the DRO velocity is too large and at perigee it is too small, but in between we get a

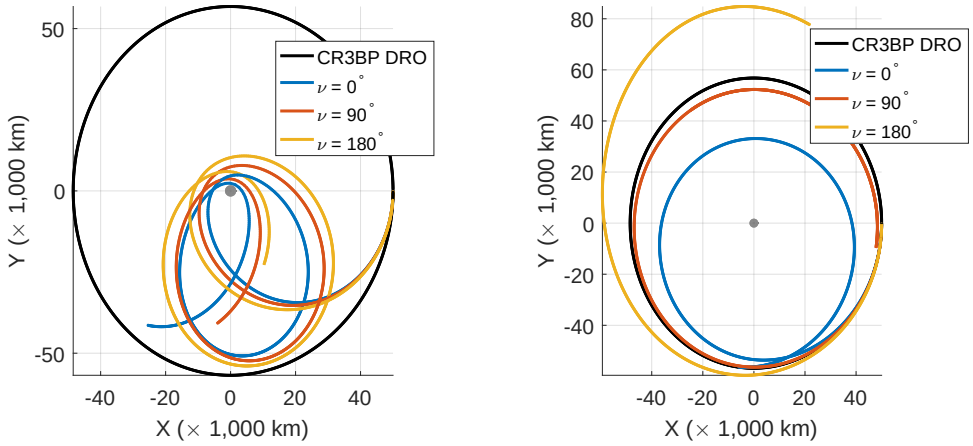

(a) Direct transformations at lunar true anomalies of $\nu = 0°$ and 180°

(b) Direct transform of positions and finite differenced velocities.

Figure 3.11: DRO initial conditions in full ephemeris inertial states

relatively good approximation of the DRO. These cases are all significantly better than directly transforming the velocity. These transformed coordinates are not perfect, but they make a good initial guess and can be refined with other algorithms.

3.3.1 Orthogonal Crossing

Another strategy is to use a shooting algorithm to modify the transformed state such that it produces a more uniform DRO. After the state has been transformed into the full ephemeris, it can be propagated for one or more orbits and then checked to meet some constraint. In this dissertation, many of the full ephemeris initial conditions for DROs are generated by enforcing an orthogonal xz-plane crossing in the rotating frame after an integer number of orbits. The initial state is propagated using the Moon-centered full ephemeris model including gravity from the Earth, Moon, and Sun. These states at each time step are transformed back into the Moon-centered synodic frame and the xz-plane crossings are interpolated from the integration results. After the $2N^{\text{th}}$ plane crossing, where N is the number of orbits desired, the residuals of the constraints ($\vec{r}$) are computed and returned to the optimizer portion of the algorithm. To enforce an orthogonal plane crossing, this residual vector will contain the x and z-velocity in the rotating frame. An additional

constraint is added that minimizes the difference between the initial and final x-positions. The final residual vector is given by:

$$\vec{r} = [\dot{x}_f, \dot{z}_f, x_f - x_0]^T \tag{3.40}$$

The goal is to adjust the initial velocity $\vec{v}_i$ such that $\vec{r}$ is driven to zero. A Levenberg-Marquardt (LM) method is used to minimize the residual vector.[48] At each step, the LM algorithm approximates a correction to the initial velocity $\Delta\vec{v}_i$ using a least squares linear system:

$$\left(\mathbf{J}^T(\vec{x}_k)\mathbf{J}(\vec{x}_k) + \mu_k\mathbf{I}\right)\Delta\vec{v}_i = -\mathbf{J}^T(\vec{x}_k)\vec{r}_k \tag{3.41}$$

Where $\mathbf{J}(\vec{x}_k) = \dfrac{\partial\vec{r}_k}{\partial\Delta\vec{v}_i}$ and can be determined analytically or computed numerically with a finite differencing method. The $\mu_k\mathbf{I}$ term prevents numerical issues from arising when the Hessian matrix $\mathbf{J}^T\mathbf{J}$ is ill-conditioned or rank-deficient. The parameter μ_k must be positive and can be arbitrarily chosen and changed between iterations. For reference, $\mu_k = 0$ is the same as solving with the Gauss-Newton method. Figure 3.12 shows the velocity of the initial conditions when transforming to the full ephemeris with an orthogonal plane crossing after two orbits. It follows the corrections from the SSDC well until about 70,000 km.

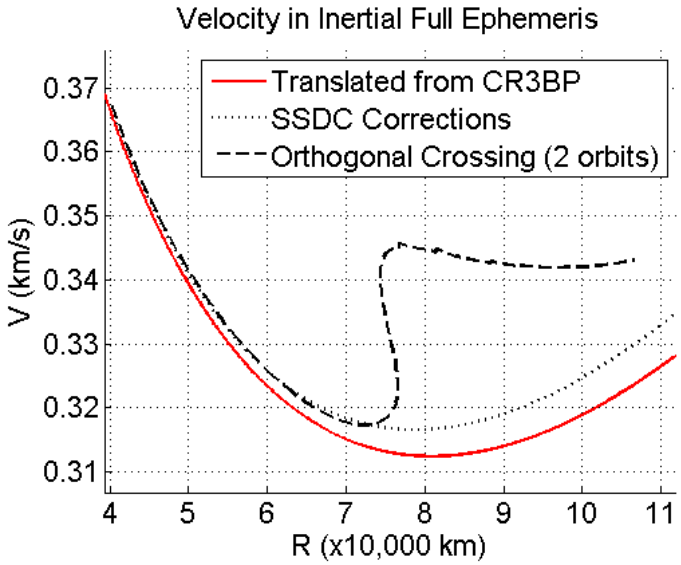

Figure 3.12: Velocity after correcting for full ephemeris.

Note that there are many different constraints that can be used in this method. For example,

one may choose to define the residual vector as the difference between the maximum and minimum y-positions of all the $\tau = \pm 90^\circ$ crossings in N orbits. Be aware that constraints such as these may have highly non-linear derivatives which may cause convergence problems. Also, because LM is a least squares algorithm, one is not limited to using exactly three constraints. More or fewer may be applied as is deemed necessary.

3.3.2 Multiple Shooting Differential Corrector

A third method for transforming states into the full ephemeris model is to use a multiple shooting differential corrector (MSDC).[93,98,130] This section will describe the strategy at a high level and the details can be found in the cited references. This strategy begins with a set of states from the orbit in the CR3BP that span several orbit periods. Each of these N states is called a *patchpoint* and consists of position and velocity ($\mathbf{X}_k = [\mathbf{R}_k, \mathbf{V}_k]^T$) and an epoch ($t_k$). The MSDC will adjust the position, velocity, and epoch of each patchpoint until the trajectory becomes continuous within the limits of machine precision or a specified tolerance. The patchpoints are transformed into the full ephemeris inertial frame at a specified epoch and each one is propagated forward to the epoch of the next patchpoint. Let the superscript f denote the state after it has been propagated from time t_k to t_{k+1}: $\mathbf{X}_k \rightarrow \mathbf{X}_k^f$ for $k = 1, \ldots, N-1$. As discussed earlier, due to the assumptions in the CR3BP, these segments will not be continuous in position or velocity, as depicted in Figure 3.13.

The next step is referred to as the first level of the MSDC and solves the position boundary value problem for each patchpoint. To do so, the velocity of all but the last patchpoint are adjusted so that the trajectory becomes continuous in position space. This constraint can be written as $\mathbf{R}_k^f = \mathbf{R}_{k+1}$ for $k \in \{1, \ldots, N-1\}$. The state transition matrix $\mathbf{\Phi}(t_{k+1}, t_k)$ can be used to iteratively correct the initial velocity $\mathbf{V}_k$, similar to the single shooting differential corrector as described in Section 3.2.

$$\delta \mathbf{R}_k = \mathbf{R}_k^f - \mathbf{R}_{k+1}$$

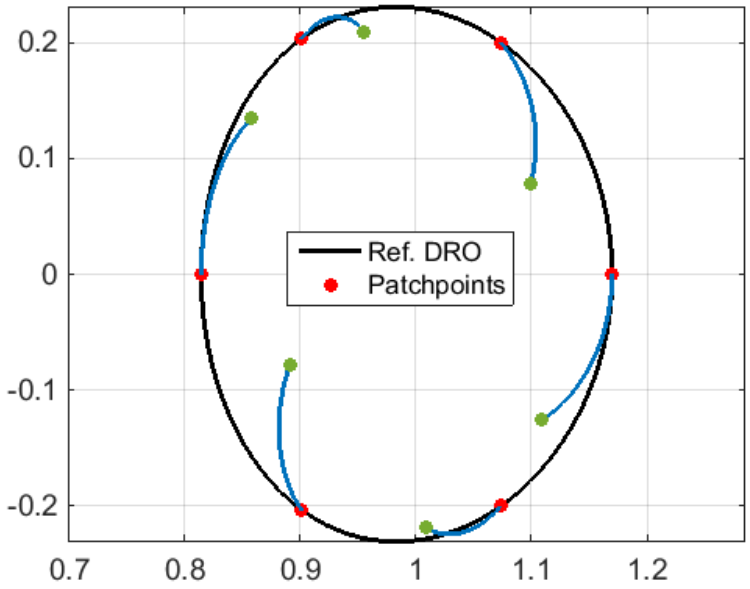

Figure 3.13: The direct transformation of the DRO patchpoints from the CR3BP to an inertial frame does not create a continuous trajectory.

$$\delta \mathbf{R}_k = \frac{\partial \mathbf{R}_k^f}{\partial \mathbf{V}_k} \delta \mathbf{V}_k = \mathbf{\Phi}_{RV}(t_{k+1}, t_k) \delta \mathbf{V}_k \tag{3.42}$$

$$\delta \mathbf{V}_k = \left[\frac{\partial \mathbf{R}_k^f}{\partial \mathbf{V}_k} \right]^{-1} \delta \mathbf{R}_k. \tag{3.43}$$

Since the positions of each patchpoint do not change, this step is independent of other patchpoints' states and can be executed in parallel for performance gains. Figure 3.14 shows an example of a trajectory after the Level 1 correction has converged. As mentioned in the previous section, transforming to the full ephemeris is prone to errors in the velocity, so it is unsurprising to see the trajectory appear to be significantly improved after Level 1 correction. This example is modified to exaggerate the velocity discrepancies between patchpoints that still exist after Level 1 correction. The true trajectory after Level 1 correction (not shown) follows the reference DRO significantly more closely. The velocity differences remaining after Level 1 correction will be fixed with Level 2 correction.

Level 2 correction is now applied to the trajectory, which attempts to eliminate the velocity discrepancies $\Delta \mathbf{V}_k = \mathbf{V}_k - \mathbf{V}_{k-1}^f$ for $k \in \{2, 3, \ldots, N-1\}$, by adjusting the position and epoch of each patchpoint. The necessary changes to the positions and epochs can be found by setting up

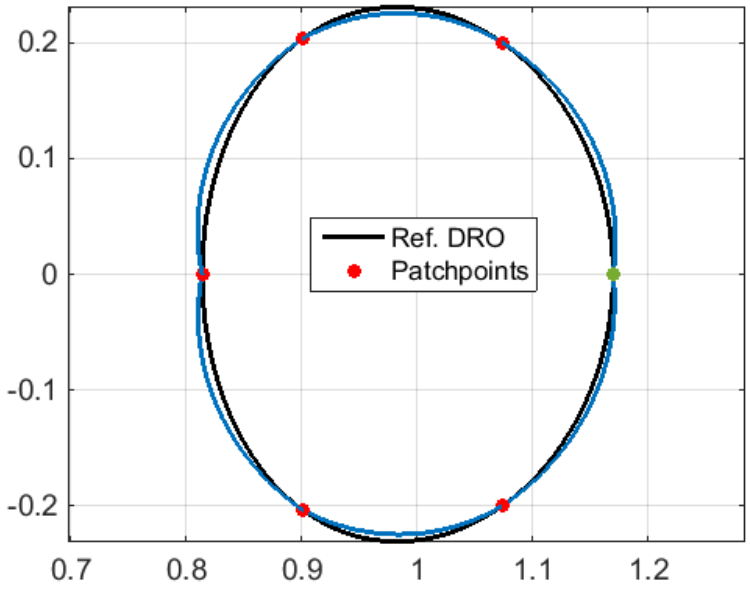

Figure 3.14: The propagated patchpoints after Level 1 correction; the trajectory is continuous in position and time, but not velocity.

the linear system

$$\begin{bmatrix} \delta\boldsymbol{\Delta}\mathbf{V}_2 \\ \delta\boldsymbol{\Delta}\mathbf{V}_3 \\ \vdots \\ \delta\boldsymbol{\Delta}\mathbf{V}_{N-1} \end{bmatrix} = \mathbf{M} \begin{bmatrix} \delta\mathbf{R}_1 \\ \delta t_1 \\ \vdots \\ \delta\mathbf{R}_N \\ \delta t_N \end{bmatrix} = \mathbf{M}\delta\mathbf{X}, \tag{3.44}$$

where matrix $\mathbf{M}$ has rows $\mathbf{M}_i$ given by:

$$\mathbf{M}_i = \left[\frac{\partial \Delta\mathbf{V}_{i+1}}{\partial \mathbf{R}_1}, \frac{\partial \Delta\mathbf{V}_{i+1}}{\partial t_1}, \ldots, \frac{\partial \Delta\mathbf{V}_{i+1}}{\partial \mathbf{R}_N}, \frac{\partial \Delta\mathbf{V}_{i+1}}{\partial t_N} \right] \tag{3.45}$$

Looking at the form of $\Delta\mathbf{V}_k$, we can see it has dependence on only three patchpoints: $k-1$, k, and $k+1$. Therefore, derivatives with respect to other patchpoints are zero resulting in a sparse matrix $\mathbf{M}$:

$$\frac{\partial \Delta\mathbf{V}_i}{\partial \mathbf{R}_j} = \frac{\partial \Delta\mathbf{V}_i}{\partial t_j} = 0 \text{ for } j < i-1 \text{ and } j > i+1. \tag{3.46}$$

The $\mathbf{M}$ matrix may be further populated to add constraints to the problem, such as limiting the range of motion of a particular patchpoint, or ensuring that the epochs of the patchpoints remain

sequential ($t_{k-1} < t_k < t_{k+1}$). Wilson outlines some options for constraints, as well as provides a numerical method for calculating the partial derivative terms that make up $\mathbf{M}$.[130] The linear system in Equation 3.44 will always be underdetermined since we use $4N$ controls to zero $3N$ velocity terms. Therefore, the minimum norm solution is the standard method for solving this system:

$$\begin{bmatrix} \delta\mathbf{R}_1 \\ \delta t_1 \\ \vdots \\ \delta\mathbf{R}_N \\ \delta t_N \end{bmatrix} = \mathbf{M}^T(\mathbf{M}\mathbf{M}^T)^{-1} \begin{bmatrix} \delta\boldsymbol{\Delta}\mathbf{V}_2 \\ \delta\boldsymbol{\Delta}\mathbf{V}_3 \\ \vdots \\ \delta\boldsymbol{\Delta}\mathbf{V}_{N-1} \end{bmatrix}. \tag{3.47}$$

Level 2 correction allows the position of each patchpoint to move freely, so the resulting solution will not be continuous in position space anymore. However, if one begins with a sufficiently close initial guess to the solution, the norm position error should be smaller than before Level 1 correction is first applied. To complete the MSDC process, Level 1 and Level 2 correction are repeated until the position and velocity errors are within a specified tolerance. We are left with a series of states that form a nearly continuous trajectory in the full ephemeris model, like the trajectory shown in Figure 3.15. Using a MSDC to transform some three-body orbits can result in a trajectory that closely resembles the reference in the middle, but the beginning and ending segments show significant deviation. This can be mitigated by adding more patchpoints and arcs than are needed to the beginning and end of the trajectory and trimming them off after the trajectory has converged. This is generally an issue for unstable orbits however, and for DROs, none of the patchpoints are shifted too far from the reference orbit.

3.3.3 Method Comparison

The initial conditions for the orthogonal crossing and the MSDC algorithm are compared in Figure 3.16 by plotting four DROs (20k, 35k, 50k, and 75k km) propagated for six periods. These methods produce similar results for most DROs. The 75,000 km DRO generated by the MSDC

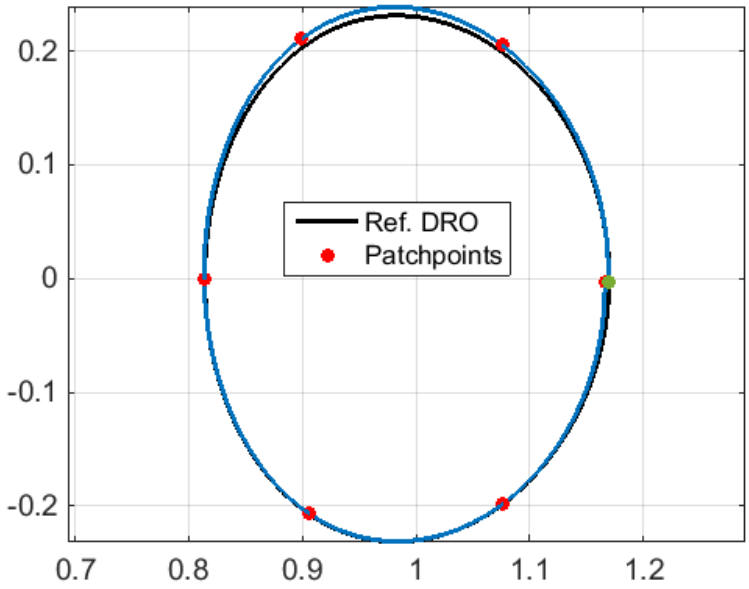

Figure 3.15: The 70,000 km DRO has been successfully transformed into an inertial, full ephemeris frame after four iterations of level 1 and level 2 correction.

has slightly less variations in y-amplitude, but in general, the methods are comparably effective. The MSDC has an advantage over the orthogonal crossing method when it comes to generating initial conditions for long trajectory arcs. The orthogonal crossing algorithm is updating a single state with a numerically computed gradient. If this orbit's constraints are being evaluated many periods downstream, then the gradient will be highly non-linear and sensitive beyond the limits of double precision. The MSDC avoids this problem by breaking up the trajectory into arcs so no patchpoints' gradients will be too sensitive. While it is more complicated, the MSDC is a more robust algorithm for generating initial conditions in the full ephemeris.

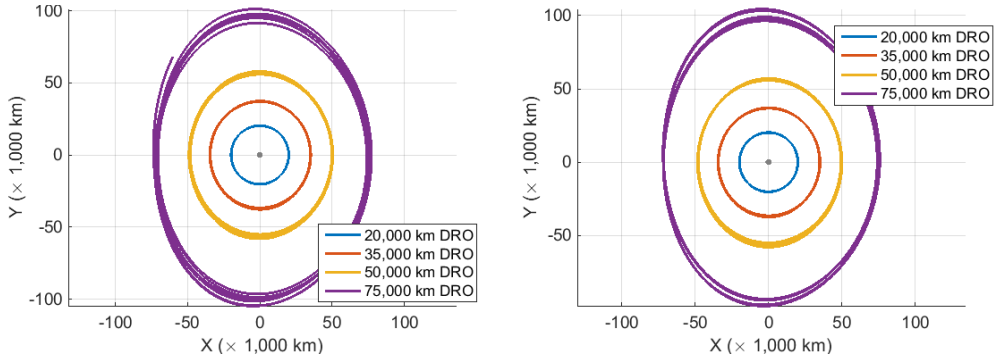

(a) Results of the Levenberg-Marquardt orthogonal algorithm.

(b) Results of the multiple shooting differential corrector.

Figure 3.16: A comparison between the two methods for generating initial conditions.

Chapter 4

Stability of Distant Retrograde Orbits

This chapter summarizes and applies the current knowledge of stability analysis as it pertains to distant retrograde orbits. We explore stability analysis in the CR3BP and then expand to higher fidelity models, which require new metrics for determining stability. We investigate century-long stability of DROs in the Earth-Moon system under a variety of perturbations and determine the principle causes for instability in these orbits. We also create a new tool, the stability map, to quantify an orbit's sensitivity compared to others, and use it to identify ideal DRO sizes.

4.1 Stability Definitions

The stability of a dynamical system can be described in several ways and we begin by presenting common definitions following the work and notation of Schaub and Junkins.[115] The simplest definition of stability is to say that a trajectory $\mathbf{X}(t)$ perturbed by an arbitrary amount $\delta\mathbf{X}(t_0)$ from some reference trajectory $\mathbf{X}_r(t)$ in a dynamical system is still bound to the reference trajectory for all future time. That is

$$\|\mathbf{X}(t) - \mathbf{X}_r(t)\| = \|\delta\mathbf{X}(t)\| < \delta \tag{4.1}$$

for some $\delta > 0$ and $t > t_0$. This is referred to as Lagrange stability. The trajectory $\mathbf{X}(t)$ is said to be in the neighborhood $B_\delta(\mathbf{X}_r(t))$ if this holds true for the selected δ. The next stability definition states that it is possible to keep the difference between the perturbed and reference state arbitrarily small through a choice in size of the initial perturbation. This is known as Lyapunov stability, and is the most common meaning when the more general term "stable" is used. Mathematically, this

definition is given as

$$\mathbf{X}(t_0) \in B_\delta(\mathbf{X}_r(t_0)) \longrightarrow \mathbf{X}(t) \in B_\epsilon(\mathbf{X}_r(t)), \tag{4.2}$$

where $\epsilon > 0$ and $\delta = \delta(\epsilon) > 0$. Thus, a state can be constrained to an arbitrarily small neighborhood B_ϵ by constraining $\delta\mathbf{X}(t_0)$ to be in a sufficiently small neighborhood B_δ.

To illustrate the differences between Lagrange and Lyapunov stability, we look at a ball under the influence of gravity in the vicinity of hills and valleys. Figure 4.1a shows an example of a system that is only Lagrange stable and a system that is Lyapunov stable. Use the equilibrium state as the reference trajectory for the ball $x_r(t) = 0$ in both cases. In the Lagrange stable example, the ball is sitting at an unstable equilibrium and any small perturbation will cause the ball to roll into one of the valleys. If there is no mechanism for energy dissipation, the ball will oscillate indefinitely around the stable equilibrium point at the bottom of the valley. For position perturbations, the motion of the perturbed ball will always be bound to $-2 < x(t) < 2$. Decreasing the size of the perturbation does not decrease these bounds to an arbitrarily smaller size, which is why this system is only Lagrange stable. On the other hand, the system on the right side of Figure 4.1 begins at a stable equilibrium point. Not only is the motion of the ball bound to a neighborhood based on the size of the perturbation, but that region can be made arbitrarily small by making the perturbation sufficiently small. Therefore, it is Lyapunov stable.

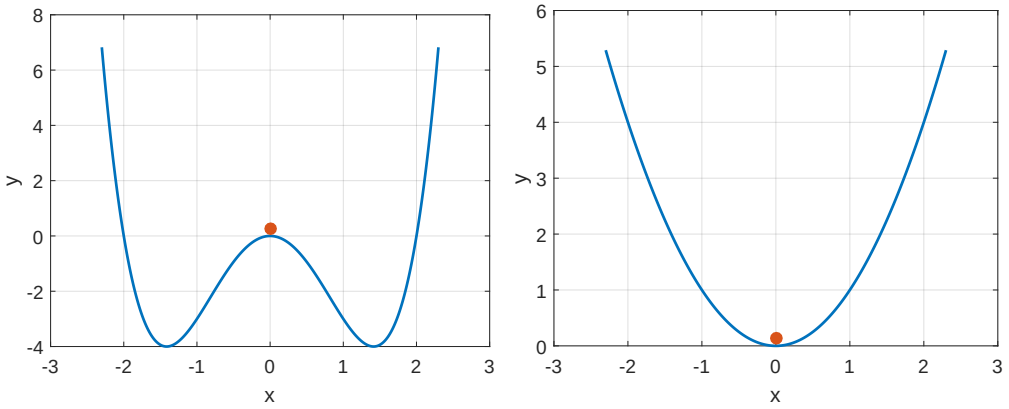

(a) Lagrange stable (b) Lyapunov stable

Figure 4.1: Examples of systems with different stability classifications

The next level of stability a trajectory can have is called asymptotic stability. In addition to being bound and having an arbitrarily small downstream error, an asymptotically stable trajectory gradually approaches the reference trajectory over time

$$\lim_{t\to\infty} \delta\mathbf{X}(t) = \mathbf{0}. \tag{4.3}$$

The system in Figures 4.1b becomes asymptotically stable if an energy dissipation mechanism is included in addition to gravity. In this definition, there is no specification made on the rate at which the system's error approaches zero. We can strengthen the stability definition further by specifying a minimum rate at which the error must decay. A trajectory is exponentially stable if it is asymptotically stable and

$$\delta\mathbf{X}(t) \leq \delta\mathbf{X}(t_0)e^{\alpha t}, \tag{4.4}$$

where $\alpha < 0$ is the decay rate.

4.2 Local Stability in the CR3BP

Determining the stability of a nonlinear dynamical system can be challenging, so it is sometimes advantageous to perform a local stability analysis on a reference trajectory. For a dynamical system governed by $\dot{\mathbf{X}} = f(\mathbf{X})$, we linearize the system about the reference trajectory $\mathbf{X}_r$ and study the growth or decay of a perturbation. Similar to Section 3.2.1, we use a Taylor series expansion to linearize the equations of motion:

$$f(\mathbf{X}) = f(\mathbf{X}_r) + \frac{\partial f(\mathbf{X}_r)}{\partial \mathbf{X}}(\mathbf{X} - \mathbf{X}_r) + \mathcal{O}(\delta\mathbf{X})^2 \tag{4.5}$$

$$\delta\dot{\mathbf{X}} \approx \frac{\partial f(\mathbf{X}_r)}{\partial \mathbf{X}}\delta\mathbf{X} \tag{4.6}$$

$$\delta\dot{\mathbf{X}} \approx \mathbf{A}\delta\mathbf{X}. \tag{4.7}$$

where $\mathbf{A}$ is the Jacobian of the equations of motion. The stability of the linearized system in Equation 4.7 can be determined by looking at the eigenvalues of $\mathbf{A}$.[115] The system is locally stable if the real part of each eigenvalue λ_i is less than zero; otherwise, it is unstable unless all eigenvalues are purely imaginary, resulting in an inconclusive determination of local stability.

We will study the CR3BP in depth using this analysis method. In the CR3BP, the Jacobian matrix $\mathbf{A}$ can be written with four submatrices, representing the derivatives of the velocity $\dot{\mathbf{r}}$ and acceleration $\dot{\mathbf{v}}$ with respect to the position $\mathbf{r}$ and velocity $\mathbf{v}$

$$\mathbf{A} = \begin{bmatrix} \frac{\partial \dot{\mathbf{r}}}{\partial \mathbf{r}} & \frac{\partial \dot{\mathbf{r}}}{\partial \mathbf{v}} \\ \frac{\partial \dot{\mathbf{v}}}{\partial \mathbf{r}} & \frac{\partial \dot{\mathbf{v}}}{\partial \mathbf{v}} \end{bmatrix}. \tag{4.8}$$

Using the equations of motion shown in Equation 2.6, the Jacobian reduces to

$$\mathbf{A} = \begin{bmatrix} \mathbf{0}_{3\times 3} & \mathbf{I}_{3\times 3} \\ \mathbf{H}(U) & \mathbf{\Omega} \end{bmatrix}, \tag{4.9}$$

where $\mathbf{H}(U)$ is the symmetric 3×3 Hessian matrix of the CR3BP potential function in Equation 2.8 with respect to $\mathbf{r}$. This submatrix expands to

$$\mathbf{H}(U) = \begin{bmatrix} U_{xx} & U_{xy} & U_{xz} \\ U_{yx} & U_{yy} & U_{yz} \\ U_{zx} & U_{zy} & U_{zz} \end{bmatrix}, \tag{4.10}$$

where subscripts indicate partial derivatives. The elements of $\mathbf{H}(U)$ are

$$\begin{aligned}
U_{xx} &= 1 + \frac{3\mu(x-1+\mu)^2}{r_2^5} - r_2^3 + \frac{3(1-\mu)(x+\mu)^2}{r_1^5} + \frac{\mu-1}{r_1^3} \\
U_{xy} &= U_{yx} = 3y\left(\frac{\mu(x-1+\mu)}{r_2^5} + \frac{(1-\mu)(x+\mu)}{r_1^5}\right) \\
U_{xz} &= U_{zx} = 3z\left(\frac{\mu(x-1+\mu)}{r_2^5} + \frac{(1-\mu)(x+\mu)}{r_1^5}\right) \\
U_{yy} &= 1 + \frac{3\mu y^2}{r_2^5} - r_2^3 + \frac{3(1-\mu)y^2}{r_1^5} + \frac{\mu-1}{r_1^3} \\
U_{yz} &= U_{zy} = 3yz\left(\frac{\mu}{r_2^5} + \frac{1-\mu}{r_1^5}\right) \\
U_{zz} &= \frac{3\mu z^2}{r_2^5} - r_2^3 + \frac{3(1-\mu)z^2}{r_1^5} + \frac{\mu-1}{r_1^3}.
\end{aligned} \tag{4.11}$$

In Equation 4.9, the submatrix $\mathbf{\Omega}$ is given by

$$\mathbf{\Omega} = \begin{bmatrix} 0 & 2 & 0 \\ -2 & 0 & 0 \\ 0 & 0 & 0 \end{bmatrix}. \tag{4.12}$$

We see from Equation 4.9 that the instantaneous value of the Jacobian, and therefore its eigenvalues, depend only on the position $\mathbf{r} = [x, y, z]^T$ in the CR3BP.

The eigenvalues λ of $\mathbf{A}$ can be found analytically by solving the characteristic equation:

$$\det(\mathbf{A} - \lambda\mathbf{I}) = 0, \tag{4.13}$$

which conveniently expands to

$$\lambda^6 + a_1\lambda^4 + a_2\lambda^2 + a_3, \tag{4.14}$$

where

$$a_1 = 4 - \text{trace}(\mathbf{H}(U)) \tag{4.15}$$

$$a_2 = U_{xx}U_{yy} + U_{xx}U_{zz} + U_{yy}U_{zz} - U_{xy}^2 - U_{xz}^2 - U_{yz}^2 - 4U_{zz} \tag{4.16}$$

$$a_3 = -\det(\mathbf{H}(U)). \tag{4.17}$$

Equation 4.14 shows, without proof, that the coefficients on the odd power terms are all zero, which is due to the large number of null elements and the symmetry in the submatrices of $\mathbf{A}$. We can simplify the characteristic equation further by substituting $u = \lambda^2$, which turns the equation into a cubic polynomial

$$u^3 + a_1u^2 + a_2u + a_3 = 0. \tag{4.18}$$

This substitution reveals several interesting facts. First, the eigenvalues will come in pairs with opposite signs ($\lambda = \pm\sqrt{u}$). Second, at least one root u has to be real since cubic polynomials always span the range $(-\infty, \infty)$, and therefore have between one and three real roots. Therefore, any trajectory in the CR3BP is guaranteed to have at least one eigenvalue with a positive real part except in the extreme case when the characteristic equation has one real root at the origin and the other two roots are purely imaginary. This means that no CR3BP orbit can be asymptotically stable, except possibly in the described exception. Even with the real root at the origin, the stability of that trajectory is inconclusive without including higher order derivatives in our Taylor series expansion. Fortunately, there are other analyses that are better suited to orbits in the CR3BP.

4.3 Stability of DROs in the CR3BP

As mentioned in the literature review in Chapter 2, DROs have been shown to be stable in many simplifications of the three-body problem including the Hill Problem[50–52] and the CR3BP.[11–13,19] This section will numerically show stability in the CR3BP. It will also discuss similar techniques applied to quasi-periodic DROs.

4.3.1 Periodic DRO Stability

The stability of any periodic orbit can be evaluated by studying its Monodromy matrix, or the STM after one complete period ($M = \Phi(t_0+T, t_0)$). The eigenvalues λ of this matrix determine if a perturbation from this periodic orbit will exponentially grow or decay. Each eigenvalue has an associated Lyapunov characteristic exponent α such that $\lambda = e^{\alpha T}$. A periodic orbit is unstable if $\max|\mathrm{Re}(\lambda_i)| > 1$, neutrally stable if $\max|\mathrm{Re}(\lambda_i)| = 1$, and stable if $\max|\mathrm{Re}(\lambda_i)| < 1$. The imaginary component of the eigenvalues means a perturbation will oscillate about the periodic reference orbit. Furthermore, Broucke showed that eigenvalues of a Monodromy matrix in the CR3BP will have two eigenvalues equal to unity due to the symplectic nature of the CR3BP. This confirms our finding in Section 4.2 that no CR3BP trajectory can be asymptotically stable, only neutrally (center) stable at best.[19] Battin showed that the remaining four eigenvalues come in two pairs of reciprocal values.[8] Bray and Goudas formulated an analytic solution for the eigenvalues of the Monodromy matrix. The non-unity eigenvalues are given by

$$\lambda_{1,2} = \frac{-p \pm \sqrt{p^2 - 4}}{2} \tag{4.19}$$

$$\lambda_{3,4} = \frac{-q \pm \sqrt{q^2 - 4}}{2}, \tag{4.20}$$

where the intermediate variables p and q are given by

$$\alpha = 2 - \text{trace}(M) \tag{4.21}$$

$$\beta = \frac{\alpha^2 - \text{trace}(M^2)}{2} + 1 \tag{4.22}$$

$$\gamma = \sqrt{\alpha^2 - 4\beta + 8} \tag{4.23}$$

$$p = \frac{\alpha + \gamma}{2} \tag{4.24}$$

$$q = \frac{\alpha - \gamma}{2}. \tag{4.25}$$

This development can tell us whether or not a periodic orbit is stable, but it doesn't give an intuitive sense of how stable an orbit is, especially when comparing two different orbits. There are several metrics that can rank the stability of different orbits, and perhaps the most intuitive is the perturbation doubling/half time.[93] If a particle on a stable, periodic orbit is given a small perturbation δ, the perturbation half-time $\tau_{1/2}$ is the duration it takes of that perturbation to halve in magnitude. $\tau_{1/2}$ is derived below:

$$\delta = \delta_0 e^{\alpha t}$$

$$\frac{\delta}{\delta_0} = \frac{1}{2} = e^{\alpha \tau_{1/2}}$$

$$\ln(1/2) = \alpha \tau_{1/2}. \tag{4.26}$$

Recall that

$$\lambda = e^{\alpha T}$$

$$\ln(\lambda) = \alpha T. \tag{4.27}$$

Divide Equation 4.26 by 4.27 to get

$$\frac{\ln(1/2)}{\ln(\lambda)} = \frac{\alpha \tau_{1/2}}{\alpha T}$$

$$\tau_{1/2} = \frac{\ln(1/2)}{\ln(\lambda)} T. \tag{4.28}$$

Using the eigenvalue λ with the smallest real part in Equation 4.28 will result in the shortest perturbation half-time.

The stability of DROs in the CR3BP between 10,000 and 100,000 km is analyzed with the described method and the results are plotted in Figure 4.2. The left plot shows the real part of the four non-unity eigenvalues are less than unity. Note that there are only two lines on the plot because complex eigenvalues come in conjugate pairs that have the same real part, causing their lines to overlap. The right plot shows the perturbation half-time for these DROs. $\tau_{1/2}$ begins at around 25 days and grows smaller as the DRO size gets bigger up until a minimum is reached at 42,000 km. $\tau_{1/2}$ exists for all DRO sizes, even when using the largest λ, which allows us to conclude that periodic DROs are neutrally stable in the CR3BP.

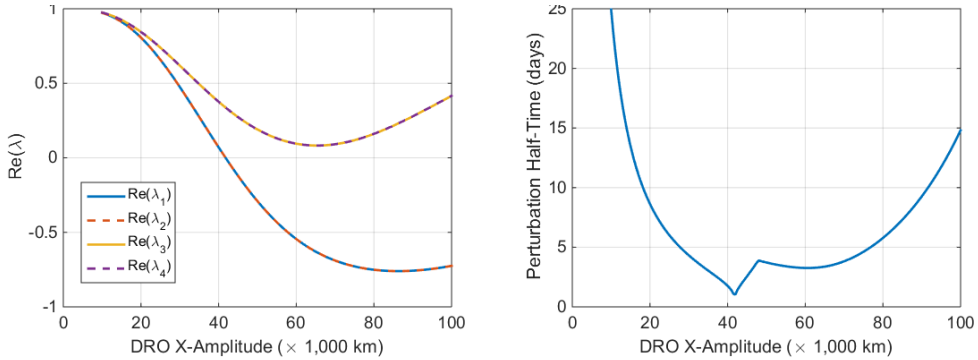

(a) Real part of the non-unity eigenvalues. (b) Perturbation half-time

Figure 4.2: Stability of DROs in the CR3BP

4.3.2 Quasi-Periodic DROs

Determining the stability of quasi-periodic orbits is a more complicated task because the monodromy matrix cannot be computed. However, linear stability information can be gained using Kolmogrorov-Arnold-Moser (KAM) theory.[5,68,83] To study a quasi-periodic orbit's stability, we begin by generating the invariant torus associated with a particular quasi-periodic orbit. If one propagates a quasi-periodic orbit for enough time, it will densely cover a surface in the six-dimensional phase space. This surface represents a flow through the phase space and a Floquet matrix can be used to describe this flow in the same way that a STM does for a trajectory.[39] A particle beginning on this surface will be on the quasi-periodic orbit, and therefore forever bound

to the surface. This means that the surface is invariant under the equations of motion, similar to how a periodic orbit is invariant. Because the surface is invariant, the Floquet matrix after a full "revolution" can offer similar stability information as the Monodromy matrix does.[63]

The surface can generally be represented as an n-dimensional torus where n is the number of angle coordinates needed to uniquely describe the state of a particle on the surface; this is not to be confused with the dimensionality of the phase space. In the CR3BP, any of the Lagrange points are examples of 0-dimensional tori as they are fixed point solutions. Periodic orbits are 1-dimensional tori since a position along the orbit can be uniquely determined by a single angle τ as discussed in Section 3.1. Quasi-periodic orbits in the CR3BP are 2-dimensional tori. The two angles required are shown on a standard torus in Figure 4.3.

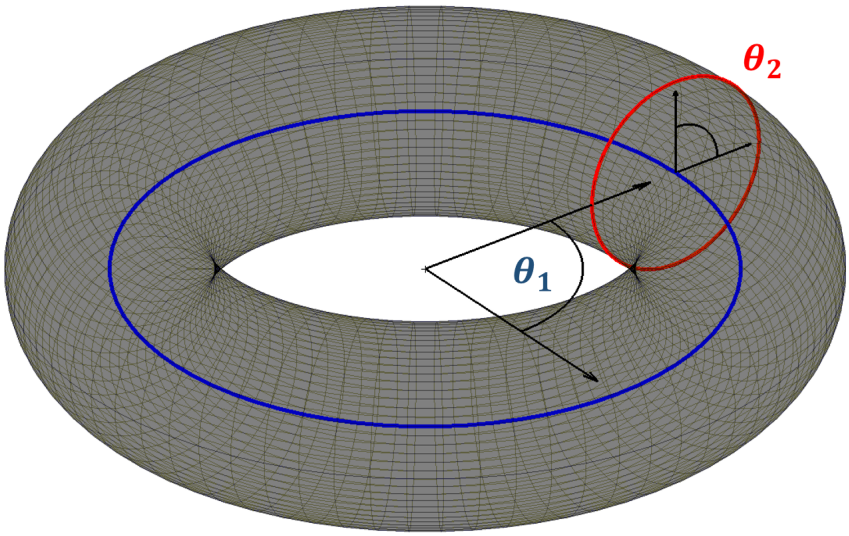

Figure 4.3: A two-dimensional torus can uniquely define a position on its surface with two angle coordinates.

We can generate a numeric approximation of the invariant torus using a number of methods by Olikara et. al.[90,91] One strategy will be presented at a high level while the details of the formulation can be found in the cited references. This torus approximation will be called the torus function $\mathbf{u}(\theta)$ which returns the six-dimensional phase space state given the input angle coordinates θ. The torus function $\mathbf{u}$ is well suited to be expressed as a Fourier series since the closed torus will

naturally repeat.

$$\mathbf{u}(\theta) = \sum_{\mathbf{k}\in Z^2} c_{\mathbf{k}} e^{i\langle \mathbf{k},\theta\rangle}. \tag{4.29}$$

The goal is to build $\mathbf{u}(\theta)$ such that it meets two conditions. First, it must be invariant under the equations of motion:

$$\sum_{i=1}^{n} \frac{\partial \mathbf{u}(\theta)}{\partial \theta_i}\frac{d\theta_i}{dt} = \sum_{i=1}^{n} \frac{\partial \mathbf{u}(\theta)}{\partial \theta_i}\omega_i = f(\mathbf{u}(\theta)), \tag{4.30}$$

where the right-hand side term is the evaluation of the derivative function for the equations of motion. The second condition is that the torus function be constructed such that ω is a constant vector so θ flows linearly in time.

An initial guess for the torus, $\hat{\mathbf{u}}$ is generated and then differentially corrected until this invariance equation (Equation 4.30) is satisfied along with several other constraints. Olikara suggests beginning with a periodic orbit and discretizing it around its τ value. These points will correspond to values of θ_1. Next, perturb the state along the eigenvector $\mathbf{y}$ associated with any complex eigenvalue obtained from the periodic orbit's Monodromy matrix. Sweep this perturbation in a discretized unit circle around the reference periodic orbit. These points correspond to θ_2 positions on the torus. A graphical representation of this discretization scheme is shown in Figure 4.4. For each value of θ_1 and θ_2 the following expression gives the torus state:

$$\hat{\mathbf{u}}(\theta_1,\theta_2) = \hat{\mathbf{u}}_0(\theta_1) + \cos(\theta_2)\mathrm{Re}[\mathbf{y}(\theta_1)] - \sin(\theta_2)\mathrm{Im}[\mathbf{y}(\theta_1)], \tag{4.31}$$

where $\hat{\mathbf{u}}_0(\theta_1)$ is the discretized periodic orbit used as a reference for the torus. Figure 4.5a shows how the initial guess is generated for a halo orbit, though the same process is used for a DRO. Figure 4.5b shows the periodic orbit, discretized along θ_1 with the eigenvectors at $\theta_2 = 0°$ and $90°$ shown as yellow and red arrows emanating from each node. After sweeping the eigenvectors through θ_2 at all nodes for θ_1, we have the torus estimate shown on the right.

We could solve the invariance condition by computing the derivative of the torus with respect to θ_1 and θ_2 using finite difference methods, but a better method exists. The dimensionality of the torus function can be reduced by removing the function's dependence on the first angle θ_1. We can

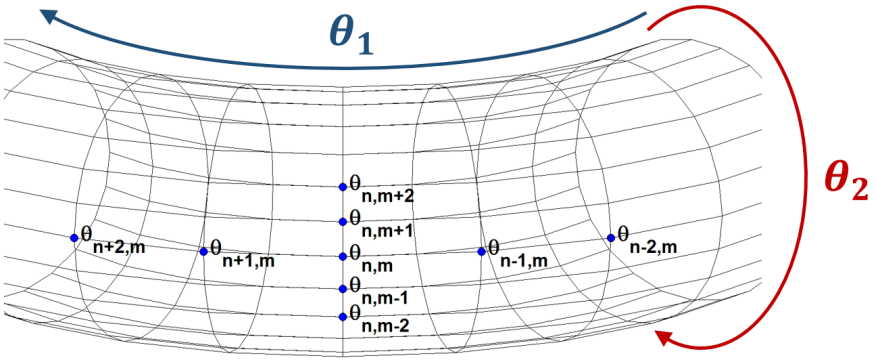

Figure 4.4: The discretization scheme shown on a standard torus. Subscript n corresponds to θ_1 and subscript m corresponds to θ_2.

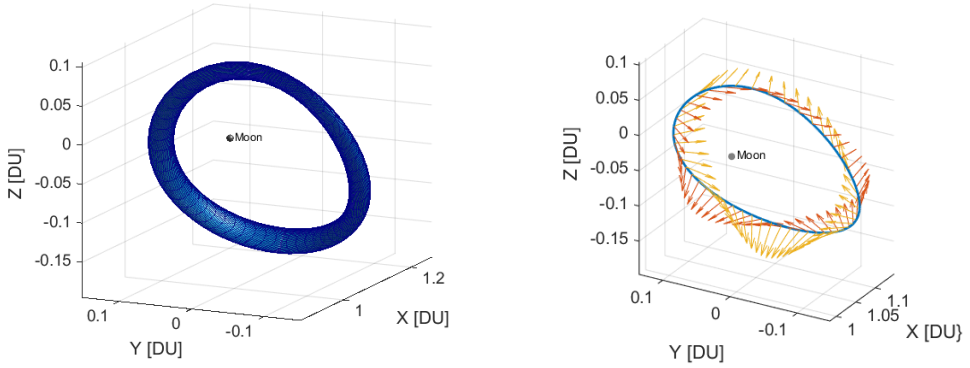

(a) The initial guess for the invariant torus (b) The torus' center stable eigenvectors

propagate the torus function for some time $T = 2\pi/\omega_1$ with

$$\bar{\mathbf{u}} = F(\mathbf{u}, T). \tag{4.32}$$

Over this propagation, the angle $\theta_1(t_0)$ will advance to $\theta_1(T) = \theta_1(t_0) + 2\pi = \theta_1(t_0)$. The orbit will also traverse along θ_2 at the constant rate of ω_2, leaving it at $\theta_2(T) = \theta_2(t_0) + 2\pi\dfrac{\omega_2}{\omega_1}$. Olikara and Scheeres[91] lay the groundwork for a method to undo this rotation about θ_2 after a period T using

$$G(\mathbf{u}, T, \omega) = R(\omega) \circ F(\mathbf{u}, T). \tag{4.33}$$

With the rotation about θ_2 canceled out, the torus propagated for one period T must equal the unpropagated torus. Therefore, the invariance condition from Equation 4.30 becomes

$$G(\mathbf{u}, T, \omega) - \mathbf{u} = \mathbf{0}. \tag{4.34}$$

This reduction in dimensionality means that $\mathbf{u}$ only needs to be discretized in the θ_2 dimension for one chosen value of θ_1. In effect, this turns the problem into a shooting algorithm with the goal of minimizing the residuals of the invariance equation and other constraints like phase and pseudo-arclength constraints. Figure 4.6 shows the initial torus $\hat{\mathbf{u}}$, which is now a 1D torus, in blue. It is propagated for time T until $\theta_1 = 2\pi$, resulting in the red torus. We can see that even if the red torus is rotated about its center axis (a rotation about θ_2) the two tori will not be aligned or the same shape. Thus the torus is not invariant and will need to be corrected. We can update our guess with any number of minimization algorithms having the general form

$$\mathbf{u}^{k+1} = \mathbf{u}^k + (J^T J + Q)^{-1}(-J^T \mathbf{r}), \tag{4.35}$$

where k defines the iteration number, $\mathbf{r}$ is the residual of the invariance equation (4.34) and other constraints, J is the Jacobian of the invariance condition with respect to the torus function, and Q is a matrix that can be chosen to help the stability of the algorithm.

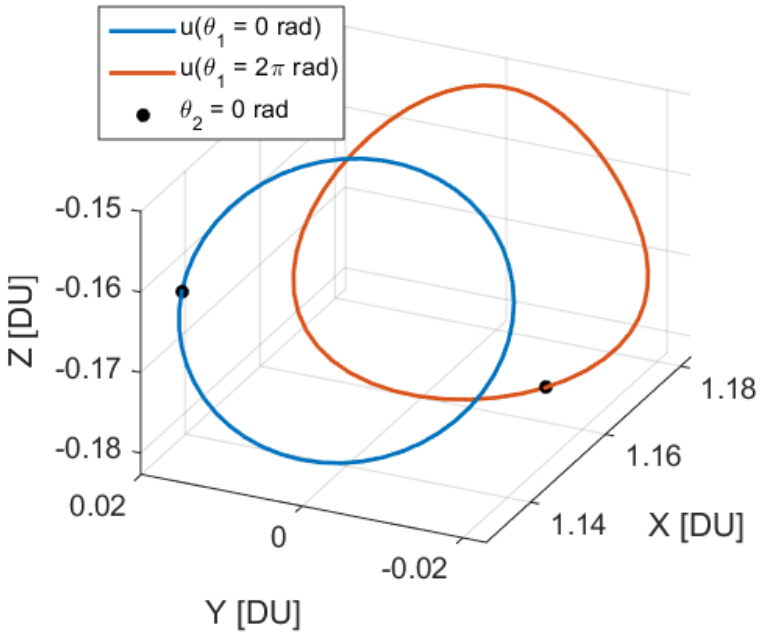

Figure 4.6: The initial guess for the 1D torus (blue). After propagating for one period, the final torus (red) does not match the initial torus and must be corrected.

Finally, after the torus has converged, we can build an approximation of the Floquet matrix

to get linear stability information. Using the rotation parameter from Equation 4.33, this matrix given by

$$B = R(\omega) \circ F_x, \tag{4.36}$$

where F_x is a block diagonal matrix consisting of the Monodromy matrices of each state propagated from the discretized values of θ_2; it has the form

$$F_x = \begin{bmatrix} \Phi(T,0)|_{\mathbf{u}(\theta_2^1)} & \mathbf{0} & \mathbf{0} & \cdots & \mathbf{0} \\ \mathbf{0} & \Phi(T,0)|_{\mathbf{u}(\theta_2^2)} & \mathbf{0} & \cdots & \mathbf{0} \\ \vdots & & \ddots & & \vdots \\ \mathbf{0} & \cdots & & & \Phi(T,0)|_{\mathbf{u}(\theta_2^N)} \end{bmatrix}. \tag{4.37}$$

Jorba showed that the eigenvalues of this matrix B are the same as the Floquet matrix defined up to a rotation in the complex plane.[63] Therefore, eigenvalues of B that lie on the unit circle are center-stable. Eigenvalues above the unit circle will cause a perturbation along its associated eigenvector to grow linearly.

4.4 Stability of DROs in High Fidelity Models

This section compares and analyzes DROs that have been propagated in high fidelity dynamical models for hundreds of years to understand the limits of stability. There are many forces that can act on a body in orbit; some are dependent on the design of the spacecraft such as specular reflecting solar radiation pressure, while others have little to no dependence on the spacecraft's shape or size, such as gravity from massive bodies in the solar system. To keep this study generalized, design-dependent accelerations are typically neglected.

4.4.1 Perturbation Analysis Setup

This study begins by analyzing the effects of the five largest perturbing forces experienced by a DRO in the Earth-Moon system. We propagate a set of DROs ranging in period from 7 to 20 days in a high fidelity dynamical model that includes gravity from the Moon and the Earth (with

full ephemeris positions from DE430) and one additional perturbing force at a time. The resulting trajectory, after a 500 year propagation, is checked to see if it remains bound to an orbit around the Moon (Lagrange stable) for the full propagation; if it does, the orbit is labeled as stable.

The five perturbations considered in this survey include gravity from the Sun, Jupiter, and Venus, the aspherical gravity field of the Moon, and solar radiation pressure (SRP). The lunar gravity field is represented with a spherical harmonic expansion using the first 20x20 coefficients from the LP150Q model.[69] Solar radiation pressure (SRP) calculations use a cannonball model with an area to mass ratio of 7.65×10^{-5} m^2/kg and a reflectance coefficient of 1.25. The choices are based on the size, density, and albedo estimates for candidate asteroids in JPL's asteroid retrieval mission according to a feasibility study.[18] Smaller, lighter satellites can experience a stronger acceleration from SRP than an asteroid. Table 4.1 shows an approximate average magnitude of the perturbing accelerations for a 65,000 km DRO. Outside of the Earth-Moon system, the Sun is the strongest perturbation, which is three orders of magnitude smaller than the gravity from the Earth and the Moon. These perturbing accelerations oscillate at a variety of frequencies and resonances can occur if a DRO's period is too close to one of these frequencies. This can lead to drastic changes in motion, and inevitably can destabilize a DRO. The sun's gravity oscillates with the Moon's synodic period, or about every 29.5 days. The slight ellipticity of the Earth's orbit around the Sun can cause an annual frequency as well. SRP directly counteracts solar gravity due to the cannonball model used, so it has the same frequencies. More advanced models for SRP depend on solar energy output, and therefore can include shorter frequencies like the Sun's rotation rate, or longer ones like the Sun's 11 year magnetic activity cycle. Jupiter and Venus have longer period frequencies computed as the synodic period between Earth and that planet (399 and 584 days, respectively).

Acceleration Source	Average Magnitude (m/s^2))
Lunar (center) Gravity	1.00×10^{-3}
Earth Gravity	1.33×10^{-3}
Solar Gravity	5.60×10^{-6}
Solar Radiation Pressure	8.66×10^{-8}
Venus Gravity	6.63×10^{-10}
Aspherical Gravity Field	1.88×10^{-10}
Jupiter Gravity	7.16×10^{-11}

Table 4.1: A list of the average magnitude of each perturbation. DRO dependent values assume a 65,000 km (∼12.5 day) orbit.

The DROs are propagated with the five perturbations individually and in combinations. Seven cases are run in total, which are labeled as follows:

Case 1: No perturbations. A full ephemeris propagation with the Earth and Moon.

Case 2: Solar gravity only.

Case 3: Venus gravity only.

Case 4: Jupiter gravity only.

Case 5: 20x20 Lunar gravity field.

Case 6: Solar radiation pressure and solar gravity. These two accelerations oppose each other, reducing the effects seen in Case 2.

Case 7: All perturbations are used to see if any combine effects in a significant way.

4.4.2 Results of the Perturbation Survey

The results from propagating this set of DROs are shown in Figure 4.7. Colored lines represent where the orbits are stable for the entire 500 year period. Note that the unstable regions do not necessarily preclude stable orbits from existing at that size, they simply aren't stable for the

generated initial conditions used in this study. However, they are indicative of regions that are less stable under perturbation. Case 1 is the control group that shows the stability of DROs without any forces other than Earth and Lunar gravity. In this case, orbits larger than 16 days (85,000 km) do not remain bound to the Moon for the full 500 year duration. There are additional gaps in stability; the most prominent one is for DROs with a period between 9.3 and 10.9 days.

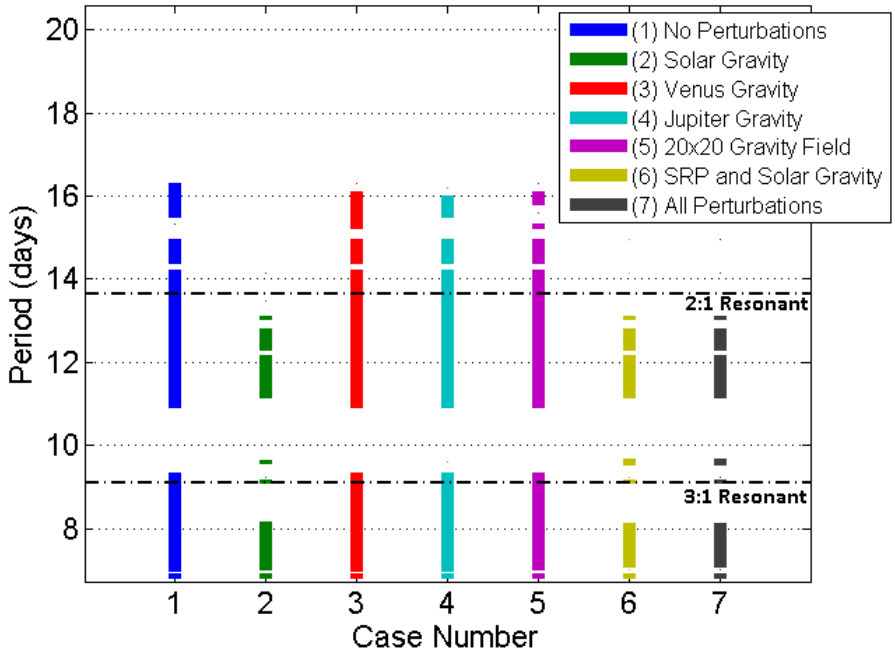

Figure 4.7: Stability of a set of DROs under different perturbations. Colored lines represent stable orbits.

Case 2 adds solar gravity to the dynamical model and this case stands out as the only significant deviation from the control case. The Sun's gravity limits the upper stability region to approximately 11.16 to 12.79 days (60,000 to 68,000 km). This removes the 2:1 resonant orbit from the stable region, meaning special care will need to be taken when designing DROs of that size. We can compare Case 2 and Case 6 since the SRP acceleration directly opposes solar gravity. However, the SRP acceleration appears to do little to alleviate the stability zone reduction, save for a small region around the 9 day (50,000 km) DRO. Again, using SRP parameters (area-to-mass ratio, albedo, etc) for common satellites instead of asteroids can increase the SRP acceleration to a point

where it can significantly counter the Sun's gravity. Cases 3, 4, and 5 all show small fluctuations in their stable regions for DROs larger than 15 days. These perturbations are all comparable in magnitude, and affect the same size DROs. Finally, it is interesting to note that adding Venus gravity to the simulation actually improved the stability of these large DROs.

Several trajectories from the stable and unstable regions of Case 2 in Figure 4.7 are viewed in an animation showing how the shape of the orbit evolves over time. The DROs are often found to oscillate into two distinct mode shapes, shown at peak amplitude in Figures 4.8. The first is

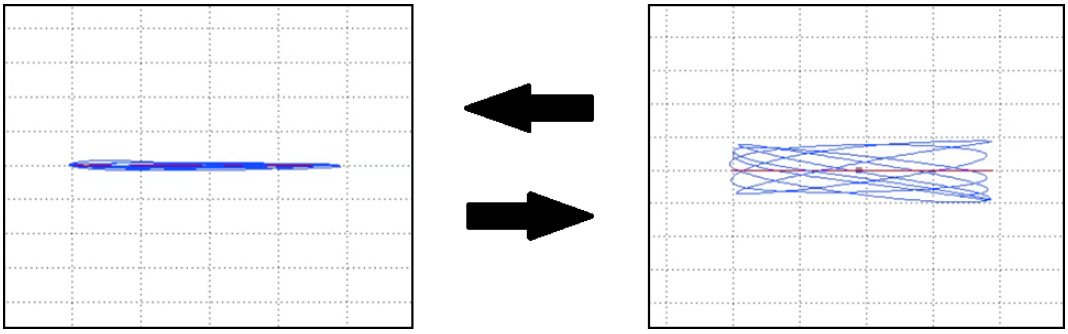

(a) Mode 1 - Z-amplitude oscillations

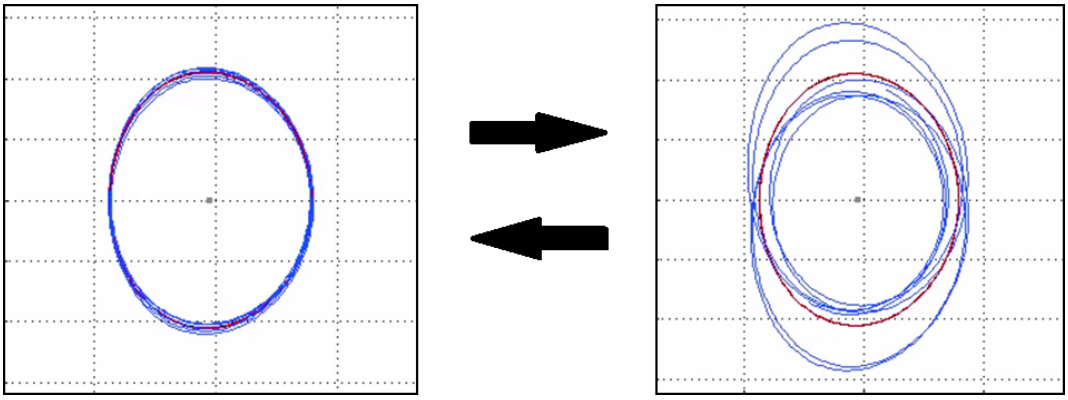

(b) Mode 2 - Leading and lagging orbits

Figure 4.8: Two mode shapes in high fidelity DROs

an oscillation in the z-amplitude over a period of several years with little change to the x- or y-amplitudes. This will be referred to as the *out-of-plane mode*. The second mode shape, referred to as the *in-plane mode*, is a planar bifurcation of the orbit into two similarly sized and shaped orbits, one leading the Moon and the other lagging behind it. In an inertial frame, this is caused when the

DRO develops a difference in phase with the Moon as they both orbit the Earth-Moon barycenter, resulting in alternating close and far passes without a significant change to the orbit size. These two modes are not always mutually exclusive, but generally one mode is dominant and oscillates with significantly more amplitude.

Trajectories in the unstable zones of Figure 4.7 often exhibit a beating pattern behavior where the amplitude of each mode shape rapidly grows large and then decays. It then remains dormant for longer than the mode is activated for. Beating patterns are indicative of being near a resonant forcing frequency with one of the perturbing forces. When the amplitude of one of these modes grows beyond a critical point, the DRO leaves its stability envelope and it departs the neighborhood of the Moon. The in-plane mode instability has been studied in the literature in the CR3BP by Scott and Spencer.[116,117] They discuss how planar quasi-periodic DROs in the CR3BP have a stability boundary, which is best visualized with a Poincaré section around a periodic solution. An example of a Poincaré section for a 65,000 km DRO in the Earth-Moon CR3BP is shown on the left side of Figure 4.9. The three corners of this section bound the stable region with an unstable

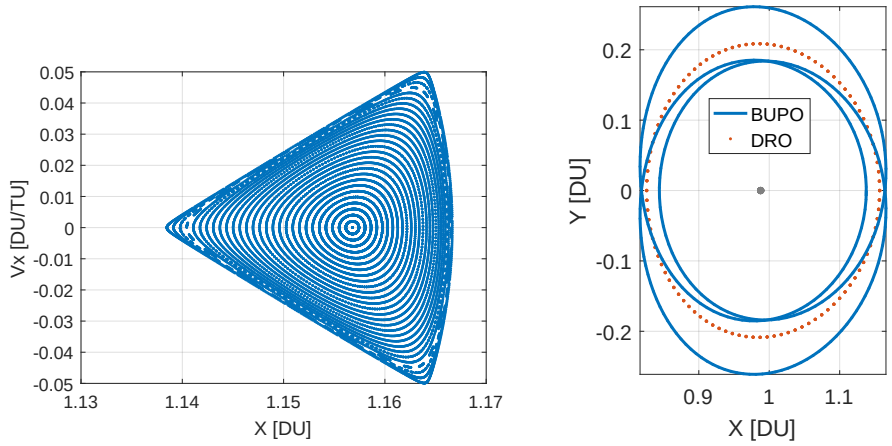

(a) Poincaré section (b) Associated BUPO

Figure 4.9: The Poincaré section of a quasi-periodic, planar 65,000 km DRO in the CR3BP and the bounding unstable periodic orbit that surrounds its stable region

period-3 orbit called a bounding unstable periodic orbit (BUPO), which is illustrated on the right side of Figure 4.9. When the in-plane mode's amplitude reaches the size of that DRO's associated

BUPO, then it departs the Moon at an exponential rate.

DROs in the stable zones in Case 2 exhibit both mode shapes, but they beat with small amplitudes that do not seem to increase over time. Smaller DROs than this stability zone generally show divergence due to the in-plane mode and unstable DROs that are larger diverge due to the out-of-plane mode. It is intuitive that larger DROs would be less susceptible to in-plane mode divergence due to the inverse square proportion for gravitational acceleration. Larger DROs experience relatively smaller differences in acceleration when they have variations in x- and y-amplitudes when compared to smaller DROs. Additionally, Lam demonstrates that large DROs around Europa cannot endure the same magnitude of out-of-plane motion that smaller DROs can, meaning that larger DROs are more susceptible to the out-of-plane mode.[73]

To further illustrate the Sun's effect on the stability zone between Case 1 and 2, Poincaré sections are generated at the xz-plane crossings (Figure 4.10). Comparing plots (a) and (c), there is growth in the x-velocity (an in-plane mode indicator) of approximately 20-30 m/s in orbits between 50,000 and 85,000 km. Additionally, the dense region below 50,000 km grows by nearly 50 m/s. Among the largest changing regions is between 50,000 and 60,000 km, which covers the unstable area just below the Case 2 stability zone. Because the in-plane mode is present in Case 1 DROs smaller than 11 days, it is likely tied to a resonant frequency in the Earth-Moon dynamics and is exacerbated by solar perturbations. Comparing plots (b) and (d) reveals that the sun does little to affect the out-of-plane velocity for orbits less than 70,000 km. Orbits larger than this experience z-velocity growth (an out-of-plane mode indicator) of around 30-40 m/s. Orbits larger than 90,000 km diverge relatively rapidly compared to smaller DROs.

To summarize, solar gravity is the dominant perturbing force on DROs and is the only perturbing force that significantly impacts the stability of DROs over the course of 500 years. It reduces the size of stable DROs to between 60,000 and 68,000 km. DROs larger than this stable band experience a growth in z-amplitude that leads to departure from the Moon. DROs smaller than this stable band generally experience in-plane perturbations leading to a BUPO configuration that is ultimately unstable.

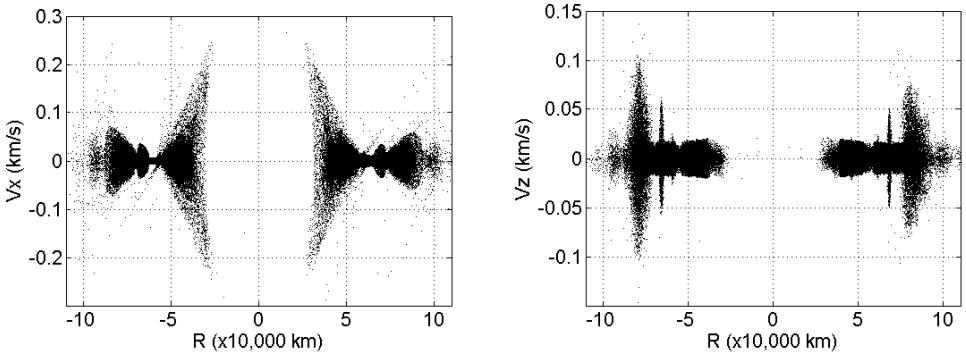

(a) Case 1: X vs Vx

(b) Case 1: X vs Vz

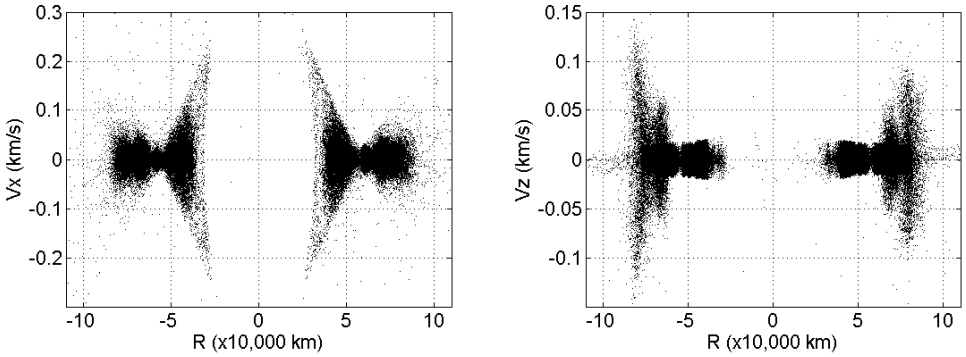

(c) Case 2: X vs Vx

Figure 4.10: Poincaré sections for all of the xz-plane crossings for orbits between 30,000 and 110,000 km. The bottom row includes the effects of solar gravity, while the top row does not have perturbations applied.

4.4.3 Inclined DRO Stability

We can expand the survey to better understand and characterize the stable regions shown in Figure 4.7 as they relate to the out-of-plane mode by considering the limits of z-amplitude that stable DROs can maintain before becoming unstable. To start, initial conditions are generated for DROs between 20,000 and 70,000 km in 500 km intervals using the methods described in Section 3.3.1. Out-of-plane (z-direction) velocity is then added to these initial conditions to give the DRO a *pseudo-inclination*: the angle between the initial velocity vector and the xy-plane. Since DROs are retrograde orbits, the pseudo-inclination has a value of 180° when the orbit is planar and values less than 180° mean the added velocity is in the $+z$ direction in the rotating frame. Adding this velocity perturbation results in a non-planar, quasi-periodic DRO with a lower Jacobi constant, but

similar x- and y-amplitudes. Each trajectory is propagated for 100 years with Earth, Moon, and solar gravity, and we track the duration that the trajectory remained within a bounding radius of 384,000 km from the Moon. Examples of these data sets are shown in Figure 4.11. These plots are similar to Lam's Red Sea Plots[73] though those plots are generated by rotating the velocity vector out-of-plane, not by adding velocity.

In these maps, the boundary between DROs that remain around the Moon and those that fall away in a few days is narrow and easily distinguishable. This shows that there is a sharp, well defined stability boundary, just as we see in the CR3BP. Stable regions for planar DROs in this plot show agreement with those found in Figure 4.7. The maximum pseudo-inclination can be used as a metric to gauge relative stability of different DROs since it relates to the maximum allowable z-velocity perturbation that can be applied. Interestingly, these maps exhibit significant variations when they begin at different epochs corresponding to different lunar true anomalies. Figure 4.11 shows several examples, separated by five days each. The most obvious changes occur in three places: the rift at approximately 40,000 km, the stable island at 47,000 km, and the rift at about 65,000 km. To determine reliable stable regions, we take the mean of 28 pseudo-inclination stability maps spanning one sidereal lunar period and highlight the regions that remain stable regardless of lunar true anomaly. This composite map is shown in Figure 4.12. This map shows that there are four primary regions, labeled A through D where a DRO is stable regardless of the lunar true anomaly at the start of the propagation. We also see from this figure that smaller DROs from region A, which spans 20,000-36,000 km, can tolerate significantly more pseudo-inclination before becoming unstable orbits. The upper limit in region A approximately follows a linear trend of with a slope of $-1°$ per 1,000 km in size. Regions B-D all have comparable upper limit on pseudo-inclinations of about 173° - 170°.

4.4.4 Two-Dimensional Stability Maps

The next logical step for this work is to add another dimension to the stability analysis and explore how a combination of in-plane and out-of-plane velocity perturbations affect the stability

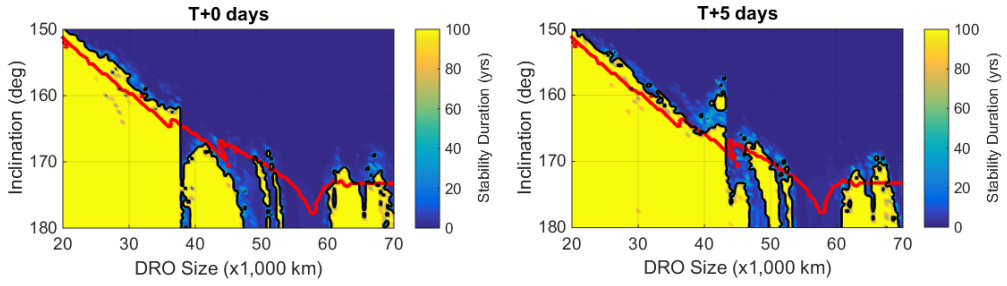

(a) Lunar True Anomaly: 167° (b) Lunar True Anomaly: 235°

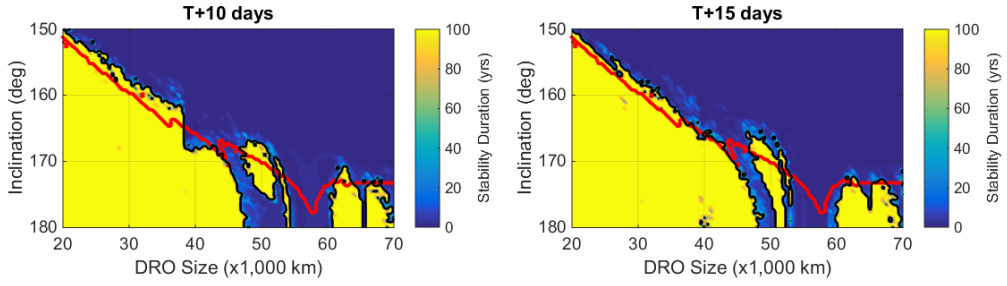

(c) Lunar True Anomaly: 279° (d) Lunar True Anomaly: 338°

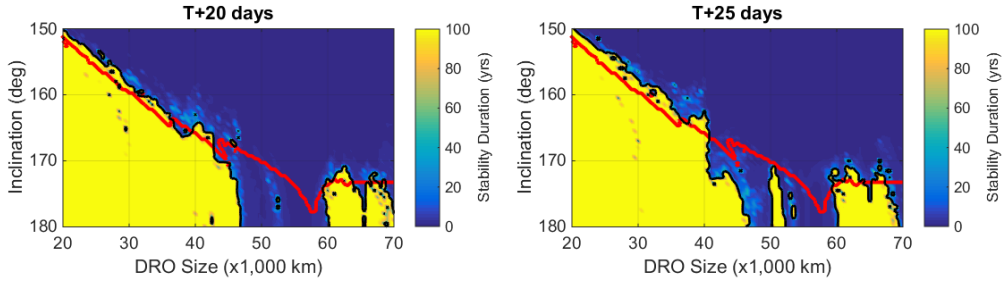

(e) Lunar True Anomaly: 47° (f) Lunar True Anomaly: 126°

Figure 4.11: The stability duration of inclined DROs between 20,000 and 70,000 km. The red line shows the boundary of the stable region in the CR3BP for comparison.

of DROs. This type of perturbation survey creates what will be referred to as a *two-dimensional (2D) stability map*. We start with the initial conditions for a specific DRO and perturb the velocity in the rotating frame's x- and z-directions by a uniform grid of values of arbitrary range. Since the initial velocity is purely in the $-y$-direction, these velocity perturbations directly express the

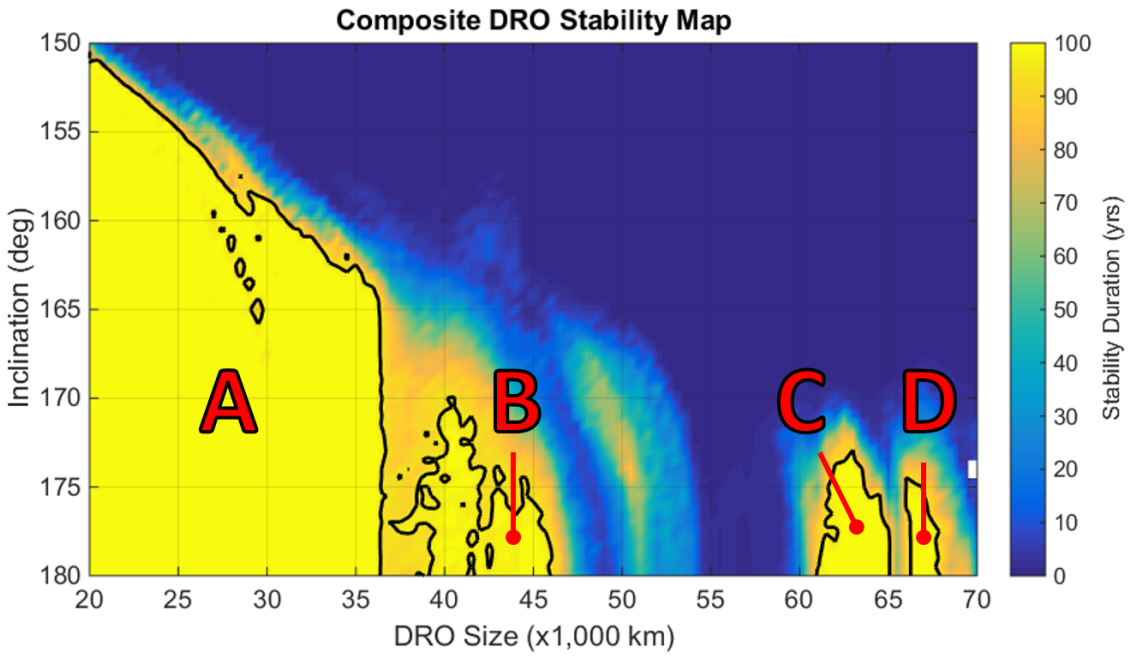

Figure 4.12: The mean of 28 inclined DRO pseudo-inclination stability maps spanning the lunar period.

in-plane and out-of-plane modes while minimally affecting the period of the orbit. We can use the center component as an alternate approach for finding the perturbation directions that activate the two mode shapes. We begin with the Monodromy matrix $\mathbf{M}$ of the periodic DRO under study, which was shown to have two pairs of complex eigenvalues with a norm of unity. The eigenvectors associated with these eigenvalue pairs represent the perturbation directions that activate the a center component mode shape. For any periodic DRO, the velocity component of one pair's eigenvector points almost exclusively in the z-direction; the other pair's eigenvector points in the xy-plane, though not exclusively in the x- or y-direction. A position shift in these directions also activates the same modes.

We can track how long a DRO remains in the neighborhood of the Moon after 2D perturbations, just as we did with pseudo-inclination stability maps. Obviously by adding a perturbation dimension, we lose the ability to represent a set of DROs in a single plot, so we will focus on a single DRO from region B of Figure 4.12. Figure 4.13 shows a 45,000 km DRO's 2D stability

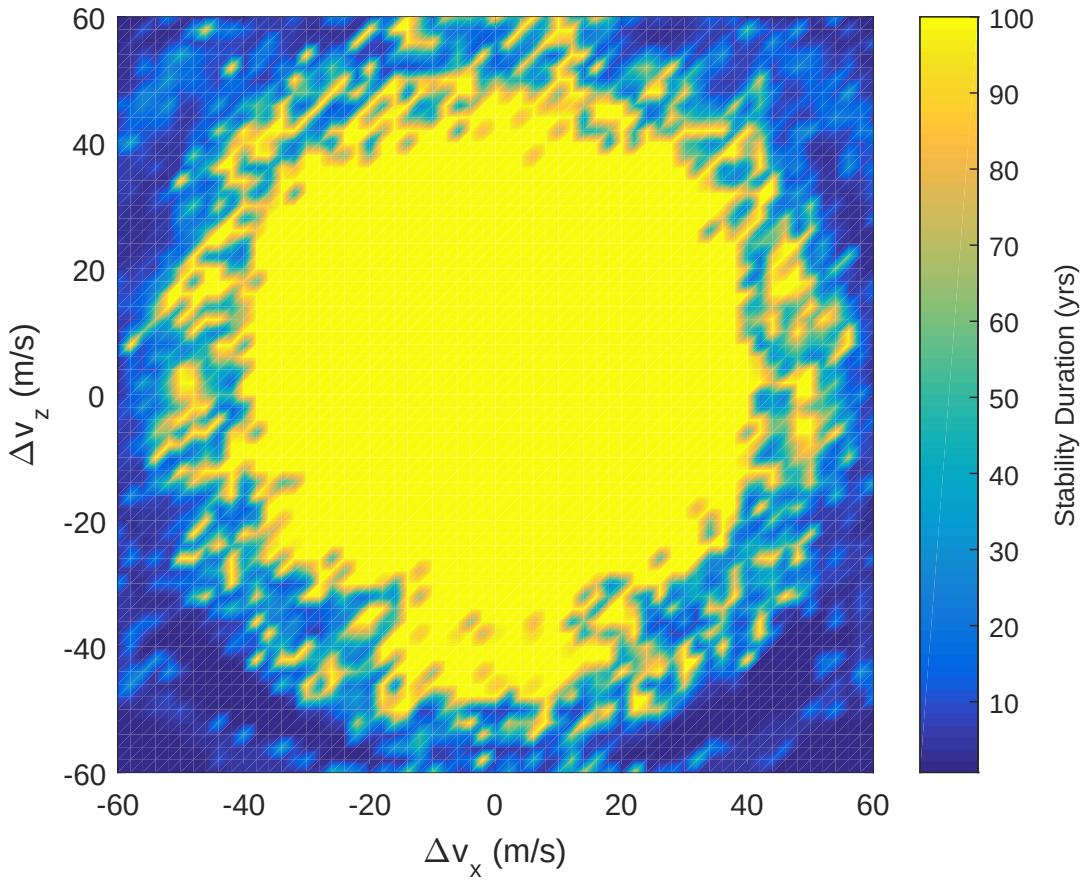

Figure 4.13: The 2D stability map for the 45,000 km DRO.

map. In this map, we see one large stable region centered on the periodic DRO where $\Delta v = (0, 0)$, spanning from -50 to +45 m/s in the z-direction and ± 40 m/s in the x-direction. This stable zone is surrounded by a band of trajectories that are stable for 30-50 years, which is dotted with stable islands. This band is about 10-15 m/s wide. This plot shows us that the division between stable and unstable trajectories is not always as obvious as it appeared in the pseudo-inclination stability maps. Chapter 5 will explore this ambiguous region in further detail.

4.4.5 Higher Dimensional Stability Maps

The brute force strategy of identifying the stability boundary could be extended to higher dimensional perturbations, but this should only be done if necessary because of the severe increase

in computation time. We have seen throughout this chapter that DROs become unstable when their in-plane and z-amplitudes become too large, and both of these modes can be activated by the perturbations in the 2D stability maps. It was also noted that position shifts in the same directions as the velocity perturbations also activate these modes.

The question then becomes whether or not we can map the state in six-dimensional phase space onto a 2D stability map that has already been generated. Of course, one could also evaluate the stability of an arbitrary state simply by building a stability map using it as the reference, but this section seeks to avoid unnecessary computations. Section 4.3.2 discusses the creation of an invariant torus to represent the state space of a quasi-periodic orbit. Building a torus that has the arbitrary state on its surface allows us to reduce the degree of freedom of the problem by one. Following the example of Poincaré, we can further reduce the degrees of freedom by looking at where the torus intersects a reference plane, preferably one that contains the origin of the stability map. The 2D torus intersecting this plane forms a 1D torus, specifically a closed curve, that still represents states in 6D phase space. Next, we can isolate the states where this curve intersects the x-axis. The x-coordinate of these intersections represent the possible DRO sizes that could produce the random state through a velocity perturbation.

At this point, we are left with three degrees of freedom corresponding to the velocity components, so a 3D stability map would be required to determine if the arbitrary state was stable or not. If there are multiple possible DRO sizes, the result from a stability map from any one of them should be sufficient to prove the stability of the others. We know that x- and y-velocity perturbations activate the same in-plane mode shape, so there may be a way to relate these two variables. If such a relationship exists, it would mean that a 2D stability map at the correct DRO size would be sufficient for describing the stability of an arbitrary state.

One place to look for this type of relationship is at the center eigenvector of a DRO's Monodromy matrix. Recall that the complex eigenvalues of this matrix with a norm of unity have eigenvectors that span the in-plane mode and the out-of-plane mode. The in-plane mode has components in the $\dot{x}$ and $\dot{y}$ directions. It may be that the size of the component in each direction

reflects the size of a perturbation that activates the same mode. As of the writing of this dissertation, this relationship has not been tested. There may also be multiple x-axis intersections with the torus, meaning several periodic DRO options exist. If one was identified with near zero error in the y-velocity term, then the 2D stability map for that DRO would be applicable.

Chapter 5

Ballistic Capture into Earth-Moon Distant Retrograde Orbits

5.1 Ballistic Capture into DROs

In Chapter 4, we discussed the use of stability maps as a metric for quantifying the stability of a periodic orbit in a high fidelity dynamical model. In the DROs we examined, there was a narrow region between stable and unstable DROs. The behavior of trajectories in this region is chaotic and can be utilized by mission designers to build low-energy transfers. This chapter explores this band on the border of stability and uses the chaos to constructs trajectories that ballistically escape from or get captured onto a DRO. In the literature, this type of analysis is related to weak stability boundary.[9,10] These results are of interest because they allow a spacecraft to target and enter nearly any stable DRO for small, often negligible fuel expenditure through the convenient use of perturbing forces.

5.1.1 Stability Maps

We begin by looking at a single DRO's two-dimensional stability map described in Section 4.4.4. However, instead of tracking the stable duration, we instead look at the behavior of the trajectory as it evolves forwards and backwards in time. It turns out that many of the trajectories in the narrow band between stable and unstable DROs behave chaotically. This often results in trajectories that are Lagrange stable in one temporal direction, but not the other. To locate these trajectories, the reference DRO's initial conditions are perturbed by a 2D velocity change $(\Delta v_x, \Delta v_z)$ and propagated forwards and backwards in time for 100 years. Next, we check if the

trajectories are Lagrange stable for the full duration in one, both, or neither temporal directions. Each trajectory can fall into one of four stability categories:

Unstable: The DRO departs the Moon when propagated forwards and backwards in time.

Forward Stable: The DRO remains within a bounded distance of the Moon when propagated forward in time, but departs the Moon when propagated backwards in time. These are ballistic capture trajectories (BCTs).

Backward Stable: The DRO remains within a bounded distance of the Moon when propagated backwards in time, but departs the Moon when propagated forwards in time. These are ballistic escape trajectories (BETs).

Two-way Stable: The DRO remains within a bounded distance of the Moon when integrated forward and backward in time.

Forward and backward stable trajectories are referred to as *one-way stable* trajectories in this dissertation. To determine if an orbit is stable or unstable, we check if the trajectory descends lower than the surface of the Moon, about 1,737.4 km, or if departs the neighborhood of the Moon by half the distance between the Earth and the Moon, about 192,374 km. We plot the perturbations along with the trajectory's classification to create what will be generally referred as a *stability map*. The term *stability map* will refer to this plot for the rest of the dissertation unless it specifies the type of map, such as *pseudo-inclination* or *two-dimensional* stability maps. In the stability maps, the *stable region* will refer to the set or sets of two-way stable trajectories.

As an example, three stability maps for the 67,500 km DRO are generated using velocity perturbations ranging between ± 50 m/s at a resolution of 2 m/s. Each map is created using a different dynamical model: the CR3BP, the full ephemeris model with Earth and lunar gravity, and the third includes solar gravity in addition to Earth and lunar gravity. These three cases are plotted for comparison in Figure 5.1. Green points show the two-way stable trajectories, blue points are forward stable, and red points are backwards stable. The CR3BP stability map has the largest stable area of the three, extending well beyond the 50 m/s velocity perturbations limits. It

also has a fine edge between stable and unstable orbits with only eight one-way stable trajectories, which is the expected level of rarity. When the high fidelity model is used without perturbations external to the Earth-Moon system, the size of the stable region decreases to about ±35 m/s in the x-direction and about ±47 m/s in the z-direction. A thin boundary of one-way stable trajectories develops around the border of the stable region. This is caused by the Moon's orbital eccentricity and, because the Moon's state comes from an ephemeris file, the indirect effects of the perturbing forces acting on the Moon but not the spacecraft. Adding solar gravity in the rightmost stability map causes the most drastic changes. It reduces the size of the stable region by about 10 m/s on each side and leaves behind a significant number of one-way stable trajectories in the region that was previously stable without solar gravity.

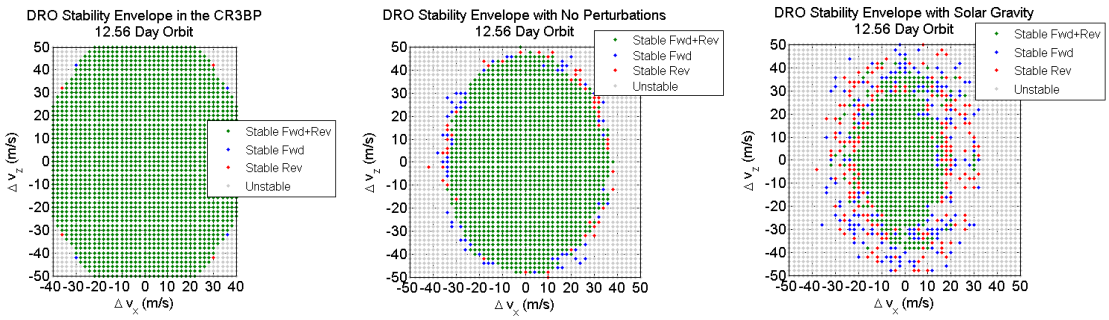

(a) CR3BP (b) Full ephemeris Moon (c) Solar gravity

Figure 5.1: Stability maps in three dynamical models.

Stability maps are generated considering all of the perturbation cases outlined in Section 4.4.2, but solar gravity has remained the only perturbation to significantly affect the DRO stability maps' stable region size and shape. Additionally, DROs outside of the stable zones from Figure 4.7 are explored, but yields plots with random scattering of stable and one-way stable trajectories. An example of an unstable orbit's stability map is shown in Figure 5.2. There is no apparent structure to the stability for these cases. Figure 5.3 shows a higher resolution view of the stability map in Figure 5.1c. The 0.5 m/s resolution reveals an intricate structure to the stable region and the chaotic envelope around it. The stable region has strong symmetry about $\Delta v_z = 0$, and has two

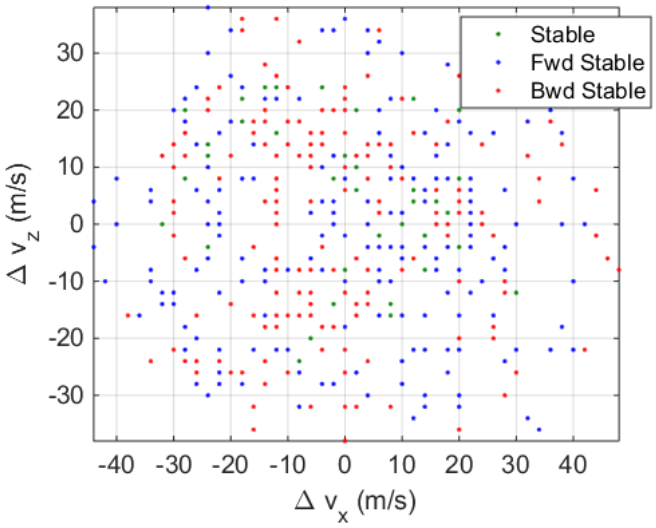

Figure 5.2: The stability map for a DRO with initial conditions outside of the case 2 stable regions found in Section 4.4.2

disjoint islands above and below the center stability zone. In between these islands lies a large concentration of forward stable trajectories, while the backwards stable trajectories lie in dense concentrations around $v_z = 0$, $v_x = -15$ m/s. There are also several regions (ex. $v_z = 20$, $v_x = 6$) where groups of forward stable trajectories cut into the main stability region. Their proximity to the stable region make them strong candidates for capture trajectories that are easy to further stabilize.

Two more stability maps are generated in the Earth-Moon system to illustrate the diversity of stable regions for different sized DROs. The first is a 50,000 km DRO, which is selected since it has the unique feature of being unstable when planar, but stable when certain z-amplitudes are permitted. This represents the island we see in the pseudo-inclination stability maps at 50,000 km in Figure 4.11(c) and (d). The second is a 70,000 km DRO, which is chosen because it is the reference orbit for the asteroid redirect mission. This DRO shows a higher density of forward-stable trajectories in the $\Delta v_z < 0$ and $\Delta v_x > 0$ region of the stability map. It also has an interesting band of one-way stable trajectories completely disjoint from the main stability region. These two stability maps use a grid resolution of 0.5 m/s and are shown in Figure 5.4. The velocity perturbation spans are determined by building a stability map with a coarser resolution (5 m/s

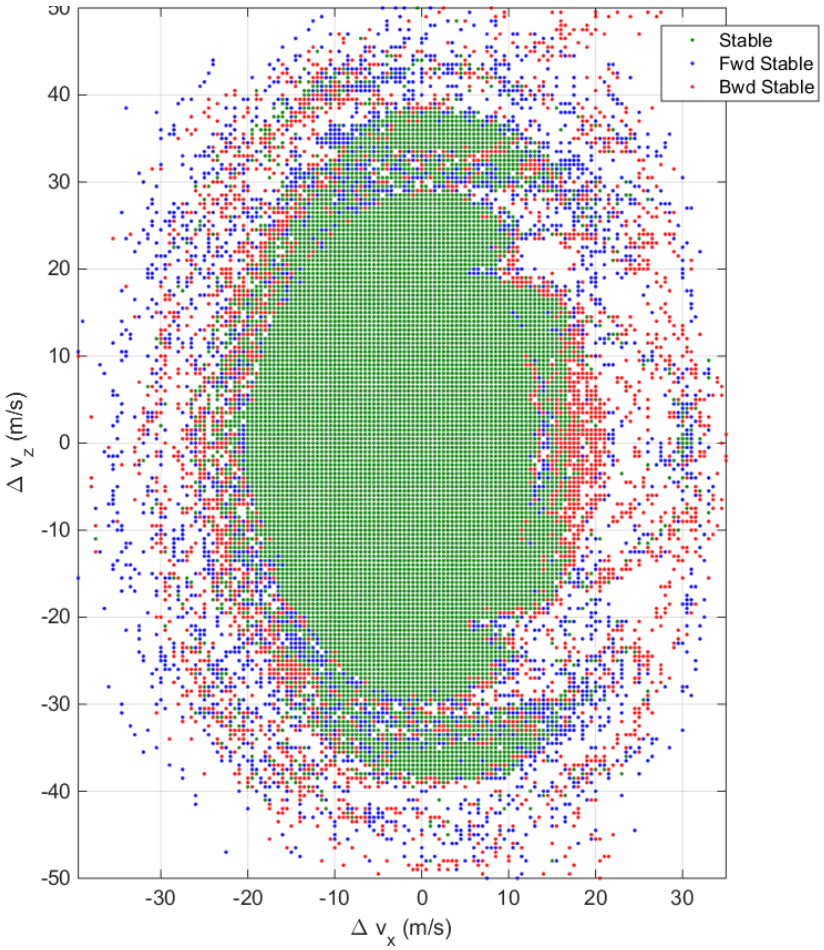

Figure 5.3: A high resolution stability envelope with solar gravity. Blue points represent ballistic capture trajectories that are stable for at least 100 years.

for example) and determining the approximate size of the stable region with some margin. The 50,000 km DRO's velocity perturbation grid spans ±50 m/s in the x-direction and ±60 m/s in the z-direction, and the 70,000 km DRO's grid spans -60 to 40 m/s in the x-direction, and ±35 m/s in the z-direction.

Table 5.1 gives a breakdown of how many two-way stable, forward stable, and backwards stable trajectories are found in each map. The 50,000 km DRO map has significantly more stable trajectories than the 70,000 km DRO and has a narrower sheath of one-way stable trajectories. This reinforces the notion that DROs are generally more stable as they become smaller, which we have seen in the pseudo-inclination stability maps generated in Section 4.4.3. Because the Sun's gravity

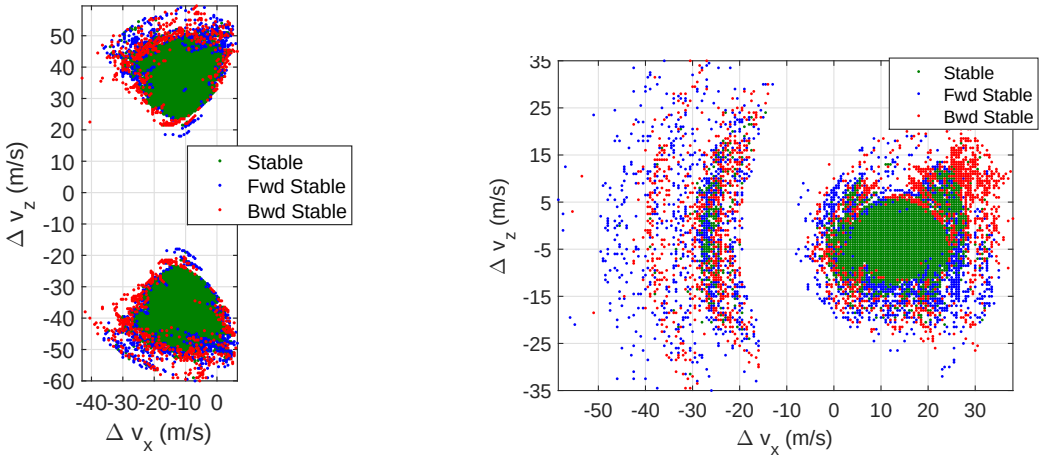

(a) 50,000 km DRO stability map.

(b) ARRM (70,000 km) DRO stability map.

Figure 5.4: The stability maps for a 50,000 km DRO (a) and a 70,000 km DRO (b).

is the primary driver in creating these chaotic trajectories, it makes sense that smaller DROs, which experience larger accelerations from the Moon's gravity, are not affected by this perturbation as much as larger DROs, and thus have smaller chaotic boundaries. Regardless, these stability maps demonstrate that smaller, more stable DROs can still be entered for zero fuel cost, the same way that larger, less-stable DROs can. The 70,000 km stability map has more than double the number of one-way stable trajectories at this resolution when compared to the 50,000 km DRO.

Stability Class	50,000 km DRO	70,000 km DRO
Stable Traj.	4,385 (71.5%)	2,047 (38.5%)
Fwd. Stable Traj.	774 (12.6%)	1,596 (30.1%)
Bwd. Stable Traj.	974 (15.9%)	1,668 (31.4%)
Total	6,133	5,311

Table 5.1: Number of trajectories in each category for the 50,000 km and 70,000 km DROs.

5.1.2 Characterizing Ballistic Capture Trajectories

Each forward-stable trajectory from the stability maps is a potential capture trajectory. Figure 5.5 shows a representative example of two different types of capture trajectories. In the top left image, the trajectory arrives at the Earth-Moon system from interplanetary space and forms an eccentric Keplerian orbit around the Earth. Over a period ranging from days to decades, this orbit

will gradually change due to the gravity of the Moon and Sun, and can change drastically if a close lunar flyby occurs. Eventually, the trajectory has a close flyby of the Moon that leads to its capture into a retrograde orbit about the Moon, as shown in the top-right image of Figure 5.5. Because of this period spent in orbit around the Earth prior to capture into the DRO, these trajectories are called *indirect capture* trajectories. There is also a set of BCTs that arrive from interplanetary space and are immediately captured into the DRO around the Moon without a close approach to the Earth, which we call *direct capture* trajectories. An example of a direct capture BCT is shown in the bottom two images in Figure 5.5. Over time, the motion of these DROs becomes more regular as the amplitude oscillations are damped. When the DRO is sufficiently uniform, a small correction maneuver, on the order of several meters per second, can optionally be used to shift the trajectory away from the chaotic stability boundary into the stable region of the stability map, which is studied in detail in Chapter 7.

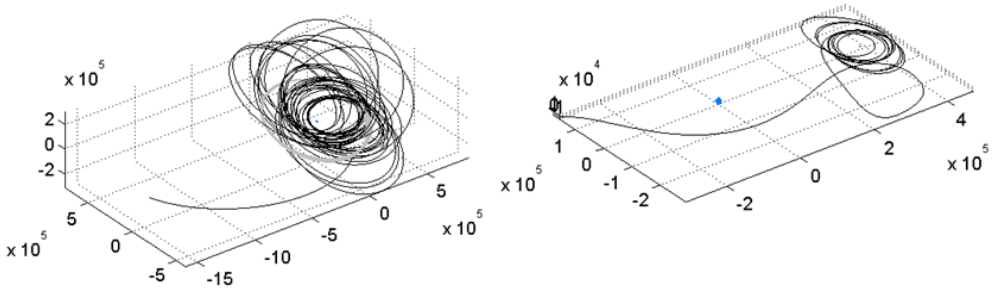

(a) Capture around Earth prior to DRO

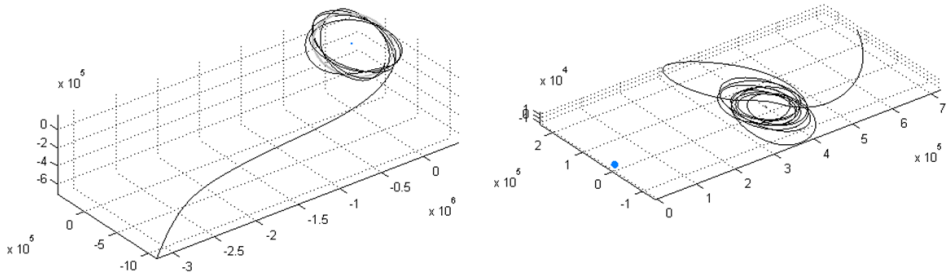

(b) Direct DRO capture

Figure 5.5: Examples of indirect (top) and direct (bottom) capture trajectories shown in the inertial (left) and rotating frames (right). Indirect captures orbit the Earth before a close flyby of the Moon brings the body into a DRO. Direct captures are immediately captured into DROs.

Since the BCTs exist in a chaotic phase space, we compile the full set of BCTs for each reference DRO and stochastically analyze it for trends and limitations rather than focus on specific examples. To analyze these capture trajectories, we begin by identifying four key events that are common to all BCTs when integrated backwards in time (the unstable temporal direction). The first event detection occurs when the spacecraft is first captured by the Earth-Moon system. This is approximated as the first time the trajectory crosses the sphere of influence (SOI) of the Earth-Moon system and remains in the in the 3×SOI neighborhood of the Earth-Moon barycenter for all future times. Looking forward in time from the first event, we identify the second event as the closest approach that the spacecraft makes to Earth. While this event is meaningless for direct capture BCTs, it is useful for using indirect capture trajectories to design ballistic trasnfers from Earth to the DRO rather than from interplanetary space.[95] The third event is triggered when the spacecraft is captured by the Moon. We identify this event by finding the last time that the trajectory crosses the yz-plane in the barycentric Earth-Moon rotating frame since an orbit around the Moon cannot cross this plane. Finally, the fourth event is the flyby of the Moon that leads to its capture into the DRO. We detect the first first lunar periapse that occurs after the third event. In most cases, this one of the most sensitive parts of the trajectory, which makes it a convenient target for mission designers. These four events must occur sequentially, with the exception of Earth periapse (second event) during a direct capture trajectory, so detection of each event is crucial to finding the next one.

We compare the time between the first and fourth events to define the *capture time*: an estimate of how long the body spends in orbit around the Earth before being captured into the DRO around the Moon. Trajectories like the indirect capture shown in the top of Figure 5.5 are less useful for mission design because a months are wasted before the target DRO is achieved. Figure 5.6 shows a logarithmic histogram of the capture time for the 70,000 km DRO. The 50,000 km DRO capture time histogram has all the same features, and so it is not shown. There are three obvious groupings of capture times: 7-20 days, 20-80 days, and 80 days-30+ years. The 7-20 day group contains the direct capture BCTs, which do not flyby the Earth before being captured into the DRO.

These are highly desirable because they arrive on the target orbit quickly and have the smallest risk of Earth impact in case of navigation or hardware complications. The second group (20-80 days) has BCTs similar to the example in the top of Figure 5.5, spending time in orbit around the Earth before being captured. Since they only make a handful of revolutions of the Earth before capture, this group is referred to as *fast indirect captures*. These types of BCTs are useful because there is a larger margin for error when targeting a capture in the Earth-Moon system. If a problem occurs and the satellite cannot be delivered to the DRO, it is still captured around Earth and the mission may be recoverable. Additionally, if a spacecraft arrives with too much hyperbolic excess velocity, a small maneuver near the Earth can put it onto this BCT. The third group contains the BCTs that spend months to decades orbiting the Earth waiting for the proper dynamical interactions to cause their capture, which earns them the title *slow indirect captures*. These trajectories can be truncated at close approaches to Earth as a starting point for building Earth-to-DRO transfers, but they are not helpful for building interplanetary BCTs.[16,95]

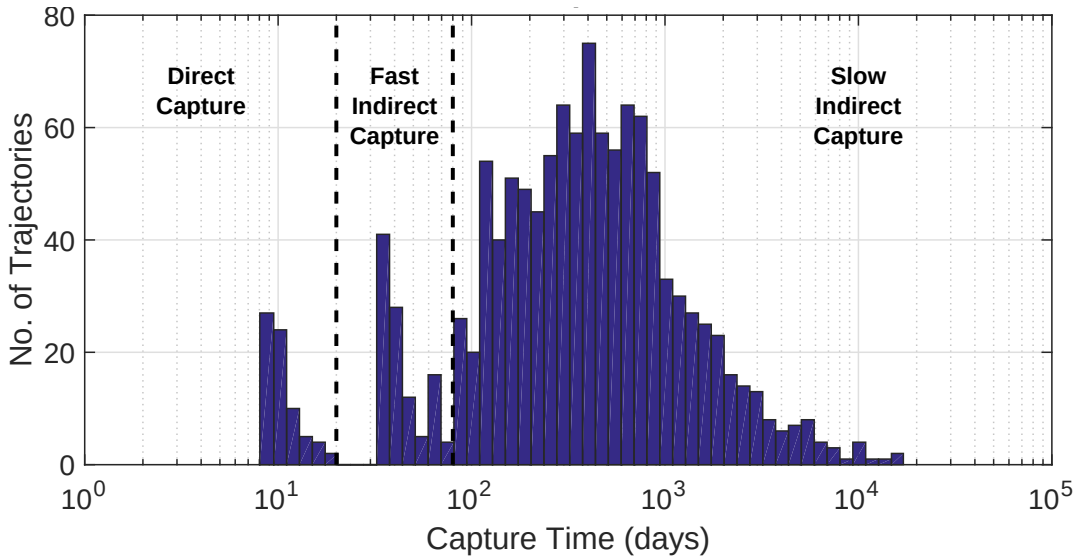

Figure 5.6: A logarithmic histogram of the time between capture in the Earth-Moon system and capture into the 70,000 km DRO.

5.1.3 Lunar Flyby Geometry

Next, we explore the BCT set for trends in the geometry beginning with the lunar flyby (the fourth event) that leads to capture into the DRO. The position and velocity of the BCTs at the lunar flyby are plotted with a vector field in Figure 5.7 where the arrows point in the velocity direction and the base of the arrow is the position of the spacecraft. Trajectories passing closer than 5,000 km are omitted from this plot, but are still used in subsequent analyses. The BCTs appear to be grouped into four curved bands, suggesting that there are four unique geometries at which a body can fly by the Moon to be captured into a DRO. Each BCT is classified into one of the geometry families based on its position and velocity direction in the rotating frame, as seen in the legends in Figure 5.7 (a) and (b). For the 70,000 km DRO, the second and fourth families contain 86% of the trajectories while the remaining 14% are evenly distributed between the first and third families. The bands extend out to about 47,500 km from the Moon. In the 50,000 km DRO, the split is 93% in families two and four, while about 7% are in families one and three. These bands are shorter, extending out to about 25,000 km. This pinwheel plot shows that it is possible to design a BCT that can remain at great distances from both the Earth and the Moon, which minimizes the risk of impact. If these bands are thought of as propellers, family one and three would be spinning counter-clockwise while family two and four would spin clockwise based on the velocity of the trajectories. While this may make it appear as though families one and three generate prograde orbits, it will be shown that they do not. The vector fields in subplots (c) and (d) of Figure 5.7 are identical to (a) and (b), respectively, but are colored to illustrate different characteristics and how they relate to the geometry of the flyby. The red arrows correspond to BCTs that have a capture time of less than 25 days, meaning they are all direct capture trajectories. The 70,000 km DRO plot shows these direct captures exclusively lie in the first family, beginning at about 7,000 km from the Moon. Furthermore, 85% of the BCTs in family one are direct capture trajectories, though this is not shown on the plot. The 50,000 km DRO only has four direct capture trajectories, but again, they lie exclusively in the first family and begin at 15,000 km from the Moon. Interestingly,

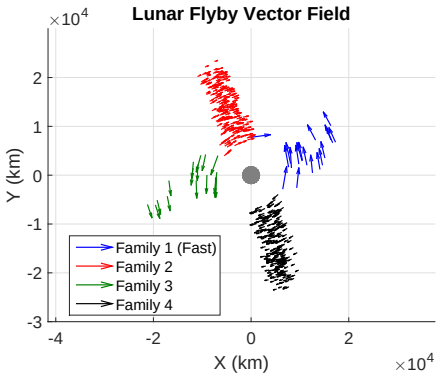

(a) 50,000 km DRO states colored by family.

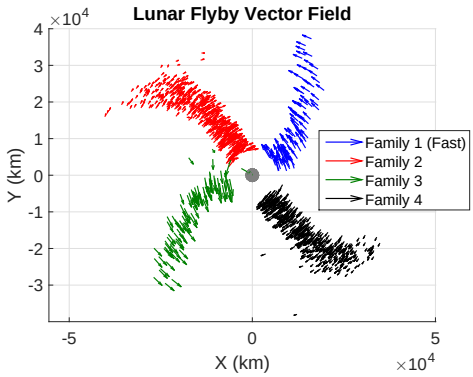

(b) ARRM (70,000 km) DRO states colored by family.

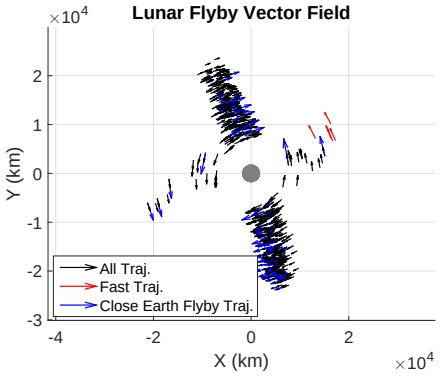

(c) 50,000 km DRO states colored by capture time.

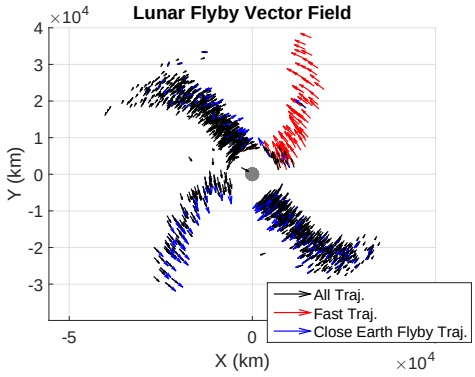

(d) ARRM (70,000 km) DRO states colored by capture time.

Figure 5.7: The vector field plots showing the states of the capture trajectories in the synodic frame at the lunar periapse prior to capture into the DRO.

approximately 91% of the fast indirect capture trajectories are found in family two. That said, the majority of family two is made up of slow indirect captures. The trend here is that for lower transfer times, geometries that flyby in front of the Moon tend to get captured more quickly. Also shown in subplots (c) and (d) in blue are trajectories that make a flyby of Earth that is less than 50,000 km at some point prior to capture. Both example DROs show that these BCTs are well distributed between families two, three, and four, but are sparse ($< 2\%$) in family one. Therefore, the proximity of the Earth flybys does not appear to have a strong influence on the geometry of the capture lunar flyby.

Figure 5.8 shows the four geometries for the 70,000 km DRO when each are propagated forward in time for 100 days. Family one and three are nearly mirror images of one another over

the xz-plane, as are family two and four. Family one and three fly significantly farther from the Moon after their capture flyby relative to the other two families, suggesting that they arrive with a larger speed relative to the Moon. Family one and three have trajectories that extend much farther than family two or four, meaning these BCTs will be more sensitive to unmodeled perturbing forces. Table 5.2 shows the range of each family's maximum altitude above the Moon for comparison. The consistent geometry across each family means that there exists a range of states that can be targeted to achieve the same final DRO. A BCT with specific characteristics can easily be interpolated from the set of states in each family.

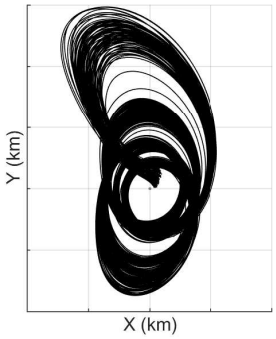

(a) Family 1 capture geometry.

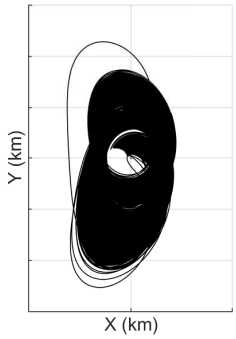

(b) Family 2 capture geometry.

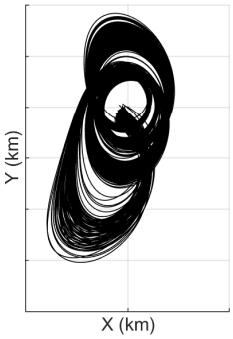

(c) Family 3 capture geometry.

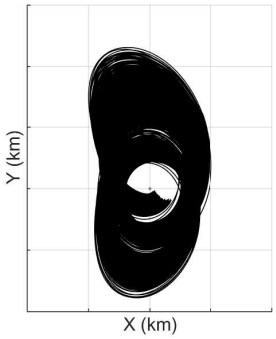

(d) Family 4 capture geometry.

Figure 5.8: The four DRO capture geometries. These plots show the states along the four bands propagated forward in time for 100 days.

The Jacobi constants C of these BCTs are evaluated at lunar periapse and are shown in a histogram in Figure 5.9. These values for both DROs form a right-skewed distribution with a peak at $C = 2.50$ for the 50,000 km DRO and $C = 2.61$ for the 70,000 km DRO. These values can be

Family	Peak altitude range ($\times 10^5$) km	
-	50,000 km DRO	70,000 km DRO
1	1.10 - 1.67	1.99 - 3.11
2	0.88 - 1.19	1.26 - 2.62
3	1.46 - 1.63	1.81 - 3.22
4	0.85 - 1.14	1.17 - 2.37

Table 5.2: Maximum altitude range of each flyby geometry after the lunar flyby.

as low as about 1.1 and as high as 2.7. For reference, the 70,000 km DRO has a Jacobi constant of 2.812, which means time that all of the BCTs spend orbiting the Moon is raising its Jacobi constant by reducing the velocity, causing the DRO to become more uniform.

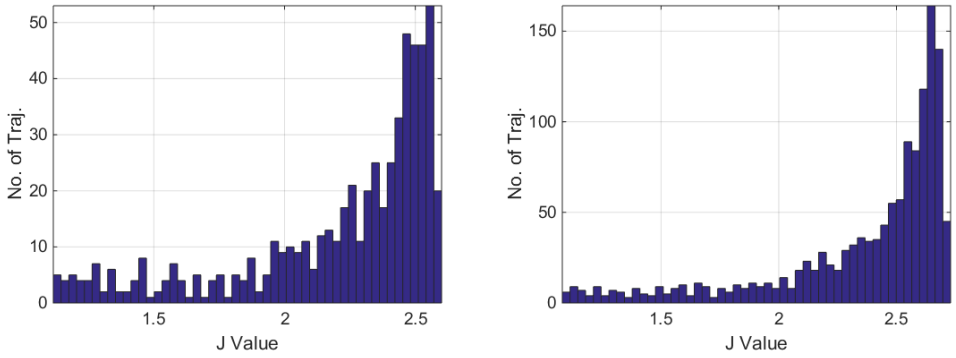

(a) 50,000 km DRO (b) ARRM (70,000 km) DRO

Figure 5.9: Histogram of the Jacobi constant for each BCT evaluated at the capture lunar flyby.

Figure 5.10 shows how the families are distributed on the stability map. Only the forward stable trajectories are plotted and each point is colored by its lunar flyby geometry. For each family alongside both axes of the scatter plot, there is a kernel density function, which is an estimate of the density of points along that axis. The kernel density function is a curve fit to the histogram of each individual family's points. In general, families one, two and four are equivalently distributed around the stability map. Family three shows slight preference to $\Delta v_x > 0$ and $\Delta v_z > 0$ in the 50,000 km DRO, and $\Delta v_z < 0$ in the 70,000 km DRO. This near uniform distribution of points suggests that these BCTs behave chaotically, which is expected given the chaotic appearance of the stability map (Figure 5.4) near the boundary of stability. A similarly chaotic result can be seen when mapping BCTs with an Earth flyby below 50,000 km to the stability map, as is done in

Figure 5.11. This chaos means a mission designer would find it challenging to target a specific point on the stability map. Rather, they would target the set of BCTs at the lunar flyby and expect the trajectory to arrive on a fairly uniform, quasi-periodic DRO with some velocity error on the order of 20-40 m/s.

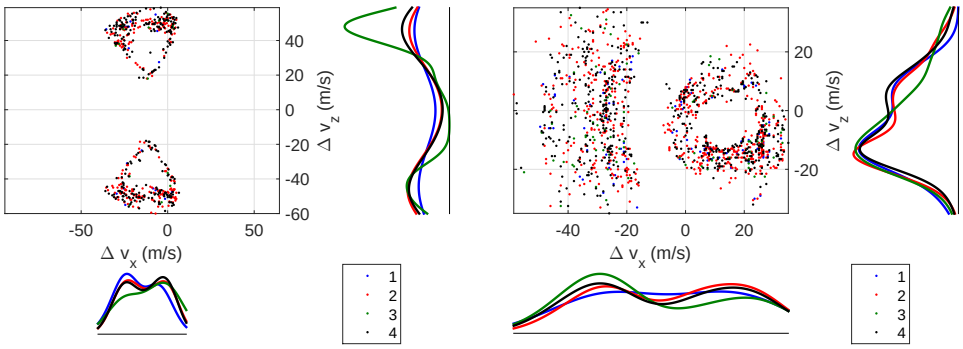

(a) 50,000 km DRO stability map colored by family.

(b) ARRM (70,000 km) DRO stability map colored by family.

Figure 5.10: The forward stable trajectory's points on the stability maps for a 50,000 km DRO (a) and a 70,000 km DRO (b), colored by their family designations. Alongside each axis are four the kernel density functions, which approximate the density of points of each family along that axis (like a histogram). Family 1 - blue, family 2 - red, family 3 - green, and family 4 - black.

The Sun-Earth-Moon (SEM) geometry is analyzed during the lunar flyby as well since solar gravity is primarily responsible for the chaotic region of one-way stable trajectories. Figure 5.12 shows a histogram, organized by family, of the SEM angle when the capture lunar flyby occurs for each BCT of the 50,000 km DRO. Angles greater than zero mean the Moon is in a waning phase, and angles less than zero mean the Moon is in a waxing phase. The 50,000 km DRO shows a trend in the SEM angle at the flyby, which is likely because it is only stable with out-of-plane motion due to solar gravity. For each family, there is a bimodal distribution with peaks separated by approximately 180°. It is also apparent that one peak is generally higher than the other, suggesting that while two Sun-Earth-Moon orientations are preferred, one appears more frequently than the other. Lunar flybys on the near side of the Moon (families 2 and 3) favor a waxing gibbous phase, while flybys on the far side of the Moon (families 1 and 4) favor a waning crescent phase. The 70,000 km DRO (not shown) has a uniform distribution for all SEM angles, suggesting that planar

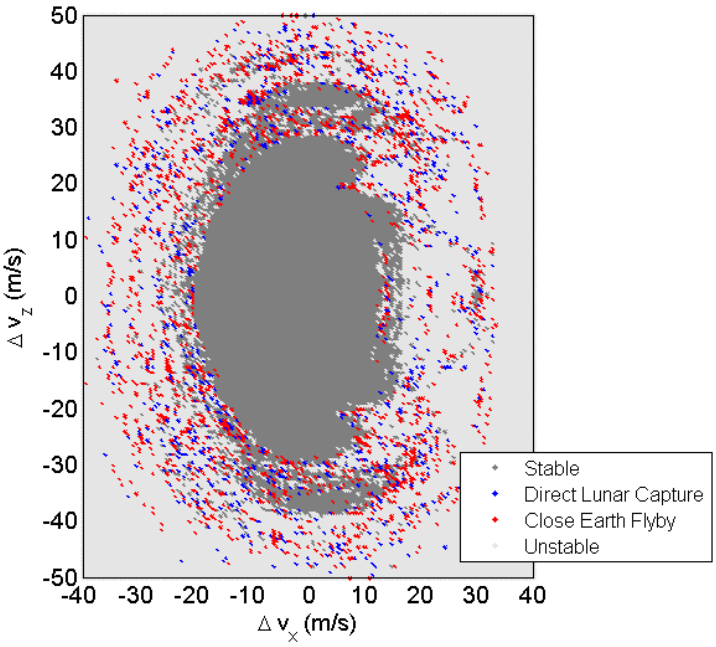

Figure 5.11: This map shows stable manifolds that are divided by their closest approach to Earth. Red points pass within 192,000 km, and blue points do not. Many of the blue points are direct capture trajectories.

DROs are not limited to a particular lunar phase for a BCT to exist. This also suggests that the 70,000 km DRO BCTs are temporarily captured due to the Earth and Moon geometry alone and the Sun's gravity gradually shifts into a more permanent captured state.

5.1.4 Trajectories Prior to Capture in the Earth-Moon System

Over 99.7% of the BCTs that are generated begin in interplanetary space. The heliocentric Keplerian orbital elements of each BCT are averaged during their interplanetary flights, up to the crossing of the SOI (event one). In many cases, the BCTs make one or more close flybys of Earth before finally being captured in the Earth-Moon system, which cause changes in these orbital elements. Therefore, only flight time between the last Earth flyby and the SOI crossing is used to find the average orbital elements. Figure 5.13 shows a scatter plot of the semi-major axis (SMA) and the eccentricity of BCTs during this portion of the flight. Also included along each axis is a histogram of the points and the kernel density functions. Interplanetary trajectories with an

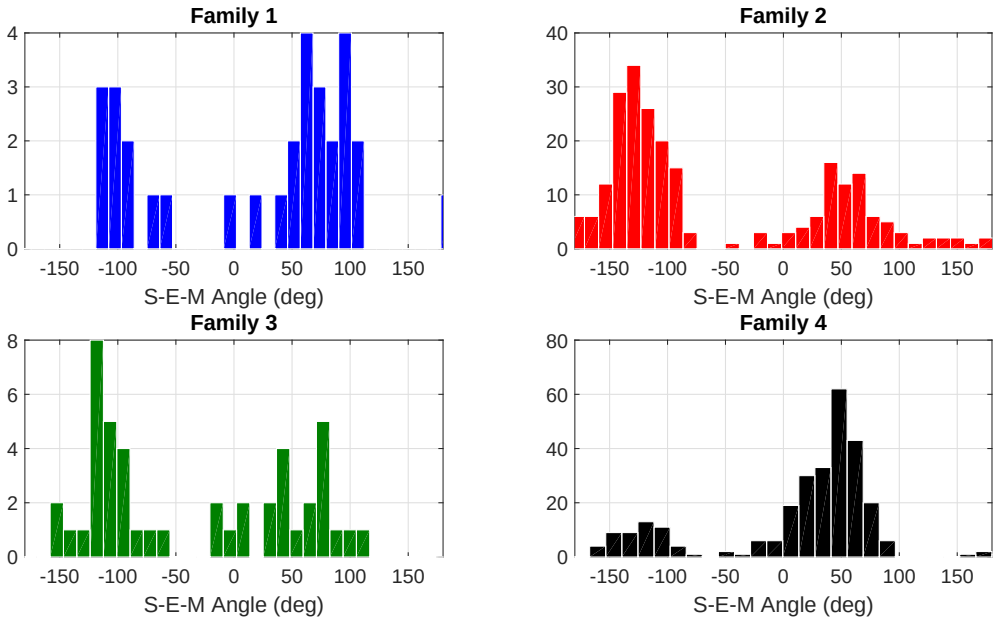

Figure 5.12: A histogram of the Sun-Earth-Moon angle at the time where each trajectory makes its capture flyby of the Moon. Angles greater than zero mean the Moon is in a waning phase, and angles less than zero mean the Moon is in a waxing phase.

SMA between 0.93 and 1.07 AU can be captured into the 50,000 km DRO with the majority of trajectories arriving from 0.95 AU and 1.05 AU. The eccentricity of arriving BCTs is nominally around 0.04, but can be as high as 0.08. These plots do not show the results divided by the four families because there are no apparent trends between the family and these orbital elements.

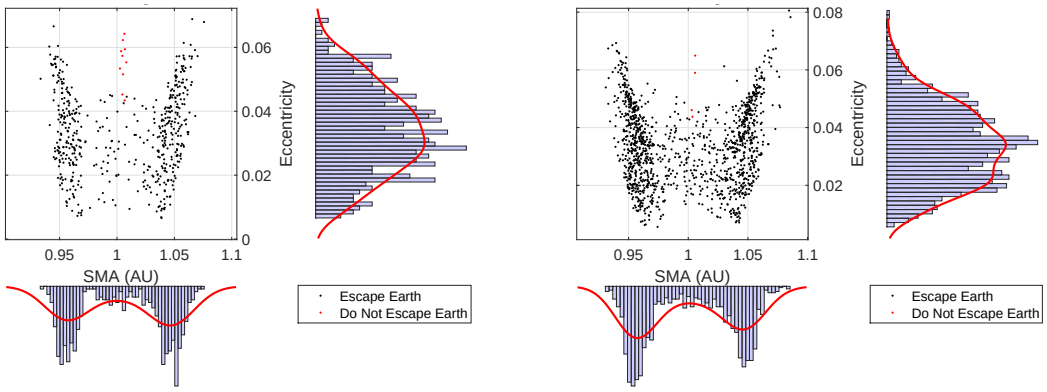

(a) 50,000 km DRO heliocentric orbital elements. (b) 70,000 km DRO heliocentric orbital elements.

Figure 5.13: A scatter plot of the heliocentric semi-major axis and eccentricity of a BCT prior to capture by the Earth-Moon system.

This range of SMA values is too small to capture a satellite traveling ballistically from Venus or Mars, as their energy would be too low/high, respectively. However, low-thrust propulsion can be used to change the heliocentric energy of a spacecraft while it is still in interplanetary space to achieve the energy required to utilize a BCT. Alternatively, a BCT can still be utilized to minimize the ΔV needed to get the spacecraft into the targeted DRO. An incoming spacecraft can target the BCT at event two (Earth periapse) or at event four (Lunar periapse) and use a maneuver to enter the BCT. Figure 5.14 shows the ΔV cost of entering a BCT while flying by the Earth after arriving with excess V_∞. Due to the Oberth effect, closer flybys of the Earth or Moon result in more efficient transfers. A Hohmann transfer from Mars to Earth would result in a V_∞ of approximately 3 km/s, which would require a burn of about 1.5 km/s at 50,000 km from Earth to put the satellite on the BCT towards the DRO. Lower Earth flybys are possible as well.

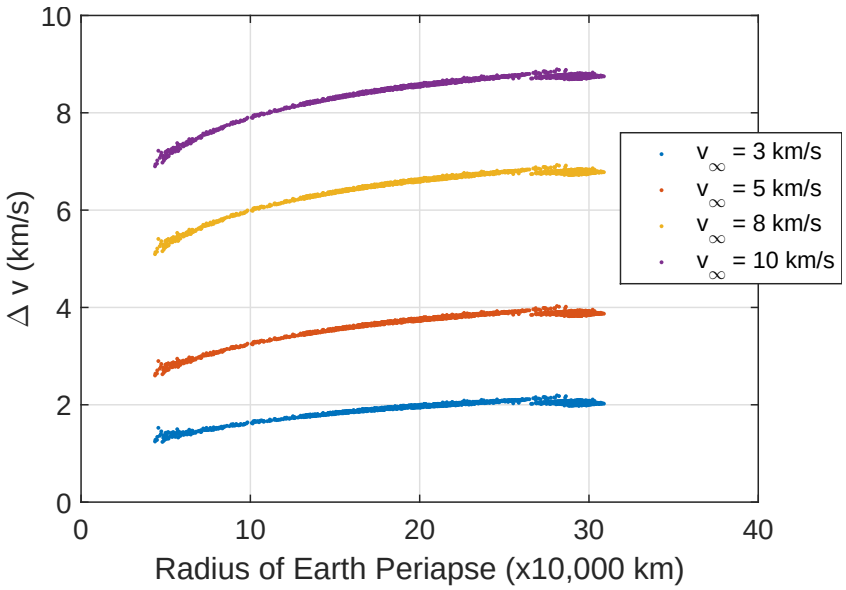

Figure 5.14: ΔV requirement at Earth periapse for entering a BCT based on V_∞ at arrival in the Earth-Moon system.

The inclination relative to the ecliptic is plotted versus the SMA in Figure 5.15. The inclination angle is nominally zero degrees in both DROs, and can be as high as $\pm 0.4°$. This is because the Moon's orbit plane is inclined to the ecliptic by only about 5.1°, so trajectories arriving with large out-of-plane velocities (i.e. highly inclined orbits) are not effectively slowed down and captured by

lunar gravity assists. Again, the families discussed in the previous section do not show any trends with these heliocentric orbital elements.

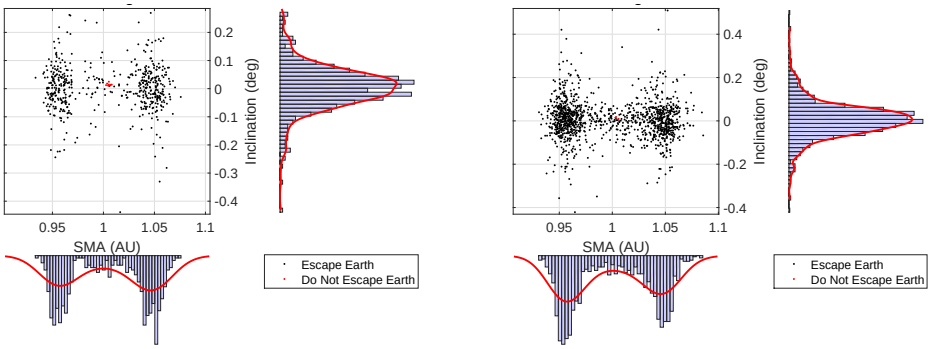

(a) 50,000 km DRO Heliocentric orbital elements.

(b) 70,000 km DRO Heliocentric orbital elements.

Figure 5.15: A scatter plot of the heliocentric semi-major axis and inclination relative to the ecliptic of a BCT prior to capture by the Earth-Moon system.

Mission designers are often interested in what V_∞ a spacecraft can have when it arrives at the Earth-Moon system. The V_∞ parameter is a defined in a two-body system, but BCTs exist in three-body systems; Mission designers would like to relate a BCT to a V_∞ value, which can be done with two methods. First, it can be measured when the body is close to the Earth with knowledge that it has not yet made a close approach of the Moon:

$$V_\infty \approx \sqrt{-\frac{\mu_\oplus}{a}} = \sqrt{2\epsilon} \tag{5.1}$$

where a is the hyperbolic semi-major axis ($a < 0$) and ϵ is the specific orbital energy. The second method is to consider the body in the Sun-Earth three-body system. We use the Tisserand constant, a known approximation of the Jacobi constant:

$$C \approx \frac{1}{\bar{a}} + 2\sqrt{\bar{a}(1-e^2}\cos(i) = T \tag{5.2}$$

Where $\bar{a}$ is the normalized semi-major axis with respect to the Sun, e is the eccentricity, and i is the inclination. Campagnola derives how the Tisserand constant can be related to V_∞ at the Earth:[22]

$$C \approx T = 3 - V_\infty^2 \tag{5.3}$$

This expression assumes that the spacecraft is near a value of $r = 1$ in normalized coordinates and that the mass parameter μ is close to zero.

Because not all trajectories have a close Earth flyby, the latter method is used to examine the stochastic spread of possible V_∞ values. These are shown for the two sets of BCTs in the histogram in Figure 5.16. These values fall into a bimodal distribution with peaks centered at 400 m/s and 410 m/s. The edges of these peaks lie at about 395 m/s to 415 m/s, so the range is quite narrow. The histogram for the 50,000 km DRO is not shown because it has the same distribution and limits.

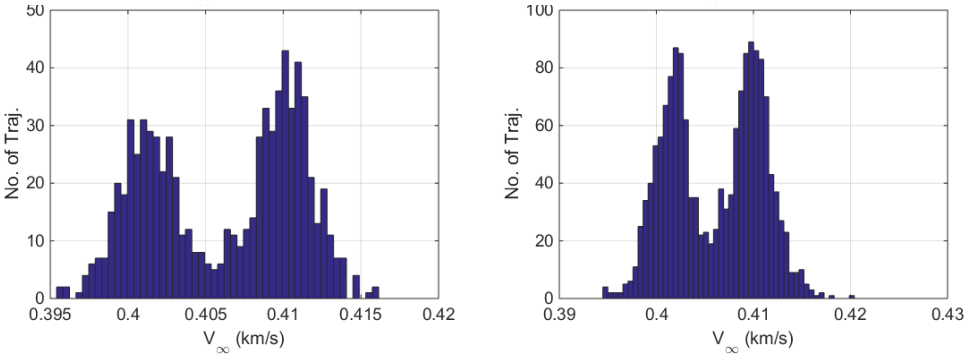

(a) 50,000 km DRO (b) 70,000 km DRO

Figure 5.16: The V_∞ histogram for the BCTs arriving at Earth from interplanetary space.

5.1.5 Geometry at Arrival of the Earth-Moon System

This section describes the geometry of the BCTs as they arrive at the Earth-Moon SOI (event one). The right ascension and declination are shown in the scatter plots in Figure 5.17. The BCTs are uniformly distributed in right ascension and the declination forms a sine wave with amplitude equal to the axial tilt of the Earth. The histogram and kernel density function for the declination are the expected shape for a uniform distribution along the declination as well. This plot indicates that the BCTs for both DROs are seemingly independent of the Earth-Sun geometry, which further indicates that the eccentricity of the Earth's orbit around the sun is not a strong contributor to the dynamics that cause the BCT to be captured on the DRO.

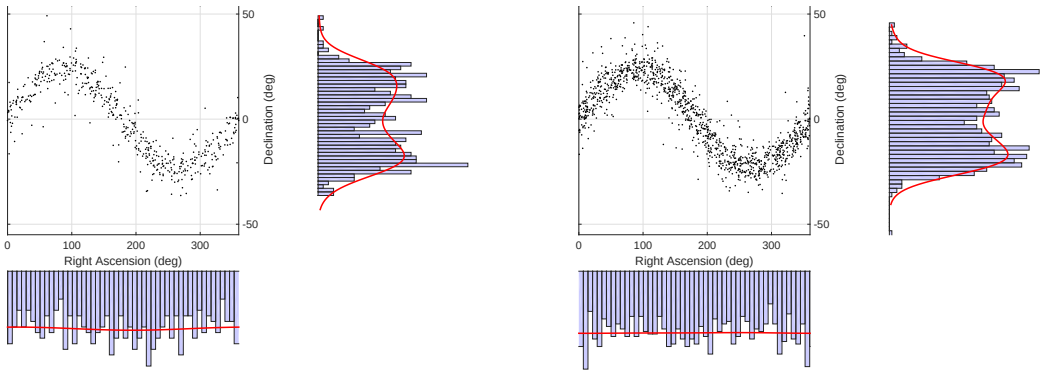

(a) 50,000 km DRO right ascension and declination at arrival in the Earth-Moon system.

(b) 70,000 km DRO right ascension and declination at arrival in the Earth-Moon system.

Figure 5.17: A scatter plot of the right ascension and declination of the BCTs as they arrive at the Earth-Moon system.

When we view the BCTs at the SOI crossing in the Earth-Moon synodic frame, we find that the Earth-Moon geometry is more significant than the Earth-Sun geometry. Figure 5.18 shows a vector field of the BCT states as they pierce the SOI. For both DRO examples, the velocity of the trajectories with respect to the Earth at the SOI has a right-skewed normal distribution with a peak at 1.5 km/s. Incoming BCTs rarely exceed 1.7 km/s, but can be as low as 0.27 km/s. The longitude of these BCTs can be measured by taking the Earth-Moon line as 0° and measuring positive counter-clockwise. The elevation angle of these incoming trajectories is taken as their angle out of the Moon's orbit plane measured from the barycenter. There is an obvious dense longitudinal zone leading the Moon by about 45°, and a sparse distribution lagging behind the Moon from about −90° to −30°. The elevation angles of incoming BCTs are normally distributed about mean 0° with a standard deviation of 8.3° for both DROs. The elevation angles span the range −30° to 45° for the 70,000 km DRO, and span −62° to 31° for the 50,000 km DRO.

Figure 5.19 breaks down the elevation and longitude angles for the 70,000 km DRO by family and displays them as histograms. The polar histograms showing the longitude distribution reveals that very few BCTs arrive with a longitude less than 30°. Family one, the direct capture trajectories, have the most narrow arrival longitude options, limited to 30° to 50°. Family three is unique in that it has a large set of trajectories existing outside the dense region. Families two

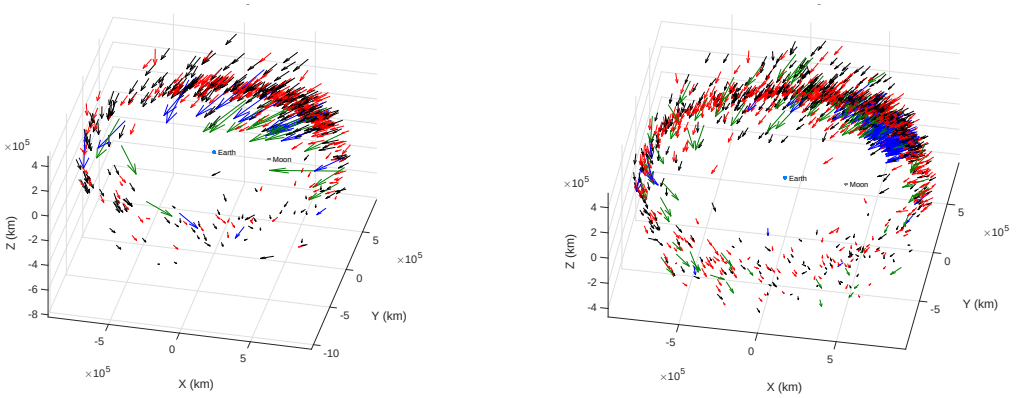

(a) 50,000 km DRO Earth-Moon arrival geometry. (b) 70,000 km DRO heliocentric orbital elements.

Figure 5.18: A vector field plot showing the incoming BCTs at the point where they enter the Earth-Moon SOI (event one).

and four are similar in their longitude and elevation distributions. These families contain a larger span of elevation angles than the other families, and would likely be the target capture geometry for BCTs arriving with high inclinations relative to the Moon's orbit plane. The elevation angle histogram for family one has the narrowest range, meaning these direct capture trajectories have the most stringent constraints on arrival geometry.

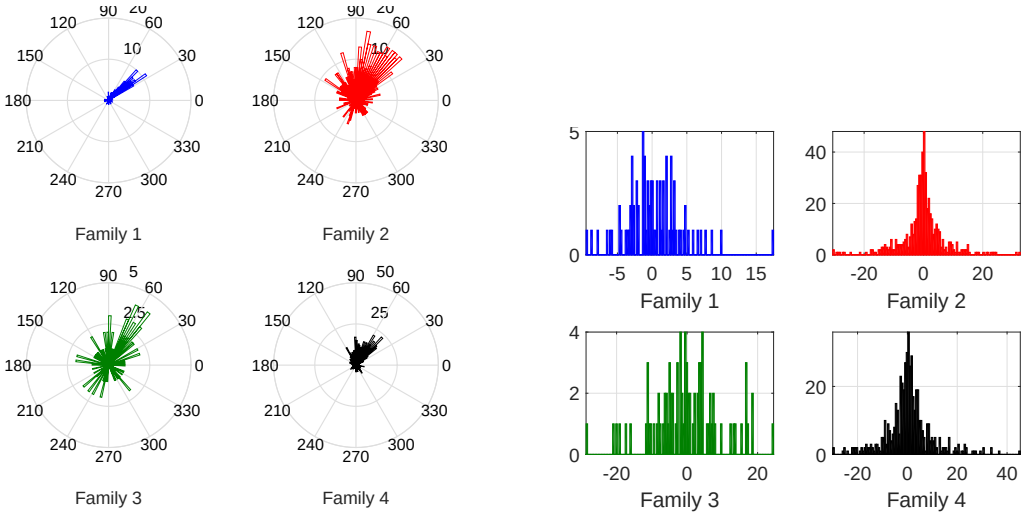

(a) A polar histogram of arrival longitudes. (b) A histogram of arrival elevation angles.

Figure 5.19: Histograms of longitude and elevation angles when the 70,000 km DRO's BCTs arrive at the Earth-Moon SOI. They are separated by family designation to show family trends.

5.1.6 Conclusions Regarding Ballistic Capture

There are four main conclusions drawn from this analysis. First, for DROs near 50,000 to 70,000 km, there are four geometries (families) when flying by the Moon that will lead to capture into the DRO. Family one is mostly composed of direct capture trajectories, but the other three families do not show significant differences between their interactions in the Earth-Moon system prior to capture. A BCT with specific characteristics, such as flyby radius or speed, can be interpolated from the BCT states in each of the four families. Second, BCTs with quick capture times (< 80 days) generally flyby in front of the Moon (families one and two), rather than behind (families 3 and 4). However, this does not mean a flyby in front of the Moon (all BCTs families one and two) will guarantee a quick capture time. Third, the Earth-Moon geometry at the BCT arrival in the Earth-Moon system is crucial to successfully being captured into the DRO, particularly for direct capture trajectories. The Earth-Sun geometry is significantly less important, meaning BCTs can approach the Earth year-round. This leaves the trade space of interplanetary BCTs relatively unrestricted. Finally, BCTs exist for interplanetary trajectories near the ecliptic plane ($\pm 0.4^\circ$ inclination) with semi-major axes between 0.93 AU and 1.07 AU. For higher or lower energy interplanetary trajectories, the Earth or Lunar periapse points can be targeted for a maneuver to set the spacecraft onto the BCT.

5.2 Changing the Epoch of a Ballistic Capture Trajectory

The ballistic capture trajectories that were studied in Section 5.1.1 only exist at the precise epoch that they were generated at and we have no means of controlling when the trajectories depart the Moon. However, the mission design process often needs to explore alternative arrival times or may prefer the geometry of a certain BCT created at a different epoch. Also, BCTs generated from the same reference DRO break away from the Moon at significantly different times, even if they have similar departure geometries. Due to the chaotic nature of these trajectories, one can imagine that they are not easy to transform through time. This section discusses heuristic strategies to alleviate

the problems associated with numeric sensitivity of these chaotic trajectories when changing their epoch.

5.2.1 Identifying Ideal Epochs

A strong choice of algorithm for transforming the BCTs to a new epoch is the multiple shooting differential corrector. First, the trajectory is discretized into patchpoints and these patchpoints are transformed into the rotating frame. These states are then transformed back into the inertial frame at the desired epoch. The patchpoints can then be differentially corrected with the MSDC until they converge on a ballistic trajectory that resembles the geometry of the original.

In practice, this method suffers from a number of issues. The high sensitivity of certain patchpoints often leads to poor convergence or BCTs that do not resemble the desired geometry. This can be mitigated by constraining the length of the trajectory arc that is discretized and transformed. A good choice for this range is a few days prior to the capture lunar flyby up to a few revolutions (fewer than 5) around the Moon. Choosing the number of patchpoints and their placement is another step that can severely impact the performance and convergence of the MSDC. Patchpoints in dynamically sensitive locations, such as a flyby of the Moon, will have very large derivatives in the $\mathbf{M}$ matrix in Equation 3.45, while patchpoints in less sensitive regions will produce small derivatives. If these differences are pronounced enough, the Level 2 correction step can become ill conditioned. Also recall that Level 1 correction in the MSDC uses a linear approximation to estimate the state update (Equation 3.43), which can lead to divergence if the initial error is too large. It is good practice to space patchpoints along the trajectory arc such that they are in higher density near flybys and other dynamically sensitive regions, and lower density elsewhere. One should avoid using an excessive number of patchpoints however as this increases the size of the problem and can lead to numeric issues. Having too many patchpoints also allows the algorithm to move them more, leading to solutions that do not resemble the desired trajectory.

The MSDC requires a sufficiently close initial guess for the patchpoints to converge and it may be the case that transforming directly to the desired epoch gives too poor of a guess. Instead,

one can transform the BCT to an epoch near their target that is dynamically similar to the original. There are many ways that this epoch can be determined and three methods are discussed in this section. First, one may simply look at epochs where the Earth-Moon or Earth-Moon-Sun geometry are close to that at the original epoch. The Moon's sidereal period is about 27.3 days, and will have approximately the same true anomaly and radius every period. However, the Sun's position will change regularly over this interval and Figure 5.1 shows influential the Sun can be on the existence of BCTs. One may also look for repeating Sun-Earth-Moon angles, which occurs over the Moon's synodic period of 29.5 days. The Moon will be at a different true anomaly however, which will affect the dynamics as well. A repeating true anomaly and relative Sun position will only be close to the original on the scale of years.

A more robust method is to determine which times surrounding the target epoch produce similar accelerations to the original BCT in the rotating frame. This is best observed at the lunar capture flyby, which is the region of highest dynamic sensitivity. This state is passed into the dynamical model to determine its acceleration. The position, velocity, and acceleration are all transformed into the rotating frame. The transformation for position and velocity is derived in Section 2.2.3. Acceleration can be transformed with the following equations using the same notation:

$$\mathbf{a}_r = \frac{d}{dt}\mathbf{v}_r = \frac{d}{dt}\left(T_i^r \mathbf{v}_i + \dot{T}_i^r \mathbf{r}_i\right) \tag{5.4}$$

$$= T_i^r \mathbf{a}_i + 2\dot{T}_i^r \mathbf{v}_i + \ddot{T}_i^r \mathbf{r}_i. \tag{5.5}$$

The only term that remains underived is $\ddot{T}_i^r$ which can be found from the derivative of the unit vectors

$$\ddot{T}_i^r = \begin{bmatrix} \ddot{\hat{R}}_1 & \ddot{\hat{R}}_2 & \ddot{\hat{R}}_3 \\ \ddot{\hat{I}}_1 & \ddot{\hat{I}}_2 & \ddot{\hat{I}}_3 \\ \ddot{\hat{C}}_1 & \ddot{\hat{C}}_2 & \ddot{\hat{C}}_3 \end{bmatrix} \tag{5.6}$$

$$\ddot{\hat{R}} = \frac{\mathbf{A}_s}{||\mathbf{R}_s||} - \frac{2(\mathbf{R}_s \bullet \mathbf{V}_s)\mathbf{V}_s}{||\mathbf{R}_s||^3} - \frac{(\mathbf{V}_s \bullet \mathbf{V}_s + \mathbf{R}_s \bullet \mathbf{A_s})\mathbf{R}_s}{||\mathbf{R}_s||^3} + \frac{3(\mathbf{R}_s \bullet \mathbf{V}_s)\mathbf{R}_s}{2||\mathbf{R}_s||^5}$$

$$\ddot{\hat{C}} \approx 0 \tag{5.7}$$

$$\ddot{\hat{I}} = \frac{d\hat{C}}{dt} \times \frac{d\hat{R}}{dt} + \hat{C} \times \ddot{\hat{R}} \approx \hat{C} \times \ddot{\hat{R}},$$

where the new term $\mathbf{A}_s$ is the geocentric acceleration of the Moon. Again, we make the two-body assumption that the Moon's angular momentum vector direction $\hat{C}$ is undergoing negligible change. Note that most ephemerides cannot directly interpolate the acceleration, but it can be approximated with finite difference methods[48]

$$\mathbf{A}_s(t) \approx \frac{\mathbf{R}_s(t + \Delta t) - 2\mathbf{R}_s(t) + \mathbf{R}_s(t - \Delta t)}{\Delta t^2} \tag{5.8}$$

or

$$\mathbf{A}_s(t) \approx \frac{\mathbf{V}_s(t + \Delta t) - \mathbf{V}_s(t - \Delta t)}{2\Delta t}. \tag{5.9}$$

After the original state has been transformed into the rotating frame, we sweep through times near the target epoch. At each time, we transform the state back into the inertial frame, compute the acceleration from the equations of motion, rotate the acceleration back into the rotating frame, and compare it to the original BCT's acceleration. Figure 5.20 shows the magnitude of these differences in accelerations for a BCT that is being moved from May 23, 1916 to the vicinity of March 26, 2016. At the exact reference date, the acceleration difference is relatively large, but there are local minima surrounding this time that make far better transition times. Figure 5.21 shows an example of a BCT in the rotating frame that has been transformed to several different epochs. In blue, we have the best epoch, or the time that produces the smallest acceleration difference, which is 92 days before the target epoch. In red is the local minima closest to the target epoch (8 days after), and in yellow, we have the transformation to the target epoch. The solutions at local minima follow the reference trajectory quite well, while the solution at the target has significantly larger errors. If the exact arrival at the Moon is allowed to vary, then there is a better chance of convergence and maintaining BCT geometry at these key transition times.

After the BCT has been moved in epoch to one of these local minima, the trajectory can be transformed to the target epoch if need be. If convergence issues are still occurring, stability

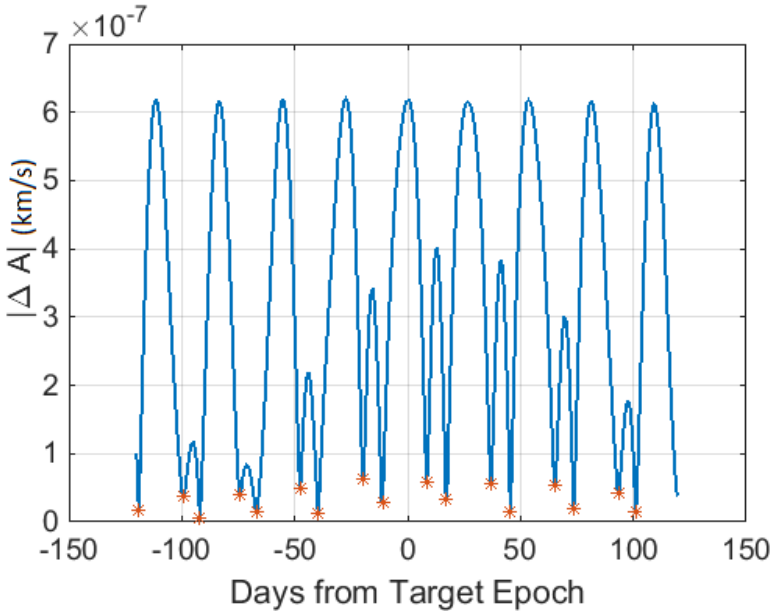

Figure 5.20: The magnitude of the acceleration difference between a BCT state at the original epoch and at times surrounding a target epoch.

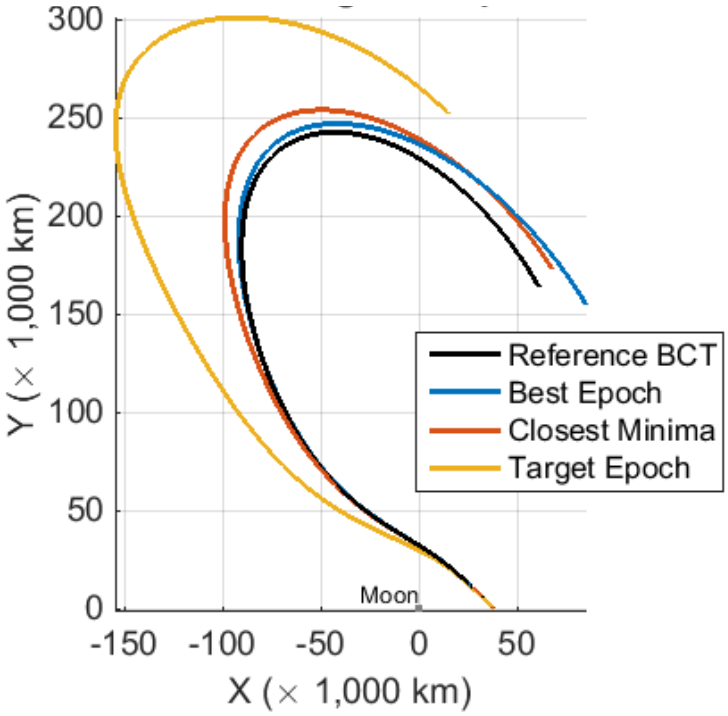

Figure 5.21: The BCT in the rotating frame translated to three different epochs: the epoch with the smallest acceleration difference (blue), the local minima that is closest to the target epoch (red), and the target epoch itself (gold).

can be improved by incrementally correcting the BCT closer and closer to the target epoch with a continuation method or by using more patchpoints. Note however that these BCTs are quite dynamically sensitive and the geometry can change significantly as the epoch moves away from the local minima in acceleration.

5.2.2 Adjusting Capture State

In the full ephemeris model, transitioning a BCT to a new epoch will always result in some change in the patchpoints used in the MSDC. This means that the final patchpoint, when integrated forward in time, may not remain bound to the Moon, or may not transition into a uniform DRO the same way it did in the original BCT. Using patchpoints that extend several revolutions around the Moon after the capture flyby reduce the likelihood that the trajectory will escape the Moon, but it is not guaranteed. It is likely, however that a state exists near the final patchpoint that does remain bound to the Moon, and this state can be located with a Particle Swarm Optimizer (PSO).

A PSO is a stochastic population-based optimization algorithm originally written by Kennedy, Eberhart, and Shi.[36] It mimics the behavior of an insect swarm or animal herd by having a population that moves through the search-space, attempting to find a minimum. Each member of the population, or particle, begins uniformly distributed across the allowable state space and has its movement changed every iteration based on three factors. The first is a randomly generated change in the movement. The second factor drives the particle to return towards the best state it has ever visited. The third factor represents the swarm intelligence dynamic; the particle moves towards the best solution found out of any of the particles in the swarm. The algorithm concludes when a sufficiently good solution has been found by the swarm. In our problem, we are looking for a state somewhere in the vicinity of our final patchpoint that remains bound to the Moon for at least some desired duration. The PSO algorithm is well suited to this problem for three reasons. One, if a viable solution exists anywhere in the defined search space, a well tuned PSO can find it, independent of the state at the final patchpoint. Two, the optimizer is metaheuristic, meaning it is designed to find a sufficiently good answer rather than a global minima. Three, the

PSO is a stochastic algorithm that does not use gradient information to pick a search direction. In the chaotic dynamic environment of quasi-periodic DROs, gradients rapidly change and are unreliable. Deterministic optimization will commonly be trapped in local minima, unable to find better solutions nearby.

MATLAB's built in PSO algorithm was used to update the state of the final patchpoint of the BCT shown in Figure 5.21. The cost function used was written to maximize the duration the trajectory remained in orbit around the Moon, as well as minimize the deviation from the original patchpoint state. This second component of the cost function was included to reduce the amount of correction the transformed BCT will have to undergo, which helps preserve its geometry. The cost function is written as the sum of four weighted components

$$J = w_t J_t + w_r J_r + w_v + J_v + w_f J_f \tag{5.10}$$

$$\begin{aligned} J_t &= \frac{T - t_u}{T} \\ J_r &= \frac{||\mathbf{r} - \mathbf{r}_0||}{\Delta r_{max}} \\ J_v &= \frac{||\mathbf{v} - \mathbf{v}_0||}{\Delta v_{max}} \\ J_f &= 1 - (T == t_u), \end{aligned} \tag{5.11}$$

where T is the minimum desired stability time, t_u is the time that the trajectory departs the Moon, and Δr_{max} and Δv_{max} are the boundaries of the search-space. In J_f, $a == b$ is a boolean operator checking for equality between the two values. The chosen weights are $w_t = 10$, $w_r = 1$, $w_v = 2$, and $w_f = 1000$. The cost function and weights are specifically chosen to sequentially minimize different factors of decreasing importance. The optimization scheme starts by minimizing the highly weighted time until departure J_t. As soon as a state is discovered that does not depart the Moon, the J_f term becomes zero, instantly reducing the cost function by w_f. When this occurs, this state becomes the new swarm target state and is technically sufficiently good for use. The remainder of the algorithm iterations are spent minimizing the J_r and J_v terms by looking for states that are still bound to the Moon ($J_f = J_t = 0$), but that are closer to the original patchpoint state. An alternate approach to minimizing the change in state is to find a state that minimizes the

variations in x-and y-amplitude. In this case, we take J_r and J_v to be the coefficient of variation for the peak x and y-values achieved each orbit:

$$J_r = \sqrt{\frac{\sigma(x_{pks})}{\mu(x_{pks})}} \text{ and } J_v = \sqrt{\frac{\sigma(y_{pks})}{\mu(y_{pks})}}, \tag{5.12}$$

where σ is the standard deviation and μ is the mean. This cost function will find the patchpoint that produces the most uniform DRO.

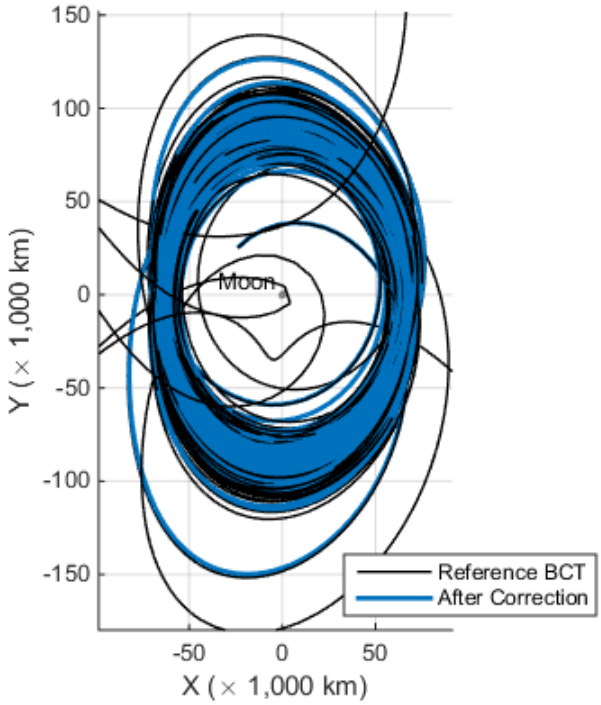

Figure 5.22: The BCT in the rotating frame before and after a PSO adjusts the final patchpoint for minimum variations in amplitude.

When the PSO converges on an answer, that state replaces the final patchpoint state. Then the MSDC can be run again on the set of patchpoints, but the final patchpoint must be fixed or heavily constrained in time, position, and velocity. Figure 5.22 shows the BCT before and after a new patchpoint state was located by the PSO using the minimum amplitude variation strategy. The blue trajectory has a correction of about 15 m/s in velocity and 1.1 km in position, and results in a DRO that is Lagrange stable and becomes more regular over time. At this stage, the BCT has been transformed in epoch, still becomes a stable DRO, and is ready for further mission design.

Chapter 6

Ballistic Capture into Mars-Phobos Distant Retrograde Orbits

Ballisitic capture into Earth-Moon DROs described in Chapter 5 is relevant to many missions, but this three-body system has one of the highest mass parameters in the solar system. Many other three-body systems can benefit from the ballistic capture strategy, specifically systems with sufficiently small mass parameters that make two-body orbits around the minor body impossible. In cases like these, a DRO is often the best option for a neutrally stable orbit around the minor body. This chapter applies the ballistic capture method to the Mars-Phobos system and investigates the differences between it and the Earth-Moon system's BCTs. In addition to having a sufficiently small mass parameter, Mars and Phobos are increasingly attractive targets for future robotic and crewed missions. Through the application to the Mars-Phobos system, this chapter will highlight the algorithms that severely reduce the computational time required to generate stability maps.

6.1 Motivation

Missions to Phobos have been considered for many years, and the moon is entering the spotlight again as NASA considers a crewed mission to Phobos as a precursor to landing astronauts on Mars. A crewed mission to Phobos would allow the agency to test critical hardware required for transport of humans to Mars in a phased and reduced-risk manner. Additionally, astronauts at Phobos can begin testing in-situ resource utilization techniques and technologies, and conduct science through near real-time, remote controlled operation of rovers on the surface of Mars.[89]

Phobos has a history of robotic visitations, some on dedicated missions and others that were

flying by on their mission at Mars. The moon has been photographed in detail by Mariner 9, Viking 1 & 2, Soviet Phobos 88, Mars Global Surveyor, Mars Odyssey Orbiter, Mars Express, and Mars Reconnaissance Orbiter.[35] Three dedicated missions have been launched to Phobos: Phobos 1 and Phobos 2 (U.S.S.R) and Fobos-Grunt (Russian Space Agency), all of which failed to meet their science objectives.[114] There are many proposed missions to Phobos from several space agencies, and most of them include a sample-return element, either through collecting ejecta from an impactor or from landing on the surface.[29,108]

This chapter presents a method for identifying and characterizing trajectories that arrive ballistically at Phobos and are captured into a distant retrograde orbit around the moon. This strategy offers a number of advantages when compared to patched-conic methods to insert into orbit about Phobos. A typical patched-conic based mission involves a spacecraft approaching Phobos on a hyperbolic flyby trajectory and at the point of closest approach, executing an orbit insertion maneuver. It requires a precise flyby trajectory and that the orbit insertion maneuver execute at the right time with little error. The ballistic capture strategy we propose involves placing the spacecraft onto a ballistic "near-field approach" trajectory that does not require a critical, sensitive orbit insertion maneuver. Rather, a sequence of maneuvers may be used to gradually bring the spacecraft into a rendezvous with Phobos, carefully targeting the orbit over time and at a distance of hundreds or thousands of kilometers from Phobos. This gives mission operators time to generate navigation solutions, troubleshoot faults with the spacecraft, and target the approach trajectory with correction maneuvers. Since these nominal trajectories are ballistic, a well navigated spacecraft that becomes uncontrollable can still arrive on its mission orbit. Upon arrival at Phobos, a spacecraft will be temporarily captured for at least 10 days, and often as long as several months. Missions that require longer stays at Phobos will require a stabilizing maneuver, typically on the order of 1 m/s.

6.2 Constructing Distant Retrograde Orbits at Phobos

The Mars-Phobos three-body system is a challenging environment to design stable orbits for because of Phobos' small orbit size and its small mass ratio, given by Equation 6.1:

$$\mu = \frac{M_P}{M_M + M_P} \approx 1.655 \times 10^{-8}, \tag{6.1}$$

where M_M is the mass of Mars and M_P is the mass of Phobos. In fact, an object on the surface of Phobos still experiences an acceleration from Mars' gravity that is two orders of magnitude larger than from Phobos' gravity. Phobos' sphere of influence is approximately 7.3 km, which is below the surface. In this environment, the assumptions of Keplerian orbits fall short and the problem is well suited to three-body mission design.

When reviewing options for three-body orbits around Phobos, distant retrograde orbits are a strong candidate for a number of reasons. First, DROs of any size are neutrally stable in the circular restricted three-body problem, which often translates to stability in a dynamical model that uses ephemeris positions for massive bodies.[19,51] Second, DROs orbit the minor body instead of a libration point, which is useful because the first two Mars-Phobos libration points are barely above the surface of Phobos. Libration point orbits, such as halo and Lyapunov orbits, are challenging because they make hazardous close approaches to the surface of Phobos.[124] They also require station keeping maneuvers about twice per orbit.

DROs are generated in the Mars-Phobos system using the methods described in Section 3.2, beginning at 9 km and increased via the continuation method until the DRO's period is in a 3:2 resonance with Phobos' orbital period around Mars (≈29.9 km). Next, the DRO family is transformed into a high-fidelity dynamical model, which is discussed in more detail in Section 6.3 using the multiple shooting differential corrector discussed in Section 3.3.2. For the MSDC, five orbits are converted with five patchpoints per orbit evenly spaced in time.

6.3 Dynamical Modeling and Orbit Propagation

Trajectories in this chapter are propagated with an 8th order Runge-Kutta integrator. The Jet Propulsion Laboratory's *mar097s.bsp* SPICE file* is used to find the positions of Mars and Phobos and the orientation of Phobos at times requested by the derivative function. The NAIF's CSPICE toolkit provides the functions for calling these states and rotation matrices. For this chapter, orbits are propagated in the MARSIAU frame: a non-rotating frame centered on Mars and based on the Mars Mean Equator. Results in this chapter are often plotted in a Mars-Phobos synodic frame that is centered on Phobos. The synodic frame's x-axis always points from Mars to Phobos, and the z-axis is normal to the Phobos' instantaneous orbit plane. Trajectories in this chapter consider Mars a point mass gravity source and use a distributed mass model for Phobos. The effect of Mars' J_2 is not considered because Phobos' orbit, and therefore planar DROs, are nearly equatorial with respect to Mars. Other perturbing forces are neglected to isolate the effects of Phobos' distributed mass.

6.3.1 Mass-Concentration Model

A mass concentration (mascon) model is used to capture the gravitational effects of Phobos' mass distribution. A set of mascons is generated from the Phobos shape file *phobos_ver64q.tab*† provided by NASA's Planetary Data System - Asteroid Archive. This shape model represents Phobos with 25,350 surface vertices linked together with 49,152 triangular faces and can be seen in Figures 6.1 and 6.18.

A set of mascons is generated from the shape model through a method published by Chanut, Aljbaae and Carruba.[25] For each face in the model, we construct a tetrahedron with the origin and the three vertices that make up the face. A mascon is generated at the centroid of this tetrahedron. We assume a uniform density so the mass of this mascon (m_i) is proportional to the volume of the

* `http://naif.jpl.nasa.gov/pub/naif/pds/pds4/maven/maven_spice/spice_kernels/spk/mar097s.bsp` (Accessed 10/2015)

† `http://sbn.psi.edu/pds/asteroid/VO1_SA_VISA_VISB_5_PHOBOSSHAPE_V1_0/data/phobos_ver64q.tab` (Accessed 11/2015)

tetrahedron (V_i) relative to the volume of the shape model. This is shown in Equation 6.2, where M and V are the mass and volume of Phobos, respectively. For a more accurate representation of the mass distribution, the tetrahedron corresponding to each face is truncated into five sections of uniform height. A mascon is placed at the centroid of each section with mass proportional to that section's volume. This technique improves the estimated accelerations near the surface of Phobos.

$$m_i = M\frac{V_i}{V} \tag{6.2}$$

Using the five tetrahedron layer method with the chosen shape model for Phobos produces 245,760 mascons. To reduce computation time evaluating the accelerations on a body in orbit around Phobos, this model was reduced in a manner that preserves the center of mass. The reduction algorithm searches for the mascon with the lowest mass in the model and computes the distance from it to each other mascon. The smallest mascon and its nearest neighbor, regardless of the neighbor's size, are replaced by a single mascon at their barycenter. Each iteration of the reduction algorithm reduces the total number of mascons by one, so it is repeated until the desired number of mascons remain. The results in the following sections use a mascon model that has been reduced from 245,760 to 1,000 mascons. The error in this model can be computed by comparing the acceleration or gravitational potential in a field of points around Phobos to a truth solution. The algorithm by Werner[127] discussed in Section 2.5.2 is used as the truth solution because it gives an exact solution for the force potential and gravitational acceleration of a polyhedron representing the shape of the body. The accuracy of this calculation is driven by the accuracy of the shape model and the assumption that the body has uniform density.

Figure 6.1 shows the acceleration error-vector's magnitude between the 1,000 mascon model and Werner's polyhedron model. The highest error is about 3×10^{-7} km/s^2, which lies close to the surface of Phobos particularly around the Stickney crater. At distances of 20+ km where DROs exist, the error is on the order of 10^{-8} to 10^{-9} km/s^2. This is approximately the same magnitude as the gravitational contribution of a single mascon. The acceleration error when comparing the 245,760 mascon model to the polyhedron model has a similar distribution and is an order of

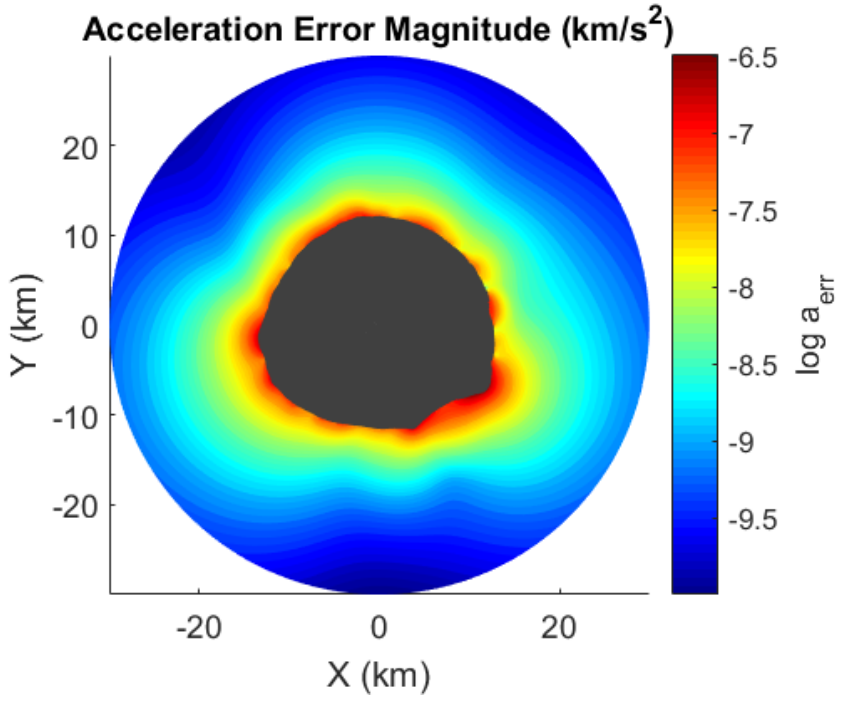

Figure 6.1: The log of the acceleration error-vector's magnitude for the 1,000 mascon model when compared to a truth solution for the Phobos shape model. These errors are computed around Phobos' equator.

magnitude smaller than the 1,000 mascon model comparison. This model error is acceptable for this work, and any trajectories that are discussed can always be converted into more accurate dynamical models in the future.

6.4 Mars-Phobos Stability Maps

This section will discuss the generation of stability maps in the Mars-Phobos system. A new meshing algorithm is used to replace the evaluation of a uniform grid of velocity perturbations. This results in a map with high resolution near the stability boundary, and lower resolution in less sensitive regions. The computation time is reduced by a factor of hundreds to thousands with this strategy because fewer orbit propagations are needed.

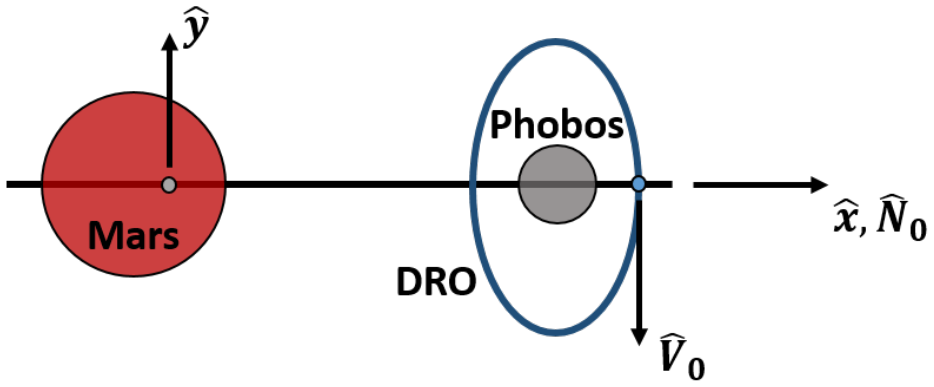

Figure 6.2: The rotating frame and the VNC coordinate frame are aligned at the starting epoch. Not drawn to scale.

6.4.1 Adaptive Meshing for Stability Maps

To build a stability map for a particular DRO, we begin with the state from the first node in the MSDC algorithm from Section 6.2. The initial velocity, expressed in the synodic frame centered on Phobos, is perturbed in the $\hat{N}$ and $\hat{C}$ directions of a Velocity-Normal-Conormal (VNC) coordinate frame where the $\hat{C}$ direction is normal to the line from Mars to Phobos and the instantaneous velocity of the spacecraft. Since the initial conditions are generated such that the trajectory is planar and begins on the rotating frame's x-axis with Phobos between the satellite and Mars, the $\hat{V}$, $\hat{N}$, and $\hat{C}$ directions coincide with the rotating frame's $-y$, $+x$, and $+z$ directions. Figure 6.2 shows this information graphically.

The perturbed state is converted into the MARSIAU frame and propagated forwards and backwards in time for 10 days. It was discovered that a significant number of unstable trajectories impact Phobos, which was not a behavior seen in the Earth-Moon system. Therefore, we classify the resulting trajectories based on whether they escape, impact into, or remains in orbit (stable) around Phobos. A trajectory "impacts" if its radius is ever less than 105% of Phobos' major axis length, which is about 14.07 km; it is not based on the local geometry of the moon. A trajectory "escapes" if it is ever more than 200 km from the center of Phobos. This creates nine possible combinations of forward time and backward time behavior, which is shown in Table 6.1.

Traj. Class	Forward Time	Reverse Time
1	stable	stable
2	stable	escape
3	escape	stable
4	escape	escape
5	stable	impact
6	escape	impact
7	impact	stable
8	impact	escape
9	impact	impact

Table 6.1: Classifications for trajectories in a stability map

The process of determining which velocity perturbations to evaluate is done through an adaptive meshing algorithm using a quadtree data structure based on the work of Nakhjiri.[85] This grants a significant decrease in computation time, often by a factor of hundreds to thousands, when compared to running a uniform grid of points at high resolution. The algorithm is initialized by dividing the velocity search space into equal quadrants, or cells. A cell in the quadtree algorithm is a square that covers some region of the velocity perturbation space and is defined by the position of its upper-left corner its edge length. Let Δv^+ and Δv^- represents the user specified maximum and minimum allowable velocity perturbations in the $\hat{N}$ and $\hat{C}$ directions. The four initial cells are drawn in Figure 6.3 with equal edge lengths shown, and the position of each cell is listed in Table 6.2. Following the generation of the four initial cells, the class of each cell is determined using the $\Delta\vec{v}$ at its center, represented by the blue points in Figure 6.3. If at least one cell, but not all of the cells are class 1 (stable forwards and backwards in time), then the initialization is complete. If that criterion is not met, then each cell is divided into four smaller cells and checked again. This process repeats until initialization is successful or the minimum cell size is reached. This initialization strategy will minimize the number of function evaluations needed, but any uniform grid can be used to initialize the algorithm, which can be useful if there are multiple stability regions in the map.

After the quadtree structure is initialized, the meshing algorithm seeks to identify the bound-

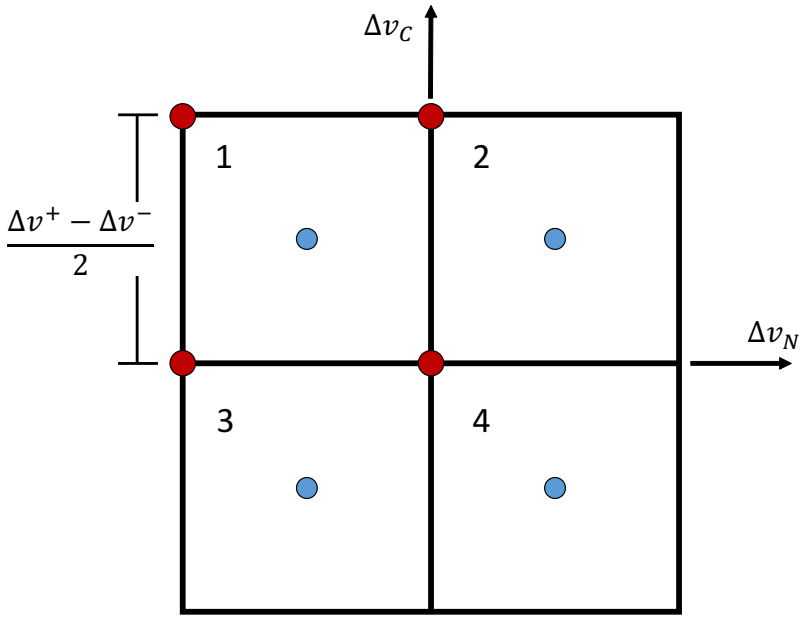

Figure 6.3: The four cells used to initialize the quadtree algorithm. Red points mark the position of the cell. Blue points show what $\Delta\vec{v}$ is used to evaluate the class of the cell.

Cell Num.	Position (x_0, y_0)
1	$(\Delta v^-, \Delta v^+)$
2	$\left(\frac{\Delta v^- + \Delta v^+}{2}, \Delta v^+\right)$
3	$\left(\Delta v^-, \frac{\Delta v^- + \Delta v^+}{2}\right)$
4	$\left(\frac{\Delta v^- + \Delta v^+}{2}, \frac{\Delta v^- + \Delta v^+}{2}\right)$

Table 6.2: Initial cells of the quadtree meshing algorithm

ary of stability by increasing resolution where class 1 cells are neighbored by cells of any other class. For each class 1 cell (also called *stable cells*), we identify all class 2 through 9 cells (also called *unstable cells*) that are adjacent, sharing either a border or a corner point with the stable cell. If there are no adjacent unstable cells, then the stable cell is bordered on all sides by other stable cells or the search-space boundaries and it is left alone. If an unstable neighbor is detected, then the current stable cell lies on the boundary of stability and requires higher resolution. A flag is set for the stable cell and all of its unstable neighbors. When every stable cell has been checked, each of the flagged cells are divided into four new cells. The new cells are evaluated to determine their class and the process is repeated until all flagged cells are less than the specified minimum cell size, which corresponds to the highest resolution in the $\Delta\vec{v}$ vector. Because each cell division results in four equal-sized cells, the set of all cells will always cover the entire velocity perturbation search-space regardless of where a refined mesh is needed. This algorithm greatly reduces the number of orbit propagations required when compared to a uniform grid of $\Delta\vec{v}$ at the expense of possibly missing small stable regions that are disjoint from the main stable region.

6.4.2 Alternate Analyses Enabled by Adaptive Meshing

The reduction in computation time opens up the possibility for several analyses involving large sets of stability maps. First, we can now generate stability maps for a wide range of DROs in a particular three-body system. This type of survey is useful for selecting a reference DRO that has a large set of BCTs to use for designing a mission. Additionally, up until this point, stability maps are always generated when the spacecraft is on the far side of the minor body. We can study how the shape of the stable regions change with the mean anomaly of the reference DRO. This type of analysis is used and discussed in Section 7.5. Another use for rapid stability maps is a survey of DRO sizes in a particular three-body system to determine where groups of stable regions lie. This "stability tube" is shown for the Earth-Moon CR3BP in Figure 6.4. At about 58,000 km, the tube collapses to a narrow stability map. Since high fidelity stability maps generally have smaller stable zones than their CR3BP counterparts, we can expect that DROs around this size will likely

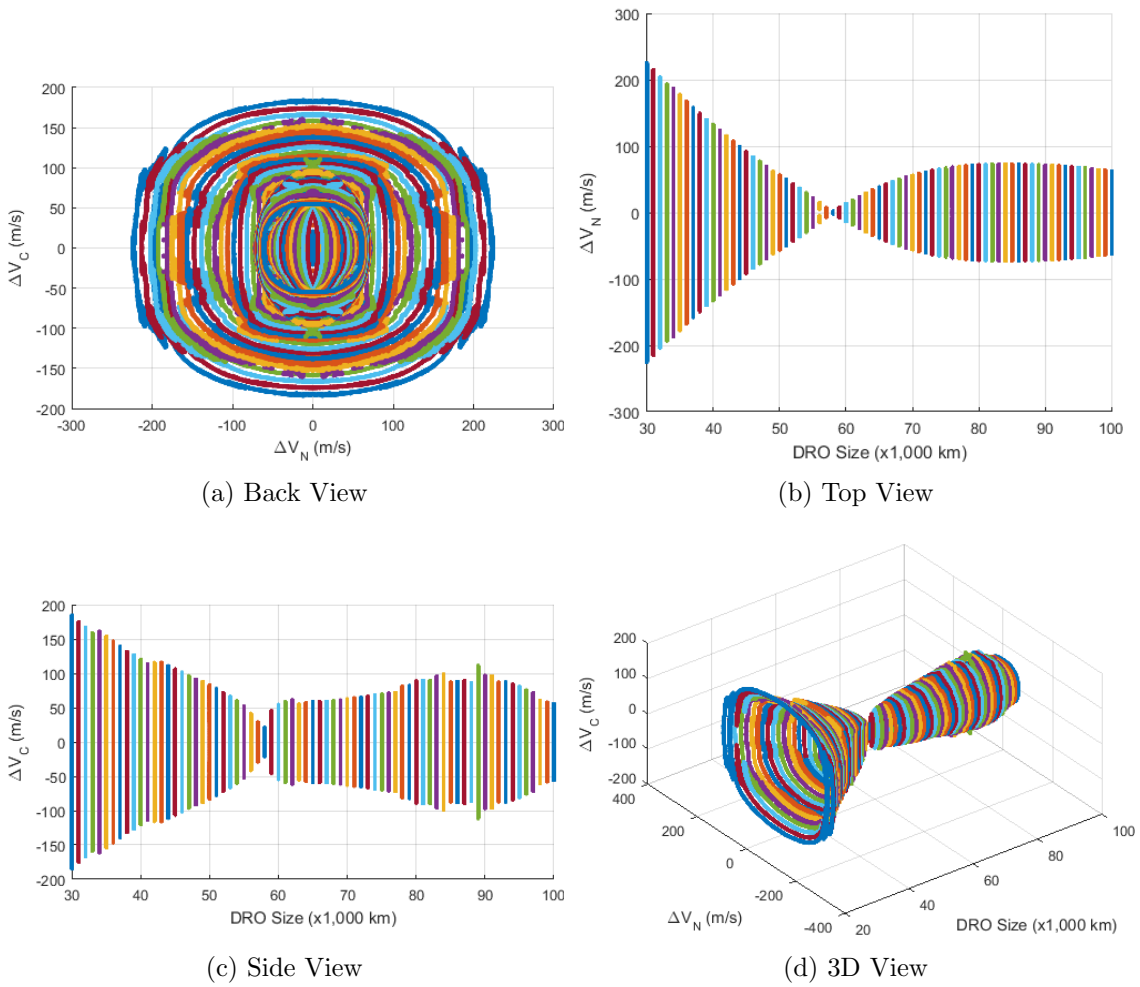

(a) Back View (b) Top View

(c) Side View (d) 3D View

Figure 6.4: Stability map boundaries for different DRO sizes in the Earth-Moon CR3BP.

be unstable.

One of the tuning parameters when building a stability map is the time each orbit is propagated for. Shorter propagation times yield larger stable regions because some of the fringe trajectories haven't had sufficient time to depart the DRO. Ideally, we'd like to choose the shortest propagation time where the size of the stable region does not appreciably differ from the stable region using much longer propagation times. Using adaptive meshing, we can quickly generate a series of stability maps using different propagation times and quickly identify the point of diminishing gain. An example of this is done for the 45,000 km DRO in the CR3BP using the Earth-Moon system's mass parameter. The trajectories are propagated between a month and 100 years and the

area of the convex hull of the stable region is used to determine the point of diminishing gain, as shown in Figure 6.5. Note that the convex hull area is used here because we know ahead of time that the stability map creates a convex shape, but this is not always true, especially for stability maps in high fidelity models. We see that after 115 days, the stable region's size reaches an elbow, meaning that the 100 year propagation time used in Chapter 5 was overkill.

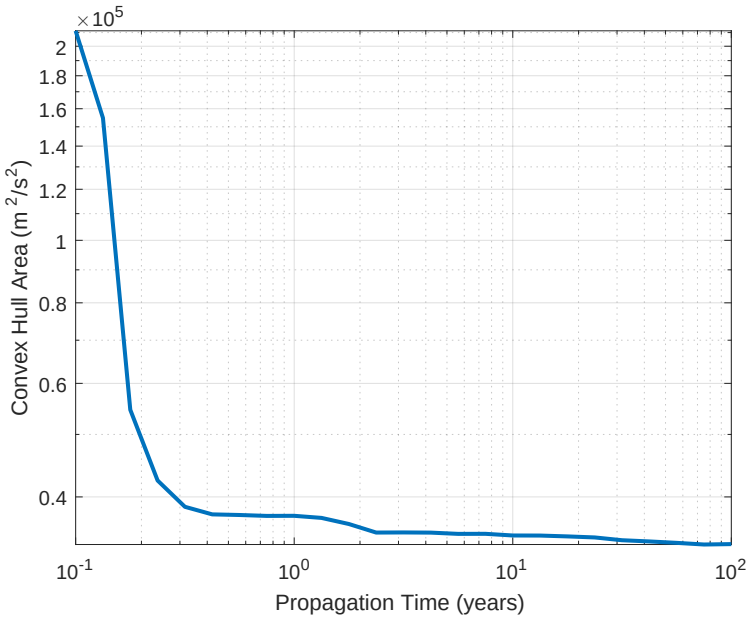

Figure 6.5: The size of the stable region in a stability map versus the propagation time.

6.4.3 Building Mars-Phobos Stability Maps

Stability maps are generated for DROs between 14 and 27.5 km in 500 meter increments using three dynamical models: the CR3BP, a full ephemeris model with Phobos as a point mass, and a high fidelity with the 1,000 mascon model representing Phobos. These maps propagate trajectories for 10 days forward and backward in time. The CR3BP stability maps give an upper bound for the size of the stability regions that can be expected with other dynamical models, but do not reveal one-way stable trajectories due to the autonomous, symplectic nature of the dynamics. The maps that treat Phobos as a point mass capture the effects of Phobos' realistic orbit around Mars including its eccentricity and the indirect effect of forces used to create the ephemerides that are

not included in this dynamical model. These effects greatly reduce the size of the stable regions and make some disappear entirely. Finally, the stability maps that model Phobos with mascons reveal the inclusion of this distributed mass model for Phobos appreciably increases the size of the stable regions. All DRO sizes between 14 and 27.5 km have at least one stable region in this dynamical model, though they are often smaller and occasionally displaced from the stable regions in the CR3BP stability maps. While Phobos' shape has a stabilizing effect, there is always a boundary of one-way stable trajectories surrounding the stable regions. An interesting observation when comparing the point-mass and mascon models is that the one-way stable regions appear to flip across the $\Delta V_N = 0$ line. In the point-mass model, forward stable trajectories are found mostly in $\Delta V_N < 0$ and backwards stable trajectories are located where $\Delta V_N > 0$. The mascon model's stability map shows the opposite. The cause of this change warrants further research.

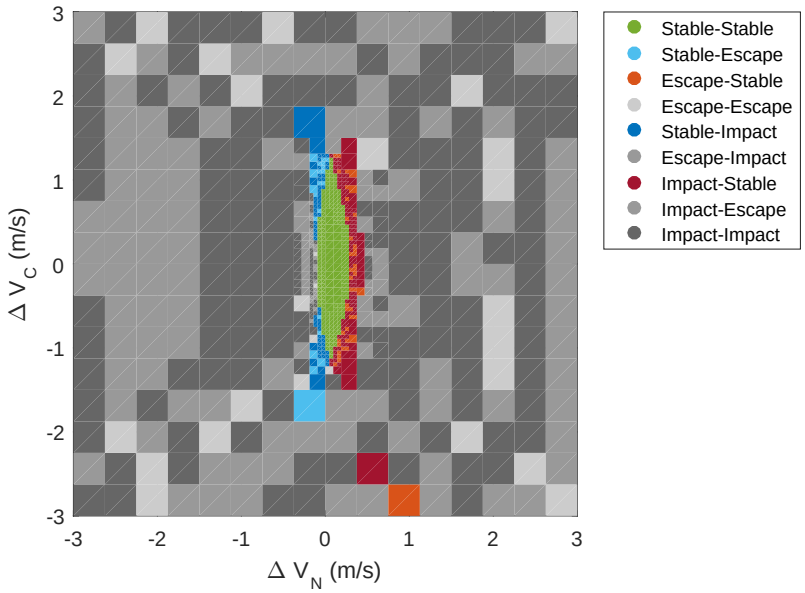

Figure 6.6: The stability map for a 26 km DRO where Phobos is treated as a point mass.

We are specifically interested in locating and characterizing a large set of class 2 trajectories (stable-escape) because these represent ballistic capture trajectories (BCTs); they arrive from far beyond Phobos and are captured onto a DRO for at least 10 days, and often much longer. In

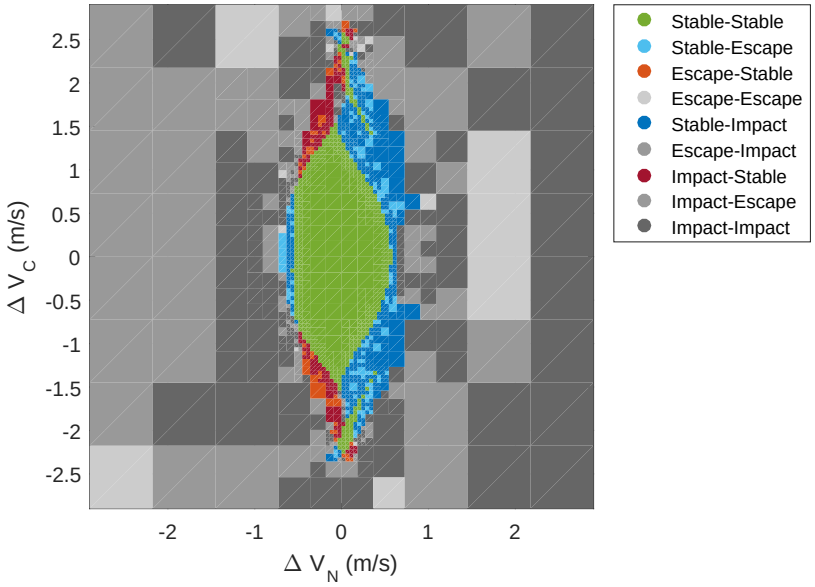

Figure 6.7: The stability map for a 26 km DRO in the Mars-Phobos system using the high fidelity dynamical model.

the point mass Phobos stability maps, the 26 km DRO map shown in Figure 6.6 contains several desirable features that warrant further investigation. It retains a stable region and contains a large area of forward stable trajectories where $\Delta V_N < 0$, indicated by dark blue (class 5: stable-impact) and light blue (class 2: stable-escape) cells. Within this forward stable region, there is a high density of class 2 trajectories compared to other DRO sizes. This DRO's mascon stability map is shown in Figure 6.7. We see that the stability region has grown to about 1 m/s wide by 2 m/s tall with two small islands of stability above and below the main region. The forward stable trajectories now dominantly exist where $\Delta V_N > 0$. This DRO also has a high density of class 2 trajectories near the stability boundary compared to other DRO sizes.

6.4.4 Refining Stability Maps

The adaptive meshing algorithm specializes in finding the boundary of stability, but we are more interested in the set of one-way stable trajectories surrounding this boundary. To ensure that all BCTs for a DRO are accounted for, the stability maps are refined to capture high resolution

information away from this stability boundary. To achieve this, we start by finding the convex hull of each stable region. The stability maps often show stability regions that can be roughly approximated with an ellipse, so we fit a minimum bounding ellipse (MBE) to the convex hull of each stable region in the map. The MBE contains all of the data points and has a minimized area. It is found using MATLAB's unconstrained function minimization algorithm *fminunc*, which searches for the best location for the ellipse center (c_x, c_y), given the centroid of the convex hull as an initial guess. For a given center, the remaining three parameters that define the ellipse (rotation angle τ, semi-major axis, and distance between foci) have optimal values, which are found with a series of golden section searches. Further discussion on MBE algorithms are published by Post.[101]

Next, ellipses with the same center and orientation as each MBE are created but with larger semi-major and semi-minor axes. These larger bounding ellipses (LBEs) mark the regions of the stability map that will be refined. Figure 6.8 shows the stable points, the convex hull, and the associated MBEs and LBEs for the 26 km DRO. In this study, these axes' dimensions are increased

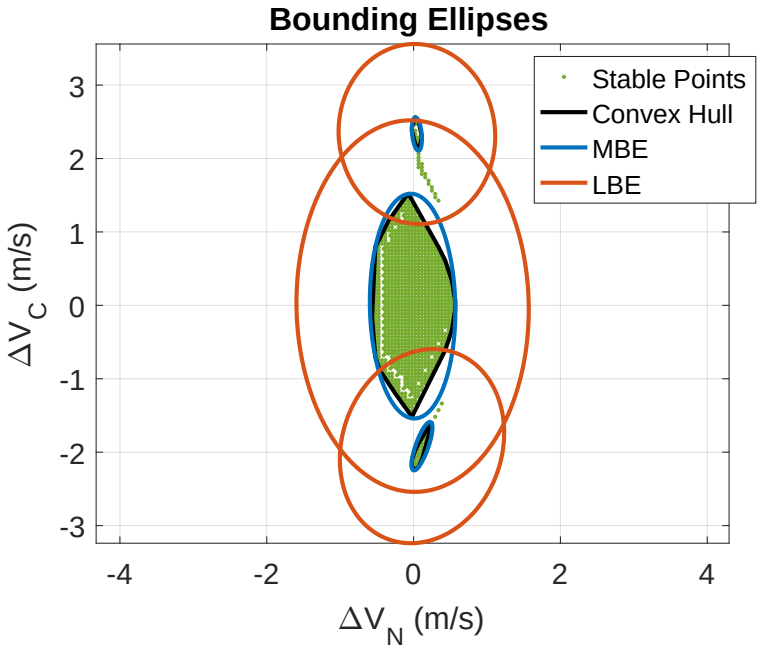

Figure 6.8: The 26 km DRO's stable points (green), the convex hulls (black) for each stable region, and the minimum bounding ellipses (blue) and larger bounding ellipses (orange).

by 1.0 m/s to fully capture the one-way stable trajectories around the stability boundary. This

choice in size increase was determined empirically. Once the LBEs have been constructed, every unstable cell in the map is checked for one of two conditions:

(1) The cell's center lies within the LBE.

(2) If the cell is divided into a set of the smallest allowable cells, would any of their centers lie within the LBE.

If either of these conditions are met, the original cell is divided into four new cells. This process is repeated until an iteration occurs where no cells are divided. Note that stable cells (class 1) are not divided in the refinement algorithm since they are of minimum size along the boundary of stability and are not useful for building a set of BCTs. After each unstable cell inside the LBE is divided to its minimum size, the cells' stability classifications are evaluated.

This refinement algorithm ensures that the search space remains completely covered by the set of cells, and that within the LBE, all cells are the minimum size, which gives the highest resolution on one-way stable trajectories. Figure 6.9 shows the 26 km map that has been refined with this method. It shows considerably more detail, structure, and symmetry in the forward-stable trajectory regions. It also reveals 194 perturbation vectors that result in BCTs as opposed to the 117 found in the unrefined stability map due to the lower resolution used around the stable zone. This amounts to a 66% increase in the number of identified forward stable trajectories. It is interesting to note that the one-way stable trajectories are not chaotic like they are in the Earth-Moon system with solar gravity considered,[16] but are instead grouped into regions. Recall in Section 6.4.1 that we refined cells to detect the boundary of stable cells, but not forward stable trajectories, which are of greater interest for this work. This is because not all three-body systems form distinct regions of one-way stable trajectories as we see them in the Mars-Phobos stability maps. The Earth-Moon system for example has a chaotic distribution of one-way stable trajectories which would not be captured without using the refinement algorithm.[16] The Mars-Phobos system is far more deterministic than the Earth-Moon system; this difference is likely due to the magnitude and nature of the perturbing forces relative to the two-body gravity from the major and minor

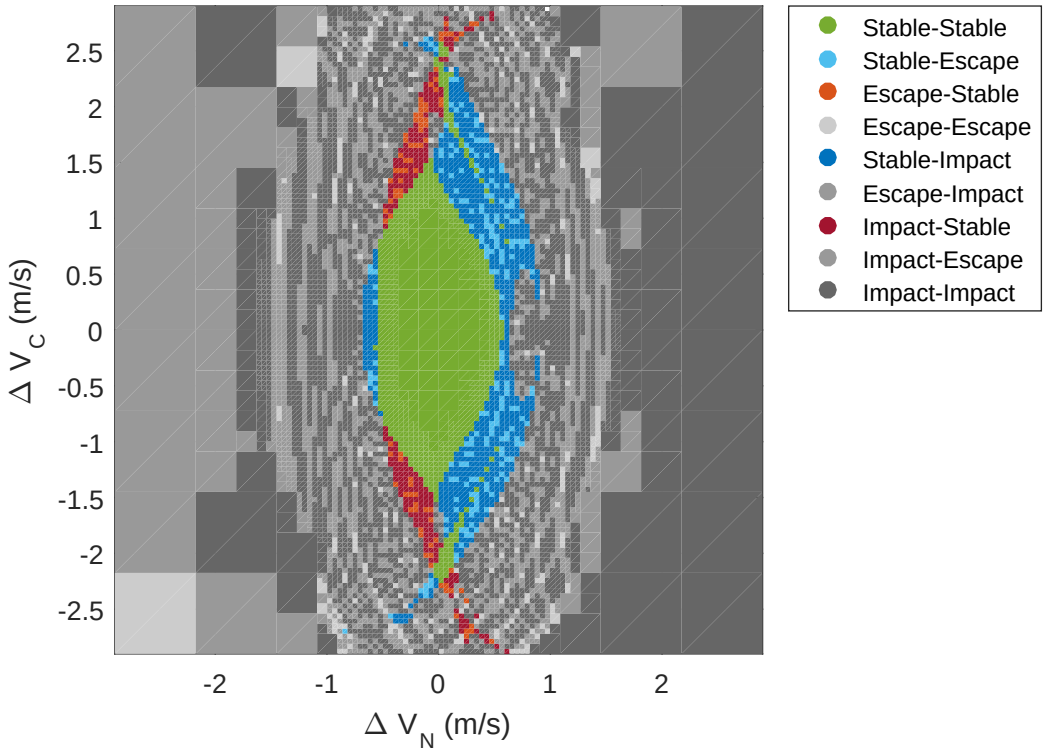

Figure 6.9: The refined stability map for a 26 km DRO, based on the larger bounding ellipses shown in Figure 6.8. Light blue points are ballistic capture trajectories. The cell borders are not drawn because they obscure high resolution data.

bodies. A 40,000 km DRO around the Moon experiences gravitational force on the same order of magnitude from the Earth, Moon, and Sun. In the Mars-Phobos system however, the gravitational acceleration from a point-mass Phobos is an order of magnitude less than that from Mars, and the perturbing acceleration from the mascon model is 2-3 orders of magnitude less than that. Since Mars dominates the motion, a spacecraft flying on a DRO is essentially flying in formation with Phobos. The existence and structure of the one-way stable regions is due to small secular trends from perturbing forces can predictably disrupt the formation.

Additionally, in the Mars-Phobos system, we find a significantly higher percentage of trajectories impact the moon instead of escaping. In the 26 km DRO, 77% of the forward stable trajectories we sampled end with an impact, while few Earth-Moon BCTs did so. This is due to

the relationship between a body's radius and mass. A uniform density sphere's mass, and therefore gravitational acceleration, increases as a function of r^3, while its surface sits at height r. This suggests that a minor body that is more massive is more likely to have one-way stable trajectories that do not impact since the DROs exist further from the surface. Note that the size of a DRO with a particular period is driven only by the mass ratio μ.[11]

6.5 One-Way Stable Trajectories

6.5.1 During and After Capture

The stability maps from Section 6.4 give a set of BCTs that can be used in mission design to capture a spacecraft into a stable orbit around Phobos with no maneuvers required. The 194 BCTs associated with the 26 km DRO are studied to show trends and limits in their geometry and energy. Previous work has shown that BCTs can be characterized by a flyby that leads to their capture into the DRO, typically closer to the minor body than the DRO nominally lies.[16,95] This flyby is detected as the first periapse after the spacecraft passes 200 km boundary. A vector field showing the position and velocity of all the BCTs at this critical flyby are plotted in the Mars-Phobos synodic frame in Figure 6.10. An interesting feature is that all of the BCTs have this flyby occur almost directly on the leading or trailing edge of Phobos. The 134 (69%) leading edge flybys are called the northern family and the 60 (31%) trailing flybys are called the southern family. This distribution suggests that Phobos is more likely to capture a spacecraft that needs an energy reduction. It may be that trajectories flying by behind Phobos are more likely to impact the surface, but this has not been explored in depth for this thesis. The northern family can have flybys from 14 km to as high as 100 km from Phobos. They can arrive between ±12.5 km out of Phobos' orbit plane and many of them arrive near 0 km. The southern family is clustered around closer flybys ranging from 15-50 km with one trajectory arriving at 63 km. The southern family BCTs arrive between ±7.4 km out of Phobos' orbit plane with only three trajectories exceeding this range.

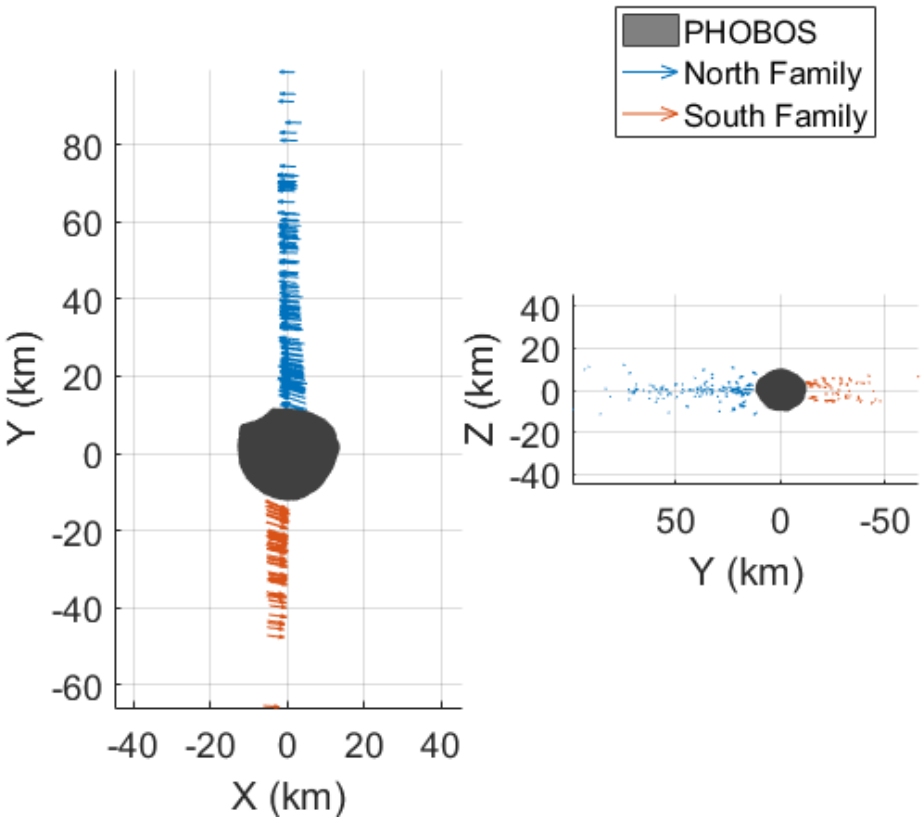

Figure 6.10: The position and velocity at the first flyby, which leads to capture into a DRO around Phobos.

Take the *capture time* to be the duration it takes an object on a BCT to travel from 200 km from Phobos to the capture flyby. Figure 6.11 shows a histogram for the capture time, separated by family. The northern family shows a right-skewed distribution with a peak at 1.41 hours. The southern family is closer to a Gaussian distribution with a peak at 1.44 hours. We've shown how sensitive these BCTs can be to state errors, and the capture time gives an idea of how long a spacecraft has to perform near-field navigation observations and computations to determine if it is on an acceptable trajectory.

It is desirable for the practical design of the mission to remain as far away from Phobos as possible to minimize the risk of impact. Figure 6.12 plots the minimum and maximum radii the set of BCTs has after the capture flyby. The top plot has a 1:1 slope line drawn, meaning BCTs on this line are never closer to Phobos than they are during the capture flyby. There are two important

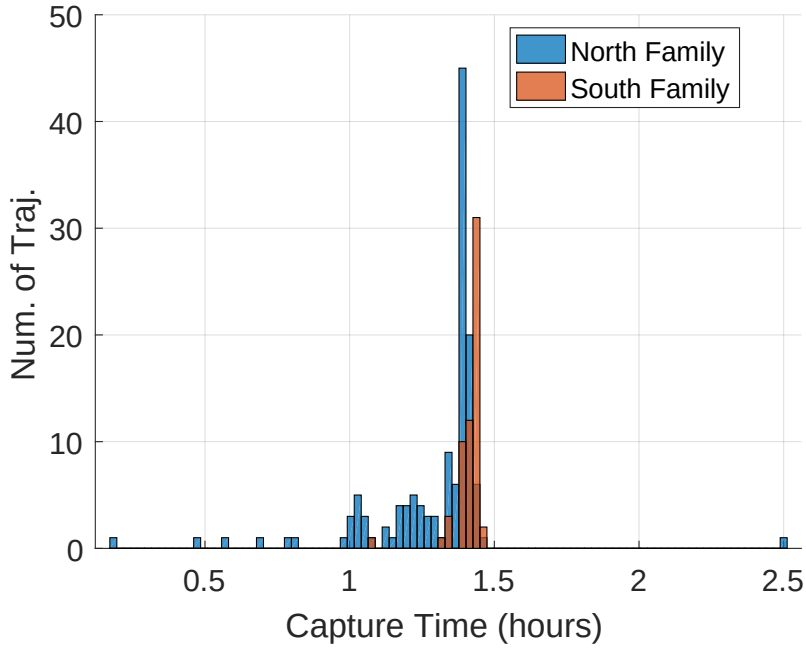

Figure 6.11: The time to travel from 200 km to the capture flyby.

observations related to the minimum radius after capture. First, the northern family almost always stays further away from Phobos than the southern family. Second, closer capture flybys generally results in trajectories that stay further away from Phobos. The ideal BCT based solely on this plot has a capture flyby radius of 24.8 km and a minimum radius of 20.1 km. This BCT will be referred to as the *reference trajectory* for the remainder of this chapter. For the 26 km DRO, there appears to be an upper bound of 20.1 km (or ≈ 8 km in altitude) on the minimum flyby radius for a ballistic capture to occur. It is desirable for a BCT to have a small maximum radius, because the spacecraft is particularly sensitive to perturbations when it is further away from Phobos. A smaller maximum radius translates to a more uniform, predictable transition into the DRO. When viewing the right plot of Figure 6.12, which shows the maximum radius after capture, we see again that it is desirable to choose a smaller capture flyby radius since it results in a smaller maximum radius. The reference trajectory mentioned previously has a maximum radius of 104.5 km.

Figure 6.13 shows the distribution for maximum out-of-plane, or z-amplitude for the set of BCTs. This histogram is not divided by family because there were no significant trends. The

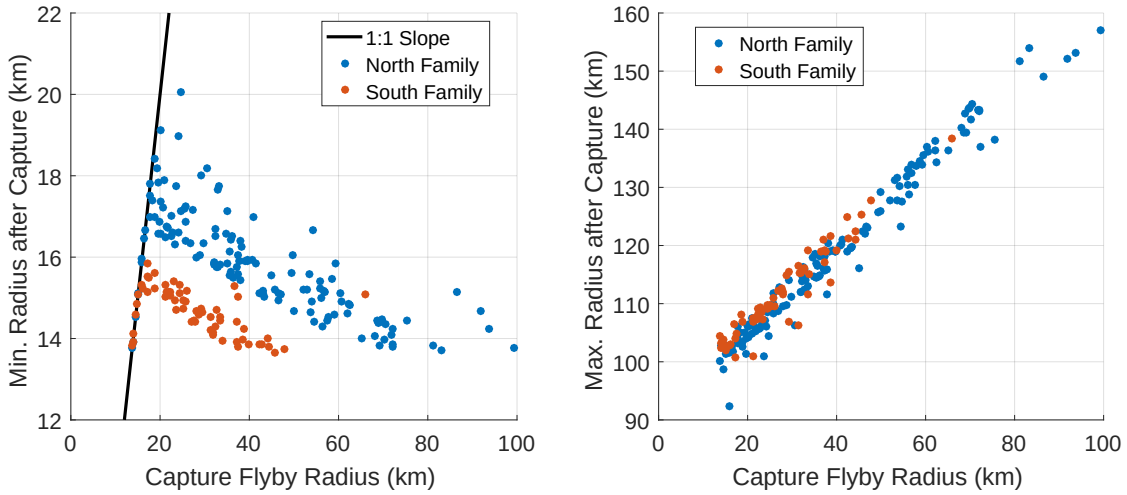

Figure 6.12: The minimum and maximum radii the BCTs have after their capture flyby. The black line shows a 1:1 slope, meaning trajectories on this line had their minimum radius when they were captured.

majority of BCTs have between 2 and 6 km of z-amplitude. About 20 trajectories gain visibility of the north and/or south pole of Phobos based on their z-amplitude.

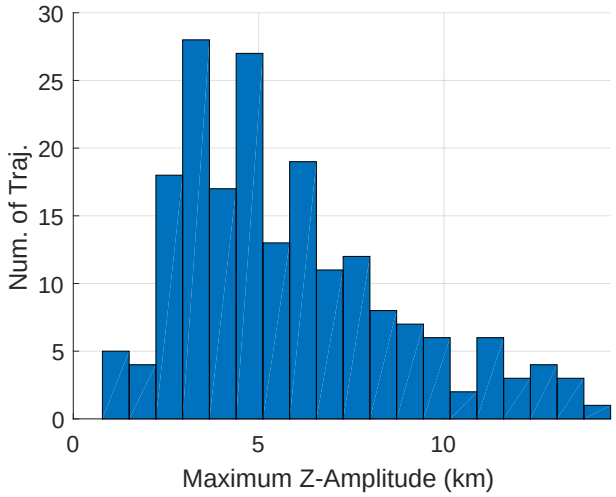

Figure 6.13: The distribution of out-of-plane or z-amplitude for the set of ballistic capture trajectories.

Finally, we investigate the geometry of the Mars-Phobos system at the time the BCTs arrive at the moon. Figure 6.14 shows the distribution of Phobos' true anomaly when each BCT has reached its capture flyby. The sample size is too small to generate meaningful statistical conclusions,

but there appears to be a tendency for BCTs to favor times when Phobos is approaching periapse. This trend is not solely tied to the choice of epoch for the stability map, because the 23 km DRO reveals the opposite: a tendency to flyby Phobos when it is at apopapse. The discussion in Section 6.2 regarding the dynamics causing the existence of one-way stable trajectories supports this observation as well. The reference trajectory arrives at 325° true anomaly.

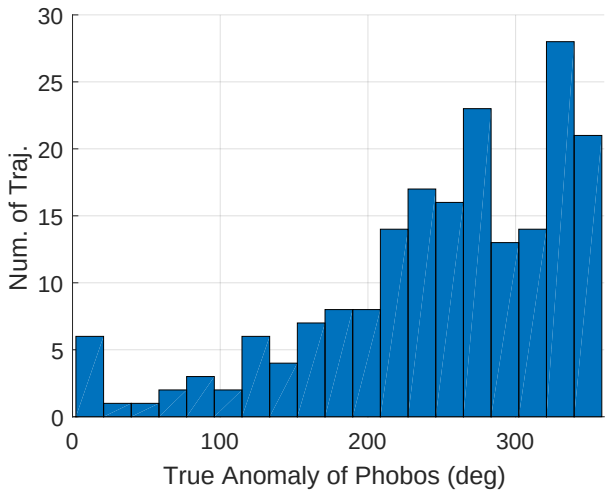

Figure 6.14: The true anomaly of Phobos at the time of each capture flyby.

6.5.2 Before Capture

The advantage of using a BCT to arrive in an orbit around Phobos is that large, critical maneuvers can be performed days or weeks in advance of arrival at Phobos. Therefore, it is important to look at the geometry and energy of BCTs prior to their capture in the DRO. Figure 6.15 shows the average semi-major axis (SMA) and inclination with respect to Mars, and includes Phobos' orbital elements as black intersecting lines. The entire southern family has an SMA (and therefore, energy) less than Phobos, while the northern family has a higher SMA and energy. This division is directly related to how the families were chosen, since the northern family consists of leading edge capture flybys, which are energy reducing maneuvers with respect to Mars. The southern family flies by Phobos on the trailing side, which raises energy with respect to Mars. A spacecraft arriving at Mars from Earth could most effectively target a northern family BCT, since it will be

performing energy reduction maneuvers. A sample return mission from the surface of Mars would target a southern BCT for the lowest cost transfer. However, the difference in energy between northern and southern family BCTs is small and the ΔV cost of targeting the other family is on the order of 1-10 m/s depending on the mission design. The SMA for both families only differs from

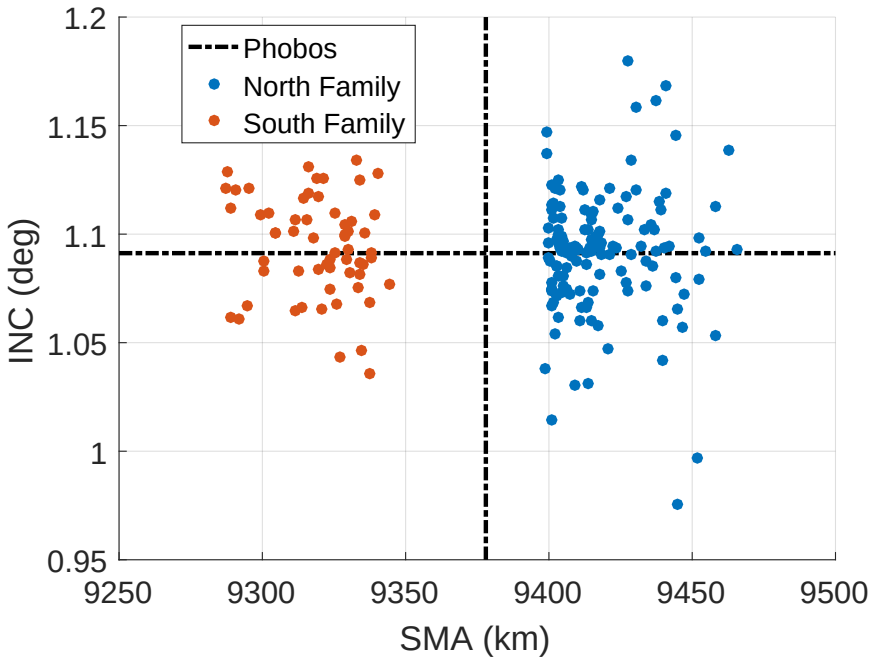

Figure 6.15: The average semi-major axis and inclination of each BCT with respect to Mars prior to capture.

Phobos' by between 20.1 and 90.5 km. This small difference is due to the low mass of the moon, which is unable to significantly change the energy of the spacecraft as it arrives. The small mass of Phobos also means that the approach trajectory in the rotating frame is decently approximated by the Clohessy-Wiltshire equations, which describe the motion of one massless body with respect to another in a two-body circular orbit. The plot also shows that the tolerance for inclination error is bound to about $\pm 0.1°$. This means that a spacecraft utilizing a BCT will place itself into a walking orbit nearly the same size as Phobos' orbit and wait for the mismatched orbital periods to bring the spacecraft to the moon.

Directly related to the SMA is the period of the BCT set. Figure 6.16 shows these periods

compared to Phobos'. This is useful for determining how long a spacecraft would have to wait to encounter Phobos again at no fuel cost if it missed its original opportunity. The synodic period T_S can be computed using the period of Phobos T_p and the period of the BCT T_{bct}:

$$T_s = \begin{cases} \left(\frac{1}{T_{bct}} - \frac{1}{T_p}\right)^{-1}, & if\ T_{bct} < T_p \\ \left(\frac{1}{T_p} - \frac{1}{T_{bct}}\right)^{-1}, & if\ T_{bct} > T_p \end{cases} \tag{6.3}$$

The fastest that a southern BCT could encounter Phobos again is after about 68 orbits (21.7 days), and the slowest it would take is about 187 orbits (59.6 days). A northern BCT can re-encounter Phobos between 72 orbits (23.0 days) and 300 orbits (95.7 days). Note that the northern family is most densely populated near Phobos' orbital period, meaning that the upper limit on synodic period is more likely. The reference trajectory selected from Figure 6.12 has a synodic period of 40.3 days.

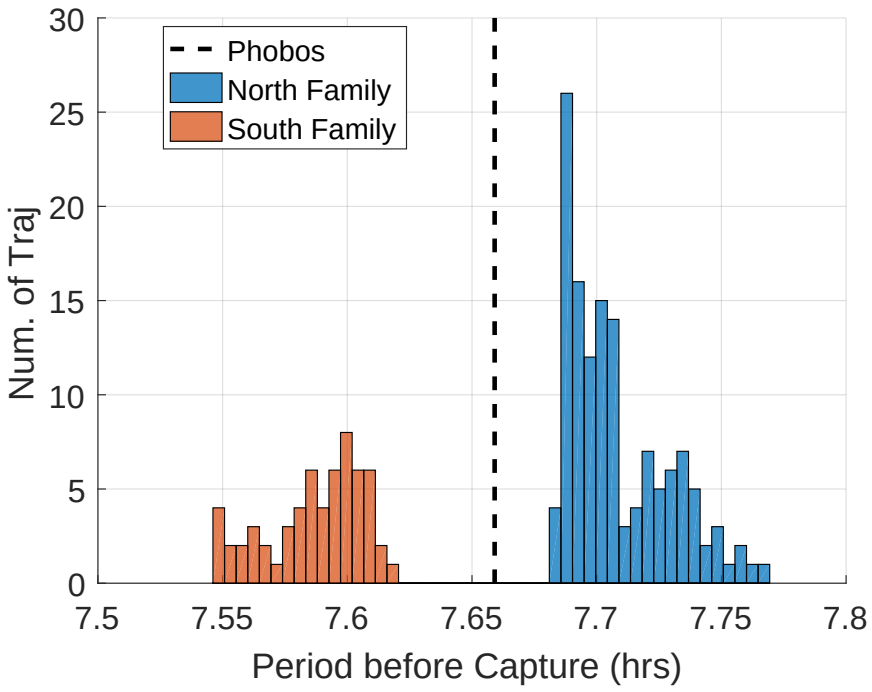

Figure 6.16: The period of the walking orbits leading to a ballistic capture at Phobos.

6.5.3 On Approach to Phobos

The advantage to arriving on a BCT many days in advance is there is sufficient time to get a navigation solution for the spacecraft and determine if it is on a proper course towards capture into a DRO. However, the stability maps show that velocity errors on the order of 1 m/s can cause drastically different outcomes. This section looks at how accurate the navigation solution must be in terms of velocity errors in the $\hat{N}$ and $\hat{C}$ directions. A stability map is generated using the state of the capture flyby state of the reference trajectory as the seed state. This map, shown in Figure 6.17, has a narrow band of acceptable velocity errors, only several millimeters per second wide. This highlights the approach trajectory's sensitivity to velocity errors, and though it isn't required, a spacecraft would benefit from autonomous navigation capabilities. The ability to perform small correction maneuvers can keep the spacecraft on the desired BCT, or divert it away from Phobos if a problem occurs and another rendezvous needs to be targeted. Note that "impacting" trajectories adjacent to this stable band impact Phobos as far as 10 days after the capture flyby, and do not indicate imminent danger to the spacecraft.

Figure 6.18 shows the reference trajectory on approach to Phobos in the synodic frame, beginning at about 200 km away, performing the capture flyby, and winding onto the DRO. The black points on the trajectory separate 30 minutes of flight time, and are shown for the first 12 hours of the approach. The reference trajectory spends 21.4 days on the DRO after the capture flyby before departing the DRO. Note that the seed DRO for the 26 km stability map remains in orbit around Phobos for at least 50 days, meaning a maneuver of approximately 2.5 m/s would allow for a significantly longer mission duration. Minute station keeping maneuvers are expected for any mission.

6.6 Conclusion

This chapter applies the ballistic capture method described in Chapter 5 to the Mars-Phobos system with some improvements using the adaptive meshing algorithm. This strategy is applicable

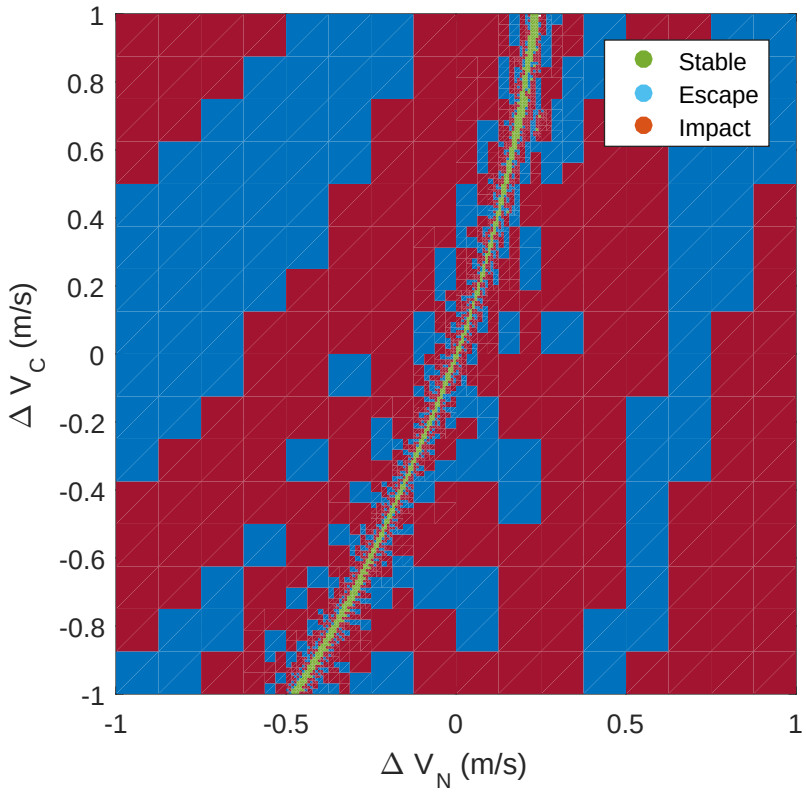

Figure 6.17: A stability map seeded from the capture flyby state of the reference trajectory. These states are only propagated forwards in time. Green states stay around Phobos for > 10 days, blue states escape, and red states impact within 10 days.

to many three-body systems, but is more versatile when there are significant perturbing forces on the spacecraft besides the two-body gravitational attraction of the two primaries, such as Phobos' co-rotating aspherical gravity field. It can be less effective for low density bodies, which may result in impacts rather than capture trajectories. The spacecraft can perform critical and large maneuvers days in advance of the capture, giving mission operators time to generate navigation solutions, target the approach, or correct faults prior to entering orbit around Phobos. The ballistic capture aspect is also advantageous because a spacecraft on approach can still be end up on its mission orbit should a fault develop while it is on approach.

A mission targeting a ballistic capture trajectory from interplanetary space would need to arrive at Mars and reduce its orbital energy and inclination to be near that of Phobos'. A stability

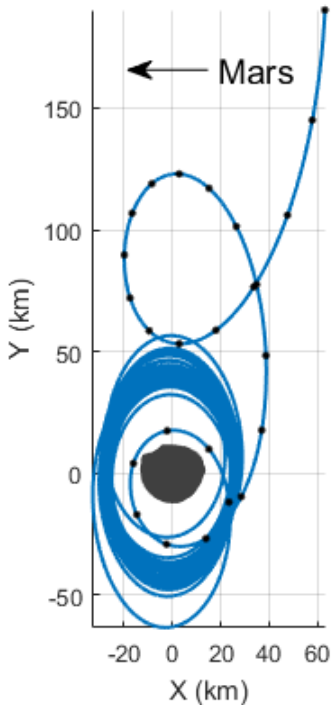

Figure 6.18: The reference trajectory as it approaches from 200 km, performs the capture flyby, and winds onto the DRO. Black points separate 30 minute increments for the first 12 hours.

map for the planned arrival time gives the options for the walking orbits that lead to ballistic capture. The spacecraft enters a walking orbit about 20 days prior to arrival with a semi-major axis about 50 km larger than Phobos' and waits for the close approach to the moon. During this time, it maximizes the accuracy of its navigation solution and can perform necessary correction maneuvers. As the spacecraft approaches Phobos, small correction maneuvers may be necessary to maintain the desired trajectory, especially through dynamically sensitive points such as the capture flyby. When arriving at Phobos, depending on the BCT that was targeted, the spacecraft will initially pass Phobos with an altitude between 0.5 and 86 km with one or more subsequent flybys passing through an altitude range of 0.5 to 6.7 km. Should any problems occur during the approach or ballistic capture, a maneuver on the order of 1 m/s is sufficient to depart Phobos and set up another rendezvous in about 20 to 90 days. Once captured into the DRO, the spacecraft will remain there for the duration analyzed in the stability map. A maneuver of 2-3 m/s will put the spacecraft from the one-way stable regions into the center of the stability region and can extend

the time spent in orbit around Phobos often by orders of magnitude. The spacecraft could also use a small maneuver to place it on an impacting trajectory to achieve a landing on Phobos.

Chapter 7

Stabilizing a Distant Retrograde Orbit

Once a spacecraft is ballistically captured onto a DRO, it will remain in orbit around the body for at least the duration used to generate the stability map, and often longer. However, these ballistic capture trajectories lie on the boundary of stability, a highly sensitive and sometimes chaotic region of phase space. This makes the orbit susceptible to unmodeled perturbing forces, errors in state estimation, and maneuver errors. It is advantageous to perform small correction maneuvers to put the spacecraft into an orbit that is less sensitive to these issues. This chapter discusses methods for building one and two-impulse transfers from quasi-periodic DROs into periodic ones. It also discusses how to generate maneuvers that minimize the orbit's sensitivity given a ΔV budget that is insufficient for transferring to a periodic DRO. These transfers are built in the Earth-Moon CR3BP, which can be used as a starting point and optimized in high-fidelity models.

7.1 Optimal Trajectory Theory

This section presents a set of first-order necessary conditions for a trajectory to be optimal. These conditions, originally developed by Lawden,[77] will be used in an indirect method to obtain optimal transfers between the stability boundary and less sensitive DROs. An indirect method is one that seeks to satisfy the necessary and sufficient conditions for optimality as opposed to a direct method which seeks to minimize a cost function. Then a method created by Lion and Handelsman[47] for optimizing a reference transfer using these necessary conditions will be shown and discussed as well. The derivations in this chapter are for trajectories that are optimized when

the fuel consumption has been minimized. We follow the work and notation of Davis, who developed the necessary conditions in the CR3BP,[30] and Hiday, who did the same for the ER3BP.[54]

7.1.1 Necessary Conditions

We begin by defining the cost function and equations of motion for a spacecraft using a constant specific impulse (CSI) engine for its maneuvers. The cost function seeks to minimize the fuel expended during maneuvers:

$$J = c \ln\left(\frac{m_0}{m_f}\right), \tag{7.1}$$

where c is the exhaust velocity, m_0 is the initial mass, and m_f is the final mass of the spacecraft. Following Lawden's derivation using calculus of variations requires we include the spacecraft mass in our state vector in addition to position and velocity:

$$\mathbf{X} = \begin{bmatrix} \mathbf{R} \\ \mathbf{V} \\ m \end{bmatrix} \text{ and } \dot{\mathbf{X}} = \begin{bmatrix} \mathbf{V} \\ \mathbf{g} + \dfrac{\beta c}{m}\hat{u} \\ -\beta \end{bmatrix}, \tag{7.2}$$

where $\mathbf{g}$ represents the ballistic accelerations in the CR3BP, given in Equation 2.6. The parameters pertaining to thrust are the mass flow rate β and the thrust direction $\hat{u}$, which is a unit vector. The instantaneous thrust magnitude can be found using $T(t) = \beta c$. The mass flow rate is defined as positive, bounded on the interval $0 \leq \beta \leq \beta_{max}$, and constrained such that

$$\beta(\beta_{max} - \beta) = \alpha^2 \tag{7.3}$$

for some non-physical parameter α.

The next step is to construct an expression for a control Hamiltonian for the problem. We start by creating a vector of adjoint variables $\vec{\lambda} = [\vec{\lambda}_R, \vec{\lambda}_V, \lambda_m]^T$, where each element of $\vec{\lambda}$ is the adjoint of the corresponding element in the state vector $\mathbf{X}$. To generate the Hamiltonian H, we multiply the adjoint vector by the equations of motion

$$H = \vec{\lambda}^T \dot{\mathbf{X}} = \vec{\lambda}_R^T \mathbf{V} + \vec{\lambda}_V^T \left(\mathbf{g} + \frac{\beta c}{m}\hat{u}\right) - \lambda_m \beta. \tag{7.4}$$

The time derivative of the adjoint vector is constructed by negating the partial derivative of H with respect to the state vector:

$$\dot{\vec{\lambda}}_R^T = -\frac{\partial H}{\partial \mathbf{R}} = -\vec{\lambda}_V^T \mathbf{H}(U) \tag{7.5}$$

$$\dot{\vec{\lambda}}_V^T = -\frac{\partial H}{\partial \mathbf{V}} = -(\vec{\lambda}_R^T + \vec{\lambda}_V^T \mathbf{\Omega}) \tag{7.6}$$

$$\dot{\lambda}_m = -\frac{\partial H}{\partial m} = \vec{\lambda}_V^T \frac{\beta c}{m^2} \hat{u}, \tag{7.7}$$

where $\mathbf{H}(U)$ and $\mathbf{\Omega}$ are two 3×3 submatrices of the Jacobian of the equations of motion defined in Equations 4.10 and 4.12, respectively.

In this form, we seek to maximize the control Hamiltonian using the control variables in order to minimize the cost J of the trajectory according to the Pontryagin's Maximum Principle.[42,54] The method of Lagrange multipliers is used to maximize the Hamiltonian while enforcing the thrusting constraints on the value of β, given by Equation 7.3, and $\hat{u}$, which must be a unit vector. These two constraints are weighted by the multipliers σ_1 and σ_2.

$$\mathcal{F}(\beta, \alpha, \hat{u}) = \sigma_1[\beta(\beta_{max} - \beta) - \alpha^2] + \sigma_2(\hat{u}^T \hat{u} - 1) - H. \tag{7.8}$$

The value of H is maximized when $\nabla \mathcal{F} = 0$:

$$\frac{\partial \mathcal{F}}{\partial \beta} = \sigma_1(\beta_{max} - 2\beta) - \vec{\lambda}_V^T \frac{c}{m} \hat{u} + \lambda_m = 0 \tag{7.9}$$

$$\frac{\partial \mathcal{F}}{\partial \alpha} = -2\sigma_1 \alpha = 0 \tag{7.10}$$

$$\frac{\partial \mathcal{F}}{\partial \hat{u}} = 2\sigma_2 \hat{u}^T - \frac{\beta c}{m} \vec{\lambda}_V^T = 0. \tag{7.11}$$

Equations 7.9-7.11 form the necessary conditions for an optimal trajectory.

7.1.2 Optimally Controlled Arcs

There are several solutions that satisfy the necessary conditions. For non-zero Lagrange multipliers σ_1, Equation 7.10 is satisfied when $\alpha = 0$. Plugging this into Equation 7.3 tells us that the mass flow rate should be either null ($\beta = 0$) or full throttle ($\beta = \beta_{max}$), which are called Null Thrust (NT) and Maximal Thrust (MT) arcs, respectively. There is also the case where

$\sigma_2 = 0$, which allows β to take on intermediate values, which are called Intermediate Thrust (IT) arcs. The constraint in Equation 7.11 gives us information about the optimal thrusting direction $\hat{u}$. While on an MT arc ($\beta = \beta_{max}$), the thrust direction needs to be parallel to the velocity adjoint vector. Given this relationship between the adjoint to the velocity vector and the optimal thrusting direction, Lawden defines it as the *primer vector* $\mathbf{p}(t) = \vec{\lambda}_V$, which has a magnitude $\|\mathbf{p}(t)\| = p(t)$.

Lawden uses the Weierstrass necessary condition to prove that they must point in the same direction for an optimal trajectory.[77] We use a superscript asterisk (*) to denote the values on the optimal trajectory and write the maximized control Hamiltonian as $H^* \geq H$. This can be rewritten as

$$\vec{\lambda}^{*T}\dot{\mathbf{X}}^* \geq \vec{\lambda}^{*T}\dot{\mathbf{X}} \tag{7.12}$$

$$\vec{\lambda}_R\mathbf{V} + \vec{\lambda}_V\left(\frac{\beta^* c}{m}\hat{u}^*\right) - \lambda_m\beta^* \geq \vec{\lambda}_R\mathbf{V} + \vec{\lambda}_V\left(\frac{\beta c}{m}\hat{u}\right) - \lambda_m\beta, \tag{7.13}$$

which can be further simplified to form the Weierstrass necessary condition:

$$\beta^*\left(\frac{c}{m}\mathbf{p}^T\hat{u}^* - \lambda_m\right) \geq \beta\left(\frac{c}{m}\mathbf{p}^T\hat{u} - \lambda_m\right). \tag{7.14}$$

On an NT arc, there is no mass flow rate ($\beta = 0$), which nulls the left-hand side of this equation and removes the dependence on β^*. This conveniently reduces to

$$\lambda_m \geq \frac{cp}{m}. \tag{7.15}$$

MT arcs use $\beta = \beta^* = \beta_{max}$ instead, which reduces Equation 7.14 to

$$\mathbf{p}^T\hat{u}^* \geq \mathbf{p}^T\hat{u}. \tag{7.16}$$

The right-hand side is maximized ($\hat{u} = \hat{u}^*$) when $\mathbf{p}$ is parallel to and in the same direction as $\hat{u}$. By substituting this into Equation 7.14 and realizing the left-hand side must be greater than zero since $\beta^* \geq \beta > 0$ on an MT arc, we can derive another conditions:

$$\frac{c}{m}\mathbf{p}^T\hat{u}^* - \lambda_m \geq 0, \tag{7.17}$$

which is simplified and rearranged as

$$\lambda_m \leq \frac{cp}{m}. \tag{7.18}$$

Finally, on IT arcs, β can be higher or lower than β^*. Hiday shows that Equation 7.14 can only be satisfied when we set the optimal thrust direction $\hat{u} = \hat{u}^*$, which causes

$$\lambda_m = \frac{cp}{m}. \tag{7.19}$$

To summarize these trajectory arcs, we know that in MT and IT arcs where thrusting is occurring, the optimal thrust direction is in the direction of the primer vector. The value of the adjoint of the mass λ_m can be defined through a *switching function*:

$$S \equiv \frac{cp}{m} - \lambda_m, \tag{7.20}$$

where

$$S \geq 0 \text{ on an MT arc,}$$

$$S \leq 0 \text{ on an NT arc,}$$

$$S = 0 \text{ on an IT arc.}$$

The mass adjoint can be written in terms of the control parameters by taking the time derivative of the switching function.

$$\dot{S} = \frac{c}{m}\dot{p} + \frac{cp\beta}{m^2} - \dot{\lambda}_m \tag{7.21}$$

Next, we substitute the mass adjoint's derivative from Equation 7.7, which gives:

$$\dot{S} = \frac{c}{m}\dot{p} + \frac{cp\beta}{m^2} - \frac{\beta c}{m^2}\mathbf{p}^T\hat{u} \tag{7.22}$$

$$\dot{S} = \frac{c}{m}\dot{p}. \tag{7.23}$$

On an NT arc, the mass is constant, so we can integrate this equation again to get

$$S = \frac{cp}{m} + k, \tag{7.24}$$

where k is a constant of integration.

Finally, we substitute the switching function into Equation 7.9, which has been unused up until this point:

$$\frac{\partial \mathcal{F}}{\partial \beta} = \sigma_1(\beta_{max} - 2\beta) - S = 0. \tag{7.25}$$

This rearranges to

$$\sigma_1 = \frac{S}{\beta_{max} - 2\beta}. \tag{7.26}$$

Plugging this into Equation 7.10 tells us that the switching function must be zero on IT arcs since these exist where $\sigma_1 = 0$. On MT arcs, $\sigma_1 = -S/\beta_{max}$ and on NT arcs, $\sigma_1 = S/\beta_{max}$.

7.1.3 Impulsive Transfers

The optimization in this chapter focuses on impulsive transfers in the CR3BP, so the optimal trajectory theory discussion will be shaped to follow that assumption. Impulsive transfers are simply NT arcs linked together by infinitesimally short MT arcs. This causes β to approach ∞, resulting in instantaneous velocity and mass changes while the position remains constant. This means that the optimal trajectory cannot contain any MT arcs ($S > 0$) and maneuvers must be performed when $S = 0$ such that $\dot{S} < 0$. An optimal two-impulse transfer connects two trajectories with a NT arc that begins and ends with a maneuver when $S = 0$. An example of the time history of this type of transfer is shown in Figure 7.1. Recall Equation 7.24 which is valid for NT arcs. We

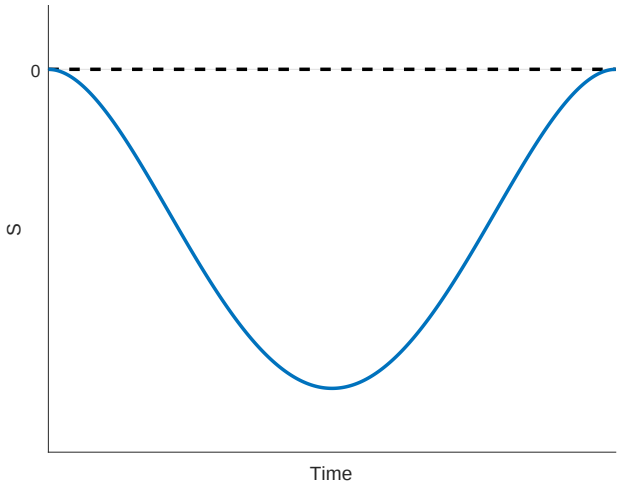

Figure 7.1: An example of a two-impulse transfer's switching function.

know that the switching function is zero at impulses, so we write

$$S = 0 = \frac{c}{m} p_i + k, \tag{7.27}$$

where p_i is the primer vector magnitude at the impulse. This allows us to solve for the constant k:

$$S = \frac{c}{m}(p - p_i) \tag{7.28}$$

Since the spacecraft mass changes instantaneously and only at impulses, all NT arcs on an optimal impulsive-thrust transfer have $p \leq p_i$ and perform their impulses when $p = p_i$. Transfers where $p > p_i$ are not optimal. Hiday uses the transversality condition[55] to find the mass adjoint at the final impulse as a function of the cost function from Equation 7.1:

$$\lambda_m(t_f) = -\frac{\partial J}{\partial m_f} = \frac{c}{m_f}. \tag{7.29}$$

Substituting this expression into Equation 7.20 at time t_f gives us

$$S(t_f) = \frac{c}{m_f}p_f - \frac{c}{m_f} = \frac{c}{m_f}(p_f - 1). \tag{7.30}$$

Equating this to Equation 7.28 reveals that $p_i = 1$. Thus, for an impulsive-thrust trajectory, whenever the primer vector's norm equals unity, an impulse is required to keep it less than unity. A heuristic explanation of this finding is that the primer vector magnitude is a metric of efficiency for performing a maneuver along a trajectory. Maneuvers are optimal when they have the direction and thrust such that the performing a maneuver anywhere else on the trajectory is less efficient ($p < 1$).

Figure 7.1 shows an example of a transfer where the switching function that smoothly approaches $S = \dot{S} = 0$. Some trajectories may approach $S = 0$ with $\dot{S} > 0$, which forms a cusp. An example of this is shown in Figure 7.2. This behavior is known as a corner in the trajectory, or a discontinuity in state variables as a result of an instantaneous change in the control variables (i.e., an impulse). Lawden applies two Weierstrass-Erdmann conditions to show when such a corner is permitted on an optimal trajectory. He finds that the adjoint vector $\vec{\lambda}$ must be continuous across the impulse at the corner, and because $\vec{\lambda}_V$ is continuous, so must the primer vector $\mathbf{p}$. Using this information in $\dot{\vec{\lambda}}_V$ of Equation 7.6 tells us that the primer vector derivative must be continuous as

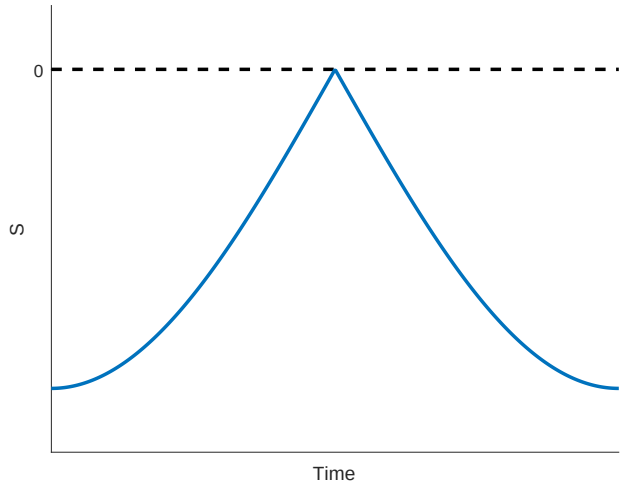

Figure 7.2: An example of an impulsive transfer with a cusp, or a discontinuity in $\dot{S}$.

well since $\vec{\lambda}_R$ and $\vec{\lambda}_V$ are continuous and $\mathbf{\Omega}$ is a constant matrix.

$$\mathbf{p}^- = \mathbf{p}^+ \tag{7.31}$$

$$\dot{\mathbf{p}}^- = \dot{\mathbf{p}}^+, \tag{7.32}$$

where superscripts $-$ and $+$ represent values immediately before and immediately after an impulse, respectively.

The second condition requires that the control Hamiltonian H be continuous as well: $H^- = H^+$. We substitute the definition of the primer vector into Equation 7.4 to get

$$H = \mathbf{p}^T\mathbf{g} + \vec{\lambda}_R^T\mathbf{V} + \left(\frac{c}{m}p - \lambda_m\right)\beta. \tag{7.33}$$

We replace unknown adjoint variables by rearranging and substituting the primer vector into Equation 7.6 as well as the switching function to give us

$$H = \mathbf{p}^T\mathbf{g} - (\dot{\mathbf{p}}^T + \mathbf{p}^T\mathbf{\Omega})\mathbf{V} + S\beta. \tag{7.34}$$

Recall that since we're looking at an impulse, $S = 0$. Equating the Hamiltonian before and after the impulse gives

$$\mathbf{p}^T[(\mathbf{g} - \mathbf{\Omega}\mathbf{V})^+ - (\mathbf{g} - \mathbf{\Omega}\mathbf{V})^-] - \dot{\mathbf{p}}(\mathbf{V}^+ - \mathbf{V})^- = 0. \tag{7.35}$$

The term $\mathbf{g}$ given in Equation 2.6 can be written as $\mathbf{g} = \mathbf{H}(U) + \mathbf{\Omega V}$. Subtracting the velocity dependent terms means that this expression is only dependent on position, and therefore it is continuous across the impulse, which only has a velocity discontinuity. The surviving terms in Equation 7.35 give the condition:

$$\dot{\mathbf{p}}(\mathbf{V}^+ - \mathbf{V}^-) = \dot{\mathbf{p}}\Delta\mathbf{V} = 0. \tag{7.36}$$

Since the thrust direction of an optimal trajectory is in the direction of the primer vector, we can substitute it in for $\Delta\mathbf{V}$:

$$\dot{\mathbf{p}}^T\mathbf{p} = 0. \tag{7.37}$$

This expression can be true if $\mathbf{p}$ and $\dot{\mathbf{p}}$ are orthogonal vectors, but Equation 7.6 shows that $\dot{\mathbf{p}} = \dot{\vec{\lambda}}_V$ has some component in the direction of $\mathbf{p} = \vec{\lambda}_V$, which proves they are not orthogonal. Since the magnitude $\|\mathbf{p}\| = 1$, the only way for this condition to hold true is for $\|\dot{\mathbf{p}}\| = \dot{p} = 0$ at an impulse. Substituting this into Equation 7.23 tells us that $\dot{S}$ must be zero at an impulse, meaning an optimal trajectory cannot have a cusp.

In summary, for an impulsive trajectory to be optimal, the primer vector must be continuous and smooth. When the primer vector has a magnitude of unity, an impulse must be applied in the direction of the primer vector. At these impulses, the primer vector's derivative must be a null vector.

7.1.4 Constructing the Primer Vector

To check if a trajectory is optimal, we need to compute the primer vector and its derivative at the impulses separating NT arcs. Begin with the adjoint differential equation in Equation 7.6 and substitute the primer vector in for $\vec{\lambda}_V$:

$$\dot{\mathbf{p}}^T = -\vec{\lambda}_R^T - \mathbf{p}^T\mathbf{\Omega}. \tag{7.38}$$

Next, we take the derivative of this expression to give

$$\ddot{\mathbf{p}} = -\dot{\vec{\lambda}}_R^T - \dot{\mathbf{p}}^T\mathbf{\Omega} - \mathbf{p}^T\dot{\mathbf{\Omega}}. \tag{7.39}$$

Since $\mathbf{\Omega}$ is a constant matrix, the third term drops out. We replace $\dot{\lambda}_R^T$ with Equation 7.5 to get

$$\ddot{\mathbf{p}}^T = \mathbf{p}^T \mathbf{H}(U) - \dot{\mathbf{p}}^T \mathbf{\Omega}. \tag{7.40}$$

Recall that the Hessian matrix $\mathbf{H}(U)$ is symmetric, so $\mathbf{H}(U)^T = \mathbf{H}(U)$. Additionally, $\mathbf{\Omega} = -\mathbf{\Omega}^T$, which allows us to write

$$\ddot{\mathbf{p}} = \mathbf{H}(U)\mathbf{p} + \mathbf{\Omega}\dot{\mathbf{p}}. \tag{7.41}$$

The acceleration of the spacecraft $\dot{\mathbf{V}}$ can be written in the same form

$$\dot{\mathbf{V}} = \mathbf{H}(U)\mathbf{R} + \mathbf{\Omega}\mathbf{V}. \tag{7.42}$$

As a result, we can use the state transition matrix $\Phi(t, t_0)$ from the trajectory propagation from t_0 to t to propagate the primer vector through time:

$$\begin{bmatrix} \mathbf{p}(t_f) \\ \dot{\mathbf{p}}(t_f) \end{bmatrix} = \begin{bmatrix} \Phi_{11}(t_f, t_0) & \Phi_{12}(t_f, t_0) \\ \Phi_{21}(t_f, t_0) & \Phi_{22}(t_f, t_0) \end{bmatrix} \begin{bmatrix} \mathbf{p}(t_0) \\ \dot{\mathbf{p}}(t_0) \end{bmatrix}. \tag{7.43}$$

We can find the initial and final primer vector based off the initial and final impulse on the NT arc using

$$\mathbf{p}(t_0) = \frac{\Delta\mathbf{V}_0}{\|\Delta\mathbf{V}_0\|} \tag{7.44}$$

$$\mathbf{p}(t_f) = \frac{\Delta\mathbf{V}_f}{\|\Delta\mathbf{V}_f\|}. \tag{7.45}$$

The initial and final primer vectors can be used to find their initial and final derivatives using Equation 7.43. The initial derivative of the primer vector can be found with

$$\mathbf{p}(t_f) = \Phi_{11}\,\mathbf{p}(t_0) + \Phi_{12}\,\dot{\mathbf{p}}(t_0) \tag{7.46}$$

$$\dot{\mathbf{p}}(t_0) = \Phi_{12}^{-1}\,[\mathbf{p}(t_f) - \Phi_{11}\,\mathbf{p}(t_0)]. \tag{7.47}$$

To find the final primer vector derivative, use the other half of Equation 7.43:

$$\dot{\mathbf{p}}(t_f) = \Phi_{21}\,\mathbf{p}(t_0) + \Phi_{22}\,\dot{\mathbf{p}}(t_0) \tag{7.48}$$

$$\dot{\mathbf{p}}(t_f) = \Phi_{21}\,\mathbf{p}(t_0) + \Phi_{22}\,\Phi_{12}^{-1}\,[\mathbf{p}(t_f) - \Phi_{11}\,\mathbf{p}(t_0)]. \tag{7.49}$$

With these quantities, the necessary conditions for optimality can be checked and a reference trajectory can be manipulated to be optimal.

7.1.5 Indirect Optimization with Primer Vector Theory

The application of primer vector theory in an indirect optimization scheme was developed by Lion and Handelsman for the two-body problem.[47] Davis achieves identical results for the CR3BP as does Hiday for the ER3BP. Beginning with a reference impulsive transfer with initial and final maneuvers occurring at t_0 and t_f and with primer vector magnitude derivatives $\dot{p}_0$ and $\dot{p}_f$, we can lower the cost of the transfer by meeting the necessary conditions through three changes. First, if $\dot{p}$ is non-zero at the beginning of the transfer, then changing the location of the initial impulse along the initial orbit will drive $\dot{p}$ to zero. Figure 7.3a shows the time history of two transfers between a quasi-periodic DRO and a periodic one, which were found using a particle swarm optimizer. We can see in each case that the final impulse is optimal, but the initial impulse has a non-zero $\dot{p}$ value. Assuming linear local motion, Lion and Handelsman show that for $\dot{p}_0 > 0$, performing the initial impulse a short time step later ($\Delta t_0 > 0$) will decrease the cost of the transfer. For $\dot{p}_0 < 0$, an earlier impulse ($\Delta t_0 < 0$) will form a lower cost trajectory.

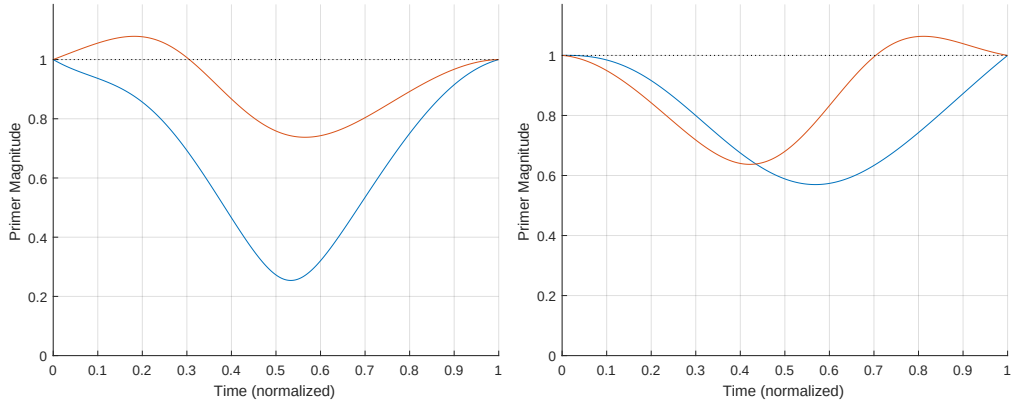

(a) Transfers with $\dot{p}_0 \neq 0$ (b) Transfers with $\dot{p}_f \neq 0$

Figure 7.3: Examples of transfers that violate the condition that $\dot{p} = 0$ at impulses.

Similarly, if $\dot{p}$ at the final impulse is non-zero, then moving the location of that impulse along the final orbit will bring $\dot{p}$ to zero. Figure 7.3b shows two examples of non-optimal final impulses. Through a proof similar to the initial impulse cost, it can be shown that if $\dot{p}_f < 0$, then an earlier final impulse ($\Delta t_f < 0$) will be closer to optimal. If $\dot{p}_f > 0$, then a later final impulse (Δt_f) is closer

to optimal. Both of these proofs assume linearized motion, so in practice, the reference trajectory must be updated with each iteration and step-size control on Δt is beneficial to prevent divergence. Additionally, Davis shows that these rules do not change if both the initial and final impulse need to be shifted as well.

In some cases, a transfer can have $\dot{p}_0 = 0$ and $\dot{p}_f = 0$, but the primer vector magnitude still exceeds unity along the transfer, which violates the necessary conditions. An example of this is shown in Figure 7.4a. When this is the case, one or more additional impulses are needed along

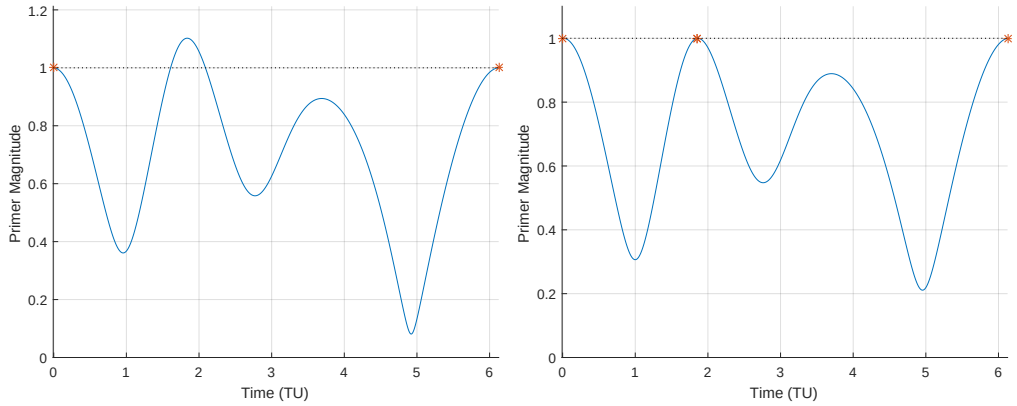

(a) Transfers with $\dot{p} = 0$, but $p > 1$ (b) Adding a third impulse makes $p \leq 1$

Figure 7.4: A trajectory that needs a third impulse to drive $p \leq 1$ for the whole transfer.

the transfer. The best first-order improvement to the cost is realized when the interior impulse is added at the time and position where the primer vector magnitude is maximized. Jezewski and Rozendaal developed a method for determining the magnitude of this interior maneuver for the two-body problem using an analytic, second order cost variation function.[62] The placement and timing of this impulse must also be modified so that a cusp is not formed, which would indicate a non-optimal trajectory. The cost variation equation based on these variables is

$$\delta J = (\dot{\mathbf{p}}_{m^+} - \dot{\mathbf{p}}_{m^-})\delta \mathbf{R}_m + (H_{m^+} - H_{m^-})\delta t_m, \tag{7.50}$$

where subscript m^- and m^+ denotes just before and after the interior impulse, respectively. δJ is the change in the cost function for a change in the maneuver position $\delta \mathbf{R}_m$ and time δt_m.

The equation shows that the cost cannot be lowered after the primer vector derivative and the Hamiltonian are continuous across the impulse, which were both criteria for optimality under the Weierstrass-Erdmann conditions. Figure 7.4b shows the trajectory in Figure 7.4a after a third impulse is added. This method is extensible to an arbitrary number of interior impulses until $p \leq 1$ across the entire transfer. In practice, each subsequent mid-course maneuvers is often several orders of magnitude smaller than the maneuver before it.

7.2 Selecting Quasi-Periodic DROs

We begin by defining the set of quasi-periodic DROs that form the boundary of the stability region for a reference periodic DRO. A stability map is generated for DROs in the Earth-Moon CR3BP spanning 30,000 to 100,000 km using the quadtree adaptive meshing strategy. These maps use a 10 year propagation time and a resolution of 0.5 m/s. These stability maps each contain a single stable region that is approximately centered on the periodic solution. The stability map for a 70,000 km DRO is shown in Figure 7.5 and has interesting features along the boundary including concavities and a thin sheath of one-way stable trajectories.

Next, for each map, the points along the boundary are identified. We take advantage of the fact that there is one stability region that is approximately centered on the origin to determine this boundary. The points at the center of the minimum size stable cells, which only exist on the boundary of stability, are converted into polar coordinates and sorted into bins based on their angular coordinate. Through an appropriate bin size, we can isolate the points on the stability boundary by searching each bin for the point with the maximum distance from the origin. Figure 7.6 shows the set of stable points from the 70,000 km DRO in the Earth-Moon CR3BP. The boundary of stability using this method is drawn in black and appropriately traces the exterior features of the map. Finally, we select 50 points with equidistant spacing around the perimeter of the stability boundary. These velocity perturbation pairs are decreased in magnitude by one percent to ensure that the trajectories they create are quasi-periodic orbits within the stable zone, but are still representative of the behavior at the boundary: large variations in x- and y-amplitudes

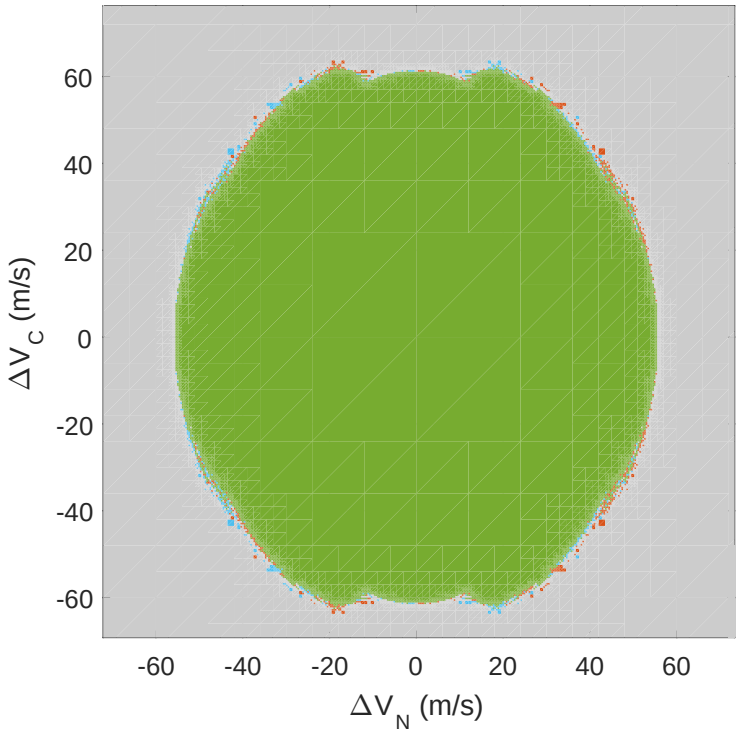

Figure 7.5: The stability map for the 70,000 km DRO in the Earth-Moon CR3BP.

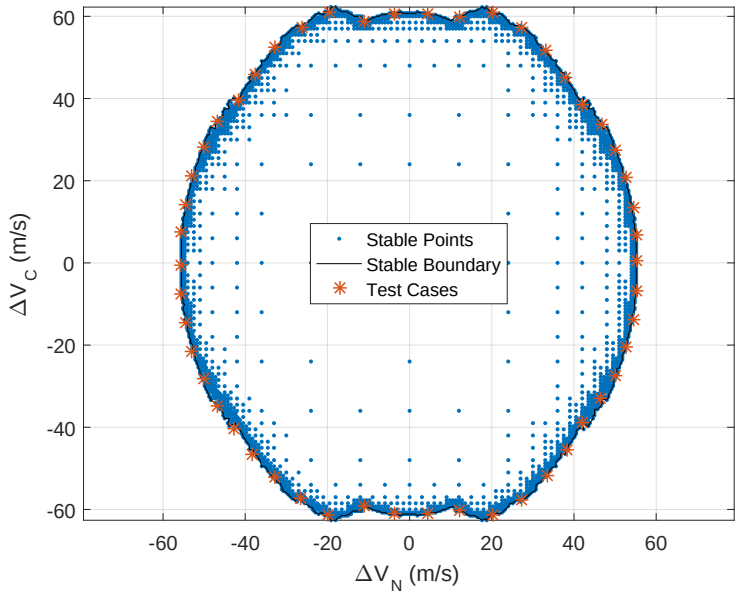

Figure 7.6: The stable points and boundary of stability for the 70,000 km DRO in the Earth-Moon CR3BP. The red points are used as a set of quasi-periodic orbits to build minimum cost transfers into less sensitive periodic DROs.

across different orbits and large out-of-plane amplitudes. Since each orbit in the set shares the same starting position, we propagate each one for one period of the reference DRO before looking for transfers to more stable orbits. Throughout the rest of this chapter, we consider the states along this quasi-periodic orbit up to 30π TU, or about 3.5 years, beyond this starting point. One could argue that using an invariant torus (Section 4.3.2) to represent each quasi-periodic orbit would be more robust. While true, the torus is a two-dimensional surface as opposed to a one-dimensional quasi-periodic orbit. Increasing the dimensionality in the analyses described in the following sections severely increases computation time while the propagation time is sufficiently long to create a representative set of states.

7.3 Targeting the Reference DRO

Given the stability map used to build the ballistic capture, the safest state for a spacecraft is at the geometric center of the stability region, which is generally the periodic reference DRO. We begin the exploration of the cost to stabilize a ballistically captured DRO by building optimal two-impulse transfers from the set of quasi-periodic orbits on the boundary of the stability to the periodic DRO at the center of the map. We build a transfer between any two states using a modified single-shooting differential corrector (SSDC) algorithm designed specifically for DROs, which orbit around the minor body unlike some libration point orbits. This algorithm works by propagating the departure state until the trajectory crosses a plane defined by the z-direction and the vector pointing from the minor body to the target position. This plane is a rotation of the xz-plane about the Moon by a *longitude* given by

$$\lambda = \text{atan}\left(\frac{y}{(1-\mu)-x}\right). \tag{7.51}$$

Using the state transition matrix and the velocity at this plane crossing, a minimum norm correction to the initial velocity is found that attempts to have the transfer's final position match the target position. This process is iterated until the final positions match, and the transfer cost is computed

as

$$J = \|\mathbf{V}_{i^+} - \mathbf{V}_{i^-}\| + \left\|\mathbf{V}_{f^+} - \mathbf{V}_{f^-}\right\| = \Delta V_t, \tag{7.52}$$

where subscript i and f denote the initial and final maneuver, and superscript $-$ and $+$ denote before and after the maneuver. This strategy of stopping propagation when the transfer is at the same longitude as the target has a several advantages. First, through step-control, we can avoid the transfer from being on the wrong side of the minor body. This avoids needing to cross the gravity singularity at the center of the minor body and helps the algorithm's robustness. Second, we no longer need a good initial guess for the transfer's initial state since we are guaranteed to stop at the minimum distance from the target. That said, a good initial guess can reduce the computation time significantly. Third, stopping the transfer at the longitude plane eliminates the transfer time as a design variable. Finally, targeting the longitude makes it a simple task to look at multiple revolution (multi-rev) transfers. Instead of stopping the trajectory at the first longitudinal plane crossing, we can also stop it after an arbitrary number of passes to see if longer, but less expensive transfers exist.

Since each quasi-periodic spans about 31 revolutions of the Moon, it is easy to imagine that the cost function will be riddled with local minima, which can make finding the optimal transfer difficult. To combat this issue, we use a brute force search method that constructs one- and two-rev transfers between 800 states on the quasi-periodic orbit and 25 states along the target periodic DRO. The results from this search on the quasi-periodic DRO formed by $\Delta v_z = 0, \Delta v_x \approx -54$ m/s are shown in Figure 7.7. In this plot, τ_1 represents the normalized time on the quasi-periodic orbit ($\tau_1 = 1 \rightarrow t = 30\pi$ TU). τ_2 is the normalized true anomaly on the periodic DRO. In this example, the quasi-periodic DRO was formed by a velocity perturbation, which we will call ΔV_q for subsequent orbits, of 53.6 m/s. The cost of all the transfers surveyed span between 13.6 m/s up to as much as 700 m/s. As anticipated, the multiple revolutions of the quasi-periodic orbit create a cost function with many hills and valleys. To further isolate the best trajectories from this sweep, we crop all transfers with a cost higher than ΔV_q. Next, we consider only the transfers with costs

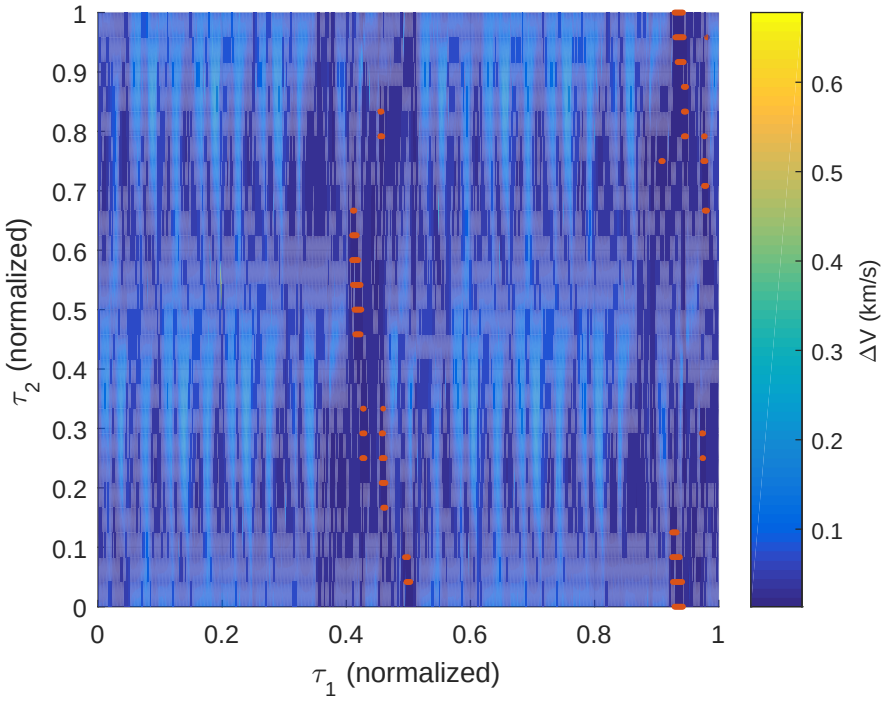

Figure 7.7: The cost of a transfer from a position on the quasi-periodic orbit (τ_1) to a position on the periodic DRO (τ_2).

in the first percentile. These transfers are plotted as red points in Figure 7.7. Even after these stringent reductions, transfers still span several basins of attraction. We isolate the best solution using MATLAB's *MultiStart* object. Each remaining transfer is optimized through the constrained minimization algorithm *fmincon* and the best transfer found for this example cost 13.4 m/s. This is repeated for each quasi-periodic DRO in the set, giving us 50 transfers from around the edge of stability to the reference DRO. Finally, each of the 50 transfers is optimized using primer vector theory algorithms discussed in Section 7.1.5. This improves the cost of the transfers on the order of m/s to mm/s. The example case is plotted in Figure 7.8 and it was improved by 1.43 m/s using primer vector theory, making its final cost 12.0 m/s.

Studying this set of optimal transfers helps identify the types of quasi-periodic DROs that are easy to stabilize. First, regarding transfer time, 42 of the 50 transfers reach their destination in less than one revolution of the Moon. 35 of them perform their final impulse less than 10 days after

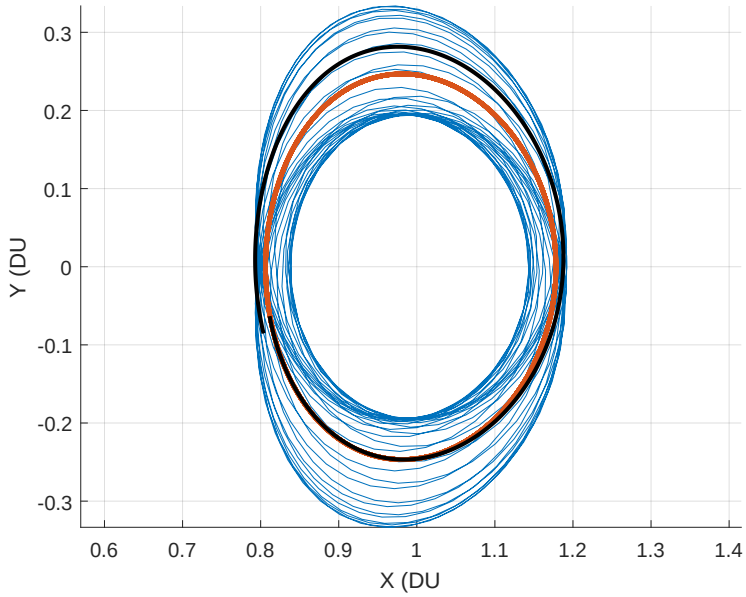

Figure 7.8: The example transfer (black) between the quasi-periodic orbit (blue) and the periodic DRO (red) after being fully optimized. It has a cost of 12.0 m/s.

beginning the transfer. The longest transfer completes nearly two full revolutions before arriving 28.7 days. There is no strong correlation between $\Delta\mathbf{V}_q$ and the transfer duration. Regarding fuel costs, Figure 7.9 graphically compares the cost of transferring to the periodic DRO versus ΔV_q. In this plot, the velocity perturbations on the edge of the stability map are drawn in red. The minimum cost transfers are plotted in blue using the formula

$$\Delta\mathbf{V}_t = \Delta V_t \bullet \frac{\Delta\mathbf{V}_q}{\|\Delta\mathbf{V}_q\|}. \tag{7.53}$$

Note that the blue points only represent magnitude relative to ΔV_q, not the direction of the impulses. It is apparent from Figure 7.9 that the cheapest transfers are those coming from planar quasi-periodic orbits. Orbits with significant out-of-plane motion have transfer costs that approximately equal to the perturbation used to generate the quasi-periodic orbit in the first place. This makes intuitive sense since we are transferring to a planar periodic orbit, so all z-motion must be arrested at an xy-plane crossing. Since the velocity at these plane crossings does not significantly vary, these types of transfers will always be more expensive than planar transfers. There is an obvious advantage for mission designers to target a planar orbit after capture if there are future

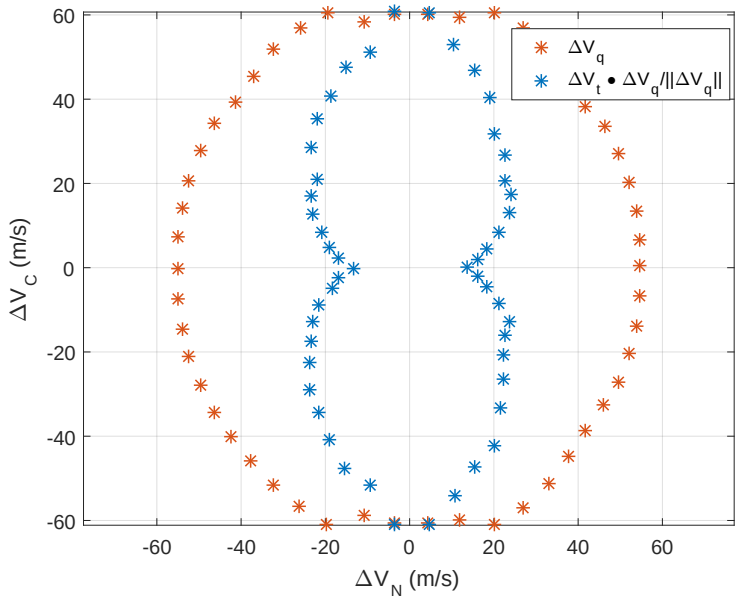

Figure 7.9: The ΔV to transfer to the periodic orbit (blue) compared with the ΔV used to generate the quasi-periodic orbit (red).

plans of stabilizing the orbit.

7.4 Transfers to an Arbitrary DRO

If the mission is not bound to a particular DRO size, significant fuel savings can be achieved when stabilizing an orbit by targeting an arbitrarily sized DRO rather than the reference DRO used to generate the stability map. The simplest way to do this is to perform a single impulsive maneuver that puts the spacecraft onto the periodic DRO that intersects the spacecraft's position. This can only occur at xz-plane crossings, so we begin by propagating each quasi-periodic orbit for 30π TU and identifying each time the z-position changes sign. For these 70,000 km DROs, we generally find about 44 plane crossings. We interpolate across each of these sign changes to identify the exact state when $z = 0$.

From here, we identify the periodic DRO that intersects the same (x, y) coordinates as the quasi-periodic DRO at each plane crossing. This involves finding the combination of DRO size r_0 and true anomaly τ_2 that minimizes the position error. To do so, we start with a coarse uniform

grid search through 10 values of $\tau_2 \in [0, 2\pi)$ and 10 values of $r_0 \in [r_{min}, r_{max}]$. The span depends upon the quasi-periodic orbit. We set r_{min} to 95% of the minimum absolute value x-position across the entire quasi-periodic orbit, and r_{max} to 105% of the maximum absolute value. The values of r_0 and τ_2 that generate the minimum position error are then optimized using MATLAB's constrained minimization algorithm *fmincon* until the position error is driven to zero. The difference between the velocity of the periodic DRO and the quasi-periodic DRO at this plane crossing is the $\Delta\mathbf{V}$ vector for the single-impulse transfer. This is repeated for each xz-plane crossing the quasi-periodic orbit makes, and each impulse is stored. If we look at the smallest impulse from each quasi-periodic DRO, we see the same story that is told in Figure 7.9. Planar quasi-periodic orbits are significantly less expensive, on the order of 10-12 m/s, while those with large z-amplitudes are closer to 60-65 m/s.

These one-impulse transfers are simple to construct, but there is no guarantee that they are optimal. We've shown in Section 7.1.5 how adding additional impulses can reduce the cost of a transfer. Therefore, the next step is to consider two-impulse transfers seeded from the set of one-impulse transfers. To do so, we take the smallest one-impulse transfer ($\Delta\mathbf{V}_1$) from each quasi-periodic DRO and use it to initialize a two-impulse transfer where $t_i = t_f$, $\Delta\mathbf{V}_i = \Delta\mathbf{V}_1$, and $\Delta\mathbf{V}_f = 0$. These transfers are locally optimized using *fmincon* in the same manner as was discussed in Section 7.3. Primer vector theory is applied to the results from *fmincon* to get locally optimal trajectories, but again, we generally see improvement on the order of mm/s or less. Figure 7.10 shows the cost of these optimized trajectories compared to ΔV_q. The results in this plot closely resemble those in Figure 7.9. Nevertheless, we see marginal improvements across all DROs, which are as high as 6.7 m/s and with a mean of 3.0 m/s. The planar quasi-periodic DRO can transfer for 11.5 m/s, and all transfers are now less expensive than their corresponding ΔV_q values.

In summary, we've shown that targeting an arbitrary DRO can reduce the cost of stabilizing a quasi-periodic DRO by several meters per second. Using one-impulse transfers to initialize two-impulse transfers is a quick and effective strategy for building low-cost transfers. A caveat to this is that while targeting an arbitrarily sized periodic DRO in the CR3BP will generally put you at the center of a stability region, this is not guaranteed in a high fidelity model. We've seen several

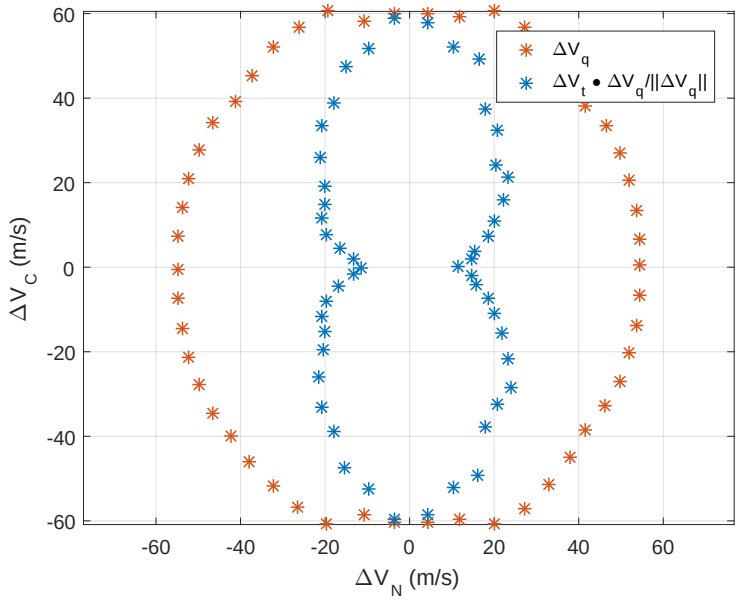

Figure 7.10: The ΔV to transfer to an arbitrary periodic orbit (blue) compared with the ΔV used to generate the quasi-periodic orbit (red).

cases in Chapter 5 and 6 where some neighboring, nearly periodic DRO's can be significantly less stable than the reference DRO.

7.5 Stabilizing Maneuvers

It was mentioned in Chapter 5 that due to the chaotic phase space near the boundary of stability, it is extremely difficult to target a specific point on the stability map. Thus a spacecraft may inadvertently find itself on a quasi-periodic orbit with larger z-amplitude than intended and lack the fuel required to transfer to a periodic DRO. This section explores options for maximizing stability in this limited fuel scenario.

We begin by identifying the periodic DRO that the current quasi-periodic DRO encapsulates. This is done by looking at a Poincaré section of the current orbit on the xz-plane over and finding the mean x-coordinate. As an example, we perturb a 70,000 km DRO by $\Delta V_N = \Delta V_C = 30$ m/s. The mean of the Poincaré section estimates the periodic DRO as 70,801 km. Recall from Chapter 4 that the Monodromy matrix for DROs have two pairs of stable eigenvalues, which give two independent

stable eigenvector directions. One of these eigenvectors lies exclusively in-plane ($v_z = v_{\dot{z}} = 0$) and the other lies exclusively out-of-plane ($v_x = v_y = v_{\dot{x}} = v_{\dot{y}} = 0$). This suggests that these two modes can be changed independently of one another.

Since we are using impulsive maneuvers to stabilize the trajectory, we explore where the trajectory has relatively low position error compared to the reference DRO. To do so, we difference states with the same longitude (see Equation 7.51) on the quasi-periodic orbit and reference DRO rather than relying on timing since the two orbits have different periods. For a single stabilizing maneuver, the location for the impulse should be where the total position error is minimized, or sufficiently small. These minima can occur at any longitude, but are more prevalent near the $\pm y$-axis. Alternatively, if multiple stabilizing maneuvers are allowed, the maneuver to reduce z-motion should be performed when $z = 0$, which occurs several times per orbit as we saw when building the one-impulse transfers discussed in Section 7.4. Then the in-plane mode can be damped when the in-plane position error is minimized at a different time. In our test case, the minimum position error we detect is about 29 km.

Next, we attempt to understand which modes are more important to damp at different longitudes around the orbit. A series of stability maps are built at even intervals around the full reference DRO. The boundary of the stable region is drawn around the reference DRO at each longitude in Figure 7.11. There are many interesting features in this array of stability maps that warrant further study, but for now we are particularly interested in the width and height of the stable zones at different longitudes. At the xz-plane where longitude is 0° and $\pm 180^\circ$, the stability map is about $\pm 55 \times \pm 60$ m/s, so DROs can withstand comparable perturbation magnitudes in both directions. A maneuver that works to damp both modes relatively equally will bring the state closest to the stable zone. At longitudes of $\pm 90^\circ$ where y-position is maximized, the stable regions become notably thinner (± 20 m/s in ΔV_N) and taller (± 109 m/s in ΔV_C). This indicates that if a stabilizing maneuver is being performed in this region, it would be more beneficial to damp the in-plane mode than the out-of-plane mode. The area in between these longitudes can be more difficult to interpret. One issue is that the stability regions are not centered on the reference

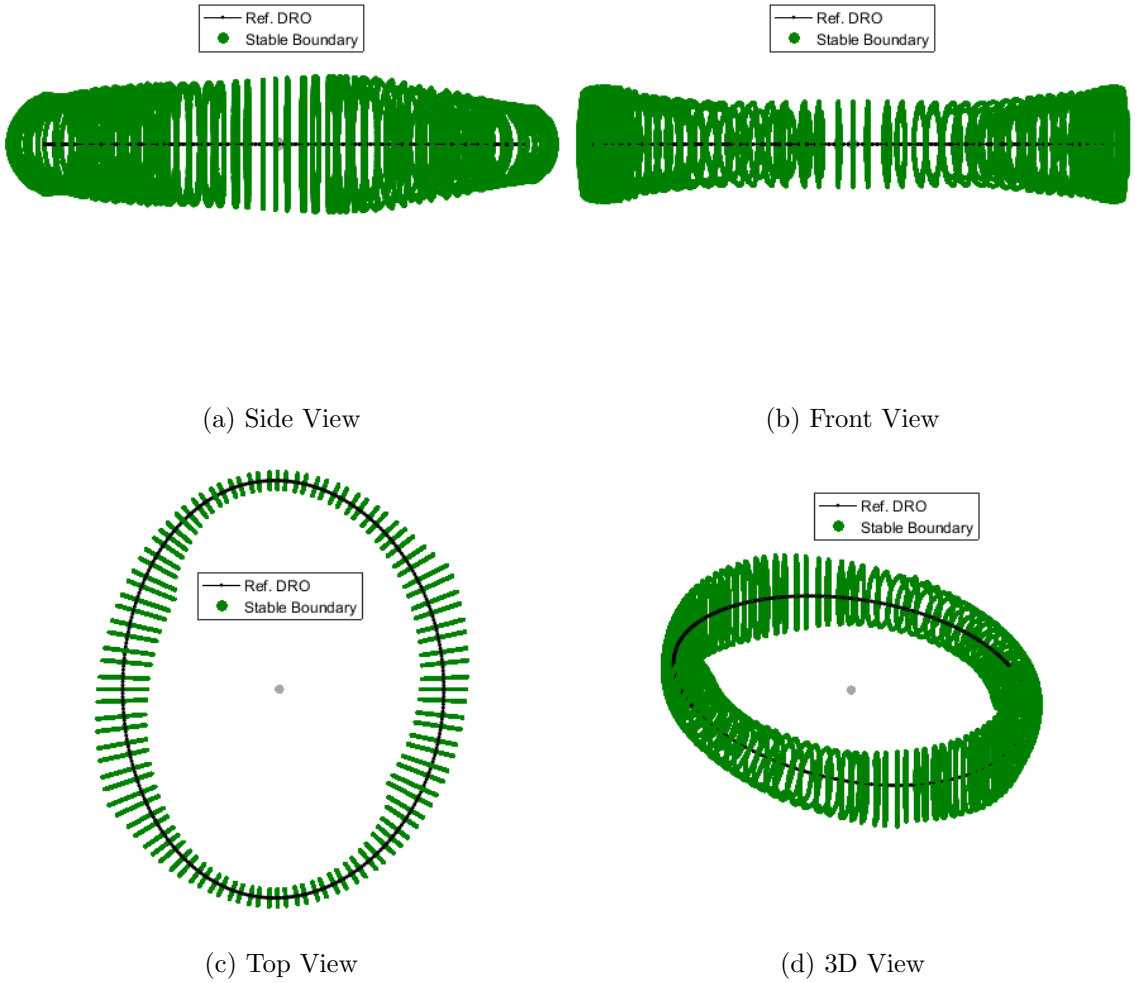

(a) Side View

(b) Front View

(c) Top View

(d) 3D View

Figure 7.11: Stability map boundaries built at various longitudes around the reference DRO. The boundary still represents velocity perturbations, but is drawn on the reference orbit to indicate its origin and longitude.

trajectory, particularly at longitudes of $\pm 45°$ and $\pm 135°$. Therefore, the sign of the velocity error when the impulse is performed can greatly influence the cost to stabilize. Another issue is that the stable regions do not form ellipses and can form extremities and concavities that are difficult to target.

Choosing the impulse to occur where there is a small position error makes initializing the maneuver simple. The vector error of the velocity at this position intersection is computed and

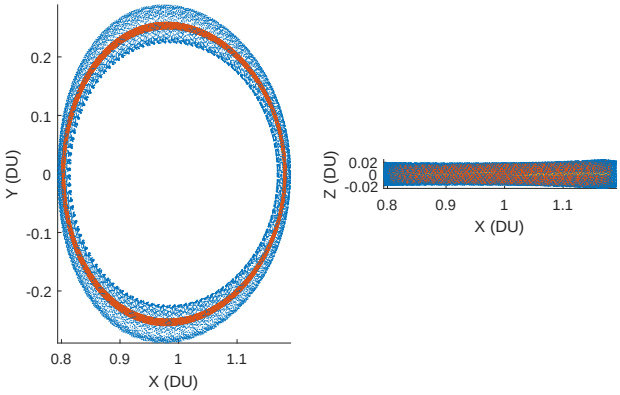

Figure 7.12: A quasi-periodic orbit before (blue) and after (red) an optimal stabilizing impulse.

the impulse is applied in the opposite direction. Then *fmincon* is used to optimize the direction of an impulse with a constrained maximum amplitude. This optimization routine adds the best estimate for the optimal impulse to the state, propagates the trajectory for 100π TU, and then computes the cost. The cost function evaluates the y-coordinates every time the trajectory crosses a longitude of $\pm 90°$ and computes the range of y-values. This is also repeated for x-coordinates at xz-plane crossings. This calculation measures the x- and y-amplitude variations at these plane crossings, which is minimized when a periodic orbit has been reached. The out-of-plane amplitudes are minimized by adding double the maximum z-coordinate found in the trajectory. For an impulse with a maximum magnitude of 10 m/s, the resulting trajectory is shown in Figure 7.12. The impulse heavily reduced oscillations in the in-plane mode and marginally reduced the out-of-plane mode. The optimal thrust direction was changed by about 57°, likely to focus on reduction of in-plane amplitudes.

It should be noted that several other methods were attempted to initialize the impulse. One strategy was uncovered by Pavlak and Howell who discovered that for NASA's ARTEMIS mission, every one of the 60+ trajectory correction maneuvers were in close alignment with the stable eigenvector from the Monodromy matrix.[97] Using the reference DRO, we generated the two stable eigenvectors and shifted them through longitude using the state transition matrix to the point of the impulse. Taking the real part of these vectors gives an initial thrust direction estimate that is

63° away from the optimal thrust, which is quite similar to our heuristic initial guess, but much larger than the pointing errors Pavlak reports. Another attempt was made using the local stability conditions discussed in Section 4.2, where we showed that a CR3BP trajectory always has at least one unstable eigenvalue of the Jacobian. We evaluate the Jacobian at the point of the impulse and use the eigenvector associated with the stable eigenvalue (the one with the smallest real part) as an initial guess. This vector is only 43° away from the optimal direction in this particular test case, which is the best seen so far. These other methods have not been explored to any degree that would allow us to draw conclusions, but there is potential for a method to produce decent initial guesses which are sufficient for finding optimized impulses.

This brief study builds transfers in the CR3BP to stabilize a trajectory. Note that in high fidelity models BCTs tend to naturally decrease their amplitudes over time by design. This can make a stabilizing transfer cheaper, but waiting also increases the risk of unanticipated dynamical effects causing an early departure from the DRO. It is also important to remember that BCTs exist near the boundary of stability for a reference trajectory. Therefore, even a small maneuver in the proper direction can greatly increase the duration they remain around the minor body.

Chapter 8

Long Duration Stability of Distant Retrograde Orbits

Once a spacecraft has successfully entered a stable DRO, as defined by the stability maps, the next point of interest is studying how long it will remain there. Drawing upon the insight gained from Section 4.4 about stable DRO sizes, we study the long duration evolution of stable DROs. This chapter considers high fidelity DROs in the Earth-Moon system propagated for up to 30,000 years using numeric methods to increase precision and maximize the accuracy of the results. The goal of this chapter is to determine the maximum duration a DRO remains bound to the Moon up to a maximum of 30,000 years. It considers perturbing forces that, while minute, form repeating geometry that can lead to secular effects on the DRO. We explore how, when, and why DROs experience relatively rapid changes in amplitudes and when those cause the DRO to become unstable.

8.1 Conventions and Nomenclature

This chapter focuses on the Earth-Moon three-body system. It makes frequent references to DROs in the *synodic frame*, which refers to the Earth-Moon rotating, pulsating frame. In this coordinate frame, the x-axis points from the center of the Earth to the center of the Moon, the z-axis is aligned with the Moon's instantaneous angular momentum vector, and the y-axis completes the orthonormal coordinate system. Any amplitude that is described in this chapter references this coordinate system centered on the Moon. For example, z-amplitude refers to the peak distance the DRO travels out of the Moon's orbit plane and x-amplitude refers to peak distance from the

Moon projected onto the Earth-Moon line. When a DRO is referred to by its size, that value is the distance between the initial condition of the orbit and the Moon. This generally corresponds with the DRO's initial x-amplitude. All DROs discussed in this chapter begin at the $y = 0$ plane on the far side of the Moon.

In this chapter, references to a DRO's stability refers to Lagrange stability. An orbit is considered stable if it remains within a bound distance from the Moon (384,000 km), for the duration under investigation. A DRO is considered unstable if it ever leaves this bounding sphere or impacts the lunar surface.

8.2 DRO Selection

Recall from Section 4.4 that DROs in the Earth-Moon system fall into stable bands separated by unstable regions based on their size and amplitude of motion out of the Moon's orbit plane (z-amplitude). Figure 4.11 shows examples of inclined (1D) stability maps across different true anomalies for the Moon at the epoch. The red line on each map shows the CR3BP solution, which has good agreement with most of the high fidelity dynamical model. The average of 28 stability maps spanning a single sidereal lunar period is shown in Figure 4.12. This figure is duplicated below in Figure 8.1 for convenience. This map highlights the regions that remain stable regardless of lunar true anomaly, and will be the basis for selecting DROs for this analysis. There are four primary regions where a DRO is stable for at least 100 years. Table 8.1 lists the boundaries of each region and the selected DRO used in this study and Figure 8.2 shows a few periods of each selected DROs in the Earth-Moon rotating frame.

Region	**Size Bounds**	**Selected Orbit**
A	$< 36,500$ km	36,000 km
B	39,000 - 46,000 km	45,000 km
C	61,000 - 65,000 km	62,500 km
D	66,000 - 68,000 km	67,000 km

Table 8.1: A list of the size bands where DROs remain stable for more than 100 years. The orbit selected from each band is listed in the third column.

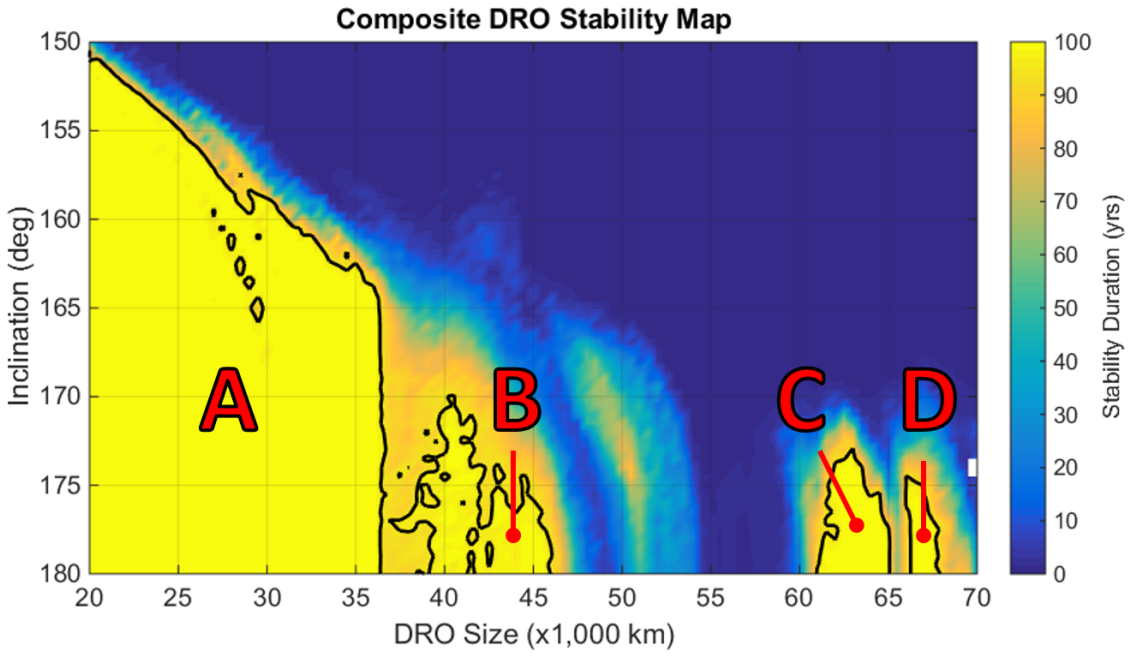

Figure 8.1: The mean of 28 inclined DRO stability maps spanning the lunar period.

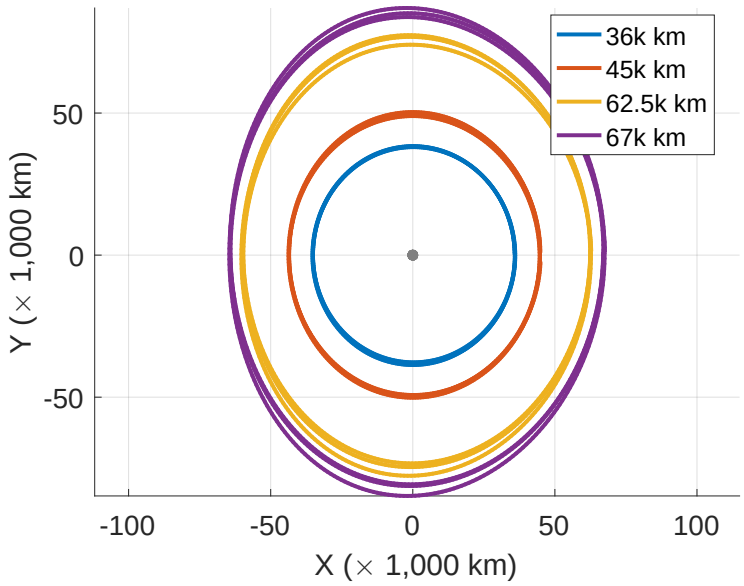

Figure 8.2: The selected DROs plotted in the Earth-Moon rotating frame for three periods.

8.3 Orbit Propagation

8.3.1 Mitigating Numerical Errors

Accurate numerical integration over long durations can be challenging on modern computers due to the limitations of using double precision floating-point arithmetic. Computers approximate

real numbers with a floating point number, which is a binary representation defined by the IEEE 754 standard. Double precision numbers use 64 binary bits, which are divided into two groups: the mantissa and the exponent. Figure 8.3 shows that 52 bits are used in the mantissa and 11 bits are used in the exponent for a double-precision number. Any floating point number can be written in the form in Equation 8.1.[48]

$$x = (-1)^s \left(d_0 + \frac{d_1}{\beta} + \frac{d_2}{\beta^2} + \ldots + \frac{d_{p-1}}{\beta^{p-1}} \right) \times \beta^e \tag{8.1}$$

where β is the base (or radix) and the string of base-β digits d_i make the mantissa. Each digit d_i has a range of $0 \leq d_i \leq \beta - 1$. Most computers use $\beta = 2$, or binary arithmetic. The number represented by e is called the exponent, and s is a single bit reserved to determine the sign of the number being stored.

The error when converting a real number to a binary representation with a finite number of bits is known as round-off error. Double precision numbers have an upper limit on round-off error of 2.22×10^{-16}, which is known as machine precision. This indicates that about 16 significant digits can be stored in a double precision number and computations that affect higher significant digits are not accurately represented. The numerical accuracy of a series of floating-point operations gradually diminishes. Furthermore, machine precision represents the smallest difference between two numbers that can be recognized by a computer. Difference calculations are used to compute error in most explicit integrators, meaning that the error tolerance is capped at machine precision. It often needs to be larger ($\approx 10^{-14}$) in practice to keep the step-size large enough to avoid significant accumulation of round-off error.

Truncation error is another error source that can accumulate while numerically integrating. Most numeric integration methods, such as Runge Kutta methods, were created using a truncated Taylor series approximation. Because the series was truncated, there is an associated error term, the order of which depends on the order of the method chosen. There is truncation error associated with every time-step the integrator takes, meaning new error is constantly being added. Error from previous steps can be amplified by the propagation as well. In integration schemes with tight

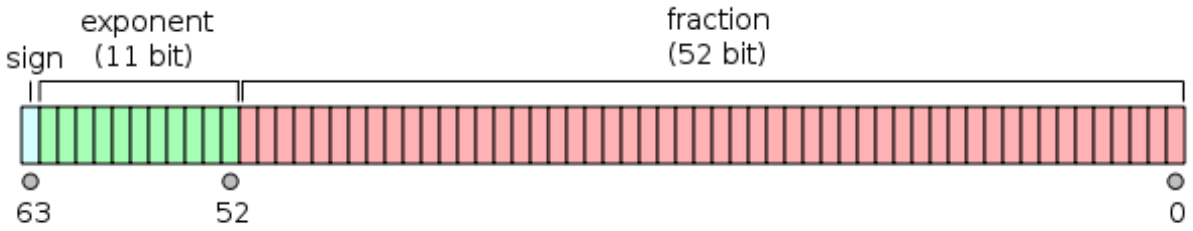

Figure 8.3: A graphical representation of the division of bits between the mantissa (fraction) and the exponent for IEEE 754 double-precision format.[48] Image retrieved from www.wikipedia.org.

error tolerances, the integrator takes smaller steps, which reduces truncation error. However, this increases the number of calculations performed, which increases the accumulation of round-off error.

Many orbit propagation problems integrate a trajectory on a time scale of days to years. With the exception of chaotic systems, double-precision is usually sufficient to provide accurate integration since there are not enough calculations to accumulate a significant amount of round-off and tight tolerances can prevent truncation error. However, this study requires accurate orbit propagation over a period of 30,000 years, which corresponds to over 401,300 orbits of the Earth, 876,000 orbits around the Moon for the 67,000 km DRO and over 1.9 million orbits of the Moon for the 36,000 km DRO. The only reliable way to conduct this propagation is to use a number format with more numerical precision than is available with double precision. The next standard format is quadruple precision, but unfortunately, most central processing units (CPUs) in computers do not support this data type. Therefore, a numerical representation can be used to enhance the precision of double precision numbers used in the computation. This can be achieved on a software level through a class of methods known as variable precision arithmetic (VPA). The terms arbitrary, multiple, and infinite precision arithmetic are synonymous with VPA.

This work uses a VPA method called double-double arithmetic (DDA), which is capable of boosting the precision of a number to about 32 significant digits. This technique stores a number X as an unevaluated sum of two double precision numbers $X = A + B$ where the 53-bit mantissas of A and B create a 106-bit mantissa for X. For example, $A = 1.234...$ and $B = 1.234... \times 10^{-16}$ span adjacent, non-overlapping bits. Table 8.2 shows a comparison of the machine precision

Name	Size (bits)	Machine Precision
Double	64	2.22×10^{-16}
DDA	128	1.23×10^{-32}
Quadruple	128	1.93×10^{-34}

Table 8.2: A comparison between double, double-double arithmetic (DDA), and quadruple precision.

between the standardized double and quadruple precision along with the precision achievable by DDA. Quadruple and DDA numbers use the same amount of memory, but have different machine precision values because quadruple precision uses a 113-bit mantissa. Many software libraries exist that enable the use of DDA based on the algorithms created by Dekker,[31] Knuth,[67] Priest,[102] and Shewchuk.[118] Each arithmetic operation is replaced by a series of calculations on the two double precision numbers. For example, adding two DDA numbers together uses 20 fixed-point arithmetic (FPA) operations. Therefore, using enhanced precision via DDA results in arithmetic taking approximately 10 to 25 times longer to compute depending on the operation. Using DDA allowed for tighter error tolerances within the integrator, which minimizes truncation error, and eliminates noticeable round-off error accumulation.

8.3.2 The Integrator

This study uses an explicit, variable step, 7(8)th order Runge Kutta (RK78) integrator to propagate the orbits. While a symplectic integrator would be ideal for long duration orbit propagations, the derivative function includes important dissipative forces, which are discussed in detail in Section 8.3.3. The relative error tolerances are set to 10^{-20}, over a million times better than the most stringent tolerance allowed by a double precision integrator. The DDA math library published by Kieth Briggs* is used throughout the integrator and the derivative function. Twelve states per year are written to a file, or one point every 30.4 days of integration time. At these error tolerances, the integrator takes about 1500 steps for the 36,000 km DRO, and 560 steps for the 67,000 km DRO in the 30.4 day window between recorded states. Initial conditions for each DRO

* Obtained December 2014 from https://boutell.com/fracster-src/doubledouble/doubledouble.html

Table 8.3: The energy drift comparison between a DDA and a double precision integrator.

	Double	DDA
ΔE (km^2/s^2)	6.45×10^{-11}	-1.13×10^{-13}
ΔR (km)	1.71×10^{-5}	-2.99×10^{-8}
ΔV (km/s)	1.75×10^{-10}	-3.07×10^{-13}

size are computed in the year 13,000 BC using the methods described by Bezrouk and Parker.[16] The DROs are integrated for 30,000 years, but allowed to stop prematurely if the trajectory departs or impacts the Moon.

To verify that the improved precision of DDA increases the accuracy of an orbit propagation, we compare the energy drift in a two-body propagation as compared to a double precision explicit RK78 integrator using a relative tolerance of 1×10^{-13}. This propagation considers a 36,000 km circular orbit around the Moon for 30,000 years. In both integrators, the energy drift was linear. Table 8.3 compares the results between the two levels of precision. It shows the energy error (ΔE), and the initial position or velocity error (ΔR and ΔV, respectively) that would cause this energy shift according to Equation 8.2 where R_1 is 36,000 km, $V_1 = \sqrt{\mu_{\leftmoon} / R_1}$ and $\mu_{\leftmoon}$ is the gravitational parameter of the Moon.

$$\begin{aligned} \Delta E &= \left(\frac{V_2^2}{2} - \frac{\mu_{\leftmoon}}{R_2}\right) - \left(\frac{V_1^2}{2} - \frac{\mu_{\leftmoon}}{R_1}\right) \\ \Delta R &= R_1 \left(\frac{\mu_{\leftmoon}}{\mu_{\leftmoon} - R_1 \Delta E} - 1\right) \\ \Delta V &= \sqrt{V_1^2 + 2\Delta E} - V_1 \end{aligned} \tag{8.2}$$

The DDA integrator is about 600 times more accurate than the double precision integrator. The reason it is not seven orders of magnitude smaller, as the error tolerances are, is because the smaller error tolerance forces the integrator to take smaller time steps, resulting in a larger accumulation of truncation error instead of round-off error. Nevertheless, the DDA integrator's error amounts to sub-millimeter level position error after 30,000 years.

8.3.3 High-Fidelity Dynamical Model

The use of of DDA allows otherwise unobtainable levels of fidelity when propagating DROs. First, the increased precision allows the dynamical model to use the solar-system barycenter as the center of integration for the entire simulation. This minimizes any errors associated with integrating in pseudo-inertial frames like Moon- or Earth-centered inertial. It also removes the need to switch between centers of integration as the object enters or leaves a body's sphere of influence. Second, the increased precision allows us to account for accelerations that are up to 32 orders of magnitude smaller than the largest acceleration as opposed to 16 orders of magnitude available with double precision. Because DROs are such large orbits, small perturbations like aspherical gravity perturbations fall beyond the range of double precision, but can have a significant effect over long periods due to their repeating geometry.

The dynamical model accounts for the gravity from the Moon, the eight planets, and the Sun. The positions for these bodies are obtained from the Jet Propulsion Laboratory's Development Ephemeris DE431. DE431 provides states for over 30,000 years, spanning 13,200 BC to 17,191 AD. The four inner planets have sub-kilometer accuracy, Jupiter and Saturn are within tens of kilometers, and Uranus and Neptune are accurate within several thousand kilometers.[40] Because the solar-system barycenter is used as the center of integration, the gravitational acceleration from each body can be computed directly without the need for third-body perturbation formulations.

A cannonball model is used to model solar radiation pressure (SRP). The reflectance coefficient C_R was set to an initial value of 1.5 ($C_{R,0}$) and exponentially decays, asymptotically approaching a value of 1.1 ($C_{R,f}$) with a time constant τ of 10 years, as shown in Equation 8.3.

$$C_R(t) = (C_{R,0} - C_{R,f})e^{-(t-t_0)/\tau} + C_{R,f} \tag{8.3}$$

An area-to-mass ratio of 0.003 m^2/kg is used for SRP calculations. These values are representative of a common satellite, and would change drastically when considering an asteroid in these DROs. Eclipse periods are not accounted due to infrequent occurrence and short durations. It is important to include SRP because it directly offsets solar gravity, which is a large destabilizing force for DROs

in the Earth-Moon system.[15,16] The acceleration due to solar radiation pressure is:[123]

$$\ddot{\mathbf{r}} = pC_R \frac{A}{m} \frac{\mathbf{r}_\odot}{\|\mathbf{r}_\odot\|}, \tag{8.4}$$

where

$$p = p_\oplus \frac{149,597,870 \text{ km}^2}{\|r_\odot\|^2} \tag{8.5}$$

$$p_\oplus = \frac{1,358 \text{ W/m}^2}{c}. \tag{8.6}$$

In these equations, A/m is the area-to-mass ratio of the spacecraft, $\mathbf{r}_\odot$ is the vector from the center of the sun to the spacecraft, c is the speed of light. Variations in solar flux due to the sun's 11 year solar cycle and other periodic effects were not modeled.

A spherical harmonic potential model is included to account for aspherical gravity from both the Earth and the Moon, as discussed in Section 2.5.1. Though the DROs orbit far from the Moon, the fact that the Moon is tidally locked means that its orientation is approximately fixed in the rotating frame. The DRO's geometry is quasi-periodic in this frame, meaning the spacecraft will encounter the same perturbations at the similar points in its orbit. While the accelerations from aspherical gravity are small, especially for spacecraft orbiting as high as DROs, these repeating accelerations have the potential to accumulate over centuries or millennia to create secular changes in the DRO. While the Earth does not have this same resonant geometry in its static geopotential model, solid tides caused by the Moon can form a resonant geometry, which is discussed later. Additionally, zonal harmonics from the Earth can have a secular effect on the DROs since they are not equatorial with respect to the Earth.

The gravity field for the Earth and Moon are modeled with a Cartesian potential function. The acceleration is computed with Gottlieb's algorithm,[45] using a recursively defined, normalized, derived Legendre function.[79] Spherical harmonic coefficients come from the Joint Gravity Model 3 (JGM-3) and the LP150Q gravity model for the Earth and Moon, respectively. Coefficients up to degree and order six are used in the simulation as a balance between accuracy and computation time. The Moon's orientation is computed from the Lunar Libration angles given by the DE431

ephemeris. The Earth's orientation is computed with the IAU-76/FK5 Reduction algorithm,[123] where polar motion is not included due to unpredictability and small impact.

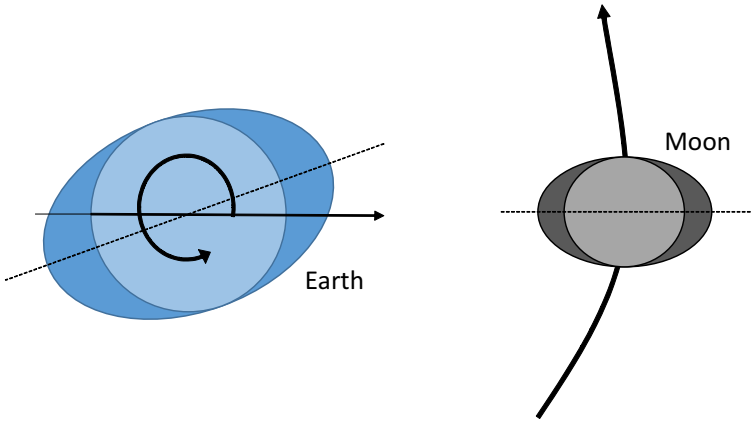

Figure 8.4: An illustration of the consistent geometry of the Earth and Moon's solid tides in the rotating frame.

Solid tides on the Earth due to the Moon are included because of their resonant geometry with DROs, as mentioned before. Because the Earth spins faster than the Moon, the raised solid mass always leads the Moon in its orbit. While this solid tide constantly shifts along the surface of the Earth, its leading angle will be relatively consistent in the Earth-Moon rotating frame, as illustrated in Figure 8.4. Again, the spacecraft in the DRO will encounter the same perturbing accelerations at the same points in its orbit, resulting in a compounding effect. The solid tides due to the Sun do not have this same effect, but they are trivial to add and are included in the model. Due to the tidal lock, solid tides on the Moon due to the Earth do not move much on the Moon's surface and are often modeled as part of the static spherical harmonic coefficients. This is also shown in Figure 8.4. The solid tides on the Earth are modeled as a correction to the spherical harmonic coefficients through degree and order four using Equation 8.7 and 8.8 based on the equations and Love numbers $k_{n,m}$ provided in the International Earth Rotation Service's (IERS) 2010 Conventions.[99]

$$\Delta\bar{C}_{n,m} - i\Delta\bar{S}_{n,m} = \frac{k_{n,m}}{2n+1}\sum_{j=2}^{3}\frac{GM_j}{GM_\oplus}\left(\frac{R_e}{r_j}\right)^{n+1}\bar{P}_{n,m}[\sin(\phi_j)]e^{-im\lambda_j} \text{ for } n \in \{2,3\} \tag{8.7}$$

In this equation, ϕ_j and λ_j are the latitude and longitude of the tide-raising body, R_e is the

equatorial radius of the Earth, r_j is the distance of the tide raising body from the Earth, and GM_j is the standard gravitational parameter of body j. For $n = 4$, we use

$$\Delta\bar{C}_{4,m} - i\Delta\bar{S}_{4,m} = \frac{k_{2,m}^{(+)}}{5} \sum_{j=2}^{3} \frac{GM_j}{GM_\oplus} \left(\frac{R_e}{r_j}\right)^3 \bar{P}_{2,m}[\sin(\phi_j)] e^{-im\lambda_j} \text{ for } n = 4,\ m \in \{0, 1, 2\}. \quad (8.8)$$

8.4 Long Duration Evolution

As discussed in Section 8.2, four DROs are propagated, representing the four identified stable regions, and we track the evolution of four parameters for each of these trajectories. Three of these parameters are the x, y, and z amplitudes with respect to the Moon when viewing the trajectory in the rotating frame. To track the evolution of these parameters, the propagated states are grouped into bins spanning 1-10 years depending on the duration the DRO remained stable. The z-amplitude is computed by looking for the maximum out-of-plane distance achieved by any data point in each bin. To calculate the x and y- amplitudes, an exterior bounding ellipse (EBE) is fit to the data in each bin. The EBE has a minimized area while containing all of the bin's data, the same as the minimum bounding ellipse from Section 6.4.4. When calculating the EBE, its center is allowed to translate in x and y-directions, and the semi-major axis is constrained to be in the $\pm y$-direction. The semi-major and semi-minor axes lengths are also degrees of freedom in the fitting process. Because DROs are quasi-periodic in a realistic dynamical model, we expect variations in these amplitudes from orbit to orbit. This variation is captured by constructing an interior bounding ellipse (IBE), which has a maximized area, but excludes all data from the bin. The IBE has its center fixed at the optimal center found by the EBE, and its semi-major axis is constrained to lie in the x or y-direction. Figure 8.5 shows the EBE and IBE for a set of data points from the propagation of the 36,000 km DRO.

The fourth parameter is the instantaneous period of the DRO, which is computed by taking a state from the high-fidelity integration every 1 to 5 years (depending on the stability duration) and propagating it in a simpler dynamical model. We look for three crossings of the xz-plane, and record the period as the time between the first and third crossing. Because states are recorded

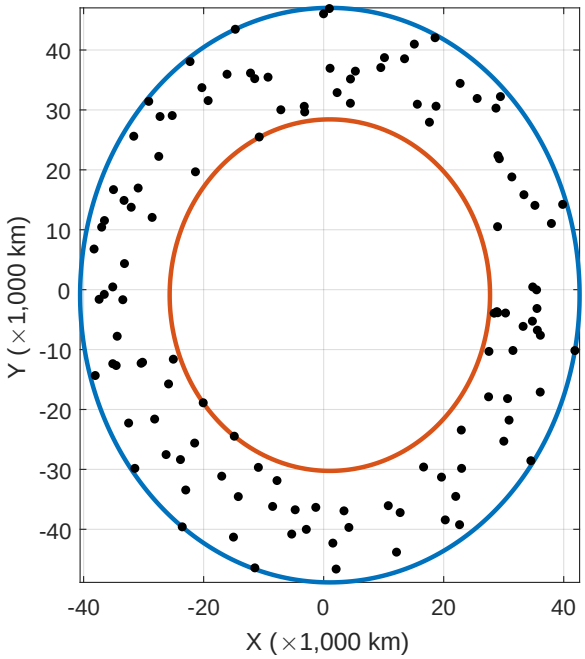

Figure 8.5: The exterior and interior bounding ellipses for 10 years of stored states from the 36,000 km DRO.

every 30.4 days and an Earth-Moon DRO must have a period less than the Moon's period (27.3 days), every recorded state is guaranteed to be on a different orbit. Plots for these four parameters are shown for each DRO in this section. In the following sections, we show the period evolution with reference to resonant frequencies that help explain the behavior. We track whole number ratios of the Moon's sidereal period, which captures effects of the lunar orbit's ellipticity, and its synodic period, which is the frequency at which the oscillation in solar gravity.

We examined two ways in which DROs can become unstable and depart the Moon.[15] The first is an in-plane mode, which has been examined several places in the literature. This mode involves a DRO evolving from a quasi-periodic orbit into a period-3 orbit, sometimes called a Bounding Unstable Periodic Orbit (BUPO), which bounds the stable region on a Poincaré map.[116] This mode can be tracked comparing the relative sizes of the EBE and IBEs since they share the same center and have their axes aligned. The second mode is an out-of-plane mode where the forces cause a growth in z-amplitude and typically a reduction in the x and y-amplitudes. Eventually, the orbit crosses the stable boundary in Figure 8.1 and departs the Moon. While both of these modes

can be expressed in a DRO, one is often the obvious cause for instability.

8.4.1 The 36,000 km DRO

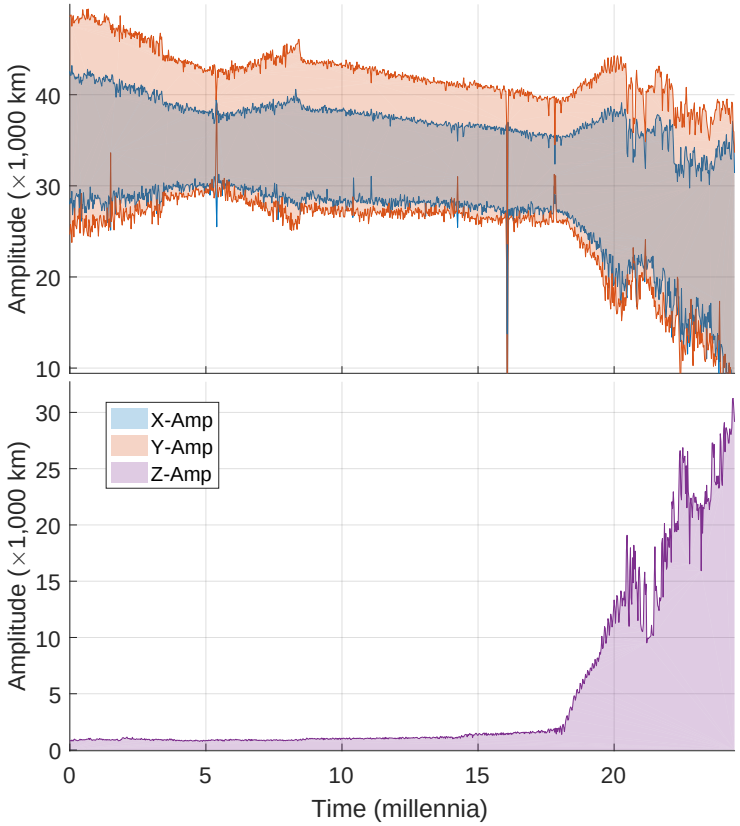

Figure 8.6: The evolution of the x, y, and z-amplitudes of the 36,000 km DRO.

The amplitude history of the 36,000 km DRO is shown in Figure 8.6, and its period history is shown in Figure 8.7. For the first 6,000 years, we observe a damping of the in-plane mode as the variations in x and y-amplitudes decrease. The exterior amplitudes decay more rapidly than the interior ones, meaning the average size of the orbit is decreasing. This causes the period to linearly decay over this interval. At 6,000 years, the period reaches a 5:1 resonance with the lunar sidereal period. An excitation of the in-plane mode is observed as the exterior x and y-amplitudes grow while the interior amplitudes shrink at comparable rates. The average size of the orbit remains the same, which causes the period to remain near this resonance. This tendency to "stick" near a

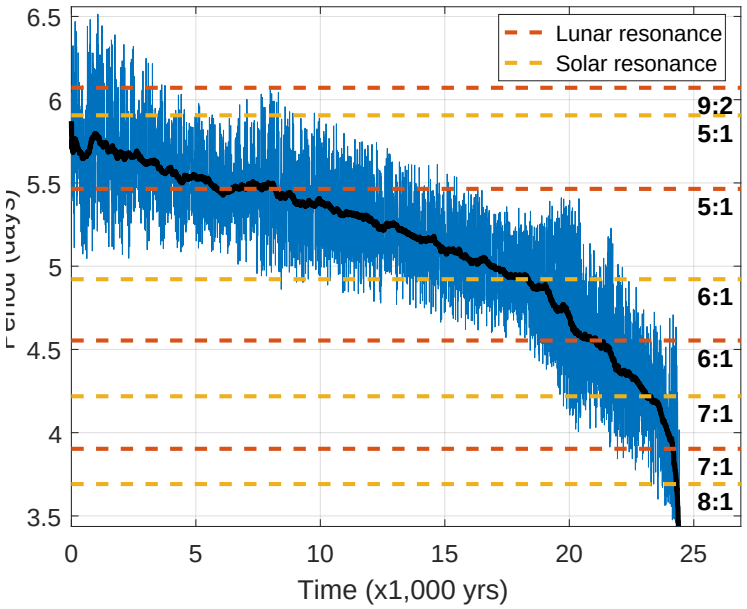

Figure 8.7: The evolution of the period of the 36,000 km DRO.

particular resonance is a common feature in chaotic systems.[84]

About 8,000 years into the propagation, the DRO's x and y-amplitudes begin to decay again after breaking from the sticky resonance. This continues linearly for the next 12,000 years. Note that the data amplitude spike at about 16,000 years is simply an artifact of the DRO being in a 6:1 resonance with the data collection period (1 point every 30.4 days), and is not indicative of strange behavior. At 17,500 years into the simulation, the period has decayed into a 6:1 resonance with the Sun (the Moon's synodic period) and sticks there for about 900 years before resuming its decay. This resonance excites the out-of-plane mode, causing the z-amplitude to grow at a relatively rapid rate of 7 km per year, which continues after the period begins decaying again. Meanwhile, the variations between interior and exterior x and y-amplitudes grow and the mean size of the orbit shrinks. The period decays at an accelerating rate with several sticky resonances occurring along the way, including the 6:1 resonance with the lunar period which coincides a temporary decrease in the z-amplitude, a damping of the out-of-plane mode.

After 24,450 years, the orbit becomes unstable and departs the Moon. During its lifetime, the DRO's average period decays from 5.9 to 4.2 days. The z-amplitude reaches nearly 30,000 km,

causing the DRO to consistently pass over latitudes of 40° and achieve a maximum of 70°. These latitudes are well above the solid tidal bulge on the Moon, meaning this dynamic effect is not being consistently encountered. The z-amplitude eventually exceeds the stable boundary, resulting in an out-of-plane mode. The Sun's gravity has the largest contribution to out-of-plane acceleration and its resonances correspond with z-amplitude growth, so it likely the cause of the instability.

8.4.2 The 45,000 km DRO

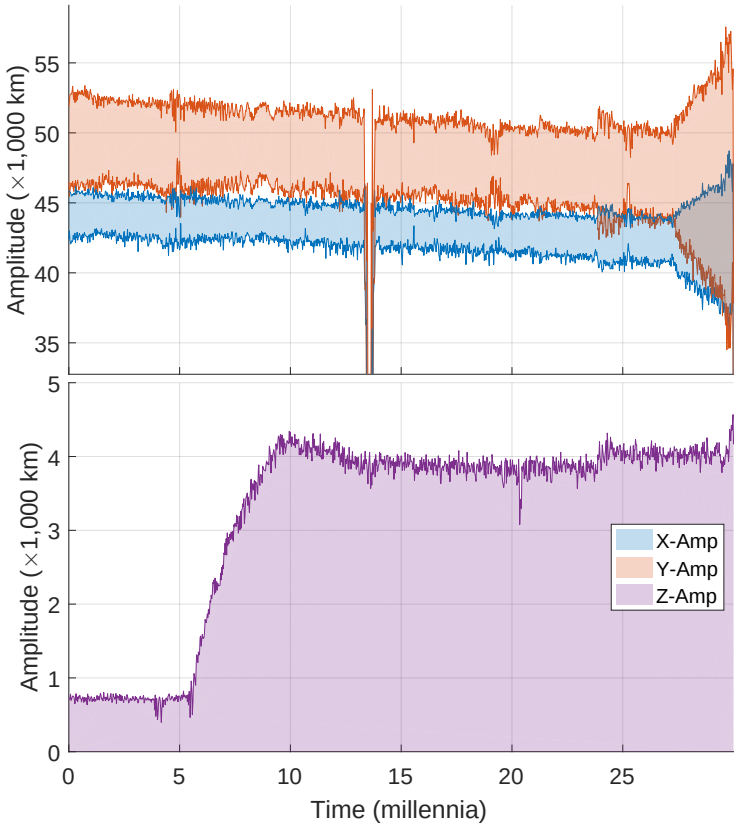

Figure 8.8: The evolution of the x, y, and z amplitudes of the 45,000 km DRO.

The 45,000 km DRO is the only examined orbit that remained stable for the entire 30,000 year integration period. Amplitude results from this integration are shown in Figure 8.8 and period results are in Figure 8.9. This DRO begins with a period of 7.8 days, which is near the 7:2 resonance with the lunar sidereal period. Contrary to the 36,000 km DRO however, this DRO does

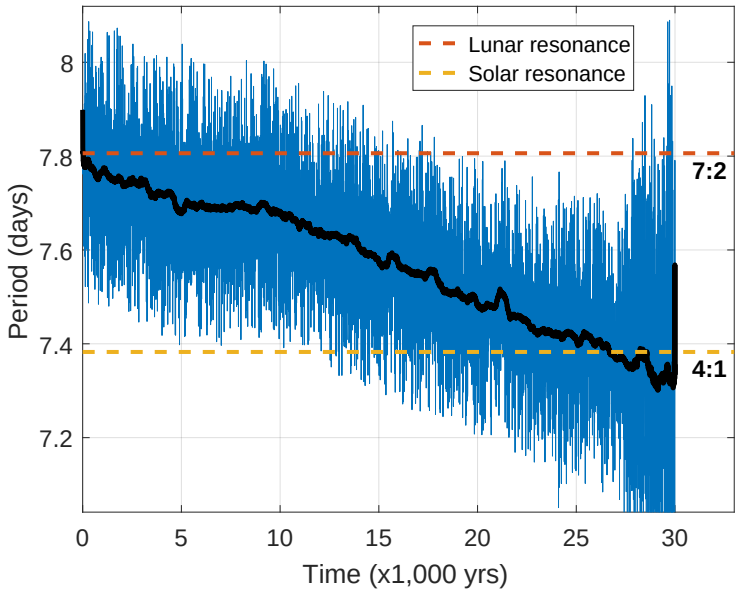

Figure 8.9: The evolution of the period of the 45,000 km DRO.

not stick at this resonance and immediately begins decaying in size at a rate of about 100 meters per millennium. As the orbit shrinks, the period also decays.

At 5,500 years, the period levels off and remains at a constant 7.7 days for about 4,000 years. At the same time, the z-amplitude grows relatively quickly at about 800 m/yr. It stops growing when the period begins decaying again at about 10,000 years and remains around 4,000 km for the rest of the simulation. This z-amplitude results in the DRO passing over $\pm 6.3^\circ$ latitude on the lunar surface, meaning it still consistently flies over the Moon's solid tide bulge. This period exhibits the same sticky resonance behavior we see repeatedly in the 36,000 km DRO, but it is far removed from the resonances we track. We suspect that Jupiter's gravity may be responsible for the behavior, so we run the 45,000 km DRO again in two cases: one without Jupiter's gravity, and one where Jupiter's gravity is doubled when acting on the spacecraft. In the former case, the period does not level off at this same location, but the z-amplitude still grows, beginning at the same time as the original case. The scenario with doubled gravity from Jupiter has more jagged period evolution, which appears to decay at a slower rate from 3,000-6,000 years, but does not hold constant. During this time, the z-amplitude grows at a rate of 1.2 km/yr. This indicates that

Jupiter contributes to, but is not solely responsible for the behavior we see from 4,000-10,000 years.

At 13,000 years, we have another artifact of the DRO period being in a 4:1 resonance with the data collection frequency. Near 26,800 years into the simulation, the period decays into the 4:1 resonance with the Sun. This is the precursor to large growth in the variations in x and y-amplitude that continue until the propagation completes at 30,000 years. The z-amplitude remains unperturbed while this occurs, but the y-amplitude spans 35,000 - 57,000 km by this time. The IBE indicates that the DRO is beginning to cross the boundary of stability region B in Figure 8.1. It is unclear whether this amplitude variation growth will continue beyond the integration period. The DRO could decay into region A, or become unstable due to the in-plane mode. Regardless, the 45,000 km DRO is stable for at least 30,000 years. Contrary to the evolution of the 36,000 km DRO, this DRO still largely resembles the original orbit after the integration albeit smaller and with more out-of-plane motion.

8.4.3 The 62,500 km DRO

The 62,500 km DRO is a much larger orbit than the previous two DROs, and it's response differs from the smaller DROs. The amplitude history for the 62,500 km DRO is shown in Figure 8.10 and its period history is in Figure 8.11 below. Unlike the previous two smaller DROs the 62,500 km DRO remains about the same size for its stable duration. The 62,500 km DRO lies exclusively outside of the Moon's Hill sphere, whereas the 36,000 km and 45,000 km DROs lay completely within the Hill sphere, indicating that the Moon's solid tide and aspherical gravity field are the cause of the decay of the smaller DROs. Section 8.5 investigates this hypothesis. For 6,000 years, we observe slow exponential growth in the variations in x and y-amplitude before the orbit suddenly departs the Moon. The z-amplitude between shows high variability from year to year, suggesting the out-of-plane motion pulses on the order of years to decades. In this time frame, the the out-of-plane motion oscillates between planar and 1,000 km amplitude every few decades.

Because the DRO is not shrinking, the average period does not have a secular trend like smaller DROs. Over its lifetime, the average period varies by about ± 21.6 hours from its starting

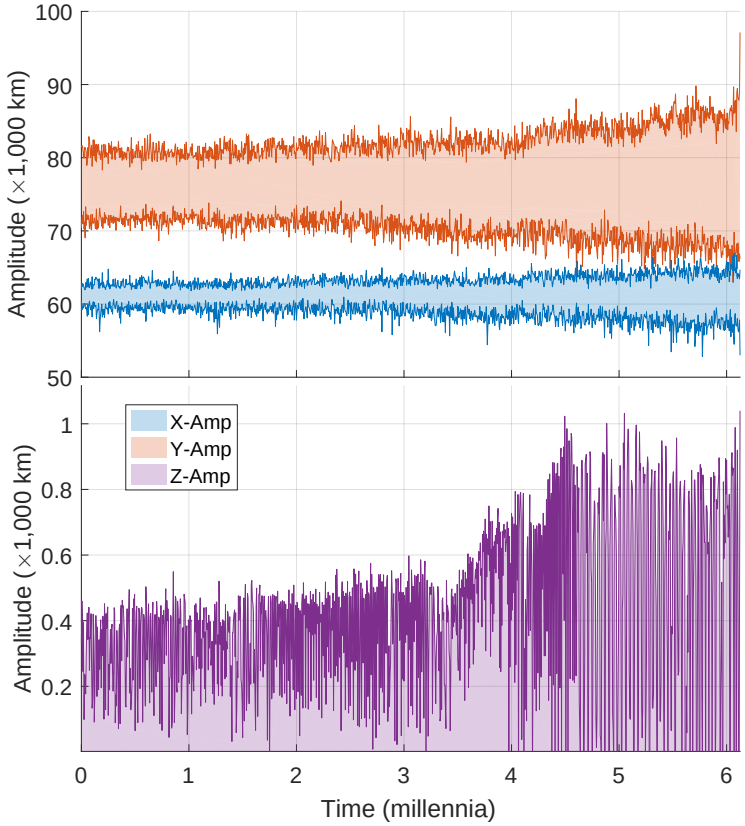

Figure 8.10: The evolution of the x, y, and z-amplitudes of the 62,500 km DRO.

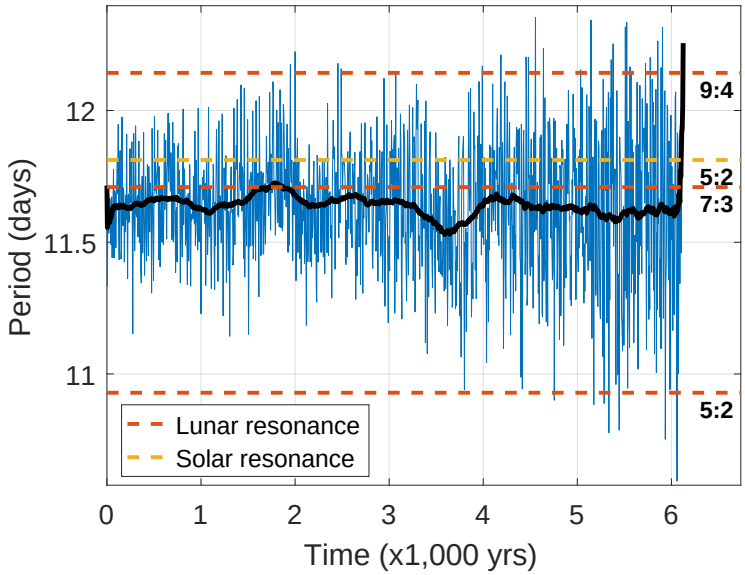

Figure 8.11: The evolution of the period of the 62,500 km DRO.

value of 11.65 days. This lies just under the 7:3 resonance with the lunar period (11.71 days), suggesting the Moon's eccentricity is causing the in-plane mode excitation we see in the amplitude data.

8.4.4 The 67,000 km DRO

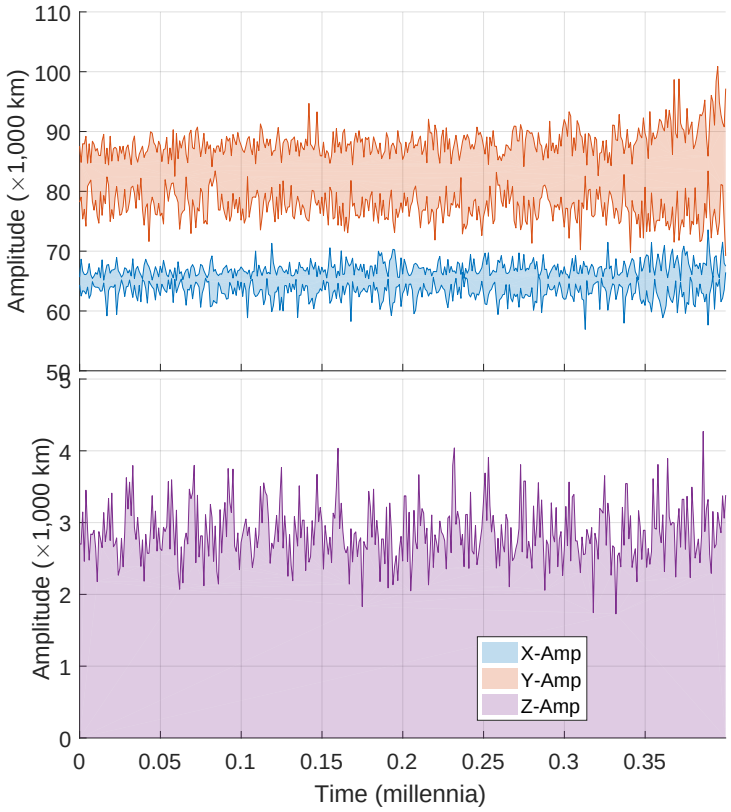

Figure 8.12: The evolution of the x, y, and z-amplitudes of the 67,000 km DRO, inclined by 178°.

The 67,000 km DRO representing Region D behaves similarly to the 62,500 km DRO, but only lasts about 400 years before departing the Moon. The amplitude is shown in Figure 8.12 and the period history is shown in Figure 8.13. We propagated the 178° inclination initial conditions since they resulted in a longer stability duration than the planar initial conditions. This DRO experiences the least amount of change to its period during its stable duration. It begins at 12.5 days and its smoothed value does not have a secular shift. This period lies close to the 7:3 solar resonance (12.66 days), but does not drift towards or away from it. While the smoothed period does

not change, the data show that the period's oscillation grows from ±0.5 days to ±1 day after the 350 year mark, which is where the y-amplitude span begins to grow noticeably. The x-amplitude has little noticeable change throughout the simulation. The z-amplitude oscillates between 2,000 and 4,000 km, cycling approximately once every 15 years. This amplitude response suggests that the larger DROs are less tolerant of y-amplitude variations than smaller DROs, likely because the Sun's gravitational perturbations are comparable or greater than the Moon's gravity.

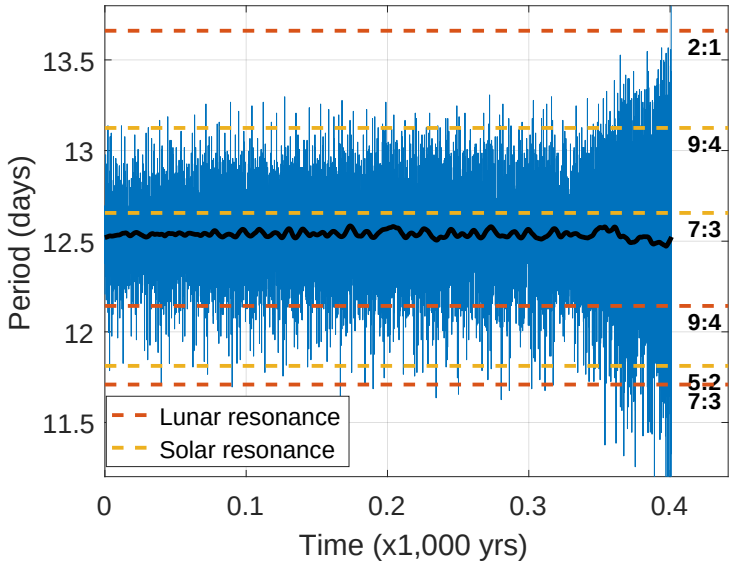

Figure 8.13: The evolution of the period of the 67,000 km DRO.

8.5 Root Cause of Unstable Evolution

The evolution of the 36,000 and 45,000 km DROs is driven by the steady decay of the orbit's size. To examine which forces are responsible for this secular trend, the same simulations are run with the Moon's aspherical gravity field and solid tides removed from the dynamical model. Figure 8.14 shows the 45,000 km DRO's amplitudes when it is not subjected to these perturbing forces. All secular trends in the orbit evolution are no longer present; there is no growth or shrinking of any amplitude, nor are there excitations of either unstable mode. Because the orbit size does not decay, the period remains constant and does not intersect dynamical resonances. The conclusion

is that the permanent solid tide on the Moon and its aspherical gravity field are the driving forces in the secular decay of these two smaller DROs. It is worth mentioning that the orbital decay we see in these smaller DROs is not expected given the relatively static aspherical gravity field of the Moon in the rotating frame. It is possible that there is some coupling between several perturbing forces, of which the gravity field plays an integral part. This should be investigated in future work, especially using a symplectic integrator.

The 62,500 and 67,000 km DROs do not appear to decay like the smaller DROs do because they are driven to in-plane instability by the Sun's gravity relatively quickly. When the Sun's gravity is removed from the dynamical model, the 62,500 km DRO survives for over 25,000 years instead of 6,000 years. Figure 8.15 this DRO's IBE decay while its EBE experiences periods of growth and decay, ending approximately at the same amplitude it began at. The rate at which the IBE decays is an order of magnitude smaller than the smaller DROs because it exists exclusively outside of the Moon's Hill sphere where the acceleration due to solid tides is several orders of magnitude smaller. Recall that acceleration from spherical harmonic coefficients of degree i are decrease with r^{-i}. We also see the excitation and damping of the out-of-plane mode, though this does not appear to be the final cause of instability. The period decays as well, sticking at the 7:3 lunar resonance shown in Figure 8.11 for about 5,000 years before decaying. When the orbit becomes unstable, the period is not at any discernible resonance.

Without the Sun's gravity considered, the 67,000 km DRO's stable lifetime is extended from 400 years to about 2,570 years. Similar to the 62,500 km DRO, there is excitation and damping of the in-plane mode, which eventually leads to instability. The z-amplitude decays from its starting amplitude of about 3,500 km down to 2,700 km. In this DRO, the period does not decay; it hovers around 12.5 days for the full stable duration. It remains far from lunar dynamical resonances, which again indicates that at these amplitudes, resonances are not required to destabilize the DROs. These test cases indicate that solar gravity is the primary destabilizing force for the larger DROs by exciting the in-plane mode. Dynamical resonances do not appear to play as strong a role for the larger DROs because the magnitude of solar gravity perturbations is comparable to or

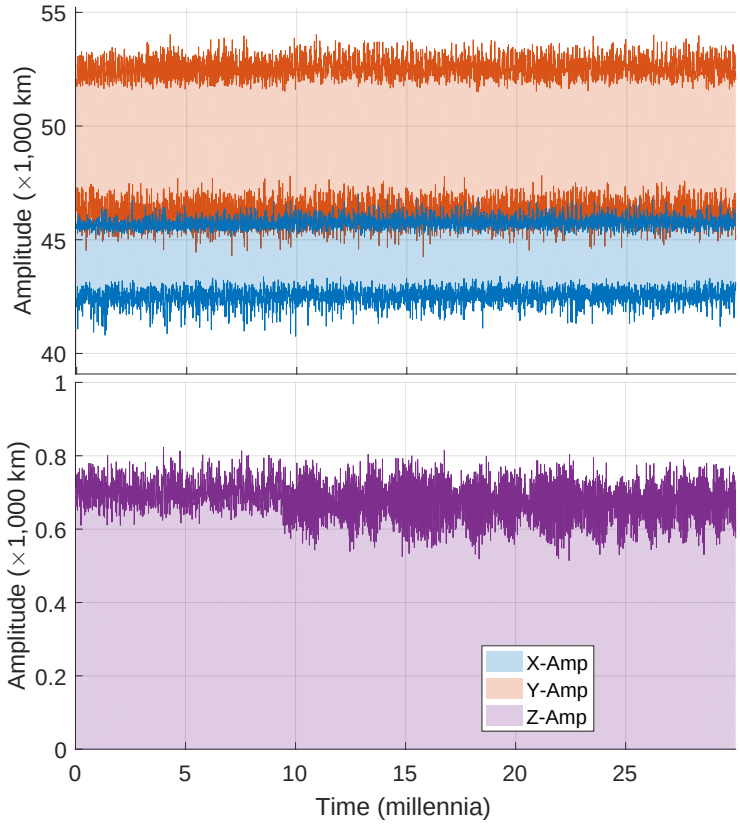

Figure 8.14: The evolution of the x, y, and z amplitudes of the 45,000 km DRO when the aspherical gravity and solid tide perturbations are not considered.

greater than the gravitational acceleration of the primary bodies, effectively creating a four-body system.

8.6 Conclusions on DRO Evolution

In the four test cases run with the high fidelity propagator, we have shown that 36,000 and 45,000 km DROs will exhibit secular decay due to the aspherical gravity field and solid tide perturbations of the Moon. This causes the DRO's period to cross resonant frequencies with dynamical forces which causes periods of rapid growth of either the z-amplitude or the variations in x and y-amplitude between orbits. Sufficient excitation of these modes leads to the trajectory departing quasi-periodic motion around the Moon. The 62,500 and 67,000 km DROs decay at a severely reduced rate, but become unstable due to solar gravity before significant trends can be

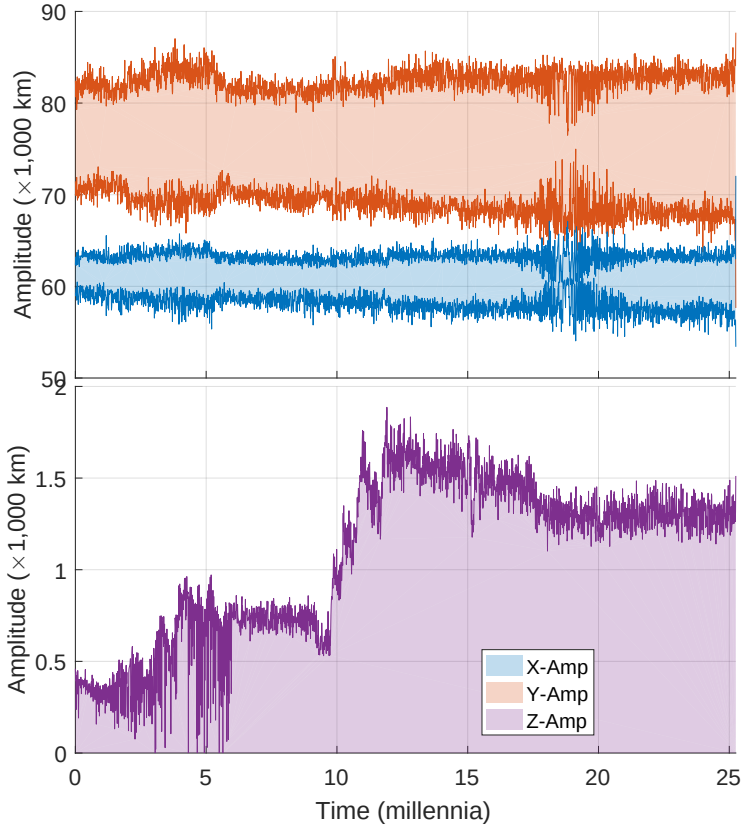

Figure 8.15: The evolution of the x, y, and z amplitudes of the 62,500 km DRO when the Sun's gravity is not considered.

observed. These two larger DROs become unstable without necessarily being near a dynamical resonance. These dynamical effects occur over the course of many millennia and are not of concern for typical spacecraft duration missions. This work applies to missions that require long duration, hands-off quarantine, such as those concerned with planetary protection protocols. There is sufficient evidence to suggest that these quasi-periodic DROs behave chaotically, but the secular trends discussed offer a guideline for how the orbit will evolve and when it will encounter resonances.

Future work on this topic should include generating a Poincaré section during the integration to confirm the in-plane unstable departure modes are indeed approaching BUPOs. It would also allow one to observe the "sticky" phenomenon seen in chaotic systems near the resonant frequencies. One or more DROs that are near the Moon's Hill sphere, but far removed from any resonant frequencies should be studied to identify the behavior in between the small and large DROs. Ad-

ditionally, the inclination stability map in Figure 8.1 indicates that DROs in the 50,000 km region are only stable when they are non-planar orbits. The driving forces behind this behavior would be interesting as well.

Chapter 9

Summary and Conclusions

The research presented in this dissertation describes a method for building, characterizing, and effectively applying low-energy ballistic transfers into distant retrograde orbits (DROs). This chapter will summarize important findings, highlight the contributions this research makes to the astrodynamics field, present concluding remarks, and suggest several ways that this research can be advanced through future work.

9.1 Contributions to the Field

The primary contribution that this research makes to the astrodynamics and mission design fields is through the construction, identification, and analysis of ballistic capture trajectories (BCTs) that develop into Lagrange stable, quasi-periodic DROs. A methodology is developed where a reference DRO is perturbed in an adaptive fashion to generate a large, representative set of BCTs. These sets are stochastically analyzed for trends, constraints, boundaries, and geometries which can all be used to identify if a particular mission will benefit from exploiting a BCT. This method is used to explore the Earth-Moon system and the Mars-Phobos system, both of which are relevant to many near-term mission concepts. As part of the development of this work, a function was also developed to return the initial conditions for a periodic DRO in the CR3BP for a wide range of mass parameters and DRO sizes. Prior to this function, initial conditions for DROs had to be pre-generated for a specific mass parameter and accessed with a lookup table.

After the construction and analysis of BCT sets, we develop other tools and analyses that are

of interest to mission designers. We investigate methods for building optimal transfers from these quasi-periodic DROs to stable periodic DROs, which can significantly extend a spacecraft's time in the DRO and makes it less sensitive to perturbing forces. Finally, we study and characterize the evolution of DROs in the Earth-Moon system over periods of tens of millennia using a high fidelity dynamical model and numerical techniques to preserve accuracy of the integration. We observe and identify root causes for the decay of DROs as the aspherical gravity field of the Moon, and more specifically, the solid tide bulge on the Moon. Resonant frequencies are also identified that can cause sudden excitation of a DRO's mode shapes, which can lead to instability. The sum of this research is two-fold; first, we provide a set of dynamical conditions that can be used to exploit a ballistic capture for the Earth-Moon and Mars-Phobos system. Second, we generate the tools to aid in mission design after a spacecraft is captured onto a DRO.

9.1.1 Summary of Ballistic Capture Techniques

In Chapter 4, we identify a distinct boundary of stability in perturbed DROs. A methodology is produced in Chapter 5 to generate a set of free ballistic capture trajectories for a reference DRO through convenient utilization of perturbing forces. This begins by perturbing the reference trajectory's velocity in an uniform grid, propagating the states forwards and backwards through time, and identifying if the resulting trajectories are stable in either, both, or neither temporal direction. We identify all trajectories that are stable forward in time, but unstable backwards in time. This method is improved upon in Chapter 6 when we introduce the adaptive meshing algorithm. This allows us to quickly identify the border between stable trajectories and BCTs. From there, a uniform grid search only in the chaotic, one-way stable region identifies the set of BCTs. This improves the algorithm's computation time by factors from ranging hundreds to thousands, which enables analyses that require many stability maps. Once a desirable BCT has been selected, tools are generated to move the reference BCT through time to the epoch of the mission. The targeted flyby state can be slightly modified to build a trajectory that rapidly descends collapses towards a periodic DRO after capture.

In the Earth-Moon system, we find that BCTs for several investigated DROs can be categorized by the geometry of their flyby of the Moon prior to being captured. Four unique geometries are identified, two of which are energy-reducing flybys and the other two are energy raising flybys. An important discovery is that these free captures do not necessarily require a close lunar flyby; some transfers can remain more than 40,000 km from the Moon for a 70,000 km DRO. BCTs can also be characterized by how long they spend in the Earth-Moon system before being captured into a DRO. The direct capture BCTs interestingly all use the same flyby geometry (Family 1) and the majority of fast indirect capture BCTs lie in the Family 2 geometry. BCTs exist year round and despite the Sun being the primary cause for their existence, there appears to be no limitations on the Sun-Earth-Moon geometry at arrival. The Earth-Moon geometry when the trajectory arrives is important, and a BCT should be built to arrive leading the Moon by between 30° and 60°. Interplanetary trajectories with semi-major axes between 0.93 and 1.07 AU have sufficient energy to be captured and must target a V_∞ between 395 and 420 m/s.

The Mars-Phobos system is significantly different from the Earth-Moon system in terms of mass parameter and distance between the primaries. We identify that one-way stable trajectories are not randomly scattered around the stability boundary as they are in the Earth-Moon system, but form large, continuous regions. BCTs in this system can fall into one of two capture flyby geometries; the northern family flies by in front of Phobos and the southern family flies by behind Phobos, and both can be useful depending on the where the spacecraft is arriving from. Due to the small mass of Phobos, BCTs are are simply walking orbits with semi-major axes 75 km larger or smaller than Phobos'. They are incapable of accessing interplanetary space, but they can still be useful in mission design. A spacecraft can avoid a critical maneuver near the moon by using a BCT, which gives a slow, cautious approach to the moon. Should a BCT miss its mark on approach to Phobos, another attempt can be made between 22 and 96 days later. A BCT accessing the 26 km DRO around Phobos has a maximum flyby distance from Phobos of 20.1 km, or about 8 km in altitude.

9.1.2 Summary of Stabilizing Maneuvers

Chapter 7 describes minimum cost transfers from a quasi-periodic orbit on the boundary of stability to a periodic orbit at the center of a stable region in the Earth-Moon CR3BP. The main conclusion drawn from this work is that DROs that are largely planar are significantly cheaper to transfer to periodic DROs, on the order of 10 m/s as opposed to out-of-plane DROs which can cost as much as 60 m/s. We show that by targeting an arbitrarily sized DRO instead of the reference DRO used to construct the BCT, we can further reduce the cost by 1-5 m/s. Steps are taken to identify global minima for these transfers, but there is no guarantee that this is the case. These results are specific to quasi-periodic orbits generated from the 70,000 km reference DRO and obviously different DROs and three-body systems will have a unique set of transfers, but the important lesson is that planar quasi-periodic DROs can return to a periodic DRO for 80% less ΔV than it took to generate the quasi-periodic orbit in the first place. This analysis helps quantify the true cost of utilizing a BCT if stabilization is required.

9.1.3 Summary of Long Duration Stability of DROs

Four DROs are propagated in a high-fidelity dynamical model including gravity from the Moon, Sun, and eight planets, solar radiation pressure, aspherical gravity fields for the Earth and Moon, and solid tide perturbations due to the Earth, Moon, and Sun. These DROs are propagated for up to 30,000 years to study their long duration evolution. The integrator is programmed to use double-double arithmetic in order to preserve accuracy throughout this long duration propagation. We show that the 36,000 and 45,000 km DROs will exhibit secular decay due to the aspherical gravity field and solid tide perturbations of the Moon. This causes the DRO's period to cross resonant frequencies with dynamical forces which causes periods of rapid growth of either the z-amplitude or the variations in x and y-amplitude between orbits. Sufficient excitation of these modes leads to the trajectory departing quasi-periodic motion around the Moon.

The 62,500 and 67,000 km DROs decay at a significantly reduced rate because of their distance

from the Moon, but become unstable due to solar gravity before significant trends can be observed. These two larger DROs depart the Moon after a few millennia without being near a dynamical resonance. This work applies to missions that require long duration, hands-off quarantine, such as those concerned with planetary protection protocols. There is sufficient evidence to suggest that these quasi-periodic DROs behave chaotically, but the secular trends discussed offer a guideline for how the orbit will evolve and when it will encounter resonances.

9.2 Conclusions

This dissertation has developed and demonstrated a method for constructing ballistic capture trajectories for any three-body system with a perturbing force outside the gravity of the two primaries. These trajectories are often chaotic, but they can be reliably targeted through the flyby of the minor body that leads to their capture. These capture trajectories are essentially free from fuel cost and arrive on a Lagrange stable quasi-periodic DRO. This work breaks many preconceived notions about the three-body problem and DROs. It shows that stable orbits can be entered for free, despite them not having a stable manifold, by utilizing a perturbing acceleration. In conventional mission design, orbits deeper in a gravity well require more fuel to arrive in, but this work reveals that many different DROs can be targeted with a ballistic capture.

9.3 Future Work

This research presented here has created tools to build and analyze ballistic capture trajectories, but certainly does not cover the breadth or depth of their applications. There are many ways in which the tools can be improved, and even more ways that they can be applied to aid the mission design process. This final section addresses a few ideas for how this research can be continued in the future.

First, we've already seen that there are significant differences between the Earth-Moon and Mars-Phobos systems in terms of their ballistic capture trajectory sets. The most stark of these differences is that one-way stable trajectories in the Mars-Phobos system form groups and regions

while they are chaotically scattered in the Earth-Moon system. While it was hypothesized in this dissertation that the primary cause is primarily due to the magnitudes of accelerations from different sources, this requires further study. This gap of knowledge was also acknowledged by Hirani and Russell.[56] Exploring other three-body systems with varying combinations of mass parameters, distances, and perturbing accelerations may reveal similarly striking differences. Specifically, the BCT analysis in the Mars-Phobos system in Chapter 6 neglects solar gravity to isolate the effects of Phobos' mass distribution. Using two or more perturbing accelerations may create different sets of BCTs with useful characteristics. Additionally, the flyby geometry in the two systems vary significantly, and perhaps other geometries exist for unstudied systems.

Even in the three-body systems we have discussed, this work only examines a handful of DROs in depth and often leaves open questions about some of the behavior. For example, we have seen that different DRO sizes alter the known flyby geometries. Understanding the relationship between this geometry and the DRO's size would help mission designers understand the consequences of errors when targeting a BCT. We saw in the Earth-Moon system that the 50,000 km DRO had appreciably fewer BCTs than the 70,000 km DRO, but it is unclear as to whether this is due to the size difference, the out-of-plane stable regions, or some other unknown factor. The evolution of the pinwheel plot, particularly the arm containing direct captures, across DRO sizes would also provide useful knowledge. In the Mars-Phobos system, only the 26 km DRO is investigated due to its high density of one-way stable trajectories. Exploring more DROs may help discover new traits that make their utilization more enticing to mission designers. Additionally, the idea of using a backwards stable trajectory is a concept that hasn't been discussed at all in this dissertation. The trajectories that intersect Phobos represent launch options that put a spacecraft into a DRO after landing on the surface, perhaps to collect material samples. They could also be used to design DROs that escape the Earth-Moon system after a mission has completed in order to prevent the accumulation of debris in cislunar space.

An interesting element with the development of the BCT sets is that they are found through circumstance. While we can identify the root cause of a one-way stable trajectory, there is no orbit

evolution theory applied. Similarly, improvements to the methodology for generating BCTs have been algorithm based instead, like adding the adaptive meshing. Application of theory that could explain the secular effects of the Sun's gravity on a DRO, for example, could improve the algorithms by giving an initial guess for where to look for stable regions and cut down on computation time. It would also aid in reinforcing mission design decisions based on stability maps. The Mars-Phobos BCTs prior to capture appear behave similarly to a rendezvous problem due to Phobos's small mass. It would be worthwhile to study how effective the Clohessy-Wiltshire equations are at reconstructing the approach leg. Other algorithms used in this work can be improved as well. Simpler dynamical models such as the elliptic restricted three-body problem or the very restricted four-body problem, which contain perturbing forces can also help develop a better understanding of how these forces create the one-way stable trajectories. The most significant improvement that can be made for a stability map is to devise a way to map an arbitrary state onto a pre-generated stability map. This is a difficult problem, but there are several potential ideas for how this might work described in Sections 4.4.5 and 7.5.

Bibliography

[1] Adamo, D.R., Lester, D., Thronson, H., Barbee, B.: A class of selenocentric retrograde orbits with innovative applications to human lunar operations. AIAA/AAS Astrodynamics Specialist Conference (2014)

[2] Alexeyev, V.M.: New examples of capture in the three-body problem. Soviet Astronomy **6**(4), 565–572 (1963)

[3] Anderson, R., Lo, M.: The role of invariant manifolds in low thrust trajectory design (part ii). Tech. Rep. 2004-5305, AIAA/AAS Astrodynamics Specialist Conference (2004)

[4] Anderson, R.L.: Low-thrust trajectory design for resonant flybys and captures using invariant manifolds. Ph.D. thesis, University of Colorado at Boulder (2005)

[5] Arnold, V.: Proof of a theorem of a.n. kolmogorov on the preservation of conditionally periodic motions under a small perturbation of the hamiltonian. Uspehi Mat. Nauk **18**, 13–40 (1963)

[6] Bailey, J.: Origin of the outer satellites of jupiter. Journal of Geophysical Research **76**(32), 7827–7832 (1971)

[7] Barrow-Green, J.: Poincaré and the Three Body Problem. The American Mathematical Society (1997)

[8] Battin, R.: An Introduction to the Mathematics and Methods of Astrodynamics. American Institute of Aeronautics and Astronautics, New York (1987)

[9] Belbruno, E.: Capture Dynamics and Chaotic Motions in Celestial Mechanics. Princeton University Press, Princeton, NJ (2004)

[10] Belbruno, E., Carrico, J.: Calculation of weak stability boundary ballistic lunar transfer trajectories. Tech. Rep. 2000-4142, AIAA/AAS Astrodynamics Specialist Conference (2000)

[11] Benest, D.: Effects of the mass ratio on the existence of retrograde satellites in the circular plane restricted problem. Astronomy & Astrophysics **32**, 39–46 (1974)

[12] Benest, D.: Effects of the mass ratio on the existence of retrograde satellites in the circular plane restricted problem ii. Astronomy & Astrophysics **45**, 353–363 (1975)

[13] Benest, D.: Effects of the mass ratio on the existence of retrograde satellites in the circular plane restricted problem iv: Three-dimensional stability of plane periodic orbits. Astronomy & Astrophysics **54**, 563–568 (1977)

[14] Bezrouk, C., Parker, J.: Investigation of practical distant retrograde orbits up to 30,000 years. AAS Astrodynamics Specialist Conference (15-743) (2015)

[15] Bezrouk, C., Parker, J.S.: Long duration stability of distant retrograde orbits. AIAA/AAS Astrodynamics Specialist Conference (14-4424) (2014)

[16] Bezrouk, C., Parker, J.S.: Ballistic capture into distant retrograde orbits from interplanetary space. AAS/AIAA Space Flight Mechanics Meeting (AAS 15-302) (2015)

[17] Bookstein, F.L.: Fitting conic sections to scattered data. Computer Graphics and Image Processing **9**(1), 56–71 (1979)

[18] Brophy, J., Friedman, L., Culick, F.: Asteroid retrieval feasibility. Aerospace Conference, 2012 IEEE pp. 2–3 (2012)

[19] Broucke, R.: Periodic orbits in the restricted three-body problem with earth-moon masses. Technical Report 32-1168, Jet Propulsion Laoratory (1968)

[20] Bruns, H.: ber die integrale des vielkrperproblems. Leipzig (1887)

[21] Byl, J., Ovenden, M.: On the satellite capture problem. Royal Astronomical Society **173**(3), 579–584 (1975)

[22] Campagnola, S., Russel, R.P.: Endgame problem part 2: Multibody technique and the tisserand-poincaré graph. Journal of Guidance, Control, and Dynamics **33**(2) (2010)

[23] Capdevila, L., Guzzetti, D., Howell, K.: Various transfer options from earth into distant retrograde orbits in the vicinity of the moon. AAS/AIAA Space Flight Mechanics Meeting (2014)

[24] Capdevila, L., Guzzetti, D., Howell, K.C.: Various transfer options from earth into distant retrograde orbits in the vicinity of the moon. AIAA/AAS Astrodynamics Specialist Conference (AAS 14-467) (2014)

[25] Chanut, T., Aljbaae, S., Carruba, V.: Mascon gravitation model using a shaped polyhedral source. Monthly Notices of the Royal Astronomical Society **450**(4), 3742–3749 (2015)

[26] Chazy, J.: Sur l'allure du mouvement dans le probleme des trois corps quand le temps croit indefiniment. Ann. Sci. Ecole Norm. Sup. pp. 29–130

[27] Colagrossi, A., Ferrari, F., Lavagna, M., Howell, K.: Dynamical evolution about asteroids with high fidelity gravity field and perturbations modeling. In: AAS/AIAA Conference, no. AAS, pp. 15–637 (2015)

[28] Conway, B.A.: Spacecraft trajectory optimization, vol. 29. Cambridge University Press (2010)

[29] Davies, R.T., Tennant, D.: The waters of mars. Journal of DW **201** (2059)

[30] Davis, K.E.: Locally optimal transfer trajectories between libration point orbits using invariant manifolds. Ph.D. thesis, University of Colorado at Boulder (2009)

[31] Dekker, T.J.: A floating-point technique for extending the available precision. Numerische Mathematik (18:224-242) (1971)

[32] Delaunay, C.: La Theorie du Mouvement de la lune, 2 Volumes (1860,1867)

[33] Demeyer, J., Gurfil, P.: Transfer to distant retrograde orbits using manifold theory. Journal of Guidance, Control, and Dynamics **30.5**, 1261–1267 (2007)

[34] Devincenzi, D.L., Race, M.S., Klein, H.P.: Planetary protection, sample return missions and mars exploration: History, status, and future needs. Journal of Geophysical Research: Planets **103**(E12), 28,577–28,585 (1998)

[35] Duxbury, T.C., Zakharov, A.V., Hoffmann, H., Guinness, E.A.: Spacecraft exploration of phobos and deimos. Planetary and Space Sciences **102**, 9–17 (2014)

[36] Eberhart, R.C., Kennedy, J.: A new optimizer using particle swarm theory. In: Proceedings of the sixth international symposium on micro machine and human science, vol. 1, pp. 39–43. New York, NY (1995)

[37] Euler, L.: De motu rectilineo trium corporum se mutuo attrahentium (1765)

[38] Fitzpatrick, P.M.: Principles of celestial mechanics. Physics and Chemistry of Minerals **1** (1970)

[39] Floquet, G.: Sur les equations differentielles lineaires a coefficients periodiques. Annales de l'Ecole Normale Superieure **12**, 47–88

[40] Folkner, W., Williams, J., Boggs, D., Park, R., Kuchynka, P.: The planetary and lunar ephemerides de430 and de431. IPN Progress Report 42-196 (2014)

[41] Gascheau, G.: Examen dune classe dquations diffrentielles et applications un cas particulier du problme des trois corps. Comptes Rendus de l'Acadmie des Sciences de Paris **16**, 393 (1843)

[42] Gelfand, I.M., Silverman, R.A., et al.: Calculus of variations. Courier Corporation (2000)

[43] Gómez, G., Jorba, A., Masdemont, J., Simó, C.: Study of the transfers between halo orbits. Acta Astronautica **43**, 493–520 (1998)

[44] Gottlieb, P.: Estimation of local lunar gravity features. Radio Science **5**(2), 301–312 (1970)

[45] Gottlieb, R.: Fast gravity, gravity partials, normalized gravity, gravity gradient torque and magnetic field: Derivation, code and data. Technical Report NASA Contractor Report 188243, NASA Lyndon B. Johnson Space Center (1993)

[46] Greenberg, M.D.: Foundations of applied mathematics. Courier Corporation (2013)

[47] Handelsman, M., Lion, P.: Primer vector on fixed-time impulsive trajectories. Aiaa Journal **6**(1), 127–132 (1968)

[48] Heath, M.T.: Scientific Computing, An Introductory Survey, 2nd edition edn. McGraw-Hill, New York, NY (2002)

[49] Heiskanen, W.A., Moritz, H.: Physical geodesy. Bulletin Géodésique (1946-1975) **86**(1), 491–492 (1967)

[50] Hénon, M.: Numerical exploration of the restricted three-body problem. International Astronomical Union pp. 157–169

[51] Hénon, M.: Numerical exploration of the restricted problem. v. hill's case: Orbits and their stability. Astronomy & Astrophysics **1**, 223–238 (1969)

[52] Hénon, M.: Numerical exploration of the restricted problem. vi. hill's case: Non-periodic orbits. Astronomy & Astrophysics **9**, 24–36 (1970)

[53] Heppenheimer, T.: On the presumed capture origins of jupiter's outer satellites. Icarus **24**, 172–180 (1975)

[54] Hiday, L.A.: Optimal transfers between libration-point orbits in the elliptic restricted three-body problem(ph. d. thesis). Ph.D. thesis, Purdue University (1992)

[55] Hiday-Johnston, L., Howell, K.: Impulsive time-free transfers between halo orbits. Celestial Mechanics and Dynamical Astronomy **64**(4), 281–303 (1996)

[56] Hirani, A.N., Russell, R.P.: Approximations of distant retrograde orbits for mission design. AAS/AIAA Space Flight Mechanics Meeting (06-116) (2006)

[57] Hobson, E.W.: The theory of spherical and ellipsoidal harmonics. CUP Archive (1931)

[58] Horedt, G.: Capture of planetary satellites. Astronomical Journal **81**(8), 675–680 (1976)

[59] Howell, K., Kakoi, M.: Transfers between the earth-moon and sun-earth systems using manifolds and transit orbits. Acta Astronautica **59(1-5)**, 367–380 (2006)

[60] Howell, K.C.: Three-dimensional, periodic, 'halo' orbits. Celestial Mechanics **32(1)**, 53–71 (1984)

[61] Jacobi, C.G.: Sur le movement d'un point et sur un cas particulier du problme des trois corps. Comptes Rendus de l'Acadmie des Sciences de Paris **3**, 59–61 (1836)

[62] Jezewski, D.J., Rozendaal, H.L.: An efficient method for calculating optimal free-space n-impulse trajectories. AIAA journal **6**(11), 2160–2165 (1968)

[63] Jorba, A.: Numerical computation of the normal behavior of invariant curves of n-dimensional maps. Nonlinearity **14**(4), 943–976 (2001)

[64] Jorba, A., Olmedo, E.: On the computation of reducible invariant tori on a parallel computer. Journal of Applied Dynamical Systems **8**, 1382–1404 (2009)

[65] Kaplan, M.H.: Modern spacecraft dynamics and control. New York, John Wiley and Sons, Inc., 1976. 427 p. **1**, 273–282 (1976)

[66] Kaula, W.M.: Statistical and harmonic analysis of gravity. Journal of Geophysical Research **64**(12), 2401–2421 (1959)

[67] Knuth, D.E.: The Art of Computer Programming: Seminumerical Algorithms, 2nd edn. Addison-Wesley, Reading Massachusetts (1981)

[68] Kolmogorov, A.: On conservation of conditionally periodic motions for a small change in hamilton's function. Dokl. Akad. Nauk SSSR **98**, 527–530 (1954)

[69] Konopliv, A., Asmar, S., E.Carranza, Sjogren, W., Yuan, D.: Recent gravity models as a result of the lunar prospector mission. Icarus **150**, 1–18 (2001)

[70] Koon, W., Lo, M., Marsen, J., Ross, S.: Dynamical systems, the three-body problem, and space mission design. International Conference on Differential Equations **1**, 2 (2000)

[71] Koon, W., Lo, M., Marsen, J., Ross, S.: Heteroclinic connections between periodic orbits and resonance transitions in celestial mechanics. Chaos **10(2)**, 427–469 (2000a)

[72] Koon, W., Lo, M., Marsen, J., Ross, S.: Low energy transfers to the moon. Celestial Mechanics and Dynamical Astronomy **81(1)**, 63–73 (2001)

[73] Lam, T., Whiffen, G.: Exploration of distant retrograde orbits around europa. Advances in Astronomical Science **05**(110), 5–12 (2005)

[74] Lambeck, K.: Geophysical geodesy. Clarendon Oxford (1988)

[75] Lawden, D.: Optimal programming of rocket thrust direction. Astronautica Acta **1**(1) (1955)

[76] Lawden, D.: Necessary conditions for optimal rocket trajectories. Quarterly Journal of Mechanics and Applied Mathematics **12**(4) (1959)

[77] Lawden, D.F.: Optimal trajectories for space navigation. Butterworths (1963)

[78] Long, A.C., Cappellari Jr, J., Velez, C., Fuchs, A.: Goddard trajectory determination system (gtds) mathematical theory (revision 1). National Aeronautics and Space Administration/Goddard Space Flight Center, FDD/552-89/001 and CSC/TR-89/6001 (1989)

[79] Lundberg, J., Schutz, B.: Recursion formulas of legendre functions for use with nonsingular geopotential models. Journal of Guidance **11**(1), 31–38 (1988)

[80] MacCullagh, J.: On the attraction of ellipsoids with a new demonstration of clairut's theorem. Transactions of the Royal Irish Academy **22** (1885)

[81] Malcuit, R., Mehringer, D., Winters, R.: Numerical simulationof gravitational capture of a lunar-like body by earth. Lunar and Panetary Science Conference pp. 581–591 (1989)

[82] Minghu, T., Ke, Z., Meibo, L., Chao, X.: Transfer to long term distant retrograde orbits around the moon. Acta Astronautica **98**, 50–63 (2014)

[83] Moser, J.: On invariant curves of area-preserving mappings of an annulus. Nachr. Akad. Wiss. Gottingen Math -Phys K1 pp. 1–20 (1962)

[84] Murray, C.D., Dermott, S.F.: Solar System Dynamics, 1st edn. Cambridge University Press, New York, NY (1999)

[85] Nakhjiri, N.: Space partitioning structures for efficient stability map generaton. Tech. Rep. 15-689, AAS Astrodynamics Specialist Conference (2015)

[86] Neto, H.V., Winters, O.: Time analysis for temporary gravitational capture: Satellites to uranus. The Astronomical Journal **122**, 440–448 (2001)

[87] Newton, I.: Philosophiae Naturalis Principia Mathematica (1687)

[88] Ocampo, C., Rosborough, G.: Transfer trajectories for for distant retrograde orbiters of the earth. American Astronautical Society **82**, 1177–1200 (1993)

[89] O'Leary, B.: Rationales for early human missions to phobos and deimos. Lunar Bases and Space Activities of the 21st Century **1** (1985)

[90] Olikara, Z.P., Howell, K.: Computation of quasi-periodic invariant tori in the restricted three-body problem. Tech. rep. (2010)

[91] Olikara, Z.P., Scheeres, D.J.: Numerical method for computing quasi-periodic orbits and their stability in the restricted three-body problem. Tech. Rep. 12-361 (2012)

[92] Owen, D.B.: Tables for computing bivariate normal probabilities. The Annals of Mathematical Statistics **27**(4), 1075–1090 (1956)

[93] Parker, J.: Low-energy ballistic lunar transfers. Ph.D. thesis, University of Colorado at Boulder (2007)

[94] Parker, J., Anderson, R.: Low-Energy Lunar Trajectory Design, 1st edn. John Wiley and Sons, Inc., Hoboken, New Jersey (2014)

[95] Parker, J.S., Bezrouk, C.: Low-energy transfers to distant retrograde orbits. AAS/AIAA Space Flight Mechanics Meeting (AAS 15-331) (2015)

[96] Patefield, M., Tandy, D.: Fast and accurate calculation of owenst function. Journal of Statistical Software **5**(5), 1–25 (2000)

[97] Pavlak, T.A.: Trajectory design and orbit maintenance strategies in multi-body dynamical regimes. Ph.D. thesis, Purdue University (2013)

[98] Pernicka, H.: The numerical determination of lissajous orbits in the circular restricted three-body problem. Master's thesis, Purdue University (1986)

[99] Petit, G., Luzum, B.: Iers conventions (2010). IERS Technical Note 36, International Earth Rotation Service (2010). URL `http://www.iers.org/TN36/`

[100] Pollack, J., Burns, J., Tauber, M.: Gas drag in primordial circumplanetary nebulae: A mechanism for satellite capture. Icarus **37**, 587–611 (1979)

[101] Post, M.J.: Minimum spanning ellipsoids. In: Proceedings of the sixteenth annual ACM symposium on Theory of computing, pp. 108–116. ACM (1984)

[102] Priest, D.M.: On properties of floating point arithmetics: Numerical stability and the cost of accurate computations. Ph.D. thesis, University of California, Berkeley (1992)

[103] Prussing, J.E.: Equation for optimal power-limited spacecraft trajectories. Journal of Guidance, Control, and Dynamics **16**(2), 391–393 (1993)

[104] Prussing, J.E.: Optimal impulsive linear-systems: Sufficient conditions and maximum number of impulses. Journal of the Astronautical Sciences **43**(2), 195–206 (1995)

[105] Prussing, J.E., Chiu, J.H.: Optimal multiple-impulse time-fixed rendezvous between circular orbits. Journal of Guidance, Control, and Dynamics **9**(1), 17–22 (1986)

[106] Prussing, J.E., Sandrik, S.L.: Second-order necessary conditions and sufficient conditions applied to continuous-thrust trajectories. Journal of Guidance, Control, and Dynamics **28**(4), 812–816 (2005)

[107] Qiu-Dong, W.: The global solution of the n-body problem. Celestial Mechanics and Dynamical Astronomy **50**(1), 73–88 (1990)

[108] Ramsley, K.R., Head, J.W.: Mars impact ejecta in the regolith of phobos: bulk concentration and distribution. Planetary and Space Science **87**, 115–129 (2013)

[109] Ross, S.: Cylindrical manifolds and tube dynamics in the restricted three-body problem. Ph.D. thesis, California Institute of Technology (2004)

[110] Rossi, A., Marzari, F., Farinella, P.: Orbital evolution around irregular bodies. Earth, planets and space **51**(11), 1173–1180 (1999)

[111] Routh, E.: On laplace's three particles, with a supplement on the stability of steady motion. Proc. London Math. Soc. **6**, 86 (1875)

[112] Roy, A.E.: Orbital motion. CRC Press (2004)

[113] Russell, R.P., Arora, N.: Global point mascon models for simple, accurate, and parallel geopotential computation. Journal of Guidance, Control, and Dynamics **35**(5), 1568–1581 (2012)

[114] Sagdeev, R., Zakharov, A.: Brief history of the phobos mission. Nature **341**(6243), 581–585 (1989)

[115] Schaub, H., Junkins, J.L.: Analytical mechanics of space systems, 2nd edn. AIAA Education Series (2003)

[116] Scott, C., Spencer, D.: Stability mapping of distant retrograde orbits and transport in the circular restricted three-body problem. Astrodynamics Specialist Conference and Exhibit (6431) (2008)

[117] Scott, C.J.: Transfer and capture into distant retrograde orbits. Ph.D. thesis, Pennsylvania State University (2010)

[118] Shewchuk, J.R.: Adaptive precision floating-point arithmetic and fast roboust geometric predicates. Discrete and Computational Geometry **18**(3), 305–363 (1997)

[119] Strange, N., Landau, D., McElrath, T., Lantoine, G., Lam, T.: Overview of mission design for nasa asteroid redirect robotic mission concept. International Electric Propulsion Conference (2013-321) (2013)

[120] Sundman, K.: Memoire sur le probleme des trois corps. Acta Mathematica **36**, 105–179 (1912)

[121] Szebehely, V.: Theory of orbits: The restricted problem of three bodies (1967)

[122] Tisserand, F.: Traite de mecanique celeste, 4 volumes (1889-1896)

[123] Vallado, D.A.: Fundamentals of Astrodynamics and Applications, 3rd edn. Microcosm Press, Hawthorne, CA (2007)

[124] Wallace, M.S., Parker, J.S., Strange, N., Grebow, D.: Orbital operations for phobos and deimos exploration. AIAA/AAS Astrodynamics Specialist Conference (AIAA 2012-5067) (2012)

[125] Weightman, J.: Gravity, geodesy and artificial satellites. a unified analytical approach. In: The use of artificial satellites for geodesy, vol. 1, p. 467 (1967)

[126] Welch, C., Parker, J.: Mission considerations for direct transfers to a distant retrograde orbit. AAS Guidance, Navigation and Control Conference (14-018) (2014)

[127] Werner, R.A.: The gravitational potential of a homogeneous polyhedron or don't cut corners. Celestial Mechanics and Dynamical Astronomy **59**(3), 253–278 (1994)

[128] Werner, R.A., Scheeres, D.J.: Exterior gravitation of a polyhedron derived and compared with harmonic and mascon gravitation representations of asteroid 4769 castalia. Celestial Mechanics and Dynamical Astronomy **65**(3), 313–344 (1996)

[129] Williams, J., Senent, J., Ocampo, C., Mathur, R., Davis, E.C.: Overview and software architecture of the copernicus trajectory design and optimization system. In: 4th International Conference on Astrodynamics Tools and Techniques, Madrid, Spain (2010)

[130] Wilson, R.: Derivation of differential correctors used in genesis mission design. Tech. Rep. JPL IOM 312.I-03-002, Jet Propulsion Laboratory (2003)

[131] Wong, L., Buechler, G., Downs, W., Sjogren, W., Muller, P., Gottlieb, P.: A surface-layer representation of the lunar gravitational field. Journal of Geophysical Research **76**(26), 6220–6236 (1971)

Appendix A

Fitted Functions for DRO Initial Conditions

A.1 Initial Velocity

Section 3.2.2.1 discusses a method for generating a fitted function that returns the initial velocity of a DRO given a distance from the minor body $r_0 \in [10^{-3}, 0.4]$ DU and the mass parameter $\mu \in [10^{-10}, 0.5]$ of the three-body system. The fitted function is a hyperbola with six coefficients determined by 6th degree polynomials. The initial velocity function has the form:

$$\dot{Y}_0 = 10^h \tag{A.1}$$

$$h = \frac{-b + \sqrt{b^2 - 4ac}}{2a} \tag{A.2}$$

$$a = c_3 \tag{A.3}$$

$$b = c_2 \log(\mu) + c_5 \tag{A.4}$$

$$c = c_1 \log(\mu)^2 + c_4 \log(\mu) + c_6 \tag{A.5}$$

where log() is the base-10 logarithm and the coefficients c_i are given by:

$$c_i = \sum_{j=0}^{6} k_{i,j} \log(r_0)^j \tag{A.6}$$

The coefficients $k_{i,j}$ are given in Table A.1.

$k_{i,j}$	$i=1$	2	3
$j=0$	5.1119914386372307e-04	-5.5601552088383126e-02	-1.3547445915790661e+00
1	2.0891127460026604e-03	-5.6272810967818532e-01	-2.3843094737662279e-01
2	-1.0156206813029603e-03	2.3206004003670975e+00	-4.7083300282660741e+00
3	-1.6946257302665774e-02	1.5447734205897878e+00	-2.743697230836347e+00
4	-9.9162988576834109e-03	2.7041061826287477e-01	-3.9112479498282521e-01
5	-3.1218882704583265e-03	1.698745765157764e-02	-4.9819738626386088e-03
6	-5.231140050309419e-04	2.5126223237367405e-03	-2.0314719487636774e-03
$k_{i,j}$	$i=4$	5	6
$j=0$	2.9561670261829948e-02	1.0252785742094457e+00	-2.0607607132606257e-01
1	4.5119488392609197e-01	1.8878815668117848e+00	-7.4038086483595777e-01
2	2.6155576007029691e-01	1.7519326105493216e+00	-7.6762461848716712e-01
3	-2.5764911916052258e+00	3.0474240174160796e+00	-8.2475707593595016e-02
4	-1.4730388628413056e+00	1.3473503615887157e+00	2.7313019622434416e+00
5	-2.1252014932181831e-01	1.5918753167029862e-01	1.5068671358590446e+00
6	-1.9785053574109045e-03	-1.1112858668501421e-03	2.0834170841963379e-01

Table A.1: The coefficients for use in Equations A.6.

A.2 Period

Section 3.2.2.2 describes the process of fitting a function to the period P of a DRO given the same range of mass parameters and initial distances from the minor body. The fitted function is a sigmoid curve, specifically having the form of the cumulative density function (CDF) for a skewed normal distribution:

$$P = 2\pi \left[\Phi\left(\frac{\log(\mu) - \mathbf{c}_1}{\mathbf{c}_2} \right) - 2T\left(\frac{\log(\mu) - \mathbf{c}_1}{\mathbf{c}_2}, \mathbf{c}_3 \right) \right]. \tag{A.7}$$

In this equation, $T(h,a)$ is Owen's T-function, given by

$$T(h,a) = \frac{1}{2\pi} \int_0^a \frac{\exp(-1/2h^2(1+x^2))}{1+x^2}\, dx \tag{A.8}$$

and $\Phi(x)$ is the CDF for a standard normal distribution, given by

$$\Phi(x) = \frac{1}{2}\left[1 + \operatorname{erf}\left(\frac{x}{\sqrt{2}} \right) \right], \tag{A.9}$$

Efficient algorithms for solving $T(h,a)$ have been researched.[92,96] The coefficient vector $\mathbf{c}$ is solved with a fifth degree polynomial:

$$\mathbf{c}_i = \sum_{j=0}^{5} k_{i,j} \log(r_0)^j, \quad i \in \{1,2,3\} \tag{A.10}$$

and the coefficients $k_{i,j}$ are given in Table A.2.

$k_{i,j}$	$i = 1$	2	3
$j = 0$	2.392044371551641000000e-01	-4.969869712178374700000e-01	-1.342949798316665500000e-01
1	5.445524705429766900000e+00	2.817547888735576500000e+00	4.516760632764377400000e+00
2	2.365706030421315600000e+00	2.821899282454266800000e+00	2.185995682808448600000e+00
3	1.141067060582275000000e+00	1.395531608084008300000e+00	1.762665407368104500000e-01
4	2.739757473536590900000e-01	3.407621075252023100000e-01	-1.022431940221859400000e-01
5	2.619841644637796100000e-02	3.289256930942190100000e-02	-1.579166592355155800000e-02

Table A.2: The coefficients for use in Equations A.10.